Inhomogeneous *d*-wave Superconductors

by

DAVID L. FEDER

B.Sc., M.Sc.

A Thesis
Submitted to the School of Graduate Studies
in Partial Fulfilment of the Requirements
for the Degree
Doctor of Philosophy

McMaster University
©Copyright by David L. Feder, 1997.

Inhomogeneous *d*-wave Superconductors

DOCTOR OF PHILOSOPHY (1997)
(Physics)

McMaster University
Hamilton, Ontario

TITLE: Inhomogeneous *d*-wave Superconductors

AUTHOR: David L. Feder

SUPERVISOR: Prof. Catherine Kallin

NUMBER OF PAGES: viii, 172

Abstract

Inhomogeneous superconductors with an order parameter of $d_{x^2-y^2}$ (d-wave) symmetry are investigated within the Ginzburg-Landau (GL) and Bogoliubov-de Gennes (BdG) formalisms. The inhomogeneities considered in detail are external magnetic fields, twin boundaries, and external currents. The Ginzburg-Landau equations are derived within the context of two microscopic lattice models used to describe the high-temperature superconductors: an extended Hubbard model and the Antiferromagnetic-van Hove model. Analytical results are obtained for the extended Hubbard model at low electron densities and weak to intermediate coupling. The variation of the coefficients in the GL equations with carrier density, temperature, and coupling constants are calculated numerically for both models. The anisotropic higher-order terms in the GL free energy are considered, with emphasis on the consequences for the structures of isolated vortices and the vortex lattice in the mixed-state. Twin boundaries are investigated numerically using the BdG formalism within the context of the extended Hubbard model. The twin boundaries are represented by tetragonal regions of variable width, with a reduced chemical potential. For sufficiently large twin boundary width and change in chemical potential, an induced s-wave component may break time-reversal symmetry at a low temperature T^*. The temperature T^*, and the magnitude of the imaginary component, are found to depend strongly on electron density. The results are compared with recent tunneling and transport measurements. The behaviour of d-wave superconductors in the presence of external currents is investigated numerically for both clean systems and those containing twin boundaries. The current response is studied with emphasis on critical currents and the superfluid density. The effect of the external currents on the subdominant s-wave components is characterized. Comparison is made with recent transport and tunneling measurements.

Acknowledgements

I am indebted to my supervisor, Prof. Catherine Kallin, for her guidance and encouragement throughout my graduate career. Her scientific perspective and integrity have profoundly affected my approach to theoretical research. I also appreciate her financial support, particularly during her research leave at Stanford University.

I am deeply grateful to Prof. Jules Carbotte for his superb courses in both superconductivity and many-body theory, and for his cheerful willingness to discuss superconductivity. I greatly appreciate Prof. John Berlinsky for his many insights and suggestions over the past few years. I would also like to thank Profs. John Preston, Bruce Gaulin, and Tom Timusk for their valuable comments as my thesis work progressed.

I would like to acknowledge the gracious hospitality of the Department of Physics at Stanford University. I am particularly indebted to Prof. Sandy Fetter, who has inspired me as a scientist. I am also grateful to Profs. Mac Beasley and Stanley Hanna for their guidance and advice.

It is impossible to thank all of the postdoctoral fellows and graduate students with whom I have been associated over the years, but without them both my work and my graduate experience would have suffered in countless ways. I especially appreciate the advice and encouragement of Lee-Wen Chen, Marcel Franz, Mark Kvale, Silvio Rabello, Markku Salkola, Pekka Soininen, and Wen-Chin Wu, as well as Peter Arberg, Bill Atkinson, Andy Beardsall, Dwayne Branch, Hamish Johnston, Chris Mathers, Ian McDonald, Chris O'Donovan, Rachid Ouyed, and Keqing Zhang.

No words could sufficiently convey the profound influence that Pina Colarusso has had on my life and work. This thesis is dedicated to her.

Contents

List of Figures

Chapter 1

Introduction

Just over a decade ago, the first of an intriguing new family of superconductors was discovered [1]. The compound was $La_{1.85}Ca_{0.15}CuO_4$, with a superconducting transition temperature $T_c = 30$ K which was 7 degrees higher than that of the previous record-holder, Nb_3Ge. A large number of similar materials subsequently have been discovered, and are collectively referred to as cuprate, oxide, or high-T_c superconductors. All share a perovskite structure characterized by copper-oxygen layers, and have unusually high superconducting transition temperatures (often well above the boiling point of liquid nitrogen, 77 K). Indeed, transition temperatures as great as $T_c \approx 240$ K have been reported for certain Bi and Hg-based materials under high pressure [2, 3].

While there are presently many cuprate superconductors, only a few are actively studied. These are $La_{2-x}Sr_xCuO_4$ (known as LSCO, maximum $T_c = 38$ K), $YBa_2Cu_3O_{6+x}$ (known as YBCO or 123, maximum $T_c = 93$ K), $Bi_2Sr_2CaCu_2O_{8+x}$ (known as BSCCO or Bi 2212, maximum $T_c = 94$ K), and $Tl_2Ba_2Ca_2Cu_3O_{10+x}$ (known as Tl 2223, maximum $T_c = 125$ K). These 'hole-doped' materials are the subject of this thesis. Their structure is presented in a simplified manner in Table 1.1 [4]. The recently-discovered superconducting perovskites without copper-oxide planes (such as compounds based on $BaBiO_3$, maximum $T_c = 30$ K) and the 'electron-doped' superconductors (based on Nd_2CuO_4, maximum $T_c = 20$ K) will not be discussed in the present work.

$La_{2-x}Sr_xCuO_4$	$YBa_2Cu_3O_{6+x}$	$Bi_2Sr_2CaCu_2O_{8+x}$	$Tl_2Ba_2Ca_2Cu_3O_{10+x}$
LSCO	YBCO, 123	BSCCO, 2212	Tl 2223
$T_c = 38$ K	$T_c = 93$ K	$T_c = 94$ K	$T_c = 125$ K
$a = 3.78$ Å	$a = 3.86$ Å	$a = 3.9$ Å	$a = 3.9$ Å
$c = 13.2$ Å	$c = 11.65$ Å	$c = 30.8$ Å	$c = 36$ Å
			CuO_2
	CuO_2	CuO_2	Ca
CuO_2	Y	Ca	CuO_2
	CuO_2	CuO_2	Ca
			CuO_2
(La/Sr)O	BaO	SrO	BaO
(La/Sr)O	CuO_x	$BiO_{1+x/2}$	$TlO_{1+x/2}$
	BaO	$BiO_{1+x/2}$	$TlO_{1+x/2}$
		SrO	BaO

Table 1.1: The structure of the most widely-studied cuprate superconductors is shown schematically. Each line corresponds to an *ab*-oriented layer in the unit cell, stacking in the *c*-direction. Unit cell lengths are given for the tetragonal phases, $x = 0$. Note that the transition temperature roughly correlates with the number of copper-oxide planes.

The cuprate superconductors have several common characteristics that immediately distinguish them from their low-T_c counterparts. Aside from high transition temperatures, these materials have extremely anisotropic and unusual transport properties in both the normal and superconducting states, great sensitivity to (low) carrier concentration, and short superconducting coherence lengths. A complete theory of the high-T_c compounds incorporating all of these features remains elusive; in fact, even the mechanism for the superconductivity is presently uncertain. Mounting experimental evidence, however, suggests that the high-T_c materials have a superconducting order parameter with an anisotropic, specifically $d_{x^2-y^2}$, symmetry. It is the goal of the present thesis to elucidate how such an unconventional order parameter symmetry affects the properties of superconductors in the presence of inhomogeneities, such as external magnetic fields, twin boundaries, and external currents.

1.1 Properties of High-T_c Superconductors

1.1.1 Normal State

Perhaps the most striking feature shared by all the high-T_c superconductors is that the parent states of these materials, which are stoichiometric with $x = 0$, are found experimentally to be insulating at low temperatures. In contrast, conventional theory predicts metallic behaviour since only 9 electrons occupy the Cu 3*d* shell, leaving one hole per unit cell. Band structure calculations indicate that the uppermost bands are predominantly composed of strongly hybridized copper $3\mathrm{d}_{x^2-y^2}$ and oxygen $2\mathrm{p}_x$, $2\mathrm{p}_y$ orbitals oriented in the $\mathrm{CuO_2}$ planes, as shown in Fig. 1.1. The theoretical results indicate large (approximately 3 eV) bandwidths, and highly anisotropic dispersions virtually independent of k_z, where $z \parallel c$ is the direction perpendicular to the *ab*-oriented copper-oxide planes [5, 6]. In addition, the cuprates all have small densities of states at the Fermi surface: $2N(0) \approx 1$, 1.2, 1.5, and 2.5 states/eV/$\mathrm{CuO_2}$ plane for Tl 2223, BSCCO, LSCO, and YBCO respectively [6]. In theory, the electronic properties of all the parent compounds appear to be well-described by a single, half-filled, two-dimensional band with an anisotropic Fermi surface, associated with a metallic CuO_2 layer [7, 8, 9, 10].

Most calculations neglect strong (non-perturbative) electronic correlations which could drastically alter the picture of extended electronic states in a conducting band. The effect of the Coulomb repulsion, for example, may be incorporated within the context of the single-band repulsive Hubbard model [11]:

$$\mathcal{H}_{\rm Hub} = -t \sum_{ij\sigma} t_{ij} c^{\dagger}_{j\sigma} c_{i\sigma} - \mu \sum_{i\sigma} n_{i\sigma} + U \sum_{i} n_{i\uparrow} n_{i\downarrow}, \tag{1.1}$$

where $c_{i\sigma}$ annihilates an electron with spin σ at site i, and the density operator $n_{i\sigma} = c^{\dagger}_{i\sigma} c_{i\sigma}$ tests whether a given site is occupied. The chemical potential fixes the carrier density. When the on-site Coulomb repulsion U is zero, the Hubbard Hamiltonian describes electrons hopping between nearby copper sites with a probability t, which is the effective 'transfer integral' characterizing the overlap of nearby atomic orbitals. In the approximation where only z nearest atomic neighbours have any finite overlap, the non-interacting electrons occupy a tight-binding band of width $2zt$ (the coordination number $z = 4$ in the cuprates). As U increases, however, the energetic cost of electrons occupying the same site grows. The carriers become more tightly-bound to their site, and the effective overlap between orbitals decreases. At half-filling $\langle n \rangle = 1$ and $U = \infty$, each spin $S = 1/2$ electron is localized to a copper site. It has been shown that the ground state of this system is a Mott-Hubbard insulator, with adjacent spins antiferromagnetically oriented [12].

Magnetic neutron scattering experiments [13] confirm the theoretical predictions that the parent compounds are in fact three-dimensional antiferromagnetic (AFM) insulators, demonstrating strong electronic correlations both within and between the copper-oxide layers. The Néel temperatures are $T_N = 300$ K and $T_N = 400$ K for LSCO and YBCO, respectively. The low-lying excitations are interpreted as the spin-waves of a highly anisotropic Heisenberg Hamiltonian [13, 14, 15, 16]:

$$\mathcal{H}_{\rm Heis} = \sum_{\langle ij \rangle} J_{ij} \mathbf{S}_i \mathbf{S}_j, \tag{1.2}$$

where the sum $\langle ij \rangle$ is over nearest-neighbours only. The (nearest-neighbour) Heisenberg exchange coupling $J_{ij} = 4t^2/U$ may be derived from the Hubbard model [12].

Since $J_{ij} > 0$, the Heisenberg model favours adjacent spins with opposite orientation, or antiferromagnetism. While the intralayer coupling is found to be approximately 100 meV, the interlayer coupling is a factor of order 10^{-4} smaller, giving rise to essentially two-dimensional spin-wave excitations [17]. A large on-site repulsion $U \approx 6$ eV is implied by the experiments; since $U \sim 2zt$ is comparable to the bandwidth, electronic correlations are indeed strong in these systems.

A small variation of the stoichiometry rapidly suppresses the long-range antiferromagnetic order. As x increases, T_N is found experimentally to decrease rapidly [13, 15]. At the same time, the materials begin to exhibit metallic properties, and become superconducting for $x \approx 0.05$ in LSCO and $x \approx 0.4$ in YBCO. For small x, AFM correlations persist in the form of antiferromagnetic spin fluctuations, as found in NMR [18], magnetic neutron [19], and Raman [20] experiments. The change in the stoichiometry is believed to remove electrons from the copper sites, creating holes in the antiferromagnetic copper-oxide layers. Even at low concentrations, mobile holes are known to effectively destroy long-range antiferromagnetic order [21]. The mechanism for this can be simply understood in terms of frustration [22]. As holes propagate through the AFM background, they leave a trail of ferromagnetically-coupled spins, locally frustrating the energetically-favoured AFM order.

For very small x, the dispersion of the holes is determined theoretically by minimizing the energy cost of weakening the background AFM order. Numerical and exact-diagonalization studies are usually carried out within the context of the Hubbard model (1.1) or the $t - J$ model [7]:

$$\mathcal{H}_{t-J} = -t \sum_{ij\sigma} t_{ij} c^{\dagger}_{j\sigma} c_{i\sigma} + \sum_{\langle ij \rangle} J_{ij} \left(\mathbf{S}_i \mathbf{S}_j - \frac{1}{4} n_i n_j \right) , \tag{1.3}$$

which is simply the Heisenberg model including charge transport. Numerical calculations within the $t-J$ model indicate that the hole dispersion $\varepsilon(\mathbf{k})$ is well-approximated by [23, 24, 25]:

$$\varepsilon(\mathbf{k}) \approx t_{\text{eff}} \left(\cos k_x + \cos k_y \right)^2 , \tag{1.4}$$

where $t_{\text{eff}} \approx J/2$. This result corresponds to a tight-binding model of holes hopping between second and third nearest-neighbours. The AFM order is preserved, since the holes remain on a single spin sublattice [26]. The minimum of the hole band is located at the wavevector $(k_x, k_y) = (\pi/2, \pi/2)$ and symmetry-related points [27]. More recent exact diagonalization studies confirm the prediction of 'hole pockets' at this band minimum, but yield a more complicated dispersion with extremely flat bands near $(0, \pi)$ and symmetry-related points [28, 29, 30, 31]. With increasing hole concentration, the hole pockets gradually evolve into a large hole Fermi surface centered at the antiferromagnetic wavevector $Q = (\pi, \pi)$, or equivalently a large electronic Fermi surface centered at $(0, 0)$ that is virtually identical to that of the non-interacting case [32, 33], with electron dispersion:

$$\varepsilon(\mathbf{k}) = -2t\left(\cos k_x + \cos k_y\right). \tag{1.5}$$

Angle-resolved photoemission spectroscopy (ARPES) experiments have confirmed the theoretical dispersion relations. Measurements on highly underdoped ($x \sim 0$) BSCCO reveal Fermi surface edges only along the diagonals of the Brillouin zone $(k_x, \pm k_y)$, and not at the corners $(0, \pm\pi)$ or $(\pm\pi, 0)$ [34, 35]. A very flat quasiparticle dispersion is found in the vicinity of $(0, \pi)$, in agreement with theory [36, 37]. The evolution of the Fermi surface with increasing x from small hole pockets to a large area centered at (π, π) has also been observed [36, 38, 39].

At intermediate stoichiometries, the high-T_c oxides have transport properties above T_c that are quite different from those of conventional superconductors. The resistivity, Hall effect, and thermopower are unlike those of ordinary metals. The resistivity $\rho(T)$ is found to have a linear temperature-dependence over a wide range of temperatures, except for $x \sim 0$ where the cuprates become insulators, and for $x \gg 0$ where $\rho(T) \sim T^2$ [40, 41]. In metals, the resistivity at low temperatures is usually proportional to T^n, where $n = 2$ or higher. The resistivities are also highly anisotropic: while the results depend somewhat on the doping, experimental data suggest $\rho_c/\rho_a \approx 10^5$, 200, 100, and 35 for BSCCO, LSCO, Tl 2223, and YBCO, respectively [40, 42, 43]. There is also pronounced in-plane anisotropy of both the resistivity $\rho_a/\rho_b \approx 2$ and conductivity $\sigma_a/\sigma_b \approx 0.4$ as x approaches unity in YBCO [41, 44]. The additional charge transport is due to the formation of b-oriented CuO_x chains (one chain per unit cell in addition to the two CuO_2 planes) that become increasingly ordered with oxygen doping. The resistivity data are corroborated by thermal conductivity measurements, which find a temperature-independent in-plane anisotropy $\kappa_b/\kappa_a \approx 1.5$ [45, 46]. The sign of the Hall coefficient R_H changes from positive to negative as x is increased from zero, reflecting the crossover from p-type to n-type carriers with doping [47]. In addition, the behaviours of R_H and the Hall angle θ_H [48], as well as that of the Seebeck coefficient S defining the thermopower [49], do not match those of conventional superconductors.

1.1.2 Superconducting State

Before briefly reviewing the plethora of fascinating and important differences between the superconducting properties of the cuprates and those of conventional metals, it is important to stress that the high-T_c superconducting state is in many respects quite standard. The characteristic discontinuity in the specific heat at the transition temperature T_c indicates the onset of a three-dimensional, bulk superfluid [50]; the phase transition belongs to the usual 3DXY-universality class [51]. The condensation is due to paired electrons, since the superconducting flux quantum is found to be $\phi_0 = hc/2e \approx 2 \cdot 10^{-7}$ G·cm^2 [52, 53], and the superconducting order parameter is a spin-singlet [54, 55, 56]. As expected, the resistivity drops to zero at T_c [41, 57], below which these materials are able to support current densities comparable with those of conventional superconductors [58]. The cuprates are all strongly type-II superconductors, exhibiting a perfect diamagnetic response below the lower critical field H_{c1} [59, 60, 61].

This superficial description of the cuprates' superfluid behaviour belies the unusual characteristics of the condensed state, which are inevitably found in the details. The most obvious of these are the unusually high superconducting transition temperatures; prior to 1986, the largest known $T_c = 23$ K had been found for Nb_3Ge. Furthermore, the transition temperatures for the cuprates are highly-dependent on stoichiometry; while for $x = 0$ the parent compounds are Mott insulators, as x increases the AFM correlations diminish and a superconducting instability appears. The associated transition temperature is a non-monotonic function of x, reaching a maximum at 'optimal doping' x_{opt}, and is smaller in both the 'underdoped' $x < x_{\text{opt}}$ and 'overdoped' $x > x_{\text{opt}}$ cases. While the value of x associated with the superconducting onset and T_c^{max} varies among the cuprates, the dependence on the number of charge carriers per site n is quite universal; superconductivity first appears for $n \approx 0.05$, while T_c^{max} occurs when $n \approx 0.15 - 0.20$ [62, 63]. It is striking that high transition temperatures are obtained in spite of the low density of charge carriers.

The high-T_c materials are characterized by extremely short superconducting coherence lengths. The zero-temperature coherence length $\xi(0)$ is often defined in terms of the upper critical field H_{c2} through $H_{c2}(0) \equiv \phi_0/2\pi\xi^2(0)$ [64]. Since the high-T_c materials have such large upper critical fields at all temperatures $T < T_c$, however, the precise values of the coherence lengths are difficult to determine. Extrapolation of resistivity data yields $H_{c2}^{c}(0) \approx 120$ T and $H_{c2}^{ab}(0) \approx 670$ T for fields along the c-axis and in the ab-plane respectively [65, 66]. By implication the coherence lengths are $\xi_{ab}(0) \approx 16$ Å $\approx 4a$ in the ab-plane and $\xi_c(0) \approx 7$ Å in the c-direction, where the latter is of the same order as the interplane distance. The size of $\xi(0)$ approximately measures the spatial extent of the Cooper pair, so the superconductivity will be locally sensitive to the presence of defects, such as impurities and weak links. Yet, the Bose-like character of the small Cooper pairs could be partially responsible for the large transition temperatures [67, 68].

The penetration depth $\lambda(T)$, the characteristic length scale for spatial variations of a magnetic field inside a superconductor, also provides a great deal of information about the superconducting properties of the cuprates. In particular, the zero-temperature penetration depths are all long compared to those found in conventional superconductors: $\lambda_c(0) \approx 5500$ Å in the c-direction, while $\lambda_a(0) \approx 1500$ Å, 2200 Å, and 3100 Å in the a-direction for optimally-doped YBCO, Tl 2223, and BSCCO, respectively; in YBCO, there is additional ab-plane anisotropy $\lambda_a/\lambda_b \approx 1.5$ [69, 70, 71, 72]. In contrast, clean aluminum, tin, and lead have penetration depths of 500 Å, 510 Å, and 390 Å, respectively [73]. The long penetration depths are due in part to the small number of charge carriers, which limits the formation of the diamagnetic screening currents required to expel the magnetic field. The quasi-two dimensional distribution of the charge carriers may be responsible for the long penetration depths in the *ab*-plane, since the charge density decreases with increasing interlayer separation. The pronounced anisotropy of the penetration depth reflects the normal-state properties, indicating weak interplane coupling but enhanced superconducting transport in the CuO_2 layers and along the *b*-oriented CuO chains in optimally-doped YBCO. Further evidence for anisotropic superconductivity comes from measurements of the lower critical field H_{c1} (the magnetic field at which vortices begin to penetrate the material), which indicate that the maximum screening currents generated in the *ab*-plane $I_c^{ab} \approx 2.5 \cdot 10^{11}$ A/m^2 are an order of magnitude larger than their *c*-axis counterparts [59, 60].

Since the coherence lengths are much shorter than the penetration depths, the Ginzburg-Landau parameter $\kappa(T) \equiv \lambda(T)/\xi(T) \gg 1$. Thus, the high-$T_c$ materials are all strongly type-II superconductors and are well-described by London, or local, electrodynamics (see Sections 2.1 and 3.2). In this regime, the inverse-square of the (London) penetration depth is proportional to the superfluid density n_s: $\lambda_a^{-2}(0) = 4\pi e^2 n_s/m_a^* c^2$, where m^* is the effective mass of the quasiparticles. From ARPES [74, 75], de Haas-van Alphen [6, 76], and optical data [77], one infers $m^* \approx 4m_e$ for optimally-doped cuprates (where m_e is the bare electron mass). Since naïve band-structure calculations predict $m^* \sim m_e$, the large renormalization of the quasiparticle mass suggests a strong interaction of the quasiparticles with an intrinsic bosonic mode, such as phonons or spin fluctuations. With the normal-state density $n(0) \approx 5 \cdot 10^{21}$ cm^{-3} and $m_a^* \approx 4m_e$, one obtains $n_s/n(0) \sim 1$ demonstrating the robustness of the superfluidity. In addition, the transition temperature of the cuprates is found to scale with the superfluid density [78]; this behaviour is inconsistent with the predictions of Bardeen, Cooper, and Schrieffer's (BCS) theory describing conventional superconductors [79], and has been cited as evidence for an unconventional pairing mechanism in the high-T_c superconductors [80]. Indeed, as will be discussed in the next two sections, experimental evidence indicates that the superconducting state of the high-T_c materials is not well-described by a conventional BCS theory.

1.2 Why *d*-wave superconductivity?

In general, the Cooper-pair wavefunction, or superconducting gap function, is written as a direct product of orbital and spin degrees of freedom [81]:

$$\Delta(\mathbf{r}_1\,,\,\mathbf{r}_2) \equiv V_{\mathbf{r}_1\mathbf{r}_2}\ {}_{N-2}\langle c_\downarrow(\mathbf{r}_1)c_\uparrow(\mathbf{r}_2)\rangle_N = \varphi(\mathbf{r}_1 - \mathbf{r}_2)\frac{(\uparrow\downarrow - \downarrow\uparrow)}{\sqrt{2}}e^{i\mathbf{p}_{\rm cm}\cdot(\mathbf{r}_1+\mathbf{r}_2)/2}, \qquad (1.6)$$

where $V_{\mathbf{r}_1\mathbf{r}_2}$ measures the interaction between the fermions on site $\mathbf{r}_1$ and $\mathbf{r}_2$, $\langle\ldots\rangle$ denotes an expectation value in the N-particle ground-state, φ is the orbital wavefunction dependent only on the relative coordinate, and $\mathbf{p}_{\rm cm}$ is the center-of-mass momentum of the Cooper pair. Since the spin wavefunction for the cuprates is a singlet, as mentioned above [54, 55, 56], the orbital wavefunction must be symmetric in order to guarantee the overall antisymmetry of the gap function Δ. Thus, allowed orbital momenta are $l = 0, 2, \ldots$, corresponding to *s*-, *d*-, *g*-,... wave states in spectroscopic notation. It must be kept in mind, however, that the definite angular momentum of the state is ill-defined, due to the presence of the crystal field; rather, the gap function and the superconducting order parameter should be interpreted as having $s/d/g$-wave symmetry:

$$\varphi(\mathbf{r}_1 - \mathbf{r}_2) = \sum_{\mathbf{k}} \varphi_k e^{i\mathbf{k}\cdot(\mathbf{r}_1-\mathbf{r}_2)}, \qquad (1.7)$$

where φ_k is an $s/d/g$-wave basis function in k-space satisfying the point group symmetry of the crystal.

The high-T_c superconductors are either tetragonal (for small x) with crystal symmetry I4/mmm and point group D_{4h}, or weakly orthorhombic with space group Abma (LSCO) or Pmmm (YBCO) and point group D_{2h} [82, 83, 84]. Assuming that the superconductivity resides predominantly in the CuO_2 planes, as indicated by the observed anisotropy in transport (see previous sections), any k_z-dependence may be neglected. For D_{4h}, and assuming singlet pairing, one obtains the one-dimensional irreducible representations [85]:

$$\varphi_k = \begin{cases} \text{const} & \text{isotropic } s\text{-wave } (\Gamma_1^+), \\ \cos k_x + \cos k_y \sim k_x^2 + k_y^2 & \text{extended } s\text{-wave } (\Gamma_1^+), \\ \cos k_x - \cos k_y \sim k_x^2 - k_y^2 & d\text{-wave } (\Gamma_3^+), \\ \cos k_x \cos k_y \sim k_x^2 + k_y^2 & s_{xy}\text{-wave } (\Gamma_1^+), \\ \sin k_x \sin k_y \sim k_x k_y & d_{xy}\text{-wave } (\Gamma_4^+), \\ \sin k_x \sin k_z \sim k_x k_z & d_{xz}\text{-wave } (\Gamma_5^+), \\ \sin k_y \sin k_z \sim k_y k_z & d_{yz}\text{-wave } (\Gamma_5^+), \end{cases} \tag{1.8}$$

where the Γ_5^+ representation has been included for completeness. In the point group symmetry D_{4h}, the isotropic s-wave, extended s-wave, and s_{xy}-wave basis functions belong to the trivial Γ_1^+ representation; these components of the total order parameter are linearly-dependent in tetragonal systems. In the lower point group D_{2h}, the d-wave basis function also belongs to Γ_1^+, while $d_{xz} \in \Gamma_2^+$, $d_{xy} \in \Gamma_3^+$, and $d_{yz} \in \Gamma_4^+$.[1] Thus, both s-wave and d-wave gap functions will be subcomponents of the total order parameter in orthorhombic superconductors [85].

In order to motivate why the high-T_c materials might have an order parameter with d-wave symmetry, it is instructive to consider the (gauge-covariant) real-space representations of Δ with the symmetries defined in (1.8):

$$\text{isotropic } s\text{-wave:} \quad \Delta_0(\mathbf{r}) \equiv V_0\langle c_\downarrow(\mathbf{r}) c_\uparrow(\mathbf{r})\rangle; \tag{1.9}$$

$$\text{extended } s\text{-wave:} \quad \Delta_s(\mathbf{r}) \equiv \frac{1}{4}\Big[\Delta_x(\mathbf{r}) + \Delta_{-x}(\mathbf{r}) + \Delta_y(\mathbf{r}) + \Delta_{-y}(\mathbf{r})\Big]; \tag{1.10}$$

$$d\text{-wave:} \quad \Delta_d(\mathbf{r}) \equiv \frac{1}{4}\Big[\Delta_x(\mathbf{r}) + \Delta_{-x}(\mathbf{r}) - \Delta_y(\mathbf{r}) - \Delta_{-y}(\mathbf{r})\Big]; \tag{1.11}$$

$$s_{xy}\text{-wave:} \quad \tilde{\Delta}_s(\mathbf{r}) \equiv \frac{1}{4}\Big[\Delta_{x-y}(\mathbf{r}) + \Delta_{-x+y}(\mathbf{r}) + \Delta_{x+y}(\mathbf{r}) + \Delta_{-x-y}(\mathbf{r})\Big]; \tag{1.12}$$

$$d_{xy}\text{-wave:} \quad \tilde{\Delta}_d(\mathbf{r}) \equiv \frac{1}{4}\Big[\Delta_{x-y}(\mathbf{r}) + \Delta_{-x+y}(\mathbf{r}) - \Delta_{x+y}(\mathbf{r}) - \Delta_{-x-y}(\mathbf{r})\Big], \tag{1.13}$$

---

[1] Throughout this thesis, extended s-wave and d-wave are taken to represent $s_{x^2+y^2}$-wave and $d_{x^2-y^2}$-wave, respectively.

where $\mathbf{r}$ is the center-of-mass coordinate, and the relative coordinate is the subscript of the 'bond gap functions':

$$\Delta_\delta(\mathbf{r}) \equiv V_\delta \langle c_\downarrow(\mathbf{r}) c_\uparrow(\mathbf{r}+\hat{\delta})\rangle. \tag{1.14}$$

In a uniform system with directionally-independent bond couplings, all the bond gaps will have equal magnitudes. The Fourier transform of the relative coordinate yields:

$$\begin{aligned}
\Delta_0(\mathbf{r}) &= \sum_{\mathbf{k}} \Delta(\mathbf{r},\mathbf{k}); && (1.15)\\
\Delta_s(\mathbf{r}) &= \frac{1}{2}\sum_{\mathbf{k}} \Delta(\mathbf{r},\mathbf{k})(\cos k_x + \cos k_y); && (1.16)\\
\Delta_d(\mathbf{r}) &= \frac{1}{2}\sum_{\mathbf{k}} \Delta(\mathbf{r},\mathbf{k})(\cos k_x - \cos k_y); && (1.17)\\
\tilde{\Delta}_s(\mathbf{r}) &= \sum_{\mathbf{k}} \Delta(\mathbf{r},\mathbf{k}) \cos k_x \cos k_y, && (1.18)\\
\tilde{\Delta}_d(\mathbf{r}) &= \sum_{\mathbf{k}} \Delta(\mathbf{r},\mathbf{k}) \sin k_x \sin k_y, && (1.19)
\end{aligned}$$

where

$$\Delta(\mathbf{r},\mathbf{k}) = V\langle c_{\mathbf{k}\downarrow}(\mathbf{r}) c_{-\mathbf{k}\uparrow}(\mathbf{r})\rangle. \tag{1.20}$$

The real-space definitions of the gap functions (1.9)-(1.13) demonstrate that an unconventional gap function symmetry is a consequence of electrons pairing on nearby sites. Only in the isotropic s-wave case do electrons pair on the same site; the extended s-wave and d-wave gaps arise from nearest-neighbour pairing, while the s_{xy}-wave and d_{xy}-wave gaps result from next-nearest-neighbour pairing. The pairing along bonds ensures that the lobes of the unconventional gap functions are oriented with the underlying lattice. The lobes point along the [100]- and [010]-directions for the extended s-wave and d-wave, and along the [110]- and [$1\bar{1}0$]-directions for s_{xy}-wave and d_{xy}-wave. Thus, in systems such as the cuprates where electron-electron correlations are significant, one would expect the condensate wavefunction to have unconventional symmetry in order to minimize the energy associated with the large on-site Coulomb repulsion. The order parameter symmetry of the physical system depends on the nature of the pairing potential.

The real-space argument for unconventional gap symmetry is valid only if the bosons mediating the pairing give rise to an instantaneous interaction. In conventional superconductors, electrons comprising the Cooper pair minimize the Coulomb repulsion by avoiding not only short-range, but also short-time interactions. Although phonons provide this retarded BCS pairing mechanism, they do not appear to play as prominent a role in the cuprates. The experimental evidence suggests that the magnitude of the isotope effect (the 'smoking gun' of a phonon-pairing mechanism) is inversely correlated with the size of T_c as x is varied, i.e. is a minimum at optimal doping [86, 87, 88]. In addition, phonon-mediated interactions are usually associated with long superconducting coherence lengths, as can be shown using a variant of Faber and Pippard's original argument [89]. The coherence length may be estimated from the uncertainty principle, $\xi \delta p \sim \hbar$. The momenta $\delta p \sim \hbar\omega_D / v_F$ of electrons participating in the condensation are in a range governed by the Debye energy $\hbar\omega_D$, the cutoff of the phonon-pairing interaction. Thus, one obtains $\xi \sim \hbar v_F / \hbar\omega_D$; since the Debye energy is much smaller than the Fermi energy, the coherence length is long. In contrast, instantaneous interactions generally have no intrinsic cutoff except (perhaps) the bandwidth, which is much larger than $\hbar\omega_D$, yielding much shorter coherence lengths.

While the mechanism for high-T_c superconductivity is controversial, there is some evidence suggesting that antiferromagnetic spin fluctuations may be important. A large quantity of theoretical work on the large-U Hubbard (1.1) and $t - J$ (1.3) models demonstrates that the ground state of these systems is an antiferromagnetic insulator at half-filling, and for small hole concentrations $\langle n \rangle < 1$ the system becomes a superconductor with an order parameter of d-wave symmetry (for excellent reviews on this subject, the reader is referred to [29, 81, 90]). Weak coupling arguments indicate that d-wave superconductivity may be favoured by the exchange of AFM spin fluctuations [91, 92]. The experimental evidence for this pairing mechanism is presently unclear, however. While short-range AFM correlations are found in the superconducting state of underdoped samples, they may be wholly absent at optimal doping [18, 19, 20].

1.3 Experimental Evidence for *d*-wave

Over the past few years, the symmetry of the superconducting order parameter in the cuprates has been the subject of furious debate. Experimental evidence is beginning to resolve the issue, however, in favour of an order parameter with d-wave symmetry. The experiments may be roughly divided into two categories: those that yield superconducting properties most compatible with a d-wave gap function (indirect experiments), and those that are able to explicitly determine the sign changes associated with d-wave symmetry (direct experiments). A summary of the experimental evidence for d-wave superconductivity in the high-T_c materials is sketched below; further details may be found in the recent reviews [81, 93, 94, 95, 96].

1.3.1 Indirect Evidence

Most experiments attempting to indirectly determine the symmetry of the superconducting order parameter search for evidence of line nodes in the gap function (extended regions in k-space where the superconductor is gapless). Line nodes are a common feature of unconventional gap function symmetries, such as extended s-wave (with nodes along $|k_x| = |k_y - \pi|$), d-wave ($|k_x| = |k_y|$), and d_{xy}-wave ($k_x = 0$, $k_y = 0$). In conventional superconductors, the number of excitations at low temperatures is exponentially activated $\sim e^{-\Delta/k_BT}$ due to the presence of a non-zero gap. When the gap has line nodes, however, the low-energy excitations lead to power-law temperature dependences of many physical observables.

The low-temperature behaviour of the penetration depth in the cuprates strongly suggests a gap with line nodes. In very clean samples of optimally-doped YBCO and BSCCO at low temperatures, a linear magnetic field-dependence of the penetration depth [97], and linear temperature dependence of the superfluid density $n_s/n \propto \lambda^2(0)/\lambda^2(T) \sim 1 - T/T_c$ was observed [98], consistent with theoretical predictions for a gap with line nodes [99, 100, 101, 102]. In contrast, the low-temperature superfluid density is essentially independent of temperature in conventional superconductors due to the absence of low-lying excitations. The temperature-dependence crosses over from linear to quadratic with the addition of non-magnetic impurities such as Zn and Co, however [103, 104, 105]. While such a crossover is evidently due to additional low-energy states caused by pair-breaking, the superfluid density of s-wave superconductors cannot be significantly affected by non-magnetic impurities by Anderson's theorem [106]. The results are more consistent with d-wave superconductors, where non-magnetic impurities are pair-breakers due to the destructive interference between the positive and negative lobes of the d-wave gap function [107, 108] (this is described in more detail in Section 4.5).

Additional experiments indicate the presence of gap nodes in the cuprates. The temperature-dependence of the specific heat is linear at low temperatures, rather than exponentially activated [109]. Consequently, the entropy gleaned from specific heat measurements falls more slowly than would be found in conventional superconductors [50]. A linear excitation spectrum is consistently obtained in single-particle tunneling experiments [110, 111, 112]. A commonly-observed zero-energy conductance peak (ZBCP) in the tunneling spectra has been interpreted as evidence for d-wave superconductivity [113], though such a feature is consistent with any gap function that changes sign (further discussion of the ZBCP may be found in Section 4.5). ARPES data clearly shows that the quasiparticles experience no gap when moving along the diagonals of the Brillouin zone, but a large gap along the $(0,\pi)$- and $(\pi,0)$-directions [38, 114]. From NMR, the absence of a coherence (Hebel-Slichter) peak in nuclear spin-relaxation rates, and the linear temperature-dependence of the spin-susceptibility obtained from the Knight shift, are most likely due to the presence of gap nodes [115, 116].

1.3.2 Direct Evidence

The most convincing evidence for d-wave superconductivity in the cuprates has been obtained from experiments sensitive to changes in the sign of the gap function [95, 96]. All of the experiments are based on the fact that the phase of the

d-wave order parameter differs by π between the [100]- and [010]-directions of the CuO_2 plane because the lobes of the gap function are aligned with the crystal axes. Under suitable conditions, this phase shift can lead to observable interference and frustration effects.

Direct confirmation of the π-phase shift has been obtained by dc SQUID (superconducting quantum interference device) measurements [95, 117, 118]. In these experiments, tunnel junctions are affixed to the (100) and (010) surfaces of a c-oriented optimally-doped YBCO sample. The two junctions are joined by a conventional s-wave superconductor, and the flux enclosed by the composite superconducting loop is measured as a function of applied bias current (alternatively, the supercurrent is measured as a function of applied field). If YBCO were an s-wave superconductor, the supercurrent should be a maximum in the absence of an applied field H. If YBCO were a d-wave superconductor, a positive lobe of the d-wave gap function would face one junction, while a negative lobe would face the other; the resulting destructive interference should yield zero supercurrent when $H = 0$, but a maximum current for $H = \phi_0/2 = \pi$. While there are many complicating factors, such as twin boundaries (which will be discussed at length in Chapter 4), orthorhombicity (where the admixture of the s-wave and d-wave components shifts the directions of the line nodes), and trapped flux, the results agree extremely well with d-wave pairing in YBCO.

The interference effect described above has interesting and observable consequences for granular d-wave superconductors, i.e. high-T_c samples composed of many c-axis superconducting domains (called grains) with arbitrary ab-plane orientations. As the grain boundary misorientation angle increases, the critical currents should decrease, reaching a minimum at 45° where there is complete frustration caused by interference between the positive and negative lobes facing the junction. In order to maintain high critical currents across the grain boundary, the d-wave superconductor would prefer to spontaneously generate a magnetic vortex $h = \phi_0/2$ in the junction. These half-integer flux quanta have been observed for special grain-boundary geometries in YBCO and tetragonal Tl 2201 by several groups using scanning SQUID microscopy [119, 120] (further details of this effect may be found in Section 4.1.2). Furthermore, the presence of the spontaneous flux at misoriented grain boundaries should give rise to diamagnetic supercurrents attempting to screen the magnetic field. Indeed, the observed paramagnetic response to applied magnetic fields (the Wohlleben effect [121, 122]) has been cited [96] as evidence for *d*-wave superconductivity in the cuprates.

1.4 Outline

The high-T_c materials are thought to be *d*-wave superconductors, characterized by short coherence lengths and highly two-dimensional transport. In this thesis, the behaviour of such superconductors in the presence of inhomogeneities is investigated both analytically and numerically. External magnetic fields, twin boundaries, and external currents are considered in Chapters 3, 4, and 5, respectively.

In Chapter 2, the phenomenological Ginzburg-Landau (GL) theories describing inhomogeneous conventional and *d*-wave superconductors are reviewed. The GL predictions for the behaviour of *d*-wave materials in external magnetic fields are outlined in Section 2.3, with emphasis on the structures of isolated magnetic vortices and the vortex lattice. In Section 2.4, the possibility of a low-temperature phase transition to a time-reversal symmetry breaking state is discussed within the context of GL theory. Both uniform and inhomogeneous *d*-wave superconductors are considered. The GL theory of critical currents for both conventional and *d*-wave superconductors are outlined in Section 2.5.

The GL equations for a *d*-wave superconductor are derived microscopically in Chapter 3. Two lattice models used to describe the cuprates are employed in the derivation: the extended Hubbard (EH) model and the Antiferromagnetic van Hove (AvH) model. In Section 3.2, the GL equations for the gap functions and the current are derived using a field-theoretic approach. The superconducting transition temperatures in the uniform state are calculated both analytically and numerically in Section 3.3. In Section 3.4, the various coefficients appearing in the GL free energy are obtained analytically for the EH model, and numerically for the AvH model. The implications of the results for *d*-wave superconductors in the presence of external magnetic fields and currents are investigated. The possibility of subdominant

s-wave components of the superconducting order parameter, induced by various inhomogeneities, is also addressed. The contribution of Fermi surface anisotropy to the GL coefficients is studied in Section 3.5. In Section 3.6, the results are summarized and compared with recent experimental data for the high-T_c materials.

Chapter 4 is concerned with the influence of twin boundaries in determining the superconducting properties of YBCO. The properties of twin boundaries and grain boundaries are reviewed in Section 4.1, and the experimental evidence for a local time-reversal symmetry breaking phase at low temperatures is discussed. The Bogoliubov-de Gennes (BdG) equations describing a twinned d-wave superconductor are derived in Section 4.2 within the context of the EH model. In Section 4.3, the behaviour of the superconducting order parameter near the twin boundary is shown, and the conditions required to elicit a time-reversal breaking state at low temperatures are determined. The free energy is evaluated numerically in Section 4.4, in order to verify the stability of the low-temperature phase. The possibility of quasiparticle localization near the twin boundary is investigated in Section 4.5. The numerical results are summarized in Section 4.6, and are compared with recent tunneling data obtained for YBCO.

The behaviour of the cuprates in the presence of external currents is investigated in Chapter 5, both for clean materials and twinned YBCO. The BdG equations for a clean d-wave superconductor with a Cooper-pair momentum are derived in Section 5.2. The current response of the system is obtained numerically. The depairing critical current, superfluid density, and penetration depth are calculated, and the results are compared with experimental data. The magnitudes of subdominant s-wave components, nucleated by the external currents, are determined. External currents in twinned systems are considered in Section 5.3, within the context of the BdG theory described in Chapter 4. The behaviours of the currents and the order parameter in the vicinity of the twin boundaries are obtained, both for time-reversal preserving and violating superconducting states. The results are compared with recent tunneling experiments on YBCO.

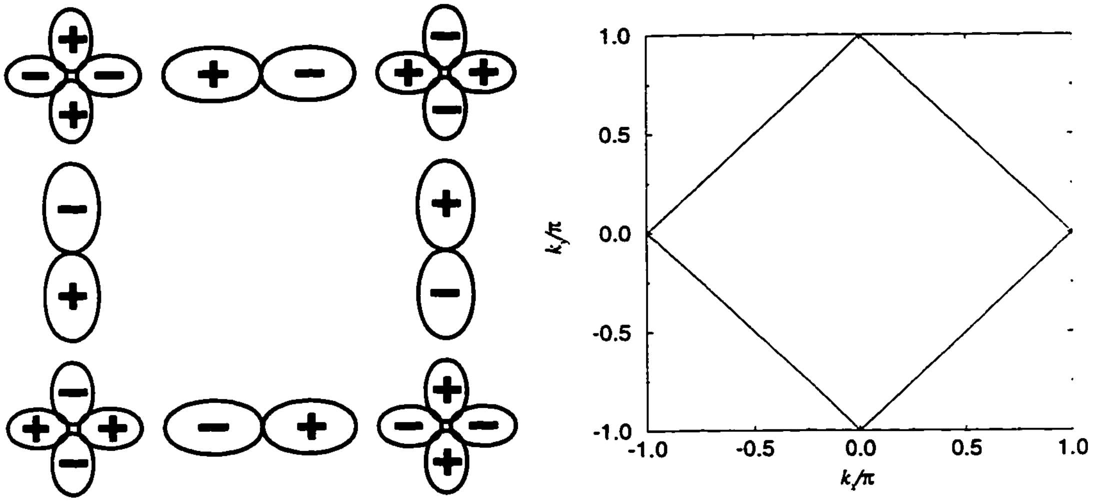

(a) (b)

Figure 1.1: In (a), the antibonding overlaps of the Cu $3d_{x^2-y^2}$ and O $2p_x$ and O $2p_y$ orbitals are illustrated for the copper-oxide planes. The associated electronic Fermi surface in (b) is large, with a band minimum at (π , π).

Chapter 2

Ginzburg-Landau Theory

The Ginzburg-Landau (GL) theory [123], a phenomenological formalism for the investigation of second-order phase transitions, has been of inestimable value for the description of a non-uniform superconducting state. Though the GL theory was developed several years before the microscopic theory of Bardeen, Cooper, and Schrieffer (BCS), it was able to describe all of the important macroscopic properties, including persistent currents, the Meissner effect, magnetic penetration depth, structures of vortices and vortex lattices, and critical currents and magnetic fields. In this Chapter, the GL theory for conventional superconductors will be briefly reviewed; the interested reader is referred to [64] for a complete treatment. Subsequently, the GL theory relevant to the high-T_c superconductors will be discussed with particular emphasis on vortex structures, the possibility of time-reversal breaking, and critical currents.

2.1 Conventional GL Theory

In GL theory, the order parameter $\psi = \psi(\mathbf{r})$ characterizing the onset of superconductivity is treated as a complex and isotropic (i.e. s-wave-symmetric) wavefunction which vanishes at the transition temperature T_c. Near T_c, the order parameter is small, and the Gibbs free energy[1] of the system may be written as a power series in

---

[1] Strictly, this is the free energy per unit volume, while the free energy is $\int d\mathbf{r}F$. Throughout this thesis, the term 'free energy' will be taken to mean the free energy density, while the 'total free energy' implies the free energy.

ψ:

$$F_s = F_n + \alpha(T)|\psi|^2 + \beta(T)|\psi|^4 + \frac{\hbar^2}{2m^*}\left|\left(-i\vec{\nabla} + \frac{e^*}{\hbar c}\mathbf{A}\right)\psi\right|^2 + \frac{h^2}{8\pi}, \tag{2.1}$$

where F_n is the free energy in the normal state, e^* and m^* are the effective charge and mass, $\mathbf{A}$ is the vector potential associated with the magnetic field inside the superconductor $\mathbf{h} = \nabla \times \mathbf{A}$, and $h^2/8\pi$ is the associated magnetic energy [124]. Gaussian units are used throughout this thesis. For a second-order phase transition, $\alpha(T)$ must change sign from positive to negative at T_c, while $\beta(T) > 0$ varies slowly with temperature near T_c:

$$\alpha(T) \approx -(1-t)\alpha \quad ; \quad \beta(T) \approx \beta(T_c), \tag{2.2}$$

where $t \equiv T/T_c$ is the reduced temperature. The minimum of the free energy in the normal state corresponds to $\psi = 0$, while

$$|\psi_0|^2 = \frac{(1-t)\alpha}{2\beta(T_c)} \tag{2.3}$$

results below T_c in zero field (i.e. ignoring spatial variations of the order parameter).

The free energy (2.1) may be used to estimate the critical magnetic field $H_c(T)$ required to destroy the superconductivity. In the presence of an external field H, the normal-state free energy is

$$F_n(H,T) = F_n(T) + \frac{H^2}{8\pi}. \tag{2.4}$$

Assuming a perfect Meissner effect, the magnetic field inside the superconductor is zero: $F_s(h,T) = F_s(T)$. At the critical field, the order parameter will vanish and one obtains:

$$F_n - F_s = \frac{H_c^2(T)}{8\pi} = \frac{\alpha^2}{4\beta(T_c)}\left(1 - \frac{T}{T_c}\right)^2, \tag{2.5}$$

where, making use of (2.3), the last term is the free energy difference in the absence of an external field.

In the presence of an external field, or another inhomogeneity giving rise to spatial variations, the total free energy $\tilde{F} \equiv \int d\mathbf{r} F_s$ must be minimized with respect to the vector potential and order parameter, $\delta\tilde{F} = 0$. After some manipulations, the GL equations for the order parameter and the (super)current are obtained:

$$\frac{\hbar^2}{2m^*}\left(-i\vec{\nabla}+\frac{e^*}{\hbar c}\mathbf{A}(\mathbf{r})\right)^2\psi(\mathbf{r})+\alpha\psi(\mathbf{r})+2\beta|\psi(\mathbf{r})|^2\psi(\mathbf{r})=0; \tag{2.6}$$

$$\frac{c}{4\pi}\vec{\nabla}\times\mathbf{h}(\mathbf{r})\equiv\mathbf{j}(\mathbf{r})=\frac{e^*\hbar}{2im^*}\left(\psi^*(\mathbf{r})\vec{\nabla}\psi(\mathbf{r})-\psi(\mathbf{r})\vec{\nabla}\psi^*(\mathbf{r})\right)+\frac{{e^*}^2}{m^*c}|\psi(\mathbf{r})|^2\mathbf{A}(\mathbf{r}), \tag{2.7}$$

where the current is related to the internal field through Ampère's law. In the derivation of these equations, the surface integral is assumed to be zero:

$$\int d\mathbf{n}\cdot\left[\delta\psi\left(-i\vec{\nabla}+\frac{e^*}{\hbar c}\mathbf{A}\right)\psi\right]=0, \tag{2.8}$$

which ensures that no current flows through the surface ($\mathbf{n}$ is the surface normal).

The GL equations may be used to define the coherence length $\xi(T)$ and penetration depth $\lambda(T)$. In terms of a (real) order parameter scaled to its zero-field value $f \equiv \psi/\psi_0$, and neglecting the vector potential, Eq. (2.6) becomes:

$$-\frac{\hbar^2}{2m^*\alpha}\nabla^2 f+f-f^3=0. \tag{2.9}$$

The coherence length defines the range of the order parameter's spatial variations:

$$\begin{aligned}\xi^2(T) &= -\frac{\hbar^2}{2m^*\alpha(T)};\\ \Rightarrow \xi(T) &= \sqrt{\frac{\hbar^2}{2m^*(1-t)\alpha}}.\end{aligned} \tag{2.10}$$

Note that $\xi(T)$ diverges near T_c, which reflects the weakening of the superconducting coherence. The penetration depth is estimated by taking the curl of the current in (2.7):

$$\vec{\nabla}\times\vec{\nabla}\times\mathbf{h}(\mathbf{r})=-\frac{4\pi {e^*}^2}{m^*c^2}\psi_0^2\mathbf{h}(\mathbf{r}). \tag{2.11}$$

Assuming $\mathbf{h}(\mathbf{r})=h_z(\mathbf{r})$ and $\mathbf{r}=x$, one finds that the field exponentially decays inside the superconductor:

$$h(x)=e^{-x/\lambda(T)}, \tag{2.12}$$

where the London penetration depth given by

$$\lambda(T) = \sqrt{\frac{m^* c^2 \beta(T_c)}{2\pi e^{*2}(1-t)\alpha}}, \tag{2.13}$$

governs the length over which the external magnetic field penetrates the superconducting sample. The London penetration depth also diverges as $(1-t)^{-1/2}$ close to T_c. In the derivation, the electrodynamics are assumed to be local, i.e. that the field at a given point is determined entirely by the currents at the same point. This assumption is likely to be valid for conventional superconductors only for temperatures near T_c, where the field varies slowly due to the long penetration depth. For local, or London, electrodynamics to hold, the GL parameter $\kappa(T) \equiv \lambda(T)/\xi(T) \gg 1$ (note from (2.10) and (2.13) that near T_c, κ is independent of temperature). The high-T_c materials should therefore be London superconductors except perhaps at very low temperatures. If the order parameter has an unconventional symmetry such as d-wave or extended s-wave, however, the coherence length diverges along the line nodes and this condition is no longer satisfied, leading to interesting effects at low temperatures [102].

The GL parameter κ characterizes the magnetic properties of superconductors. Since the expulsion of an external field increases the energy of the superconductor by $H^2/8\pi$, Eq. (2.5), the system could lower its energy by differentiating into normal and superconducting regions. If the energy of the superconductor/normal interface is positive, corresponding to $\kappa \ll 1$, this differentiation would not be favourable; these type I superconductors exhibit Meissner screening until H_c. In type II superconductors where $\kappa \gg 1$, the interface energy is negative, and above a lower critical field $H_{c1} < H_c$ the field penetrates the sample in the form of vortices which have normal-state cores, with magnetic flux quantized in units of $hc/e^* = hc/2e = 2 \cdot 10^{-7}$ G·cm^2. These vortices arrange themselves into an 'Abrikosov lattice,' which is generally triangular in conventional superconductors [125, 126]. Only at a much higher field $H_{c2} \gg H_c$ is the superconductivity destroyed in the bulk of the sample.[2] The high-T_c superconductors are all highly type-II materials. Many intriguing properties of vortices in

---

[2] Actually, superconductivity may persist near the surface up to an even higher critical field H_{c3}.

the cuprates will be discussed throughout this thesis, particularly in Section 2.3 and Sections 3.4-3.6.

2.2 Order-parameter Symmetry Mixing

As discussed in Chapter 1, the high-T_c superconductors are all tetragonal or orthorhombic materials, and are characterized by large anisotropies of both normal and superconducting transport properties. One may assume that the superconductivity is essentially two-dimensional, residing in the *ab*-oriented copper-oxide planes (and chains if applicable). It should be kept in mind, however, that a nominal coupling in the *c*-direction is required to stabilize the off-diagonal long-range order. The gap function, which is proportional to the total order parameter, may be written as a combination of all components allowed by symmetry:

$$\psi(\mathbf{r}) \propto \Delta_0(\mathbf{r}) + \Delta_s(\mathbf{r}) + \Delta_d(\mathbf{r}) + \tilde{\Delta}_s(\mathbf{r}) + \tilde{\Delta}_d(\mathbf{r}) + \ldots, \tag{2.14}$$

where the various components are defined in Eqs. (1.9)-(1.13). Since Δ_0, Δ_s, and $\tilde{\Delta}_s$ mix, the free energy of high-T_c superconductors should be written in terms of a total order parameter with just *s*-wave and *d*-wave components. The order parameter symmetry of the superconducting state depends on which component is stabilized at the highest temperature; this gap function is referred to as the 'dominant component', while all other gap functions are 'subdominant components.'

The free energy for the high-T_c superconductors is [127, 128]:

$$F_s = F_n + F_0^{\rm tet} + F_0^{\rm orth} + F_1^s + F_1^d + \frac{h^2}{8\pi}, \tag{2.15}$$

where F_n is the normal-state free energy, $F_0^{\rm tet}$ and $F_0^{\rm orth}$ are the lowest-order contributions to the free energy with tetragonal and orthorhombic symmetries, respectively, and $F_1^{s,d}$ are higher-order tetragonal contributions involving *s*-wave or *d*-wave components only (the motivation for including these will be discussed in the next section). Assuming spatial variations only within the copper-oxide layers oriented in the xy-plane, the various terms in the free energy are written:

$$F_0^{\rm tet} = \alpha_s|\Delta_s(\mathbf{r})|^2 + \alpha_d|\Delta_d(\mathbf{r})|^2 + \beta_1|\Delta_s(\mathbf{r})|^4 + \beta_2|\Delta_d(\mathbf{r})|^4$$

$$\begin{aligned}
&+ \beta_3|\Delta_s(\mathbf{r})|^2|\Delta_d(\mathbf{r})|^2 + \beta_4\left(\Delta_s^*(\mathbf{r})^2\Delta_d^2(\mathbf{r}) + \Delta_d^*(\mathbf{r})^2\Delta_s^2(\mathbf{r})\right) \\
&+ \gamma_s|\vec{\Pi}\Delta_s(\mathbf{r})|^2 + \gamma_d|\vec{\Pi}\Delta_d(\mathbf{r})|^2 \\
&+ \gamma_\nu\Big[(\Pi_y\Delta_s(\mathbf{r}))^*(\Pi_y\Delta_d(\mathbf{r})) - (\Pi_x\Delta_s(\mathbf{r}))^*(\Pi_x\Delta_d(\mathbf{r})) + H.c.\Big]; \qquad (2.16)
\end{aligned}$$

$$\begin{aligned}
F_0^{\text{orth}} &= \alpha_{sd}\Big(\Delta_s^*(\mathbf{r})\Delta_d(\mathbf{r}) + H.c.\Big) \\
&+ \beta_5\Big(\Delta_s^*(\mathbf{r})\Delta_d(\mathbf{r}) + H.c.\Big)|\Delta_s(\mathbf{r})|^2 + \beta_6\Big(\Delta_s^*(\mathbf{r})\Delta_d(\mathbf{r}) + H.c.\Big)|\Delta_d(\mathbf{r})|^2 \\
&+ \gamma_s'\Big(|\Pi_y\Delta_s(\mathbf{r})|^2 - |\Pi_x\Delta_s(\mathbf{r})|^2\Big) + \gamma_d'\Big(|\Pi_y\Delta_d(\mathbf{r})|^2 - |\Pi_x\Delta_d(\mathbf{r})|^2\Big) \\
&+ \gamma_\nu'\Big[(\Pi_y\Delta_s(\mathbf{r}))^*(\Pi_y\Delta_d(\mathbf{r})) + (\Pi_x\Delta_s(\mathbf{r}))^*(\Pi_x\Delta_d(\mathbf{r})) + H.c.\Big]; \qquad (2.17)
\end{aligned}$$

$$F_1^s = \eta_s|\Delta_s(\mathbf{r})\vec{\Pi}\Delta_s(\mathbf{r})|^2 + \gamma_{s+}|\vec{\Pi}^2\Delta_s(\mathbf{r})|^2 + \gamma_{s-}|(\Pi_y^2 - \Pi_x^2)\Delta_s(\mathbf{r})|^2; \qquad (2.18)$$

$$F_1^d = \eta_d|\Delta_d(\mathbf{r})\vec{\Pi}\Delta_d(\mathbf{r})|^2 + \gamma_{d+}|\vec{\Pi}^2\Delta_d(\mathbf{r})|^2 + \gamma_{d-}|(\Pi_y^2 - \Pi_x^2)\Delta_d(\mathbf{r})|^2, \qquad (2.19)$$

where $\vec{\Pi} = -i\vec{\nabla} + (e^*/\hbar c)\mathbf{A}(\mathbf{r})$ and the magnetic field $\mathbf{h}(\mathbf{r}) = h_z(\mathbf{r}) = \vec{\nabla} \times \mathbf{A}(\mathbf{r})$ is assumed to be in the z-direction. This free energy mixes components with s-wave and $d_{x^2-y^2}$-wave symmetries; s_{xy} and d_{xy}-wave gap functions are not considered for reasons discussed below. For a tetragonal superconductor very near T_c, only the dominant component exists and the free energy describes a pure-symmetry superconducting state that is indistinguishable from the conventional one, Eq. (2.1), except that $\psi(\mathbf{r}) = \Delta_{s/d}(\mathbf{r})$. Note, however, that rotational symmetry is broken both by orthorhombicity and by higher-order gradient terms.

In the absence of inhomogeneities giving rise to spatial variations, the stability conditions for bulk d-wave or s-wave superconductivity are [129, 130]:

$$\alpha_d < 0 \quad ; \quad (\beta_3 - 2\beta_4)\alpha_d - 2\beta_2\alpha_s < 0; \qquad d\text{-wave} \qquad (2.20)$$

$$\alpha_s < 0 \quad ; \quad (\beta_3 - 2\beta_4)\alpha_s - 2\beta_1\alpha_d < 0; \qquad s\text{-wave} \qquad (2.21)$$

In orthorhombic superconductors such as YBCO or BSCCO, there exists a low-order 'mixed-power' coupling term between Δ_s and Δ_d (the term proportional to α_{sd} in F_0^{orth}) so both components become finite at the same transition temperature. The existence of one component drives the creation of the other. Of course, this term could have been anticipated since the d-wave and s-wave components belong to the same irreducible representation Γ_1^+ in orthorhombic superconductors. Only the lowest-order orthorhombic terms are included in $F_0^{\rm orth}$ because the s-wave component in YBCO is thought to be no more than 10% of Δ_d [131]. While s-wave and d-wave channels may exist simultaneously in uniform tetragonal systems such as Tl 2223, the appearance of a driven subdominant component will only occur at lower temperatures, since the mixed-power terms with coefficients β_3 and β_4 are fourth-order in gaps. Thus, the transition temperature for a subdominant component in the presence of a uniform dominant component is much lower than its bare transition temperature, and may be zero or negative (this topic is discussed further in Section 3.3).

In non-uniform tetragonal superconductors, a subdominant component may be nucleated at higher temperatures through the 'mixed-gradient term' with coefficient γ_ν [132]. In the vicinity of inhomogeneities, the spatial variations of the dominant component give rise to variations of the subdominant gap function. The coherence length of the dominant component governs the length scale. While the admixture of the various components is a purely dynamic effect, the magnitude of the induced subdominant component will depend on the size of the various GL coefficients. The relative sizes of the components may only be obtained by a microscopic derivation of the GL free energy, and is a major goal of this thesis. The derivation and interpretation of the GL free energy for a d-wave superconductor is the subject of Chapter 3. In orthorhombic superconductors, the other mixed gradient term proportional to γ'_ν will locally enhance the existing subdominant component.

Minimizing the GL free energy (2.15) with respect to $\Delta_d^*(\mathbf{r})$ and $\Delta_s^*(\mathbf{r})$, one obtains the GL equations for the two gap functions (the $\mathbf{r}$-dependence has been dropped for simplicity):

$$\begin{aligned} 0 &= \alpha_d\Delta_d + 2\beta_2|\Delta_d|^2\Delta_d + \beta_3|\Delta_s|^2\Delta_d + 2\beta_4\Delta_s^2\Delta_d^* \\ &+ \alpha_{sd}\Delta_s + \beta_5|\Delta_s|^2\Delta_s + \beta_6(\Delta_d^2\Delta_s^* + 2|\Delta_d|^2\Delta_s) \\ &+ \gamma_\nu(\Pi_x^2 - \Pi_y^2)\Delta_s + \gamma'_d(\Pi_x^2 - \Pi_y^2)\Delta_d + \gamma'_\nu\Pi^2\Delta_s \\ &+ \eta_d\Big(2\Delta_d^2\Pi^2\Delta_d^* + 4|\Delta_d|^2\Pi^2\Delta_d + 6\Delta_d|\Pi\Delta_d|^2 + 2\Delta_d^*(\Pi^*\Delta_d)(\Pi\Delta_d)\Big) \\ &+ \gamma_{d+}\Pi^4\Delta_d + \gamma_{d-}(\Pi_x^2 - \Pi_y^2)^2\Delta_d\ ; \end{aligned} \tag{2.22}$$

$$\begin{aligned}
0 &= \alpha_s\Delta_s + 2\beta_1|\Delta_s|^2\Delta_s + \beta_3|\Delta_d|^2\Delta_s + 2\beta_4\Delta_d^2\Delta_s^* \\
&+ \alpha_{sd}\Delta_d + \beta_5(\Delta_s^2\Delta_d^* + 2|\Delta_s|^2\Delta_d) + \beta_6|\Delta_d|^2\Delta_d \\
&+ \gamma_\nu(\Pi_x^2 - \Pi_y^2)\Delta_d + \gamma_s'(\Pi_x^2 - \Pi_y^2)\Delta_s + \gamma_\nu'\Pi^2\Delta_d \\
&+ \eta_s\Big(2\Delta_s^2\Pi^2\Delta_s^* + 4|\Delta_s|^2\Pi^2\Delta_s + 6\Delta_s|\Pi\Delta_s|^2 + 2\Delta_s^*(\Pi^*\Delta_s)(\Pi\Delta_s)\Big) \\
&+ \gamma_{s+}\Pi^4\Delta_s + \gamma_{s-}(\Pi_x^2 - \Pi_y^2)^2\Delta_s\ . \qquad (2.23)
\end{aligned}$$

The equation for the current follows from minimizing the free energy with respect to the vector potential $\mathbf{A}(\mathbf{r})$. Only the leading-order contributions to the GL current will be expressly shown, since the full expression is complicated and is not of significance to this thesis; the procedure for the calculation of the higher-order corrections is straightforward. The current density in the *ab*-plane with a *c*-oriented external field is then

$$\begin{aligned}
\mathbf{j} &= \delta\frac{4\pi c}{\phi_0}\Big[\gamma_d\Delta_d^*\vec{\Pi}\Delta_d + \gamma_s\Delta_s^*\vec{\Pi}\Delta_s \\
&- \hat{x}\gamma_\nu\Big(\Delta_s^*\Pi_x\Delta_d + \Delta_d^*\Pi_x\Delta_s\Big) + \hat{y}\gamma_\nu\Big(\Delta_s^*\Pi_y\Delta_d + \Delta_d^*\Pi_y\Delta_s\Big) \\
&- \hat{x}\Big(\gamma_s'\Delta_s^*\Pi_x\Delta_s + \gamma_d'\Delta_d^*\Pi_x\Delta_d\Big) + \hat{y}\Big(\gamma_s'\Delta_s^*\Pi_y\Delta_s + \gamma_d'\Delta_d^*\Pi_y\Delta_d\Big) \\
&+ \gamma_\nu'\Big(\Delta_s^*\vec{\Pi}\Delta_d + \Delta_d^*\vec{\Pi}\Delta_s\Big) + H.c.\Big], \qquad (2.24)
\end{aligned}$$

where the anisotropy factor δ =(layer thickness/layer spacing) is introduced in order to model the layered structure of the cuprate superconductors. In the present two-dimensional model, $\delta \to 0$, which reflects the inability of the system to sustain screening currents. Neglecting higher-order terms, Eqs. (2.22)-(2.24) are subject to the following boundary conditions:

$$\mathbf{n}\cdot\left[\gamma_d\vec{\Pi}\Delta_d + \gamma_\nu\left(\hat{y}\Pi_y - \hat{x}\Pi_x\right)\Delta_s + \gamma_d'\left(\hat{y}\Pi_y - \hat{x}\Pi_x\right)\Delta_d + \gamma_\nu'\vec{\Pi}\Delta_s\right] = 0; \qquad (2.25)$$

$$\mathbf{n}\cdot\left[\gamma_s\vec{\Pi}\Delta_s + \gamma_\nu\left(\hat{y}\Pi_y - \hat{x}\Pi_x\right)\Delta_d + \gamma_s'\left(\hat{y}\Pi_y - \hat{x}\Pi_x\right)\Delta_s + \gamma_\nu'\vec{\Pi}\Delta_d\right] = 0, \qquad (2.26)$$

where $\mathbf{n}$ is the unit vector normal to the surface of the superconductor. The superconducting coherence lengths $\xi(T)$ and penetration depths $\lambda(T)$ near T_c can now be estimated:

$$\xi_{s(d)}(T) = \sqrt{\frac{\gamma_{s(d)}}{|\alpha_{s(d)}|}} \qquad (2.27)$$

$$\lambda_{s(d)}(T) = \frac{\phi_0}{2\pi}\sqrt{\frac{\beta_{1(2)}}{8\pi\delta\gamma_{s(d)}|\alpha_{s(d)}|}} \tag{2.28}$$

where the flux quantum $\phi_0 = hc/e$.

It is important to point out that the free energy (2.15) is expressed in terms of Δ_s and a *single* kind of d-symmetric gap function, specifically $d_{x^2-y^2}$. The Δ_s may be taken to represent a linear combination of on-site, extended s-wave, and s_{xy}-wave components. As discussed in Section 1.2, however, d_{xy} and $d_{x^2-y^2}$ belong to different irreducible representations, and therefore each should have terms in the free energy. A number of reasons preclude the addition of d_{xy}-symmetric terms. Assuming that d_{xy} is not the symmetry of the superconducting order parameter in the high-T_c materials, as indicated by experiments, a gap function with this symmetry ($\tilde{\Delta}_d$) would only enter the free energy in a 'mixed-power' or 'mixed-gradient' term. By symmetry, the lowest-order mixed-gradient terms go like $(\Pi_x\Pi_y)\tilde{\Delta}_d^*(\Pi_x^2 - \Pi_y^2)\Delta_d$ and $(\Pi_x\Pi_y)\tilde{\Delta}_d^*\vec{\Pi}^2\Delta_s$ [133]. These are fourth-order in derivatives, unlike the conventional mixed gradient terms with coefficients γ_ν and γ_ν' which are second-order in derivatives. Mixed-gradient terms involving $\tilde{\Delta}_d$ should have less physical significance, since spatial variations are slow near T_c: $\Pi \sim \sqrt{1-t}$ because $\nabla \sim \xi^{-1}(T) \sim \sqrt{1-t}$ from (2.10) and $\mathbf{A} \sim H\lambda(T) \sim \sqrt{1-t}$ from (2.5) and (2.13). The lowest-order mixed-power terms are proportional to $\tilde{\Delta}_d^2\Delta_d^2$ and $\tilde{\Delta}_d^2\Delta_s^2$, since terms like $\tilde{\Delta}_d^*\Delta_d$ are not allowed by symmetry. Thus, a second phase transition to a bulk subdominant d_{xy}-symmetric state could occur in principle, but this is unlikely as discussed above.

A more physical reason for neglecting $\tilde{\Delta}_d$ terms in the free energy is that the experimental (and theoretical) evidence for the cuprates is strongly in favour of an order parameter with $d_{x^2-y^2}$ symmetry. A gap function with this symmetry arises from nearest-neighbour pairing of electrons. Unless the microscopic mechanism for the superconductivity allows for more than one pairing channel (such as a second-nearest neighbour coupling giving rise to $\tilde{\Delta}_d$ and $\tilde{\Delta}_s$), it is more natural to consider a free energy with terms involving both Δ_d and an extended s-wave component resulting from the *same* nearest-neighbour attraction. Throughout most of this thesis, the superconductor is assumed to undergo a bulk $d_{x^2-y^2}$-symmetric (d-wave) instability, and components with d_{xy}-wave or s_{xy}-wave symmetry are not considered.

It is clear just from the complicated structure of the GL free energy (2.15) that the physics of inhomogeneous d-wave superconductors is likely to be quite interesting. In the following three sections, certain predictions of this GL theory will be briefly reviewed. In particular, the structures of isolated vortices and the vortex lattice, the effect of twin boundaries, and the behaviour of d-wave superconductors in the presence of external currents will be discussed.

2.3 Vortices

One of the most interesting predictions of the GL theory presented above is that the structures of isolated vortices and the Abrikosov lattice may be considerably different from those of conventional superconductors. In particular, asymmetric vortices and centered-rectangular vortex lattices are thought to result in d-wave superconductors [133, 134, 135, 136, 137, 138, 139]. The most important causes of anisotropy are the s-wave component induced in the vicinity of the vortex core, Fermi surface geometry, and orthorhombic distortions. The discussion in this section follows the analysis of [134] and [135].

In tetragonal systems near T_c, the mixed-gradient term in (2.16) governs the admixture of an s-wave component in an inhomogeneous d-wave superconductor.[3] In order to examine the influence of this term on the vortex structure, first consider the equation (2.22) for a pure d-wave state to leading order:

$$(\alpha_d + \gamma_d \Pi^2)\Delta_d + 2\beta_2 |\Delta_d|^2 \Delta_d = 0, \tag{2.29}$$

whose asymptotic solution near the vortex core is:

$$\Delta_d(r, \varphi) \approx (d_1 r + d_3 r^3) e^{i\varphi}, \tag{2.30}$$

where φ is the azimuthal angle. The equation for Δ_d to this order is rotationally symmetric and is identical to that obtained for a conventional, isotropic s-wave super-

---

[3] Throughout this section, the discussion will assume bulk d-wave superconductivity. It should be kept in mind, however, that the phenomenological free energy does not itself determine which component yields the highest T_c. All the results are equally applicable to a bulk s-wave superconductor with a d-wave admixture, simply by interchanging the s- and d-indices of the gap functions.

conductor (2.6). Assuming the induced s-wave component is small, one may linearize Eq. (2.23):

$$(\alpha_s + \gamma_s \Pi^2)\Delta_s + \gamma_\nu(\Pi_y^2 - \Pi_x^2)\Delta_d = 0. \tag{2.31}$$

Substituting (2.30) into (2.31) gives [137]

$$\Delta_s(r, \varphi) \approx s_1 r e^{-i\varphi} + s_3 r^3 e^{3i\varphi}. \tag{2.32}$$

The leading-order solution for the induced s-wave component has been solved to yield [135]:

$$s_1 \approx \frac{1}{2}\left(\frac{\gamma_\nu}{\alpha_s \xi_d^2}\right) d_1, \tag{2.33}$$

where $\xi_d \equiv \sqrt{\gamma_d/|\alpha_d|}$ is the d-wave coherence length. Moving in the $x = y$ direction from the center of the vortex, the induced subdominant order parameter reaches a maximum, then decreases algebraically; there exist extra nodes in the $x = 0$ or $y = 0$ directions. The maximum value of the s-wave component nucleated in the vortex core is estimated to be [135]

$$\frac{\Delta_s^{\max}}{\Delta_d^{\text{bulk}}} \approx \frac{1}{4}\left(\frac{\gamma_\nu}{\alpha_s \xi_d^2}\right). \tag{2.34}$$

The estimate for the magnitude of the subdominant component is reliable as long as $\Delta_s^{\max} < \Delta_d^{\text{bulk}}/4$, which is always satisfied sufficiently near T_c (see below).

A number of interesting results may be obtained from this simple analysis. The magnitude of the maximum induced s-wave component is proportional to the size of the mixed-gradient coefficient γ_ν, and also ξ_d^{-2}. Since ξ_d is known experimentally to be quite small, the local s-wave component could be quite large at low temperatures $T \ll T_c$, depending on the magnitude of γ_ν. One would expect, however, that it would be energetically unfavourable to induce a subdominant component comparable to Δ_d solely through spatial variations of the d-wave component. One of the primary goals of this work is the determination of γ_ν, and the maximum s-wave gap, in the high-T_c materials. Furthermore, since $\xi_d \sim 1/\sqrt{1-t}$ from (2.10) and $\Delta_d \sim \sqrt{1-t}$ from (2.3), one finds

$$\Delta_s \sim (1-t)^{3/2}. \tag{2.35}$$

Thus, the induced s-wave component disappears more rapidly near T_c than does the dominant d-wave component. Indeed, the same behaviour is immediately apparent from Eq. (2.31); ignoring spatial variations of Δ_s, which are a correction of order $(1-t)$, one obtains:

$$\Delta_s \approx -\frac{\gamma_\nu}{\alpha_s}(\Pi_y^2 - \Pi_x^2)\Delta_d. \tag{2.36}$$

One recovers (2.35) since $\Pi \sim \sqrt{1-t}$.

The temperature-dependence of the s-wave gap (or the subdominant component in general) finally permits the justification of carrying the GL free energy (2.15) to fourth-order in derivatives. The lowest-order term in the free energy involving Δ_s is $\alpha_s|\Delta_s|^2$, which varies near T_c as $(1-t)^3$. The largest terms in F_0^{tet} involving only d-wave components, however, approach T_c only as $(1-t)^2$. Thus, for consistency, all terms allowed by symmetry up to $(1-t)^3$ must be included in the free energy. These terms are given in F_1^d; in case bulk s-wave superconductivity is favoured, F_1^s is included in the free energy for generality.

The simplified equation for Δ_s (2.36) may be used to demonstrate that an induced s-wave component leads to four-fold anisotropy. In the zeroth-order approximation, one sets $\Delta_s = 0$ and the tetragonal free energy F_0^{tet} has rotational symmetry. To first-order in a (small) s-wave component, one may substitute (2.36) to obtain:

$$\begin{aligned} F_0^{\text{tet}} + F_1^d \;&\approx\; \alpha_d|\Delta_d(\mathbf{r})|^2 + \beta_2|\Delta_d(\mathbf{r})|^4 + \gamma_d|\vec{\Pi}\Delta_d(\mathbf{r})|^2 + \eta_d|\Delta_d(\mathbf{r})\vec{\Pi}\Delta_d(\mathbf{r})|^2 \\ &+\; \gamma_{d+}|\vec{\Pi}^2\Delta_d(\mathbf{r})|^2 + \left[\gamma_{d-} - \frac{\gamma_\nu^2}{\alpha_s}\right]|(\Pi_y^2 - \Pi_x^2)\Delta_d(\mathbf{r})|^2. \end{aligned} \tag{2.37}$$

It is clear from the last term that the induced s-wave order parameter, parametrized by the mixed-gradient coefficient γ_ν, breaks rotational symmetry in precisely the same way as a fourth-order d-wave gradient term. In fact, this term gives rise to a four-fold symmetric (in other words, square) vortex core [136, 139, 140]. From F_0^{orth} it is evident that orthorhombic distortions would also break the rotational symmetry of the vortex core; orthorhombicity has been found to lead to a two-fold symmetry, however [138].

Several other points are worth noting. The fourth-order anisotropic gradient terms in F_1^s and F_1^d are allowed by symmetry, and should therefore appear even for isotropic

s-wave superconductors. These terms, however, do not arise in the derivation of the GL equations from the BCS theory [141]; the coefficient γ_{s-} is zero because the Fermi surface, in addition to the interaction, is assumed to be isotropic. Thus, the degree of Fermi surface anisotropy will partly determine the size of $\gamma_{s/d-}$ and the contribution to four-fold symmetry of the vortex core. Furthermore, from (2.37) it appears that the contributions from Fermi surface anisotropy and the s-wave admixture are competing effects, since they enter the free energy with opposite signs. These issues will be discussed further in Section 3.5.

The finite s-wave component nucleated in the vortex core for fields near H_{c1} is predicted to yield an oblique structure for the vortex lattice near H_{c2}. The Abrikosov lattice would be intermediate between the usual triangle and a square [134, 135, 142]. The degree of 'obliqueness' is mostly dependent on the gradient coefficient ratio γ_ν/γ_d. For $\gamma_\nu/\gamma_d = 0$, the s-wave component vanishes, yielding a triangular lattice. The Abrikosov lattice deforms continuously away from a triangle as γ_ν/γ_d is increased; for $\gamma_\nu/\gamma_d = 0.45$, the angle between primitive vectors $\phi = 76°$. For $\gamma_\nu/\gamma_d \sim 0.6$ and higher, the flux lattice is square. Other work has confirmed that four-fold gradient terms in the free energy, possibly arising from Fermi surface anisotropy, deform the Abrikosov lattice to a similar degree [136]. The GL predictions are consistent with two recent experimental observations for YBCO of flux lattices with $\phi \approx 73°$ [143] and 77° [144]. It is not yet clear, however, whether the $a - b$ anisotropy associated with the orthorhombicity of YBCO is alone sufficient to account for the distortion in the flux lattice [138, 145].

2.4 Time-Reversal Breaking

As alluded to in Section 2.2, the GL free energy (2.15) allows for the possibility of an additional second-order phase transition at a temperature $T' < T_c$. In this section, the possibility of a low-temperature time-reversal breaking phase is investigated. It should be noted at the outset that while GL theory is strictly applicable only for temperatures near T_c, it is often qualitatively accurate for much lower temperatures. Indeed, the intriguing predictions of the theory discussed below have been corroborated in detail by the microscopic calculations presented in Chapter 4. The discussion follows the recent article by Sigrist *et al.* [130].

The onset of a second phase transition is defined by the stability criteria (2.20) and (2.21). For a bulk d-wave tetragonal superconductor, the subdominant transition temperature T' is defined by

$$(\beta_3 - 2\beta_4)\alpha_d(T') - 2\beta_2\alpha_s(T') = 0, \tag{2.38}$$

which, of course, is equivalent to $\Delta_s(T') = 0$. Near T', the d-wave and s-wave components in this new phase are defined by

$$|\Delta_d|^2 = \frac{(\beta_3 - 2\beta_4)\alpha_s - 2\beta_1\alpha_d}{4\beta_1\beta_2 - (\beta_3 - 2\beta_4)^2}; \tag{2.39}$$

$$|\Delta_s|^2 = \frac{(\beta_3 - 2\beta_4)\alpha_d - 2\beta_2\alpha_s}{4\beta_1\beta_2 - (\beta_3 - 2\beta_4)^2}. \tag{2.40}$$

The magnitudes of the subdominant components, and the associated transition temperature T', are governed mostly by the lowest-order mixed-power terms with coefficients β_3 and β_4 in F_0^{tet}, and by the α_{sd}, β_5, and β_6 terms in F_0^{orth} (recall that in orthorhombic superconductors Δ_s and Δ_d both appear at T_c due to the second-order mixed-power term α_{sd}). It is important to note that the β_4 term favours a relative phase $\theta = \pm\pi/2$ between Δ_d and Δ_s if $\beta_4 > 0$. The resulting order parameter would be proportional to the linear combination $\psi \sim \Delta_d \pm i\Delta_s$. In contrast, all the orthorhombic mixed-power terms, as well as $\beta_4 < 0$, favour a relative phase of $\theta = 0$ or π corresponding to $\psi \sim \Delta_d \pm \Delta_s$.

The presence of an imaginary s-wave component breaks time-reversal symmetry $\mathcal{T}$. The time-reversal operator transforms the order parameter to its complex conjugate: $\mathcal{T}\psi \rightarrow \psi^*$. If time-reversal symmetry is preserved, ψ and ψ^* are identical to within a common spatially-independent phase; in other words, the two states may be related through a gauge transformation. If time-reversal symmetry is broken, ψ and ψ^* are distinct states, but the free energy is the same for each. Orthorhombicity suppresses a low-temperature transition to a $\mathcal{T}$-violating state.

The presence of an imaginary s-wave component $i\Delta_s$ leads to a total order parameter with a gap for quasiparticle excitations everywhere except perhaps at isolated points on the Fermi surface. As a result, the superconducting properties should be similar to those of a conventional BCS superconductor. Yet, if the $i\Delta_s$ admixture were weak, the physical gap along the original node-direction could be sufficiently small to yield the predominantly d-wave characteristics observed experimentally. Indeed, there is presently no experimental evidence to suggest that the uniform bulk state of high-T_c superconductors violates time-reversal symmetry [146]. The experimental null results may be due to the fact that the GL coefficients appropriate for the cuprates, appearing in (2.38), conspire to ensure that $T' \leq 0$. Another possibility is that $\beta_4 < 0$. These issues will be investigated microscopically in Chapters 3 and 4.

The criteria for a low-temperature $\mathcal{T}$-violating phase change when defects are present in the superconductor. In the vicinity of pair-breaking inhomogeneities, the dominant d-wave component is locally suppressed. Ignoring spatial variations for simplicity, the dominant d-wave component from (2.29) is approximately $\Delta_d^2 \approx -\alpha_d/2\beta_2$, and the equation for the subdominant transition temperature in a tetragonal superconductor becomes

$$(\beta_3 - 2\beta_4)\Delta_d^2(T^*) + \alpha_s(T^*) = 0. \tag{2.41}$$

A suppression of Δ_d would clearly lead to an increased subdominant transition temperature $T^* > T'$; in other words, a time-reversal breaking phase is more likely to appear at finite temperatures near the inhomogeneity. Evidently, local $\mathcal{T}$-violation is most likely to occur in the vicinity of strong d-wave pair-breakers, such as extended impurities, (110) or $(1\bar{1}0)$ surfaces, large-angle grain boundaries, and twin boundaries.

The analysis of the full GL free energy (2.15), including spatial variations of the dominant d-wave component, is complicated and only the central conclusions will be presented here; a full treatment may be found in [130]. The imaginary s-wave component, induced near inhomogeneities below T_c, is quite different from the real s-wave component discussed in the previous section, which arises due to spatial variations of Δ_d. In particular, the $\mathcal{T}$-violating component is the result of a local second-order phase transition. As such, its magnitude may be large compared to Δ_d^{bulk}, and its characteristic length scale ξ_{is} would diverge just below T^*. In contrast, a subdominant component induced through spatial variations alone must be small compared to Δ_d, and vary over the d-wave coherence length ξ_d. To summarize, while the mechanism for local $i\Delta_s$-generation depends on a strong perturbation of Δ_d, the subdominant pairing channel behaves as if it were essentially decoupled from the d-wave superconductivity.

In orthorhombic superconductors such as YBCO, the presence of a real s-wave component at all temperatures $T < T_c$ has several interesting consequences. The finite real s-wave component would suppress the transition temperature T^* to a locally $\mathcal{T}$-violating state, unless the perturbing inhomogeneity were itself tetragonal. In fact, as discussed in Section 4.1, large-angle grain boundaries and twin boundaries are thought to be oxygen depleted regions which may be tetragonal ($x \to 0$). Furthermore, the overall order parameter must change from $\Delta_d \pm i\Delta_s$ near the inhomogeneity to $\Delta_d \pm \Delta_s$ in the bulk, i.e. the relative phase must be spatially varying. This implies spontaneous supercurrents $j \propto \nabla\theta$ near the perturbation.

For the case of (110) or $(1\bar{1}0)$ surfaces, (or weak-link grain and twin boundaries oriented in this direction), it is straightforward to show within the GL theory that the phase variations lead to currents in the vicinity of the inhomogeneity. Defining

$$\Delta_d(\mathbf{r}) \equiv d \quad ; \quad \Delta_s(\mathbf{r}) \equiv e^{i\theta(\mathbf{r})}s, \tag{2.42}$$

where s and d are real and assumed to be constant throughout the sample, the expression for the current (2.24) neglecting the vector potential becomes:

$$\mathbf{j} = \delta\frac{4\pi c}{\phi_0}2sd\sin\theta\Big[\left(\gamma_\nu - \gamma_\nu'\right)\hat{x}\nabla_x\theta - \left(\gamma_\nu + \gamma_\nu'\right)\hat{y}\nabla_y\theta\Big]. \tag{2.43}$$

Defining the directions perpendicular and parallel to the inhomogeneity to be $r = r_\perp \equiv \hat{y} - \hat{x}$ and $R = r_{||} \equiv \hat{y} + \hat{x}$ respectively, one obtains these expressions for the currents:

$$\begin{aligned} j_r = j_\perp &= -\delta\frac{4\pi c}{\phi_0}2sd\sin\theta\Big[\left(\gamma_\nu + \gamma_\nu'\right)\nabla_y\theta + \left(\gamma_\nu - \gamma_\nu'\right)\nabla_x\theta\Big] \\ &= -\delta\frac{4\pi c}{\phi_0}2sd\sin\theta\left[\gamma_\nu\nabla_R\theta + \gamma_\nu'\nabla_r\theta\right]; \end{aligned} \tag{2.44}$$

$$j_R = j_{||} = -\delta\frac{4\pi c}{\phi_0}2sd\sin\theta\left[\gamma_\nu'\nabla_R\theta + \gamma_\nu\nabla_r\theta\right]. \tag{2.45}$$

One may set $\nabla_R\theta = 0$ because the relative phase has no spatial variations in the direction parallel to the twin boundary. Thus,

$$j_r = j_\perp = -\gamma'_\nu \delta \frac{4\pi c}{\phi_0} 2sd \sin\theta \nabla_r \theta \quad ; \quad j_R = j_\parallel = -\gamma_\nu \delta \frac{4\pi c}{\phi_0} 2sd \sin\theta \nabla_r \theta. \tag{2.46}$$

In tetragonal systems, $\gamma'_\nu = 0$, and spontaneous currents flow only in the parallel-direction. In orthorhombic materials, spontaneous currents should also exist in the perpendicular direction, which are smaller than the parallel currents by approximately γ'_ν/γ_ν. In addition, since $\sin\theta$ is odd around the extended defect, the currents flow in opposite directions on either side. The currents are expected to vanish in the bulk due to Meissner screening.

2.5 Critical Currents

Many practical applications of high-T_c materials require that the superconducting state supports large current densities. Due to the short coherence length, however, even very narrow intrinsic defects such as twin boundaries and wide-angle grain boundaries act as weak superconducting links. In clean systems, the critical current is due to depairing and dissipation due to vortex flow. In granular superconductors, the critical current is governed by the electromagnetic coupling across weak junctions, and the vortex-pinning potential of stronger junctions. While these issues will be addressed further in Chapter 5, it is useful to review the GL theory of critical currents both in systems with and without weak links. The discussion of critical currents in conventional and d-wave superconductors is based on Refs. [73, 147, 148].

2.5.1 Conventional Superconductors

For the investigation of critical currents limited by depairing, it is simplest to consider clean two-dimensional systems, such as defect-free thin films of conventional superconductor or the copper-oxide planes of high-T_c superconductors. If the thickness d is smaller than both $\xi(T)$ and $\lambda(T)$, then the magnitudes of the order parameter, internal field, and current densities may be assumed to be constant even in the presence of strong external electric or magnetic fields. Neglecting the vector potential (which will be justified below), and setting $\psi(\mathbf{r}) \equiv |\psi|e^{i\varphi(\mathbf{r})}$, the GL current (2.7) is written

$$\mathbf{j} \equiv e^*|\psi|^2\mathbf{v}_s = \frac{e^*\hbar}{m^*}|\psi|^2\vec{\nabla}\varphi. \tag{2.47}$$

A current $\mathbf{j}$ might result from the application of an external electric field, $e\mathbf{E} = m^*\partial\mathbf{v}_s/\partial t$. Since the superfluid velocity is $\mathbf{v}_s = (\hbar/m^*)\vec{\nabla}\varphi$, the GL free energy (2.1) becomes

$$F_s = F_n + \alpha|\psi|^2 + \beta|\psi|^4 + \frac{1}{2}mv_s^2|\psi|^2. \tag{2.48}$$

Minimizing with respect to ψ^*, one obtains the gap equation

$$\alpha|\psi| + 2\beta|\psi|^3 + \frac{m^*j^2}{2e^{*2}|\psi|^3} = 0. \tag{2.49}$$

Introducing the normalized order parameter $f \equiv \psi/\psi_0$, and making use of $|\psi_0|^2 = -\alpha/2\beta$ and $\xi^2(T) = -\hbar^2/2m\alpha(T)$, one obtains the current:

$$j = |\mathbf{j}| = e^*|\psi_0|^2\left(\frac{\hbar}{m^*\xi(T)}\right)f^2\sqrt{1-f^2}. \tag{2.50}$$

In combination with (2.47), this equation relates the magnitude of the order parameter to the superfluid velocity. As j increases, the normalized order parameter decreases from unity until the critical current is reached, at which point no solution for f can be found. The critical current is defined by $\partial j/\partial f = 0$, which yields $f^2 = 2/3$ and

$$j_c = \frac{2e^*}{3\sqrt{3}}|\psi_0|^2\left(\frac{\hbar}{m^*\xi(T)}\right). \tag{2.51}$$

Thus, for currents just below j_c the order parameter is reduced by a factor $\sqrt{2/3}$, while just above j_c the superconductivity is destroyed. Physically, this depairing current is a maximum when the kinetic energy of the superfluid is equal to the condensation energy. Note that the critical current approaches zero rapidly near T_c, varying as $(1-t)^{3/2}$.

Neglecting the vector potential in (2.47) is equivalent to ignoring self-field effects. If the internal field h generated by the supercurrents is of order H_{c2}, the penetration and subsequent flow of vortices in the sample will dissipate energy, lowering the above estimate of the critical current. For $h \sim H_{c1}$, however, self-field effects are likely to be negligible. The largest internal field h_c associated with the critical current may be estimated from Ampère's Law:

$$\begin{aligned} h_c &\sim \frac{4\pi\lambda}{c} j_c \\ &= \frac{4\pi}{c\lambda}\left(\frac{m^* c^2 \beta}{2\pi e^{*2}}\right)\left(\frac{2e^*|\psi_0|^2}{3\sqrt{3}}\right)\left(\frac{\hbar}{m^*\xi}\right) \\ &= \frac{\phi_0}{2\pi}\left(\frac{1}{3\sqrt{3}\xi\lambda}\right), \end{aligned} \tag{2.52}$$

where $e^* = 2e$ and $\phi_0 = hc/e$ have been fixed. In type-I superconductors, this field is approximately half the thermodynamic critical field $H_c = \phi_0/2\pi\sqrt{2}\xi\lambda$ [64]. In extreme type-II superconductors, such as the high-T_c materials, this field is much lower than the upper critical field $H_{c2} \equiv \phi_0/2\pi\xi^2$ [73]; assuming $\kappa \sim 100$, one obtains

$$\frac{H_{c2}}{h_c} = 3\sqrt{3}\kappa \approx 520. \tag{2.53}$$

Since the lower critical field for high-κ superconductors is $H_{c1} = (\phi_0/4\pi\lambda^2)\ln\kappa$ [64], one has

$$\frac{h_c}{H_{c1}} = \frac{2}{3\sqrt{3}}\frac{\kappa}{\ln\kappa} \approx 8. \tag{2.54}$$

While this ratio is larger than unity, it is sufficiently small that one expects relatively few vortices in the entire system. In the present work, only the contribution of depairing to the critical currents is considered.

2.5.2 *d*-wave Superconductors

The relevant GL free energy for tetragonal d-wave superconductors F_0^{tet} is given explicitly in Eq. (2.16). Spatial variations of the d-wave gap function amplitude may be neglected in sufficiently thin geometries and in the absence of intrinsic defects. Since the external currents give rise to phase variations, however, a subdominant s-wave component may still be nucleated through the mixed-gradient mechanism discussed in Section 2.3. Since $s \sim (1-t)^{3/2}$, the subdominant s-wave component may be assumed to be zero very near T_c. The free energy then becomes indistinguishable from Eq. (2.1) and the derivation above holds. Setting $\Delta_d(\mathbf{r}) \equiv d e^{i\varphi_d(\mathbf{r})}$, one obtains:

$$j_c = \frac{8e\gamma_d d^2}{3\sqrt{3}\xi_d}\delta \quad ; \quad v_s^c = 2\delta\gamma_d|\vec{\nabla}\varphi_d^c| = \frac{4\delta\gamma_d}{3\sqrt{3}\xi_d}. \tag{2.55}$$

In orthorhombic systems, both Δ_s and Δ_d must be included at the outset, but their phase variations will be in concert.

At lower temperatures, a small real s-wave component will be nucleated by the spatial variations of the d-wave gap function's phase. While the magnitude of s is a complicated function of the GL parameters, close to T_c one obtains the simple estimate [147]:

$$\frac{s}{d} \sim \frac{\gamma_\nu}{\gamma_d}\frac{|\alpha_d|}{\alpha_s}(1 - f^2)\cos 2\theta, \tag{2.56}$$

where the normalized gap function is $f \equiv d/d_0$, and $d_0^2 = |\alpha_d|/2\beta_2$ is the d-wave component in the absence of an external field. The angle θ defines the orientation of the superfluid velocity, and the resulting current, with respect the underlying lattice; $\theta = 0$ or $\pi/2$ correspond to currents along $\hat{x}$ or $\hat{y}$.

It is important to note from Eq. (2.56) that the magnitude of the induced s-wave component depends not only on the mixed-gradient coefficient γ_ν, but also on the angle θ. In tetragonal superconductors, at this level of approximation, currents oriented along $\hat{x} \pm \hat{y}$ induce no subdominant component. Furthermore, the sign of the s-wave component reverses as the orientation of the applied current rotates through 90°. Since this result is derived purely from symmetry considerations, it is most likely correct at all temperatures. In orthorhombic superconductors the two-fold symmetry would probably alter the angular dependence in Eq. (2.56). In these systems, therefore, one would expect additional subdominant components induced from currents oriented along $\hat{x} \pm \hat{y}$.

Another interesting consequence of Eq. (2.56) is that the magnitude of the s-wave component induced by external currents is approximately four times larger than that nucleated in the core of a magnetic vortex, Eq. (2.34). Both inhomogeneities generate subdominant components through mixed-gradient terms. It is possible, however, that the induction of an s-wave component through phase variations of the d-wave gap costs less energy than the induction through amplitude variations.

The results obtained for clean materials are no longer applicable if there are additional inhomogeneities giving rise to spatial variations of the order parameter amplitude. Neglecting the subdominant component in the zeroth-order approximation, the gap equation (2.29) is modified:

$$\gamma_d \nabla^2 d + \alpha_d d + 2\beta_2 d^3 + \frac{j^2}{16\gamma_d d^3} = 0. \tag{2.57}$$

This equation is impossible to solve in closed form, without some additional information characterizing the defect and therefore the spatial variations of d. Some numerical calculations of critical currents in the vicinity of wide-angle grain boundaries in the high-T_c materials have been performed [148]. Experimental data used for boundary conditions are the oxygen concentration as a function of grain boundary angle (negatively correlated), and the variation of T_c with oxygen concentration (positively correlated); these together yield the local T_c (and therefore the gap function) at the grain boundary. It must be emphasized that for lower temperatures, Eq. (2.57) is not even remotely correct, since it excludes the possibility of subdominant s-wave components nucleated through spatial variations of both the amplitude and the phase of the d-wave gap function. Evidently, the numerical solution of the full equations that result would be a formidable task. Critical currents in the vicinity of twin boundaries (which are essentially wide-angle grain boundaries) will be investigated in more detail using a more convenient and fully microscopic approach in Chapter 5.

Chapter 3

Derivation of the GL Equations

3.1 Introduction

While phenomenological GL theory has been highly successful in predicting many interesting properties of *d*-wave superconductors in external fields, the relative magnitudes of the various coefficients appearing in the free energy and their dependence on temperature and filling are presently unknown. Earlier derivations of the free energy from a continuum model could not include lattice effects that are believed to be important in theories of *d*-wave superconductivity [136, 137, 138]. In the present chapter, the GL free energy is derived microscopically within the context of two lattice models for the high-T_c superconductors: the extended Hubbard and 'Antiferromagnetic-van Hove' models.

The extended Hubbard (EH) model, which includes a nearest-neighbour attraction in addition to the usual on-site repulsion, is one of the simplest lattice models which allows for a *d*-wave superconducting instability. It has been employed in several analytical and numerical investigations of *d*-wave superconductivity [129, 149, 150]. The EH model has recently been shown, however, to favour *d*-wave superconductivity only in a very small parameter space, preferring a phase separated or spin-density wave state [151].

The 'Antiferromagnetic-van Hove' (AvH) model [31] strongly favours *d*-wave superconductivity while incorporating the coexisting antiferromagnetic correlations observed in NMR [18], neutron scattering [19], and Raman [20] experiments. High transition temperatures are obtained in the model due to the presence of a van Hove singularity in the hole density of states near the Fermi energy. In the AvH model, holes are constrained to move within a single sublattice of a uniform antiferromagnetic background in order to minimize frustration. The hopping parameters are chosen to best fit the quasiparticle dispersion for YBCO measured using ARPES [152, 153]. The resulting band is extended and flat near $(\frac{\pi}{2}, \frac{\pi}{2})$ in momentum space, which is consistent with numerical results for a single hole propagating through an antiferromagnetic background [23, 24, 25, 28], and with experimental evidence [36].

Both the EH and AvH models represent tetragonal systems. While orthorhombicity could be introduced through a two-fold anisotropy in either the kinetic term or the nearest-neighbour attraction, it is neglected in this chapter. Orthorhombic effects are known to be minor even in optimally-doped YBCO, which has fully-formed b-oriented chains contributing to the electronic transport [131]. Furthermore, the presence of orthorhombicity would significantly complicate both the derivation of the GL equations and the presentation of the results. In Chapters 4 and 5, orthorhombic effects are investigated numerically within the context of the EH model using the more convenient Bogoliubov-de Gennes formalism.

In Section 3.2, the Ginzburg-Landau equations for the gap functions and supercurrent are derived microscopically for both the EH and AvH lattice models using a finite-temperature Green function method. The relations defining the transition temperatures are investigated in Section 3.3. It is found that either s-wave or d-wave superconductivity is stable in the EH model. While s-wave is favoured at low electron densities, d-wave is favoured either at high densities or at lower densities with strong on-site repulsion. The equations for T_s (the s-wave transition temperature) and T_d are found analytically in the limit of weak-coupling and low electron densities. The AvH model, in contrast, only has a d-wave superconducting instability. The d-wave transition temperature $T_d \sim 100$ K is consistent with the high-temperature oxides. Analytical solutions for the AvH model are difficult to obtain due to the complicated angular dependence of the AvH dispersion. The GL free energy is derived for both models in Sections 3.4 and 3.5. The coefficients of the GL equations are found analytically for the EH model in the same limit described above. The coefficients are calculated numerically for the EH model and for the AvH model near optimal doping. In Section 3.6, the results are summarized with emphasis on experimental implications for the vortex structure, time-reversal breaking, and critical currents.

3.2 The Lattice GL Equations

The Hamiltonians for the extended Hubbard (EH) and antiferromagnetic-van Hove (AvH) models are respectively:

$$\mathcal{H}^{\rm EH} = -t \sum_{\langle ij\rangle\sigma} c^{\dagger}_{i\sigma} c_{j\sigma} e^{i\frac{2\pi}{\phi_o}\int_j^i \mathbf{A}\cdot d\mathbf{l}} - \mu \sum_{i\sigma} n_{i\sigma} + V_0 \sum_i n_{i\uparrow} n_{i\downarrow} - \frac{1}{2} \sum_{\langle ij\rangle\sigma\sigma'} V_{ij} n_{i\sigma} n_{j\sigma'}; \quad (3.1)$$

$$\begin{aligned} \mathcal{H}^{\rm AvH} &= t_{11} \sum_{\langle\langle ij\rangle\rangle\sigma} c^{\dagger}_{i\sigma} c_{j\sigma} e^{i\frac{2\pi}{\phi_o}\int_j^i \mathbf{A}\cdot d\mathbf{l}} + t_{20} \sum_{\langle\langle\langle ij\rangle\rangle\rangle\sigma} c^{\dagger}_{i\sigma} c_{j\sigma} e^{i\frac{2\pi}{\phi_o}\int_j^i \mathbf{A}\cdot d\mathbf{l}} - \mu \sum_{i\sigma} n_{i\sigma} \\ & \qquad -\frac{V}{2} \sum_{\langle ij\rangle\sigma\sigma'} n_{i\sigma} n_{j\sigma'}, \end{aligned} \quad (3.2)$$

where $n_{i\sigma} = c^{\dagger}_{i\sigma} c_{i\sigma}$, $\mathbf{A}$ is the vector potential associated with an external magnetic field oriented in the $\hat{z}$-direction perpendicular to the copper-oxide planes, $\phi_o = hc/e$ is the flux quantum, and μ is the chemical potential which is included to fix the density. In the EH model the carriers are electrons, and positive V_0 and V_{ij} imply on-site repulsion and nearest-neighbour attraction, respectively. The superconducting carriers in the AvH model are holes propagating through the antiferromagnetic background of the undoped parent state. Second and third nearest-neighbour hopping is represented by $\langle\langle\rangle\rangle$ and $\langle\langle\langle\rangle\rangle\rangle$, respectively. The transfer integrals $t_{11} = 0.04125$ eV and $t_{20} = 0.02175$ eV have been fixed in Ref. [31]. The absence of nearest-neighbour hopping in the AvH model reflects the restricted Hilbert space of the carriers; holes are constrained to move within a single spin sublattice in order to minimize frustration and preserve antiferromagnetic correlations. The values of t_{11} and t_{20} are chosen to result in a van Hove singularity near the bottom of the hole band, located at $(\pi/2, \pi/2)$ in momentum space. The large density of states, together with the nearest-neighbour attraction $V = 0.075$ eV, yields a d-wave transition temperature $T_d \sim 100$ K at optimal doping ($\mu \approx -0.075$ eV, or hole density $\langle n \rangle \sim 0.2$), consistent with experimental results for YBCO.

If the lattice sites i and j are nearest-neighbours, the mean-field EH Hamiltonian can be written

$$\begin{aligned}\mathcal{H}_{\text{eff}}^{\text{EH}}(B) &= -t\sum_{\mathbf{r},\vec{\delta},\sigma} c_\sigma^\dagger(\mathbf{r}+\vec{\delta})c_\sigma(\mathbf{r})e^{i\phi_\delta} - \mu\sum_{\mathbf{r},\sigma} c_\sigma^\dagger(\mathbf{r})c_\sigma(\mathbf{r}) \\ &+ \sum_{\mathbf{r}}\left[\Delta_o^*(\mathbf{r})c_\downarrow(\mathbf{r})c_\uparrow(\mathbf{r}) + H.c.\right] \\ &- \frac{1}{2}\sum_{\mathbf{r},\vec{\delta}}\left[\Delta_\delta^*(\mathbf{r})c_\downarrow(\mathbf{r})c_\uparrow(\mathbf{r}+\vec{\delta}) - \Delta_\delta^*(\mathbf{r})c_\uparrow(\mathbf{r})c_\downarrow(\mathbf{r}+\vec{\delta}) + H.c.\right], \end{aligned} \tag{3.3}$$

where

$$\phi_\delta = \frac{2\pi}{\phi_o}\int_{\mathbf{r}}^{\mathbf{r}+\vec{\delta}} \mathbf{A}\cdot d\mathbf{l}, \tag{3.4}$$

and $\vec{\delta} = \pm\hat{x}, \pm\hat{y}$ (the lattice constant is taken to be unity for convenience). The 'on-site' (isotropic-s) and nearest-neighbour gap functions are defined as follows:

$$\Delta_o(\mathbf{r}) \equiv V_0\langle c_\downarrow(\mathbf{r})c_\uparrow(\mathbf{r})\rangle; \tag{3.5}$$

$$\begin{aligned}\Delta_\delta(\mathbf{r}) &\equiv V_\delta\langle c_\downarrow(\mathbf{r})c_\uparrow(\mathbf{r}+\vec{\delta})\rangle \\ &\equiv -V_\delta\langle c_\uparrow(\mathbf{r})c_\downarrow(\mathbf{r}+\vec{\delta})\rangle,\end{aligned} \tag{3.6}$$

assuming the existence of pairing in only the spin-singlet channel, in accordance with experimental results for the cuprate superconductors [54, 55, 56]. The mean-field Hamiltonian for the AvH model is written:

$$\begin{aligned}\mathcal{H}_{\text{eff}}^{\text{AvH}}(B) &= t_{11}\sum_{\mathbf{r},\vec{\delta}_{11},\sigma} c_\sigma^\dagger(\mathbf{r}+\vec{\delta}_{11})c_\sigma(\mathbf{r})e^{i\phi_{\vec{\delta}_{11}}} + t_{20}\sum_{\mathbf{r},\vec{\delta}_{20},\sigma} c_\sigma^\dagger(\mathbf{r}+\vec{\delta}_{20})c_\sigma(\mathbf{r})e^{i\phi_{\vec{\delta}_{20}}} \\ &- \mu\sum_{\mathbf{r},\sigma} c_\sigma^\dagger(\mathbf{r})c_\sigma(\mathbf{r}) - \frac{1}{2}\sum_{\mathbf{r},\vec{\delta}}\left[\Delta_\delta^*(\mathbf{r})c_\downarrow(\mathbf{r})c_\uparrow(\mathbf{r}+\vec{\delta}) + H.c.\right],\end{aligned} \tag{3.7}$$

where $\mathbf{r} = m\hat{r}_1 + n\hat{r}_2$, such that $\hat{r}_1 \equiv \hat{x} + \hat{y}$ and $\hat{r}_2 \equiv \hat{x} - \hat{y}$ are primitive vectors of a single sublattice, and each lattice site has the two-point basis $\hat{0}$, $\hat{x}$. Then, $\vec{\delta}_{11} = \pm\hat{r}_1, \pm\hat{r}_2$, $\vec{\delta}_{20} = \pm(\hat{r}_1 + \hat{r}_2), \pm(\hat{r}_1 - \hat{r}_2)$, and $\vec{\delta} = \pm\hat{x}, \pm\hat{y}$. Throughout the remainder of this section calculations will be presented within the context of the EH model. A comparison of the EH and AvH Hamiltonians indicates that analogous results for the AvH model can be obtained at any stage by eliminating the on-site gap function, and reversing the sign of the kinetic term.

One of the most useful analytical approaches to the solution of the many-body Hamiltonians (3.3) and (3.7) is the finite-temperature Green function method [154, 155], which allows many-body correlations to be treated in a perturbative manner. The single-particle Green function is defined as follows:

$$\begin{aligned} \mathcal{G}_{\uparrow}(\mathbf{r},\tau\,;\,\mathbf{r}',0) &\equiv -\left\langle T_\tau\left[c_{\uparrow}(\mathbf{r},\tau)c^{\dagger}_{\uparrow}(\mathbf{r}',0)\right]\right\rangle \\ &\equiv -\frac{\mathrm{Tr}\left\{e^{-\beta\mathcal{H}}T_\tau\left[c_{\uparrow}(\mathbf{r},\tau)c^{\dagger}_{\uparrow}(\mathbf{r}',0)\right]\right\}}{\mathrm{Tr}\left\{e^{-\beta\mathcal{H}}\right\}}, \end{aligned} \tag{3.8}$$

where $\beta = 1/T$ is the inverse temperature (k_B is set to unity) and $\langle\rangle$ in this context defines a grand canonical expectation value over the N-particle ground state $|0\rangle$ at equilibrium (note that the chemical potential has been included in the definition of $\mathcal{H}$). The fermion fields have acquired time-dependence through the Heisenberg transformation

$$c(\mathbf{r},\tau) \equiv e^{\mathcal{H}\tau}c(\mathbf{r})e^{-\mathcal{H}\tau}. \tag{3.9}$$

It is important to notice that in the finite-temperature Green function formalism, $\tau \equiv it$ is a fictitious imaginary time which varies on an interval $[-1/T, 1/T]$ rather than on $[-\infty,\infty]$ [156]. Since the single-particle Green function characterizes the propagation of a fermion through the $N-1$-particle ground state from point $\mathbf{r}$ at imaginary time $it = 0$ to point $\mathbf{r}'$ at $it = \tau$, it is 'time-ordered' through the operator T_τ:

$$\mathcal{G}_{\uparrow}(\mathbf{r},\tau\,;\,\mathbf{r}',0) = \begin{cases} -\left\langle c_{\uparrow}(\mathbf{r},\tau)c^{\dagger}_{\uparrow}(\mathbf{r}',0)\right\rangle, & \tau > 0 \\ +\left\langle c^{\dagger}_{\uparrow}(\mathbf{r}',0)c_{\uparrow}(\mathbf{r},\tau)\right\rangle, & \tau < 0 \end{cases} \tag{3.10}$$

While the single-particle Green function gives information about the single-particle excitations of the system, the anomalous Green function

$$\mathcal{F}^{\dagger}_{\downarrow\uparrow}(\mathbf{r},\tau\,;\,\mathbf{r}',0) \equiv -\left\langle T_\tau\left[c^{\dagger}_{\downarrow}(\mathbf{r},\tau)c^{\dagger}_{\uparrow}(\mathbf{r}',0)\right]\right\rangle \tag{3.11}$$

governs the propagation of (singlet) pair correlations. In fact, the anomalous Green function is closely related to the gap functions (3.5) and (3.6):

$$\Delta^*_\alpha(\mathbf{r}) = V_\alpha \mathcal{F}^\dagger_{\downarrow\uparrow}(\mathbf{r},0\,;\,\mathbf{r}+\alpha,0), \tag{3.12}$$

where $\alpha = 0, \vec{\delta}$. Since there are no spin-orbit terms in the Hamiltonians, $\mathcal{G} \equiv \mathcal{G}_\uparrow = \mathcal{G}_\downarrow$ and $\mathcal{F}^\dagger \equiv \mathcal{F}^\dagger_{\downarrow\uparrow} = \mathcal{F}^\dagger_{\uparrow\downarrow}$; that is, the equations of motion are spin-independent.

The Green function method consists of deriving, and solving, the equations of motion for the propagators:

$$\frac{\partial \mathcal{G}(\mathbf{r},\tau\,;\,\mathbf{r}',0)}{\partial\tau} \;=\; -\left\langle T_\tau \left(\frac{\partial c_\uparrow(\mathbf{r},\tau)}{\partial\tau}\right) c^\dagger_\uparrow(\mathbf{r}',0)\right\rangle - \delta\,(\mathbf{r}-\mathbf{r}')\,\delta(\tau); \tag{3.13}$$

$$\frac{\partial \mathcal{F}^\dagger(\mathbf{r},\tau\,;\,\mathbf{r}',0)}{\partial\tau} \;=\; -\left\langle T_\tau \left(\frac{\partial c^\dagger_\downarrow(\mathbf{r},\tau)}{\partial\tau}\right) c^\dagger_\uparrow(\mathbf{r}',0)\right\rangle. \tag{3.14}$$

The time-derivatives of the fermion fields may be explicitly evaluated by noting that

$$\frac{\partial c^{(\dagger)}(\mathbf{r},\tau)}{\partial\tau} = -\left[c^{(\dagger)}(\mathbf{r},\tau)\;,\;\mathcal{H}\right], \tag{3.15}$$

which may be obtained directly from (3.9). After some tedious but straightforward algebra, one obtains two coupled first-order differential equations:

$$\begin{aligned}\frac{\partial \mathcal{G}(\mathbf{r},\tau\,;\,\mathbf{r}',0)}{\partial\tau} \;=\;& t\sum_{\vec{\delta}} e^{-i\phi_\delta}\mathcal{G}(\mathbf{r}+\vec{\delta},\tau\,;\,\mathbf{r}',0) + \mu\mathcal{G}(\mathbf{r},\tau\,;\,\mathbf{r}',0) - \delta\,(\mathbf{r}-\mathbf{r}')\,\delta(\tau)\\ & -\Delta_0(\mathbf{r})\mathcal{F}^\dagger(\mathbf{r},\tau\,;\,\mathbf{r}',0) + \sum_{\vec{\delta}}\Delta_\delta(\mathbf{r})\mathcal{F}^\dagger(\mathbf{r}+\vec{\delta},\tau\,;\,\mathbf{r}',0);\end{aligned} \tag{3.16}$$

$$\begin{aligned}\frac{\partial \mathcal{F}^\dagger(\mathbf{r},\tau\,;\,\mathbf{r}',0)}{\partial\tau} \;=\;& -t\sum_{\vec{\delta}} e^{-i\phi_\delta}\mathcal{F}^\dagger(\mathbf{r}+\vec{\delta},\tau\,;\,\mathbf{r}',0) - \mu\mathcal{F}^\dagger(\mathbf{r},\tau\,;\,\mathbf{r}',0)\\ & -\Delta^*_0(\mathbf{r})\mathcal{G}(\mathbf{r},\tau\,;\,\mathbf{r}',0) + \sum_{\vec{\delta}}\Delta^*_\delta(\mathbf{r})\mathcal{G}(\mathbf{r}+\vec{\delta},\tau\,;\,\mathbf{r}',0).\end{aligned} \tag{3.17}$$

It is instructive to rewrite these two coupled equations as a single matrix equation [157], although the motivation for doing this will only become clear in Section 4.2. This is accomplished by introducing the two component field

$$\Psi(\mathbf{r},\tau) \equiv \begin{bmatrix} c_\uparrow(\mathbf{r},\tau) \\ c^\dagger_\downarrow(\mathbf{r},\tau)\end{bmatrix}, \tag{3.18}$$

and the 2×2 matrix Green function

$$\begin{aligned} \boldsymbol{\mathcal{G}}(\mathbf{r},\tau\,;\,\mathbf{r}',0) &\equiv -\langle T_\tau\,[\Psi(\mathbf{r},\tau)\Psi(\mathbf{r}',0)]\rangle \\ &= \begin{bmatrix} \mathcal{G}(\mathbf{r},\tau\,;\,\mathbf{r}',0) & \mathcal{F}(\mathbf{r},\tau\,;\,\mathbf{r}',0) \\ \mathcal{F}^\dagger(\mathbf{r},\tau\,;\,\mathbf{r}',0) & -\mathcal{G}(\mathbf{r},\tau\,;\,\mathbf{r}',0) \end{bmatrix}. \end{aligned} \tag{3.19}$$

Equations (3.16) and (3.17) then become

$$\begin{pmatrix} \frac{\partial}{\partial\tau} + \hat{\xi} & \hat{\Delta} \\ \hat{\Delta}^* & \frac{\partial}{\partial\tau} - \hat{\xi}^* \end{pmatrix} \boldsymbol{\mathcal{G}}(\mathbf{r},\tau\,;\,\mathbf{r}',0) = -\mathbf{1}\delta(\mathbf{r}-\mathbf{r}')\delta(\tau), \tag{3.20}$$

where the kinetic energy and gap function operators are explicitly

$$\hat{\xi}X(\mathbf{r}) = -t\sum_{\vec{\delta}} e^{-i\phi_\delta} X(\mathbf{r}+\vec{\delta}) - \mu X(\mathbf{r}); \tag{3.21}$$

$$\hat{\Delta}X(\mathbf{r}) = \Delta_\circ(\mathbf{r})X(\mathbf{r}) - \sum_{\vec{\delta}} \Delta_\delta(\mathbf{r})X(\mathbf{r}+\vec{\delta}). \tag{3.22}$$

The matrix equation (3.20) in this form has the appearance of an eigenvalue equation, with eigenoperators $\partial/\partial\tau$.

The coupled equations may be greatly simplified by expanding all quantities dependent on τ in a Fourier series:

$$X(\tau) \equiv T\sum_{\omega_n} e^{-i\omega_n\tau} X(\omega_n), \tag{3.23}$$

where

$$\omega_n \equiv (2n+1)\pi T, \qquad n = 0, 1, 2, \ldots \tag{3.24}$$

are the fermionic Matsubara frequencies [158, 159]. It immediately follows that the gap functions are the Fourier sum of the anomalous propagators:

$$\Delta_\circ^*(\mathbf{r}) = TV_0\sum_{\omega_n} \mathcal{F}^\dagger(\mathbf{r},\mathbf{r},\omega_n), \tag{3.25}$$

$$\Delta_\delta^*(\mathbf{r}) = TV_\delta\sum_{\omega_n} \mathcal{F}^\dagger(\mathbf{r},\mathbf{r}+\vec{\delta},\omega_n), \tag{3.26}$$

Eqs. (3.16) and (3.17) then become

$$\Big[i\omega_n + \mu + t\sum_{\vec{\delta}} e^{-i\phi_\delta}\hat{P}_\delta(\mathbf{r})\Big]\mathcal{G}(\mathbf{r},\mathbf{r}',\omega_n)$$

$$-\Big[\Delta_\circ(\mathbf{r}) - \sum_{\vec{\delta}} \Delta_\delta(\mathbf{r})\hat{P}_\delta(\mathbf{r})\Big]\mathcal{F}^\dagger(\mathbf{r},\mathbf{r}',\omega_n) = \delta(\mathbf{r}-\mathbf{r}'); \tag{3.27}$$

$$\begin{aligned}\Big[-i\omega_n + \mu + t\sum_{\vec{\delta}} e^{-i\phi_\delta}\hat{P}_\delta(\mathbf{r})\Big]&\mathcal{F}^\dagger(\mathbf{r},\mathbf{r}',\omega_n)\\ +\Big[\Delta_\circ(\mathbf{r}) - \sum_{\vec{\delta}} \Delta_\delta(\mathbf{r})\hat{P}_\delta(\mathbf{r})\Big]&\mathcal{G}(\mathbf{r},\mathbf{r}',\omega_n) = 0,\end{aligned} \tag{3.28}$$

where $\hat{P}_\delta(\mathbf{r})X(\mathbf{r}) \equiv X(\mathbf{r}+\vec{\delta})$. Equations (3.27) and (3.28), subject to the self-consistency criteria (3.25) and (3.26), are the fundamental field equations for the superconductor on a tight-binding lattice.

While these exact equations are analytically intractable, under certain circumstances they may be solved perturbatively. Formally, this is more conveniently accomplished by re-expressing the coupled differential equations as coupled integral equations. The latter may be obtained by making use of the equations of motion for the normal-state single-particle Green functions $\tilde{\mathcal{G}}^\circ$ (and its Hermitian conjugate), obtained by setting $\Delta \propto \mathcal{F}^\dagger$ equal to zero in (3.27). One then obtains the lattice version of the Gor'kov equations [141]:

$$\begin{aligned}\mathcal{G}(\mathbf{r},\mathbf{r}',\omega_n) &= \tilde{\mathcal{G}}^\circ(\mathbf{r},\mathbf{r}',\omega_n) + \sum_{\mathbf{r}''}\tilde{\mathcal{G}}^\circ(\mathbf{r},\mathbf{r}'',\omega_n)\Big[\Delta_\circ(\mathbf{r}'')\\ &\qquad\qquad - \sum_{\vec{\delta}}\Delta_\delta(\mathbf{r}'')\hat{P}_\delta(\mathbf{r}'')\Big]\mathcal{F}^\dagger(\mathbf{r}'',\mathbf{r}',\omega_n);\end{aligned} \tag{3.29}$$

$$\mathcal{F}^\dagger(\mathbf{r},\mathbf{r}',\omega_n) = -\sum_{\mathbf{r}''}\tilde{\mathcal{G}}^\circ(\mathbf{r}'',\mathbf{r},-\omega_n)\Big[\Delta_\circ^*(\mathbf{r}'') - \sum_{\vec{\delta}}\Delta_\delta^*(\mathbf{r}'')\hat{P}_\delta(\mathbf{r}'')\Big]\mathcal{G}(\mathbf{r}'',\mathbf{r}',\omega_n). \tag{3.30}$$

Though superficially these equations appear more involved than the original ones, their form is in fact quite simple, and much more conducive to perturbative analysis. Their structure may be represented by:

$$\mathcal{G} = \tilde{\mathcal{G}}^\circ + \tilde{\mathcal{G}}^\circ\Delta\mathcal{F}^\dagger \quad ; \quad \mathcal{F}^\dagger = -\tilde{\mathcal{G}}^{\circ *}\Delta^*\mathcal{G}, \tag{3.31}$$

where $\tilde{\mathcal{G}}^\circ(\mathbf{r},\mathbf{r}',-\omega_n) = \tilde{\mathcal{G}}^{\circ *}(\mathbf{r},\mathbf{r}',\omega_n)$ is the normal-state single-particle Green function in the presence of the vector potential. Iterating these equations gives

$$\mathcal{G} = \tilde{\mathcal{G}}^\circ - \tilde{\mathcal{G}}^\circ\Delta\tilde{\mathcal{G}}^{\circ *}\Delta^*\tilde{\mathcal{G}}^\circ + \ldots, \quad \text{and} \tag{3.32}$$

$$\mathcal{F}^\dagger = -\tilde{\mathcal{G}}^{\circ *}\Delta^*\tilde{\mathcal{G}}^\circ + \tilde{\mathcal{G}}^{\circ *}\Delta^*\tilde{\mathcal{G}}^\circ\Delta\tilde{\mathcal{G}}^{\circ *}\Delta^*\tilde{\mathcal{G}}^\circ + \ldots. \tag{3.33}$$

Thus, the integral equations allow both the single-particle and anomalous Green functions to be written as a perturbation series in the normal-state Green function. The perturbing potential is the order parameter field, as can be made more explicit by re-writing (3.32) and (3.33) as

$$\begin{aligned} \mathcal{G}^{-1} &= \left(\tilde{\mathcal{G}}^{\circ}\right)^{-1} + \Delta\tilde{\mathcal{G}}^{\circ *}\Delta^{*}; & (3.34) \\ \left(\mathcal{F}^{\dagger}\right)^{-1} &= -\left(\tilde{\mathcal{G}}^{\circ *}\Delta^{*}\tilde{\mathcal{G}}^{\circ}\right)^{-1} - \Delta. & (3.35) \end{aligned}$$

The expressions (3.34) and (3.35) represent Dyson's equations for the ordinary and anomalous Green functions, respectively. In the absence of an order parameter field $\mathcal{G} = \tilde{\mathcal{G}}^{\circ}$ as expected, but with $\Delta \neq 0$ the single-particle propagator is renormalized, with a self-energy $\Sigma = -\Delta\tilde{\mathcal{G}}^{\circ *}\Delta^{*}$. In contrast, the self-energy of the anomalous propagator is simply the gap function because $\mathcal{F} \propto \Delta$; physically, this means that the gap function must be a self-consistent solution of the coupled Dyson's equations.

The perturbation theory just described should be valid whenever the order parameter field is a weak disturbance. Thus, one would expect it to apply close to the superconducting critical temperature T_c in arbitrary external magnetic fields, and at lower temperatures for fields sufficiently close to H_{c2}. Combining the conditions (3.25) and (3.26) with (3.33), one obtains the self-consistent equations for the gaps:

$$\Delta^{*} \approx -TV \sum_{\omega_n} \left\{ \tilde{\mathcal{G}}^{\circ *}\Delta^{*}\tilde{\mathcal{G}}^{\circ} - \tilde{\mathcal{G}}^{\circ *}\Delta^{*}\tilde{\mathcal{G}}^{\circ}\Delta\tilde{\mathcal{G}}^{\circ *}\Delta^{*}\tilde{\mathcal{G}}^{\circ} \right\}. \tag{3.36}$$

More formally, these are written

$$\begin{aligned} \frac{1}{V_\alpha}\Delta^{*}_{\alpha}(\mathbf{r}) &= -T \sum_{\mathbf{r}'', \omega_n} \tilde{\mathcal{G}}^{\circ}(\mathbf{r}'', \mathbf{r}, -\omega_n)\Delta^{*}(\mathbf{r}'')\tilde{\mathcal{G}}^{\circ}(\mathbf{r}'', \mathbf{r} + \vec{\alpha}, \omega_n) \\ &+ T \sum_{\mathbf{r}'', \mathbf{r}_1, \mathbf{r}_2} \sum_{\omega_n} \tilde{\mathcal{G}}^{\circ}(\mathbf{r}'', \mathbf{r}, -\omega_n)\Delta^{*}(\mathbf{r}'')\tilde{\mathcal{G}}^{\circ}(\mathbf{r}'', \mathbf{r}_1, \omega_n) \\ &\qquad \times \Delta(\mathbf{r}_1)\tilde{\mathcal{G}}^{\circ}(\mathbf{r}_2, \mathbf{r}_1, -\omega_n)\Delta^{*}(\mathbf{r}_2)\tilde{\mathcal{G}}^{\circ}(\mathbf{r}_2, \mathbf{r} + \vec{\alpha}, \omega_n), \qquad (3.37) \end{aligned}$$

where

$$\begin{aligned} \Delta^{*}(\mathbf{x}) &\equiv \Delta^{*}_{\circ}(\mathbf{x}) - \sum_{\vec{\delta}} \Delta^{*}_{\delta}(\mathbf{x})\hat{P}_{\delta}(\mathbf{x}) \\ &\equiv \sum_{\vec{\alpha}} (-1)^{|\vec{\alpha}|}\Delta^{*}_{\alpha}(\mathbf{x})\hat{P}_{\delta}(\mathbf{x}) \qquad (3.38) \end{aligned}$$

and $\vec{\alpha} = \hat{0}$, $\pm\hat{x}$, or $\pm\hat{y}$.

In the strong type-II limit, appropriate for the high-T_c oxides, the penetration depth $\lambda(T)$ exceeds both the coherence length $\xi(T)$ governing spatial variations of the gap functions, and the Fermi wavelength $k_F^{-1} \sim a$ characterizing the single-particle excitations (where a is the lattice spacing ≈ 3.8 Å from Section 1.1). The single-particle Green function is then approximately translationally invariant (first line below), and the electrodynamics is local (second line below):

$$\begin{aligned} \tilde{\mathcal{G}}^{\circ}(\mathbf{r}, \mathbf{r}', \omega_n) &\approx \mathcal{G}^{\circ}(\mathbf{r} - \mathbf{r}', \omega_n) e^{-i\frac{2\pi}{\phi_0}\int_{\mathbf{r}}^{\mathbf{r}'} \mathbf{A}\cdot d\mathbf{l}} \\ &\approx \mathcal{G}^{\circ}(\mathbf{r} - \mathbf{r}', \omega_n) e^{i\frac{2\pi}{\phi_0}\mathbf{A}(\mathbf{r})\cdot(\mathbf{r}-\mathbf{r}')}, \end{aligned} \tag{3.39}$$

where $\mathcal{G}^{\circ}(\mathbf{r} - \mathbf{r}', \omega_n)$ is the normal-state lattice Green function in the absence of an external field. The normal-state Green function is obtained by Fourier transforming Eq. (3.27):

$$\mathcal{G}^{\circ}(\mathbf{x}, \omega_n) = \sum_{\mathbf{k}} \frac{e^{i\mathbf{k}\cdot\mathbf{x}}}{i\omega_n - \xi_k}, \tag{3.40}$$

and the sum is over wavevectors in the first Brillouin zone. The dispersion relations for the EH and AvH models are respectively

$$\begin{aligned} \xi_k^{\mathrm{EH}} &= -2t(\mathrm{cos}k_x + \mathrm{cos}k_y) - \mu & (3.41) \\ \xi_k^{\mathrm{AvH}} &= 2t_{11}(\mathrm{cos}k_1 + \mathrm{cos}k_2) + 4t_{20}\mathrm{cos}k_1\mathrm{cos}k_2 - \mu, & (3.42) \end{aligned}$$

where k_1 and k_2 are reciprocal vectors of a given sublattice.

In the high-temperature superconductors, the coherence length is unusually short: $\xi(0) \sim 3a - 4a$. Since rapid variations of the order parameter field are associated with large energies, the perturbative treatment is expected to be most valid near T_c, where the spatial variations are slower due to the divergence of the coherence length $\xi(T) \sim 1/\sqrt{1 - T/T_c}$. Sufficiently near T_c, therefore, one may assume that the gap functions vary over distances much longer than k_F^{-1}, the characteristic length scale of the single-particle Green functions. Thus, Eq. (3.37) can be expanded up to fourth-order in lattice derivatives (see Sections 2.3 and 3.5). Since the derivation is quite involved, it is relegated to Appendix A. The self-consistent equations for the gap functions in the EH model eventually become:

$$\begin{aligned}
\Delta^*_\alpha(\mathbf{r}) &= -TV_\alpha \sum_{\omega_n} \sum_{\vec{\alpha}'} (-1)^{\alpha'} \sum_{m,n} \mathcal{G}^\circ(m\hat{x}+n\hat{y},-\omega_n)\mathcal{G}^\circ(m\hat{x}+n\hat{y}+\vec{\alpha}'-\vec{\alpha},\omega_n) \\
&\times\ e^{-i\frac{2\pi}{\phi_0}\mathbf{A}(\mathbf{r})\cdot(\vec{\alpha}-\vec{\alpha}')}\Big\{1-\epsilon^{\mathrm{EH}}_{x,1}\left(\hat{x}\Pi_x\right)^2-\epsilon^{\mathrm{EH}}_{y,1}\left(\hat{y}\Pi_y\right)^2-\epsilon^{\mathrm{EH}}_{x,2}\left(\hat{x}\Pi_x\right)^4-\epsilon^{\mathrm{EH}}_{y,2}\left(\hat{y}\Pi_y\right)^4 \\
&\quad -\epsilon^{\mathrm{EH}}_{xy,2}\left(\hat{x}\Pi_x\right)^2\left(\hat{y}\Pi_y\right)^2\Big\}\Delta^*_{\alpha'}(\mathbf{r}) \\
&+\ TV_\alpha \sum_{\mathbf{k},\omega_n} \frac{e^{i\mathbf{k}\cdot\vec{\alpha}}e^{-i\frac{2\pi}{\phi_0}\mathbf{A}(\mathbf{r})\cdot\vec{\alpha}}}{(\omega_n^2+\xi_k^2)^2}\Big\{|\Delta_\circ(\mathbf{r})|^2\Delta^*_\circ(\mathbf{r})-2|\Delta_\circ(\mathbf{r})|^2M(\mathbf{r}) \\
&\quad +2|M(\mathbf{r})|^2\Delta^*_\circ(\mathbf{r})-\Delta^{*2}_\circ(\mathbf{r})M^*(\mathbf{r})+\Delta_\circ(\mathbf{r})M^2(\mathbf{r})-|M(\mathbf{r})|^2M(\mathbf{r})\Big\}, \qquad (3.43)
\end{aligned}$$

where

$$\begin{aligned}
i\left(\hat{z}\Pi_z\right)\Delta^*_{-z}(\mathbf{r}) &\equiv e^{i\frac{4\pi}{\phi_0}A_z(\mathbf{r})}\Delta^*_z(\mathbf{r})-\Delta^*_{-z}(\mathbf{r}) \qquad (3.44) \\
&\Rightarrow \left[\left(\hat{z}\frac{\partial}{\partial z}\right)+i\frac{4\pi}{\phi_0}A_z(\mathbf{r})\right]\Delta_{-z}(\mathbf{r}), \qquad (3.45)
\end{aligned}$$

where Eq. (3.45) is the derivative in the continuum limit, and

$$M(\mathbf{r}) \equiv \sum_{\vec{\delta}'=\pm\hat{x},\pm\hat{y}} \Delta^*_{\delta'}(\mathbf{r})e^{i\mathbf{k}\cdot\vec{\delta}'}e^{i\frac{2\pi}{\phi_0}\mathbf{A}(\mathbf{r})\cdot\vec{\delta}'}. \qquad (3.46)$$

Note that all gap functions are taken at the same point **r** in the last term of Eq. (3.43). This approximation simplifies the resulting equations but is not always appropriate, as discussed in Section 3.5. The coefficients of the gradient terms ϵ have a complicated dependence on the coordinate variables m and n, and are explicitly written in Appendix A. As discussed in this Appendix, the gradient terms with odd powers of $\hat{x}\Pi_x$ and/or $\hat{y}\Pi_y$ vanish by symmetry for tetragonal systems. The GL equations for the gap functions in the AvH model are given by:

$$\begin{aligned}
\Delta^*_\delta(\mathbf{r}) &= \frac{TV}{2}\sum_{\vec{\delta}'}\sum_{m,n}\sum_{\omega_n}\mathcal{G}^\circ(m\hat{r}_1+n\hat{r}_2,-\omega_n)\mathcal{G}^\circ(m\hat{r}_1+n\hat{r}_2+\vec{\delta}'-\vec{\delta},\omega_n) \\
&\times\ e^{-i\frac{2\pi}{\phi_0}\mathbf{A}(\mathbf{r})\cdot(\vec{\delta}-\vec{\delta}')}\Big\{1-\epsilon^{\mathrm{AvH}}_{x,1}\left(\hat{x}\Pi_x\right)^2-\epsilon^{\mathrm{AvH}}_{y,1}\left(\hat{y}\Pi_y\right)^2 \\
&\quad -\epsilon^{\mathrm{AvH}}_{x,2}\left(\hat{x}\Pi_x\right)^4-\epsilon^{\mathrm{AvH}}_{y,2}\left(\hat{y}\Pi_y\right)^4-\epsilon^{\mathrm{AvH}}_{xy,2}\left(\hat{x}\Pi_x\right)^2\left(\hat{y}\Pi_y\right)^2\Big\}\Delta^*_{\delta'}(\mathbf{r}) \\
&-\ \frac{TV}{2}\sum_{\mathbf{k},\omega_n}\frac{e^{i\mathbf{k}\cdot\vec{\delta}}e^{-i\frac{2\pi}{\phi_0}\mathbf{A}(\mathbf{r})\cdot\vec{\delta}}}{(\omega_n^2+\xi_k^2)^2}|M(\mathbf{r})|^2M(\mathbf{r}), \qquad (3.47)
\end{aligned}$$

with

$$\begin{aligned} (\hat{r}_1\Pi_{r_1}) &\equiv i\,(\hat{x}\Pi_x)\,(\hat{y}\Pi_y) + (\hat{x}\Pi_x) + (\hat{y}\Pi_y)\,; && (3.48) \\ (\hat{r}_2\Pi_{r_2}) &\equiv -i\,(\hat{x}\Pi_x)\,(\hat{y}\Pi_y) + (\hat{x}\Pi_x) - (\hat{y}\Pi_y)\,. && (3.49) \end{aligned}$$

The coefficients ϵ are also given in Appendix A.

The total current in the superconductor is obtained using [160]

$$\mathbf{j}(\mathbf{r}) = i\langle[\mathcal{H},\mathbf{P}]\rangle, \tag{3.50}$$

where the polarization operator is defined by

$$\mathbf{P} \equiv \sum_{\mathbf{r}\sigma} \mathbf{r} c_\sigma^\dagger(\mathbf{r}) c_\sigma(\mathbf{r}). \tag{3.51}$$

Since the density operator commutes with itself, one need only consider the kinetic energy contribution to (3.50), which for the EH model yields:

$$\begin{aligned} \mathbf{j}^{\mathrm{EH}}(\mathbf{r}) &= it\sum_{\vec{\delta},\sigma} \vec{\delta} e^{i\phi_\delta} \left\langle c_\sigma^\dagger(\mathbf{r}+\vec{\delta}) c_\sigma(\mathbf{r}) \right\rangle \\ &= -2tT\sum_{\vec{\delta},\omega_n} \Pi'_\delta(\mathbf{r}')\mathcal{G}(\mathbf{r},\mathbf{r}',\omega_n)\Big|_{\mathbf{r}=\mathbf{r}'} && (3.52) \\ &\Rightarrow -2t\left[\vec{\Pi}'^*(\mathbf{r}) + \vec{\Pi}'(\mathbf{r}')\right] T\sum_{\omega_n} \mathcal{G}(\mathbf{r},\mathbf{r}',\omega_n)\Big|_{\mathbf{r}=\mathbf{r}'} && (3.53) \end{aligned}$$

where (3.53) represents the continuum limit of the lattice current, and

$$\begin{aligned} i\left(\hat{\delta}'\Pi'_\delta\right)(\mathbf{r})f(\mathbf{r}) &\equiv e^{i\frac{2\pi}{\phi_0}\mathbf{A}(\mathbf{r})\cdot\vec{\delta}} f(\mathbf{r}+\vec{\delta}) - f(\mathbf{r}); && (3.54) \\ \vec{\Pi}'(\mathbf{r}) &\equiv -i\vec{\nabla} + \frac{2\pi}{\phi_0}\mathbf{A}(\mathbf{r}). && (3.55) \end{aligned}$$

Using the perturbative solution (3.32) of the single-particle Green function appearing in (3.52), the total current becomes:

$$\begin{aligned} \mathbf{j}^{\mathrm{EH}}(\mathbf{r}) &= 2tT\sum_{\mathbf{R}_1,\mathbf{R}_2}\sum_{\vec{\alpha}_1,\vec{\alpha}_2}\sum_{\vec{\delta},\omega_n} e^{i\frac{2\pi}{\phi_0}\mathbf{A}(\mathbf{r})\cdot(\vec{\alpha}_2-\vec{\alpha}_1)}(-1)^{|\alpha_1|}(-1)^{|\alpha_2|} \\ &\times\ \mathcal{G}^\circ(-\mathbf{R}_1,\omega_n)\mathcal{G}^\circ(\mathbf{R}_2-\mathbf{R}_1-\vec{\alpha}_1,-\omega_n)\hat{\Delta}_{-\delta}(\mathbf{R}_2)\mathcal{G}^\circ(\mathbf{R}_2+\vec{\alpha}_2,\omega_n) \\ &\times\ \left\{\Delta^*_{\alpha_2}(\mathbf{r})\left[m\,(\hat{x}\Pi_x)^* + n\,(\hat{y}\Pi_y)^*\right]\Delta_{\alpha_1}(\mathbf{r})\right. \\ &\quad \left. +\Delta_{\alpha_1}(\mathbf{r})\left[m'\,(\hat{x}\Pi_x) + n'\,(\hat{y}\Pi_y)\right]\Delta^*_{\alpha_2}(\mathbf{r})\right\}, && (3.56) \end{aligned}$$

where $\mathbf{R}_1 = m\hat{x} + n\hat{y}$ and $\mathbf{R}_2 = m'\hat{x} + n'\hat{y}$. A similar expression for the AvH model can be obtained by setting $t \to -t_{11}, -t_{20}$ with $\vec{\delta} \to \vec{\delta}_{11}, \vec{\delta}_{20}$ and $\mathbf{R}_1 = m\hat{r}_1 + n\hat{r}_2$, $\mathbf{R}_2 = m'\hat{r}_1 + n'\hat{r}_2$, and making the replacements $(\hat{x}\Pi_x) \to (\hat{x}\Pi_x) + (\hat{y}\Pi_y)$ and $(\hat{y}\Pi_y) \to (\hat{x}\Pi_x) - (\hat{y}\Pi_y)$.

The various integrals and sums appearing in the gap equations, Eq. (3.43) and Eq. (3.47), and the expression for the current Eq. (3.56) in general can be determined only numerically. One case, however, is analytically tractable: the EH model at low electron densities and weak to intermediate coupling. For $V_\delta = 0$ and $V_0 \to -V_0$, this limit corresponds to ordinary BCS theory.

3.3 Determination of T_c

3.3.1 Extended Hubbard Model

At temperatures sufficiently near T_c, the gap equations (3.43) and (3.47) can be linearized. Making use of the definition of the normal-state Green function (3.40), one obtains for the EH model:

$$\Delta_o^*(\mathbf{r}) = TV_0 \sum_{\omega_n,\mathbf{k}} \frac{2a_k\Delta_s^*(\mathbf{r}) - \Delta_o^*(\mathbf{r})}{\omega_n^2 + \xi_k^2}, \tag{3.57}$$

$$\Delta_s^*(\mathbf{r}) = \frac{TV_1}{2} \sum_{\omega_n,\mathbf{k}} \frac{a_k\left[2a_k\Delta_s^*(\mathbf{r}) - \Delta_o^*(\mathbf{r})\right]}{\omega_n^2 + \xi_k^2}, \tag{3.58}$$

$$\Delta_d^*(\mathbf{r}) = TV_1 \sum_{\omega_n,\mathbf{k}} \frac{b_k^2\Delta_d^*(\mathbf{r})}{\omega_n^2 + \xi_k^2}, \tag{3.59}$$

where $a_k = \cos k_x + \cos k_y$ and $b_k = \cos k_x - \cos k_y$. The extended s-wave and d-wave gap functions are related to the bond gap functions through the gauge-invariant versions of (1.10) and (1.11):

$$\begin{aligned}\Delta_s(\mathbf{r}) \equiv \frac{1}{4}\Big[& e^{-i\frac{2\pi}{\phi_0}A_x(\mathbf{r})}\Delta_x(\mathbf{r}) + e^{i\frac{2\pi}{\phi_0}A_x(\mathbf{r})}\Delta_{-x}(\mathbf{r}) \\ & + e^{-i\frac{2\pi}{\phi_0}A_y(\mathbf{r})}\Delta_y(\mathbf{r}) + e^{i\frac{2\pi}{\phi_0}A_y(\mathbf{r})}\Delta_{-y}(\mathbf{r})\Big],\end{aligned} \tag{3.60}$$

$$\begin{aligned}\Delta_d(\mathbf{r}) \quad &\equiv \quad \frac{1}{4}\Big[e^{-i\frac{2\pi}{\phi_0}A_x(\mathbf{r})}\Delta_x(\mathbf{r}) + e^{i\frac{2\pi}{\phi_0}A_x(\mathbf{r})}\Delta_{-x}(\mathbf{r}) \\ &\qquad -e^{-i\frac{2\pi}{\phi_0}A_y(\mathbf{r})}\Delta_y(\mathbf{r}) - e^{i\frac{2\pi}{\phi_0}A_y(\mathbf{r})}\Delta_{-y}(\mathbf{r})\Big]. \qquad (3.61)\end{aligned}$$

The inversion of these equations is not trivial; the proof may be found in Appendix B.

The equations that determine the s-wave and d-wave transition temperatures T_s and T_d are

$$[V_1 I_2(T_s) - 2]\,[V_0 I_0(T_s) + 2] = V_0 V_1 I_1^2(T_s); \qquad (3.62)$$

$$I_3(T_d) = \frac{2}{V_1}, \qquad (3.63)$$

where

$$I_n(T_s) \quad \equiv \quad \sum_{\mathbf{k}} \frac{a_k^n}{\xi_k}\tanh\left(\frac{\xi_k}{2T_s}\right), \quad n = 0, 1, 2; \qquad (3.64)$$

$$I_3(T_d) \quad \equiv \quad \sum_{\mathbf{k}} \frac{b_k^2}{\xi_k}\tanh\left(\frac{\xi_k}{2T_d}\right). \qquad (3.65)$$

It is clear from Eq. (3.62) that if $V_1 = 0$, no s-wave superconducting instability can occur for positive temperature.

The elimination of the Matsubara sums in Eqs. (3.57) through (3.59) is accomplished by expanding the denominator as a partial fraction:

$$\frac{1}{\omega_n^2 + \xi_k^2} = \frac{1}{2\xi_k}\left(\frac{1}{i\omega_n + \xi_k} - \frac{1}{i\omega_n - \xi_k}\right). \qquad (3.66)$$

The fermionic Matsubara frequencies satisfy [160]

$$T\sum_{\omega_n} \frac{1}{i\omega_n - x} = \frac{1}{2} + \frac{1}{\exp(x/T) + 1}, \qquad (3.67)$$

where the right hand side is the Fermi distribution. Combining (3.66) and (3.67) and making use of standard trigonometric identities yields

$$T\sum_{\omega_n} \frac{1}{\omega_n^2 + \xi_k^2} = \frac{1}{2\xi_k}\tanh\left(\frac{\xi_k}{2T}\right). \qquad (3.68)$$

In order to analytically solve the sums I_{0-3}, Eqs. (3.64) and (3.65), one may employ the standard transformation to an integration over energies, making use of the single-particle density of states (DOS)

$$\begin{aligned} N(\varepsilon) &\equiv \sum_{\mathbf{k}} \delta(\varepsilon - \varepsilon_{\mathbf{k}}) \\ &\approx \begin{cases} N(0) + N(1)\ln\left|\frac{D}{\varepsilon}\right|, & \text{if } |\varepsilon| \le D; \\ 0, & \text{otherwise,} \end{cases} \end{aligned} \tag{3.69}$$

where $D = 4t$ is the half-bandwidth and $\varepsilon_k \equiv \xi_k + \mu$. The DOS is approximated by a constant plus a term reflecting the van Hove singularity at half-filling ($\varepsilon = 0$), as is shown in Fig. 3.1. The best fit is obtained when $N(0) = 0.31/D$ (the DOS for free electrons in two dimensions is $1/\pi D$) and $N(1) = 0.19/D$ (note that the DOS at half-filling is approximately $(2/\pi^2 D)\ln|D/\varepsilon|$) [149]. Using the relation $a_k = -2(\xi + \mu)/D$, the sums I_{0-2} can be solved to yield:

$$I_0(T_s) \approx 2N'\ln\left(\frac{T^*}{T_s}\right) - \frac{2D}{\mu}N(1); \tag{3.70}$$

$$I_1(T_s) \approx -\frac{4\mu}{D}N'\left[\ln\left(\frac{T^*}{T_s}\right) - 1\right] + \frac{4\mu}{D}\left(1 + \frac{D}{\mu}\right)N(1); \tag{3.71}$$

$$\begin{aligned} I_2(T_s) &\approx \frac{8\mu^2}{D^2}N'\ln\left(\frac{T^*}{T_s}\right) + \frac{4(D^2 - 3\mu^2)}{D^2}N(0) \\ &+ \frac{2}{D^2}\left[- 4\mu D + 6\mu^2\ln\left|\frac{\mu}{D}\right| - 5\mu^2 + D^2\right]N(1), \end{aligned} \tag{3.72}$$

where

$$N' = N(0) - N(1)\ln\left|\frac{\mu}{D}\right|, \tag{3.73}$$

and

$$T^* \equiv \frac{2e^{\gamma}\sqrt{D^2 - \mu^2}}{\pi}. \tag{3.74}$$

For all terms proportional to $N(1)$, it is assumed that $T_c \ll D$ (weak-coupling), so that

$$\tanh\left(\frac{\varepsilon - \mu}{2T}\right) \approx \begin{cases} -1, \varepsilon < \mu; \\ +1, \varepsilon > \mu. \end{cases} \tag{3.75}$$

Note that in this lattice model, all interactions are instantaneous and therefore the bandwidth is the only possible energy cutoff. Since b_k cannot be written exactly in

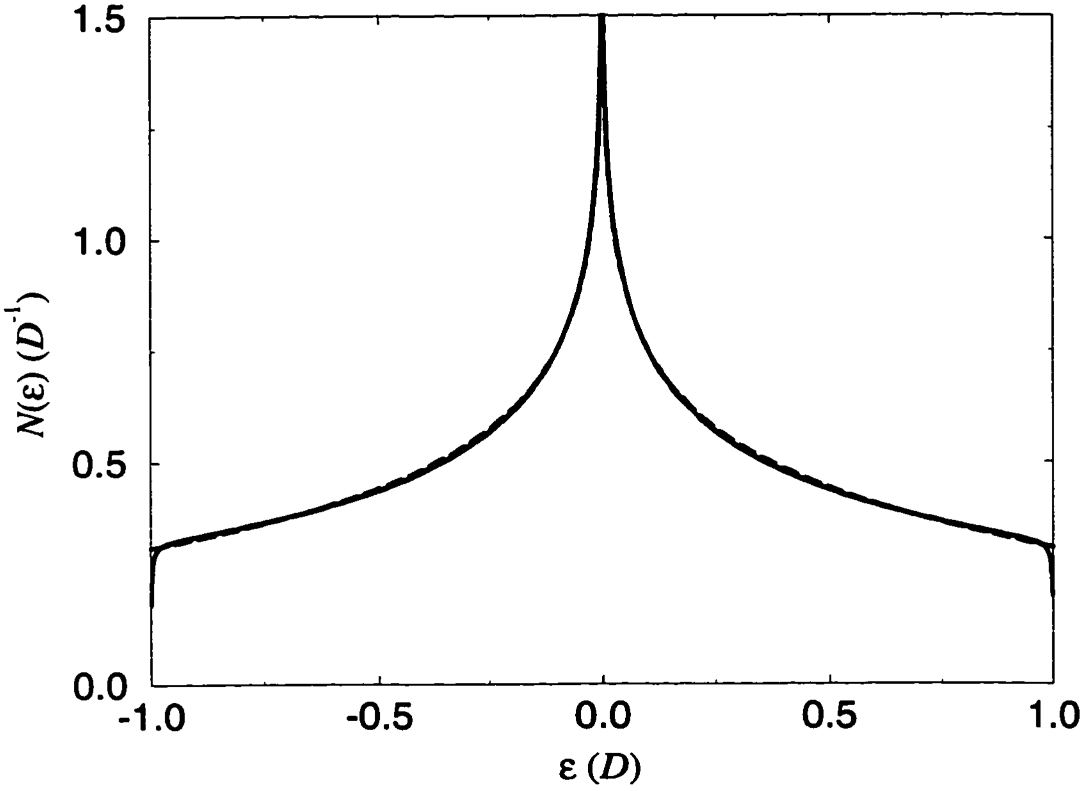

Figure 3.1: The density of states N(ε) for tight-binding electrons on the square lattice is shown as the solid curve. The energy scale is the half-bandwidth $D = 4t$. The best fit, the dashed line, is found to be $N(\varepsilon) = \frac{0.31}{D} + \frac{0.19}{D}\ln\left|\frac{D}{\varepsilon}\right|$.

terms of ξ_k, some simplifying assumption must be made in order to evaluate I_3. At low densities (the continuum limit of the lattice model), $\xi_k \approx tk^2 - D - \mu$ and thus $b_k \approx -2\cos 2\theta(\xi + D + \mu)/D$. It follows that

$$\begin{aligned} I_3(T_d) &\approx \frac{4(\mu+D)^2}{D^2} N' \ln\left(\frac{T^*}{T_d}\right) + \frac{2}{D^2}\left(D^2 - 4\mu D - 3\mu^2\right) N(0) \\ &+ \frac{2}{D^2}\left[\frac{-2D}{\mu}(\mu+D)^2 + \mu(3\mu+4D)\ln\left|\frac{\mu}{D}\right| \right. \\ &\left. + \frac{D^2 - 8\mu D - 5\mu^2}{2}\right] N(1). \end{aligned} \tag{3.76}$$

For $V_0 = 0$, the equation for the s-wave transition temperature T_s that results from the application of Eq. (3.62) is:

$$T_s = T^* \exp\left\{\frac{-D^2 - V_1\left[6\mu^2 N' - 2D^2 N(0) - \left(D^2 - 4\mu D - 5\mu^2\right) N(1)\right]}{4\mu^2 V_1 N'}\right\}. \tag{3.77}$$

The corresponding equation for the d-wave transition temperature T_d from Eq. (3.63) is:

$$\begin{aligned} T_d &= T^* \exp\left\{\left[D^2 N(0) - \frac{1}{2\mu}\left(4D^3 + 7D^2\mu + 12D\mu^2 + 5\mu^3\right) N(1)\right]/2N'(\mu+D)^2\right\} \\ &\times \exp\left\{\left[-D^2 - V_1 N' \mu(4D + 3\mu)\right]/2(\mu+D)^2 V_1 N'\right\} \end{aligned} \tag{3.78}$$

The transition temperatures for the cases $V_1 = t$ and $V_1 = 3t$ are shown as functions of chemical potential in Figures 3.2 and 3.3 respectively. Near the bottom of the tight-binding band ($\mu \approx -D$), an s-wave transition is strongly favoured for any V_0 and V_1, whereas a d-wave transition is favoured near half-filling ($\mu \approx 0$). The value of the chemical potential at which the preferred symmetry of the dominant gap function changes is extremely sensitive to the strengths of the respective interactions. As the on-site repulsion is increased, the magnitude of T_s is suppressed while T_d is unaffected [149]. As a result, d-wave superconductivity is favoured for virtually all densities for sufficiently large V_0. It should be noted that the magnitude of the subcritical transition temperature, associated with the subdominant gap function, is in fact further decreased due to the presence of the dominant gap function. The relevant equation for the subcritical transition temperature, one of Eqs. (3.57)-(3.59), is modified by replacing $\sqrt{\xi_k^2 + \Delta_k^{\mathrm{DOM}^2}}$ for ξ_k, where Δ_k^{DOM} is the magnitude of the dominant gap function. As shown within GL theory in Section 2.2, the subcritical transition temperature may be set to zero without loss of generality.

The overall form of the phase diagrams may be understood in a qualitative manner by considering the structures of Eqs. (3.64) and (3.65). The tight-binding dispersion (3.41) is $\xi_k = -2ta_k - \mu$. Near the bottom of the tight-binding band, $\mu \to -D$ and $k_x \approx k_y$, so $\xi_k \to 0$ and $b_k \to 0$ while $a_k \gg 0$. Thus, the sums I_{0-2} have a larger contribution than I_3, stabilizing s-wave superconductivity. Similarly, near half-filling $\mu \to 0$ and $k_x \approx k_y + \pi$, so $\xi_k \to 0$ and $a_k \to 0$ while $b_k \gg 1$, leading to a larger I_3 and T_d. Evidently, the band structure, in addition to the pairing interaction, is crucial in determining which order parameter symmetry is stabilized in the physical system.

3.3.2 Antiferromagnetic-van Hove Model

The equations for the s-wave and d-wave transition temperatures T_s and T_d in the AvH model are respectively

$$1 = \frac{V}{4}\sum_{\mathbf{k}} \frac{1 + \cos k_1 \cos k_2 + \cos k_1 + \cos k_2}{\xi_k} \tanh\left(\frac{\xi_k}{2T_s}\right), \tag{3.79}$$

$$1 = \frac{V}{4}\sum_{\mathbf{k}} \frac{1 + \cos k_1 \cos k_2 - \cos k_1 - \cos k_2}{\xi_k} \tanh\left(\frac{\xi_k}{2T_d}\right). \tag{3.80}$$

While these equations are not analytically tractable, due to the complicated angular-dependence of the dispersion (3.42), they may be solved numerically. In practice, the transition temperature T_d is evaluated for a given chemical potential μ which fixes the (normal-state) hole density:

$$\langle n \rangle = \frac{1}{2}\sum_{\mathbf{k}} \left[1 - \tanh\left(\frac{\xi_k}{2T_d}\right)\right]. \tag{3.81}$$

Note that there is a factor of 1/2 in the expression for the particle density in the normal-state, since the holes move on a single sublattice and are therefore considered 'spinless.' As shown in Fig. 3.4, the allowed values for μ are between $\varepsilon_k \equiv \xi_k + \mu = -4t_{20} = -0.087$ eV at the bottom of the hole band, and $\varepsilon_k = 4(t_{11} + t_{20})$ at the top.

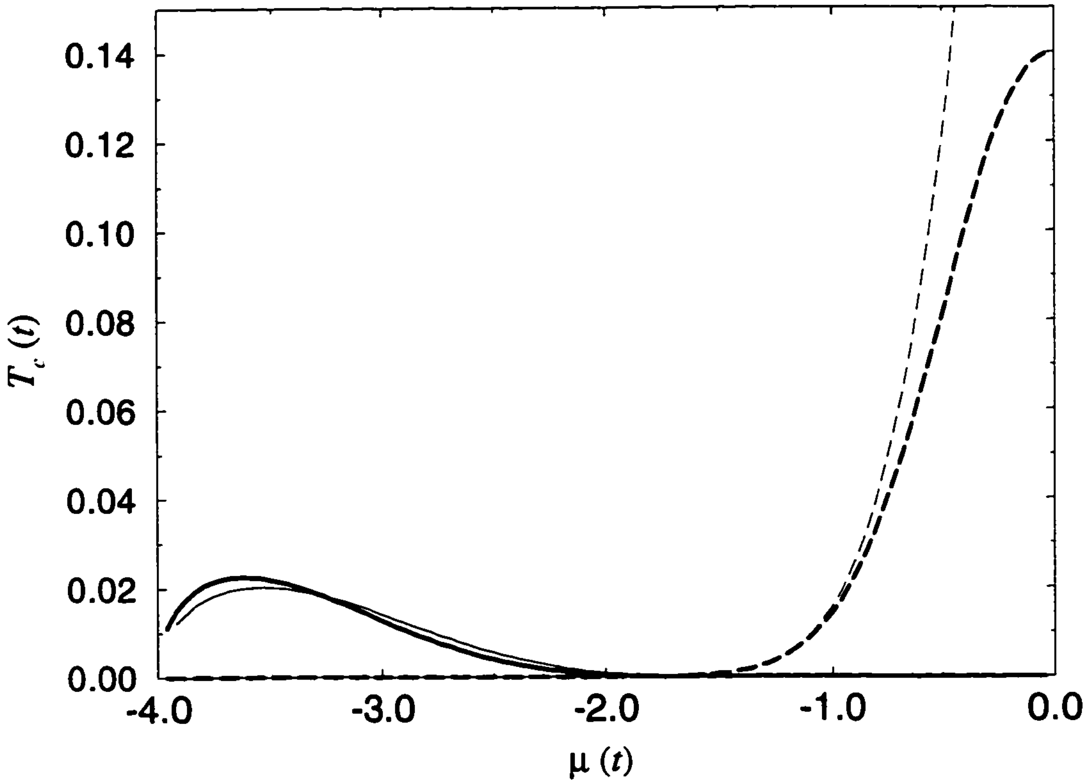

Figure 3.2: The transition temperatures T_c are given as functions of chemical potential μ for nearest-neighbour attraction $V_1 = t$ and $V_0 = 0$. The results for T_s and T_d are given by solid and dashed lines, respectively. The analytical results (lighter lines) are found to compare well with the numerical results (darker lines) in the applicable low-density regime.

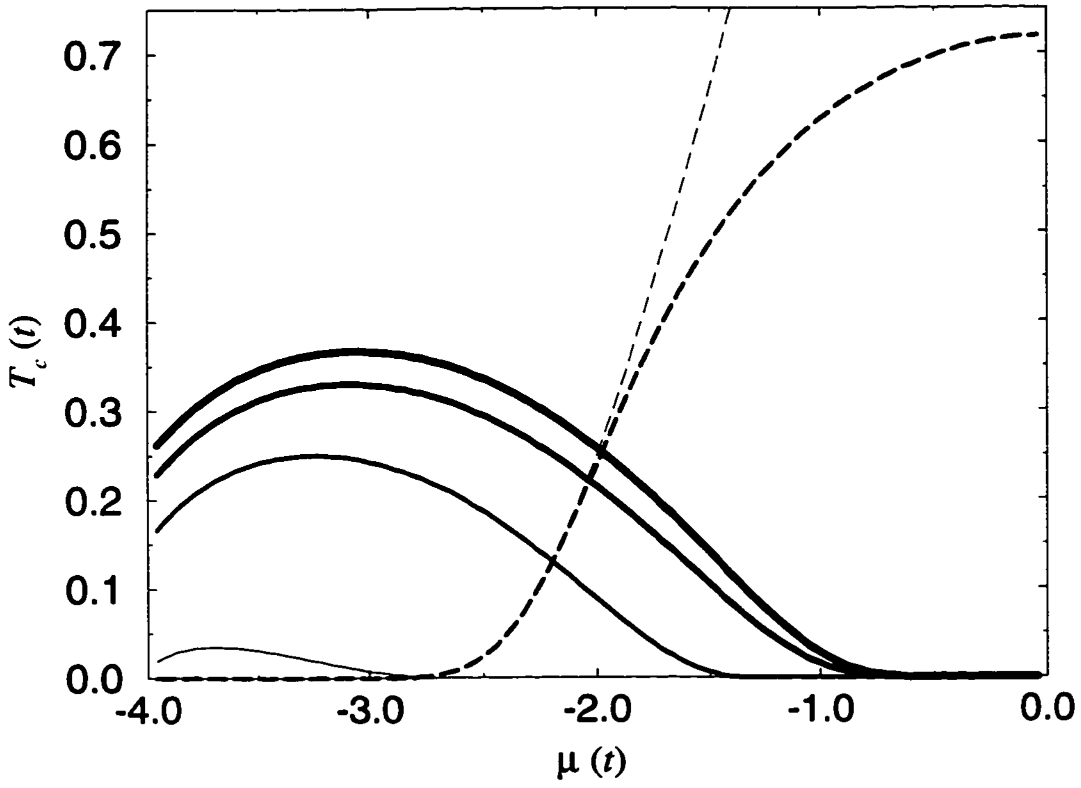

Figure 3.3: The transition temperatures T_c are given as functions of chemical potential μ for $V_1 = 3t$. The solid lines correspond to the numerical evaluation of T_s for on-site repulsion $V_0 = 0$, $2.5t$, $3.5t$, and $\sim \infty$; linewidth decreases with increased V_0. The d-wave transition temperature T_d (dashed lines) is unaffected by changes in V_0. Note that the analytical (lighter dashed line) and numerical (darker dashed line) results for T_d still agree closely at low densities in this intermediate-coupling regime. The correspondence between the numerical and analytical results for T_s (not shown) continues for intermediate coupling but is found to improve with increased V_0, or decreased T_s.

Note that there is a van Hove singularity when $\varepsilon_k = -t_{11}^2/t_{20} \approx -0.078$ eV, where the gradient of the energy vanishes: $|\vec{\nabla}_k \varepsilon_k| = 0$.

The AvH model strongly favours a d-wave transition temperature for all relevant hole concentrations, as indicated in the inset of Fig. 3.4. At optimal doping, corresponding to $\mu \approx -0.075$ eV, the transition temperature is approximately 90 K and the average hole density is $\langle n \rangle \approx 0.2$ (where 1 eV=11.60445 K). The large transition temperature at optimal doping is due to the proximity of the Fermi level to the van Hove singularity. No s-wave superconductivity is stabilized at any density in the AvH model.

The physical explanation for the stability of d-wave superconductivity in the AvH model follows the arguments of the previous subsection. Since both the chemical potential and the van Hove singularity are located very near the bottom of the band, the AvH dispersion (3.42) may be approximately written

$$\xi_k^{\mathrm{AvH}} \approx \zeta \left(\cos k_1 + \cos k_2 + \cos k_1 \cos k_2 + 1 \right), \tag{3.82}$$

where ζ is of order $4t_{20} \sim 2t_{11}$. When this dispersion approaches zero, the numerator of (3.79) also approaches zero, while the numerator of (3.80) remains finite. Furthermore, since $\xi_k \to 0$ for many k-points near the van Hove singularity, d-wave superconductivity is strongly favoured over s-wave.

3.4 Calculation of the GL Coefficients

3.4.1 Extended Hubbard Model

For sufficiently large systems, the lattice sums in Eq. (3.43) can be transformed into k-space integrals. Neglecting fourth-order derivatives and making use of the expressions for the s-wave (3.60) and d-wave (3.61) gap functions as well as the normal-state Green function (3.40), the following three gap equations for the EH model are obtained:

$$\Delta_\circ^* = 4TV_0 \sum_{\omega_n} \int \frac{d^2k}{(2\pi)^2} \Big\{ \frac{s^*(\mathbf{r},\mathbf{k})}{\omega_n^2 + \xi_k^2} - \frac{1}{(\omega_n^2 + \xi_k^2)^2} \big[16 |s(\mathbf{r},\mathbf{k})|^2 s^*(\mathbf{r},\mathbf{k})$$

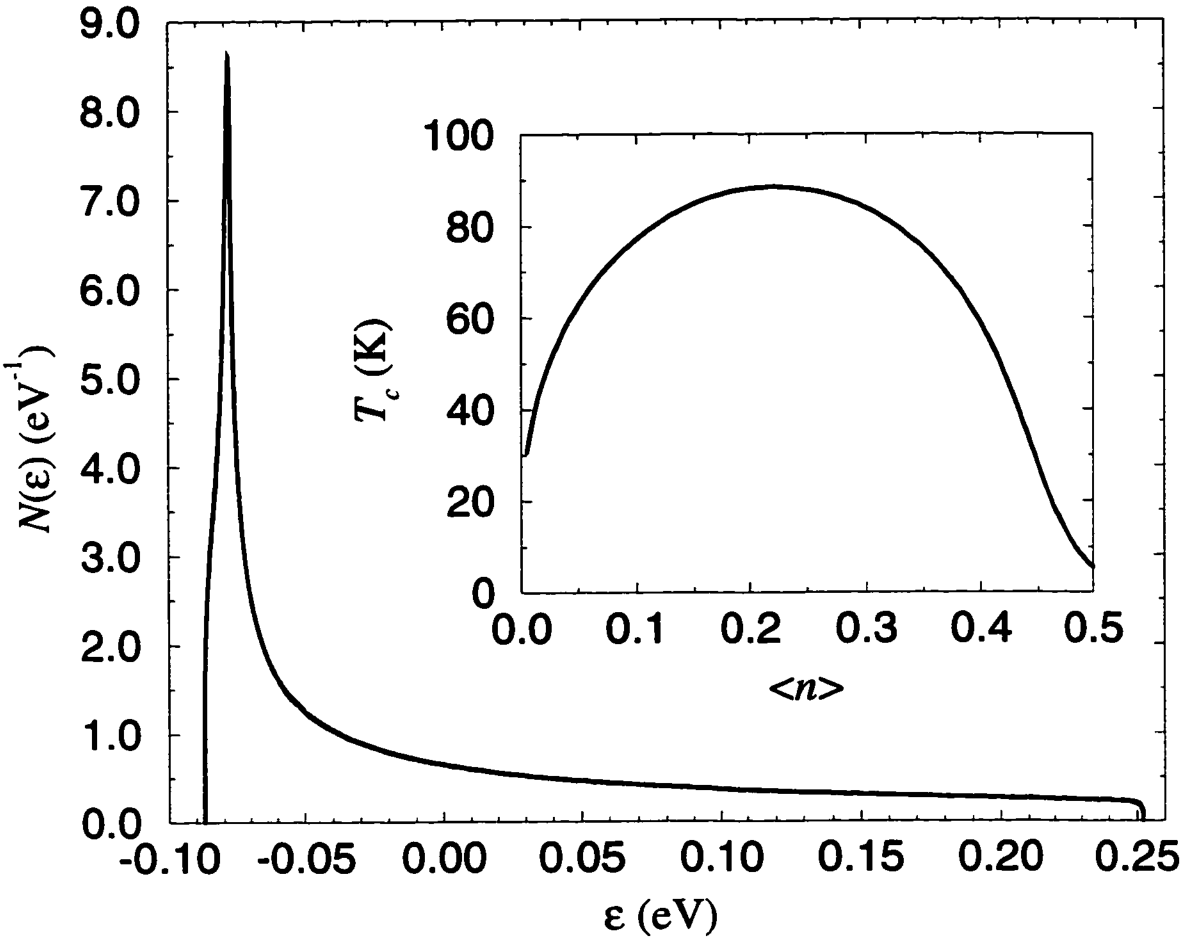

Figure 3.4: The density of states per hole is shown as a function of energy for the AvH model. In the inset, the (*d*-wave) transition temperature in Kelvin is plotted as a function of the hole density at T_c. Optimal doping corresponds to $\mu \approx -0.075$ eV, while the van Hove singularity is at $t_{11}^2/t_{20} \approx -0.078$ eV.

$$
\begin{aligned}
&+32|d(\mathbf{r},\mathbf{k})|^2 s^*(\mathbf{r},\mathbf{k}) + 16d^{*2}(\mathbf{r},\mathbf{k})s(\mathbf{r},\mathbf{k})\Big] \\
&- \int d^2z\frac{z^2}{2}\int \frac{d^2k'}{(2\pi)^2}\frac{e^{i(\mathbf{k}+\mathbf{k}')\cdot\mathbf{z}}}{(-i\omega_n-\xi_{k'})(i\omega_n-\xi_k)}\left(\cos^2\theta\Pi_x^2+\sin^2\theta\Pi_y^2\right) \\
&\times\left[s^*(\mathbf{r},\mathbf{k})+d^*(\mathbf{r},\mathbf{k})\right]\Big\};
\end{aligned}
\tag{3.83}
$$

$$
\Delta_s^* = 2TV_1\sum_{\omega_n}\int\frac{d^2k}{(2\pi)^2}a_k\Big\{\text{as above}\Big\}
\tag{3.84}
$$

$$
\begin{aligned}
\Delta_d^* = {} & 2TV_1\sum_{\omega_n}\int\frac{d^2k}{(2\pi)^2}b_k\Big\{\frac{d^*(\mathbf{r},\mathbf{k})}{\omega_n^2+\xi_k^2}-\frac{1}{(\omega_n^2+\xi_k^2)^2}\Big[16|d(\mathbf{r},\mathbf{k})|^2d^*(\mathbf{r},\mathbf{k}) \\
&+32|s(\mathbf{r},\mathbf{k})|^2d^*(\mathbf{r},\mathbf{k})+16s^{*2}(\mathbf{r},\mathbf{k})d(\mathbf{r},\mathbf{k})\Big] \\
&- \int d^2z\frac{z^2}{2}\int \frac{d^2k'}{(2\pi)^2}\frac{e^{i(\mathbf{k}+\mathbf{k}')\cdot\mathbf{z}}}{(-i\omega_n-\xi_{k'})(i\omega_n-\xi_k)}\left(\cos^2\theta\Pi_x^2+\sin^2\theta\Pi_y^2\right) \\
&\times\left[s^*(\mathbf{r},\mathbf{k})+d^*(\mathbf{r},\mathbf{k})\right]\Big\},
\end{aligned}
\tag{3.85}
$$

where $s(\mathbf{r},\mathbf{k}) \equiv \frac{a_k}{2}\Delta_s(\mathbf{r}) - \frac{1}{4}\Delta_o(\mathbf{r})$, $d(\mathbf{r},\mathbf{k}) \equiv \frac{b_k}{2}\Delta_d(\mathbf{r})$, θ is the angle between $\mathbf{r}$ and $\mathbf{z}$ $(= m\hat{x} + n\hat{y})$, and the continuum limit of the lattice derivative (3.45)

$$
\Pi_z \equiv -i\frac{\partial}{\partial z} + \frac{4\pi}{\phi_0}A_z(\mathbf{r})
\tag{3.86}
$$

acts only on the center of mass coordinate $\mathbf{r}$. Eqs. (3.83)-(3.85) can be simplified by noting that $\Delta_o(\mathbf{r}) = \epsilon\Delta_s(\mathbf{r})$, where ϵ depends on temperature and chemical potential. This relation follows from the observation that Eqs. (3.83) and (3.84) are not linearly independent, since $\Delta_o(\mathbf{r})$ and $\Delta_s(\mathbf{r})$ have the same symmetry (see Section 1.2). Near T_c the magnitude of the s-wave component is small. From Eq. (3.57), one infers $\epsilon \approx V_0I_1/(1+V_0I_0/2)$, where I_0 and I_1 are defined in Eq. (3.64) and are evaluated in the weak-coupling and low-density limit in Eqs. (3.70) and (3.71). The integrals involving gradients of the gap functions can be greatly simplified by means of the identity:[1]

$$
\int d^2z\; x^2G^{\circ}(\mathbf{z},-\omega_n)G^{\circ}(\mathbf{z}+\vec{\alpha},\omega_n) \equiv \int\frac{d^2k}{(2\pi)^2}e^{-i\mathbf{k}\cdot\vec{\alpha}}\left|\nabla_{k_x}G^{\circ}(\mathbf{k},\omega_n)\right|^2,
\tag{3.87}
$$

---

[1] I am indebted to Prof. Jules Carbotte for drawing my attention to a variant of this integral.

and similarly for integrals involving y^2. Thus,

$$\begin{aligned}
\frac{1}{4}\Delta_s^*(\mathbf{r}) &= TV_1\left(1-\frac{V_1\epsilon^2}{4V_0}\right)^{-1}\sum_{\omega_n}\int\frac{d^2k}{(2\pi)^2}\frac{a_k'}{\omega_n^2+\xi_k^2}\Big\{a_k'\Delta_s^*(\mathbf{r}) \\
&- \frac{1}{\omega_n^2+\xi_k^2}\Big[16{a_k'}^3|\Delta_s(\mathbf{r})|^2\Delta_s^*(\mathbf{r})+8a_k'b_k^2|\Delta_d(\mathbf{r})|^2\Delta_s^*(\mathbf{r})+4a_k'b_k^2\Delta_d^{*2}(\mathbf{r})\Delta_s(\mathbf{r}) \\
&+ \frac{D^2}{16}\left(\sin^2k_x\Pi_x^2+\sin^2k_y\Pi_y^2\right)\left[2a_k'\Delta_s^*(\mathbf{r})+b_k\Delta_d^*(\mathbf{r})\right]\Big]\Big\},
\end{aligned}\tag{3.88}$$

$$\begin{aligned}
\frac{1}{4}\Delta_d^*(\mathbf{r}) &= TV_1\sum_{\omega_n}\int\frac{d^2k}{(2\pi)^2}\frac{b_k}{\omega_n^2+\xi_k^2}\Big\{\frac{1}{4}b_k\Delta_d^*(\mathbf{r}) \\
&- \frac{1}{\omega_n^2+\xi_k^2}\Big[b_k^3|\Delta_d(\mathbf{r})|^2\Delta_d^*(\mathbf{r})+8{a_k'}^2b_k|\Delta_s(\mathbf{r})|^2\Delta_d^*(\mathbf{r})+4{a_k'}^2b_k\Delta_s^{*2}(\mathbf{r})\Delta_d(\mathbf{r}) \\
&+ \frac{D^2}{32}\left(\sin^2k_x\Pi_x^2+\sin^2k_y\Pi_y^2\right)\left[2a_k'\Delta_s^*(\mathbf{r})+b_k\Delta_d^*(\mathbf{r})\right]\Big]\Big\},
\end{aligned}\tag{3.89}$$

where $a_k' \equiv \frac{a_k}{2}-\frac{\epsilon}{4}$. Comparing Eqs. (3.88) and (3.89) with the GL gap equations (2.23) and (2.22) immediately yields:

$$\alpha_s = \frac{1}{V_1}-\frac{\epsilon^2}{4V_0}-4T\sum_{\omega_n}\int\frac{d^2k}{(2\pi)^2}\frac{{a_k'}^2}{\omega_n^2+\xi_k^2}\tag{3.90}$$

$$\alpha_d = \frac{1}{V_1}-T\sum_{\omega_n}\int\frac{d^2k}{(2\pi)^2}\frac{b_k^2}{\omega_n^2+\xi_k^2},\tag{3.91}$$

$$\{\beta_1\,,\ \beta_2\,,\ \beta_3\,,\ \beta_4\} = T\sum_{\omega_n}\int\frac{d^2k}{(2\pi)^2}\frac{\{32{a_k'}^4\,,\ 2b_k^4\,,\ 32{a_k'}^2b_k^2\,,\ 8{a_k'}^2b_k^2\}}{(\omega_n^2+\xi_k^2)^2},\tag{3.92}$$

$$\{\gamma_s\,,\ \gamma_\nu\,,\ \gamma_d\} = \frac{D^2}{8}T\sum_{\omega_n}\int\frac{d^2k}{(2\pi)^2}\sin^2k_x\frac{\{4{a_k'}^2\,,\ -2a_k'b_k\,,\ b_k^2\}}{(\omega_n^2+\xi_k^2)^2}.\tag{3.93}$$

The coefficients of the tetragonal GL free energy $F_0^{\rm tet}$ (2.16) can be calculated analytically in the same low-density and weak-coupling limit employed earlier by setting $a_k \approx -2\mu/D$, $b_k \approx -2(\mu+D)\cos2\theta/D$ and $\sin^2k_x \approx 4(\mu+D)\cos^2\theta/D$. Making use of

$$T\sum_{\omega_n}\int\frac{d^2k}{(2\pi)^2}\frac{1}{(\omega_n^2+\xi_k^2)^2}\approx\frac{7\zeta(3)N'}{8\pi^2T^2},\tag{3.94}$$

where $\zeta(3) \approx 1.202$ is a Riemann zeta function, one immediately obtains:

$$\alpha_s = -\frac{1}{V_1}\left(\frac{\mu}{D}+\frac{\epsilon}{4}\right)^2\left(1-\frac{T}{T_s}\right) \quad , \quad \alpha_d = -\frac{1}{V_1}\left(\frac{\mu+D}{D}\right)^2\left(1-\frac{T}{T_d}\right), \tag{3.95}$$

$$\{\beta_1 \, , \, \beta_2\} = 4\gamma\left\{\left(\frac{\mu}{D}+\frac{\epsilon}{4}\right)^4, \, \frac{3}{8}\left(\frac{\mu+D}{D}\right)^4\right\}, \tag{3.96}$$

$$\{\beta_3 \, , \, \beta_4\} = 4\gamma\left\{2\left(\frac{\mu}{D}+\frac{\epsilon}{4}\right)^2\left(\frac{\mu+D}{D}\right)^2, \, \frac{1}{2}\left(\frac{\mu}{D}+\frac{\epsilon}{4}\right)^2\left(\frac{\mu+D}{D}\right)^2\right\}, \tag{3.97}$$

$$\{\gamma_s \, , \, \gamma_\nu \, , \, \gamma_d\} = \gamma\frac{v_F^2}{16}\left\{2\left(\frac{\mu}{D}+\frac{\epsilon}{4}\right)^2, \, -\left(\frac{\mu}{D}+\frac{\epsilon}{4}\right)\left(\frac{\mu+D}{D}\right), \, \left(\frac{\mu+D}{D}\right)^2\right\}, \tag{3.98}$$

where

$$\gamma = \frac{7\zeta(3)N'}{\pi^2 T^2}, \tag{3.99}$$

and $v_F^2 = D^2 k_F^2/4 \approx D(\mu + D)$. From Eqs. (3.70) and (3.71) follows:

$$\epsilon = -\frac{4\mu}{D}\frac{V_0 N' \ln\left(\frac{T^*}{T}\right) - V_0 N'}{V_0 N' \ln\left(\frac{T^*}{T}\right) + 1}. \tag{3.100}$$

The expressions for α_s and α_d are only valid near their respective critical temperatures. Since the subcritical transition temperature is much lower than the dominant transition temperature, the corresponding coefficient for the subdominant order parameter can be assumed approximately $1/V_1$ for all values of $T < T_c$ (i.e. the contribution of the appropriate integral in either of (3.91) will be negligible). Note that in the limit $V_1 = 0$, $V_0 \to -V_0$, Δ_s and Δ_d vanish, and the relevant gap equation is therefore Eq. (3.83) with $s(\mathbf{r},\mathbf{k}) = \Delta_0(\mathbf{r})$ and $d(\mathbf{r},\mathbf{k}) = 0$. Then Eq. (2.15) becomes the two-dimensional continuum BCS GL free energy:

$$F_s^{\mathrm{BCS}} = F_n - \frac{1}{V_0}\left(1-\frac{T}{T_s}\right)|\Delta_o(\mathbf{r})|^2 + \frac{7\zeta(3)N(0)}{16\pi^2T^2}|\Delta_o(\mathbf{r})|^4 + \frac{7\zeta(3)N(0)}{32\pi^2T^2}v_F^2|\vec{\Pi}\Delta_o(\mathbf{r})|^2 + \frac{h^2}{8\pi}. \tag{3.101}$$

The coefficients (3.95)-(3.98) of the GL free energy (2.15) imply that the d-wave component vanishes at the bottom of the band ($\mu = -D$), yielding a pure s-wave superconductor. At half-filling ($\mu = 0$) only the d-wave component remains, with the caveat that these analytical results become decreasingly valid near half-filling. At intermediate densities all the GL coefficients are non-zero. In general, both d-wave and s-wave superconductors in the presence of inhomogeneities will have coexisting d-wave and s-wave components for any temperature $T < T_c$.

The GL coefficients may be used to measure the subdominant components induced by inhomogeneities such as external magnetic fields and currents. As discussed in Section 2.3, the GL theory predicts that the maximum amplitude attained by the subdominant order parameter in the core of a magnetic vortex is given by [135]:

$$\frac{\Delta_s(\Delta_d)^{\max}}{\Delta_d(\Delta_s)^{\text{bulk}}} \approx \frac{1}{4}\frac{\gamma_\nu}{\gamma_{d(s)}}\frac{|\alpha_{d(s)}|}{\alpha_{s(d)}} \approx \frac{1}{4}\left(1 - \frac{T}{T_{d(s)}}\right)\frac{\gamma_\nu}{\gamma_{d(s)}}, \qquad T_{d(s)} > T_{s(d)}, \tag{3.102}$$

where $\Delta_s^{\max}$ is the maximum value of the induced subdominant s-wave order parameter compared with the magnitude of the critical d-wave order parameter Δ_d^{bulk} far from the vortex core, and vice versa. From Section 2.5, the subdominant component induced by external currents is predicted to be approximately four times larger than the above estimate, Eq. (3.102). In both cases, the gradient coefficient ratio $\gamma_\nu/\gamma_{d(s)}$ governs the magnitude of the subdominant component.

From (3.98), one obtains:

$$\frac{\gamma_\nu}{\gamma_d} \approx \left|\frac{\mu + D\epsilon/4}{\mu + D}\right|, \qquad T_d > T_s. \tag{3.103}$$

$$\frac{\gamma_\nu}{\gamma_s} \approx \frac{1}{2}\left|\frac{\mu + D}{\mu + D\epsilon/4}\right|, \qquad T_s > T_d, \tag{3.104}$$

The gradient coefficient ratios (3.103) and (3.104) are compared with the appropriate numerical results in Fig. 3.5 for the $V_0 = 0$ case. The analytical results capture the essential physics in their regime of applicability, which is at low densities and weak to intermediate coupling. Better quantitative agreement at intermediate coupling can be obtained by including in a_k, b_k, etc. terms higher order in ξ_k. Near half-filling, where d-wave superconductivity is most stable, the gradient coefficient ratio γ_ν/γ_d grows with increased coupling. The coefficient γ_ν/γ_s exhibits a similar behaviour near zero-filling, where s-wave superconductivity is favoured. As a result, a significant component of the subdominant order parameter would only exist for stronger coupling in these two density regimes. It should be kept in mind, however, that as the on-site repulsion V_0 (and therefore ϵ) increases from zero, the magnitude of the s-wave component is suppressed for all densities; a d-wave subcomponent would be thereby enhanced in a bulk s-wave superconductor. The magnitude of the subdominant order parameter can be significantly larger even for weak coupling at intermediate densities. Not only is the gradient coefficient ratio enhanced, but also the ratio $|\alpha_{\text{dom}}|/\alpha_{\text{sub}}$ increases because $\alpha_{\text{sub}} \to 0$ as the subdominant superconducting instability is approached. Fig. 3.6 in the following section provides further quantitative details.

There are in general two characteristic length scales ξ_s and ξ_d governing spatial variations of the s-wave and d-wave order parameters, respectively. Near T_c, however, the induced subdominant order parameter is negligible compared to the critical order parameter by (2.35). Inserting the relevant analytical expressions from Eqs. (3.95) through (3.98) into Eqs. (2.27) and (2.28), one obtains:

$$\xi_s(T) \approx \left(\frac{v_F}{2\pi T}\right)\sqrt{\frac{7\zeta(3)V_1N'}{2(1-T/T_s)}} \quad ; \quad \xi_d(T) \approx \left(\frac{v_F}{2\pi T}\right)\sqrt{\frac{7\zeta(3)V_1N'}{4(1-T/T_d)}}; \tag{3.105}$$

$$\lambda_s(T) \approx \frac{\phi_0}{2\pi}\sqrt{\frac{4V_1}{\pi\delta v_F^2(1-T/T_s)}} \quad ; \quad \lambda_d(T) \approx \frac{\phi_0}{2\pi}\sqrt{\frac{3V_1}{\pi\delta v_F^2(1-T/T_d)}}. \tag{3.106}$$

Note that the penetration depths are effectively infinite for an isolated layer. The magnitudes of the coherence lengths can be estimated for parameters stabilizing either s-wave or d-wave superconductivity (see Section 3.3). For example, with $\mu = -2t$ and $V_1 \sim 3t$ the transition temperature $T_c \sim 0.2t$ corresponds to bulk s-wave superconductivity when $V_0 = 0$, but d-wave superconductivity when $V_0 \gg 0$. For these parameters at $T = 0.9T_c$, the d-wave and s-wave coherence lengths are respectively $\xi_d \sim 6a$ (when $V_0 \gg 0$) and $\xi_s \sim 8a$ (when $V_0 = 0$). The coherence lengths tend to become progressively shorter with increased electron density. Fig. 3.7 in the next section gives further details.

It is useful to compare the GL free energy (2.15) with that derived in the continuum model of Ren *et al.* [137]. Defining $s \equiv -\left(\frac{\mu}{D} + \frac{\epsilon}{4}\right)\Delta_s$ and $d \equiv \frac{\mu+D}{D}\Delta_d$ (dropping reference to the center of mass coordinate **r** for convenience), one obtains:

$$\begin{aligned} F_s &= F_n - \left(1 - \frac{T}{T_s}\right)|s|^2 - \left(1 - \frac{T}{T_d}\right)|d|^2 \\ &+ 4\gamma\Big\{|s|^4 + \frac{3}{8}|d|^4 + 2|s|^2|d|^2 + \frac{1}{2}\left(s^{*2}d^2 + d^{*2}s^2\right)\Big\} \\ &+ \gamma\frac{v_F^2}{16}\Big\{2|\vec{\Pi}s|^2 + |\vec{\Pi}d|^2 + \Big[(\Pi_y s)^*(\Pi_y d) - (\Pi_x s)^*(\Pi_x d) + H.c.\Big]\Big\} + \frac{h^2}{8\pi}. \end{aligned} \tag{3.107}$$

While the various coefficients appearing in the above free energy appear to be similar to those found by Ren *et al.*, one important distinction must be emphasized: the free energy (3.107) mixes a d-wave component with both extended and isotropic s-wave components. In the continuum, all gap functions with s-wave symmetry are indistinguishable. Components with d-wave and isotropic s-wave symmetry must result from different pairing channels. In the absence of an on-site interaction, the s-wave component is always zero even in the presence of inhomogeneities. In lattice models, both Δ_s and Δ_d are generated by the same nearest-neighbour pairing interaction V_1. The analytical and numerical results clearly indicate that the s-wave component is finite for virtually all densities and $T < T_d$ in inhomogeneous superconductors, even when the on-site interaction is zero (see Fig. 3.5). There is therefore no limit in which the EH model reduces to the continuum theory.

3.4.2 Antiferromagnetic-van Hove Model

Neglecting fourth-order derivatives, the equations for the gap functions in the thermodynamic limit of the AvH model from Eq. (3.47) are:

$$\begin{aligned} \Delta_s^*(\mathbf{r}) &= \frac{TV}{2}\sum_{\omega_n}\int\frac{d^2k}{(2\pi)^2}\Big\{\frac{c_k\Delta_s^*(\mathbf{r})}{\omega_n^2 + \xi_k^2} - \frac{1}{4(\omega_n^2 + \xi_k^2)^2}\Big[c_k^2|\Delta_s(\mathbf{r})|^2\Delta_s^*(\mathbf{r}) \\ &\quad +2c_kd_k|\Delta_d(\mathbf{r})|^2\Delta_s^*(\mathbf{r}) + c_kd_k\Delta_d^{*2}(\mathbf{r})\Delta_s(\mathbf{r})\Big] \\ &- \int d^2z\frac{z^2}{2}\int\frac{d^2k'}{(2\pi)^2}\frac{e^{i(\mathbf{k}+\mathbf{k}')\cdot\mathbf{z}}}{(-i\omega_n - \xi_{k'})(i\omega_n - \xi_k)}\left[\vec{\Pi}^2 + \sin2\theta\left(\Pi_x^2 - \Pi_y^2\right)\right] \\ &\quad \times\left[c_k\Delta_s^*(\mathbf{r}) + e_k\Delta_d^*(\mathbf{r})\right]\Big\}; \end{aligned} \tag{3.108}$$

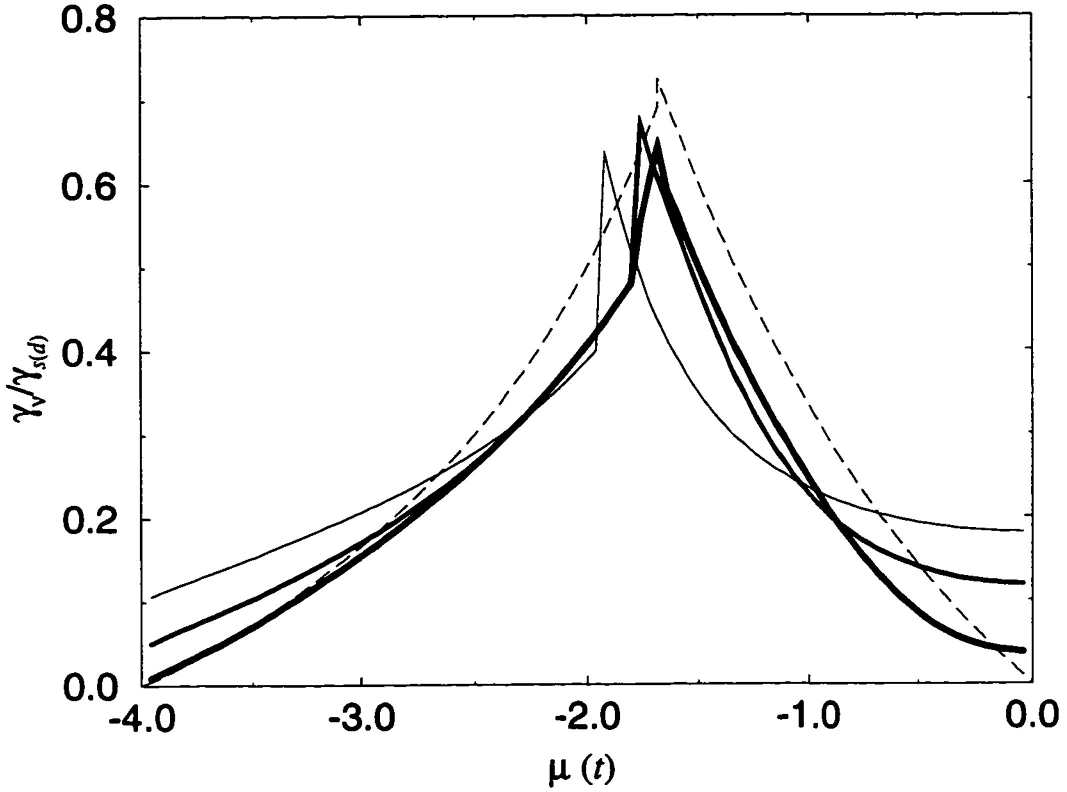

Figure 3.5: The ratio of the mixed gradient coefficient γ_ν to the ordinary gradient coefficient of the dominant order parameter γ_s or γ_d is given as a function of chemical potential μ. The solid and dashed lines correspond to numerical and analytical results respectively. The solid lines become progressively thicker as V_1 is decreased from $3t$ to t in increments of t; V_0 is taken to be zero. The discontinuity reflects the transition from an s-wave to d-wave bulk superconductor. The dashed line assumes that this occurs for $\mu = -1.65t$. All values are determined at the appropriate T_c.

$$\begin{aligned}\Delta_d^*(\mathbf{r}) &= \frac{TV}{2}\sum_{\omega_n}\int\frac{d^2k}{(2\pi)^2}\Bigg\{\frac{d_k\Delta_d^*(\mathbf{r})}{\omega_n^2+\xi_k^2} - \frac{1}{4(\omega_n^2+\xi_k^2)^2}\Big[d_k^2|\Delta_d(\mathbf{r})|^2\Delta_d^*(\mathbf{r}) \\ &\quad +2c_kd_k|\Delta_s(\mathbf{r})|^2\Delta_d^*(\mathbf{r}) + c_kd_k\Delta_s^{*2}(\mathbf{r})\Delta_d(\mathbf{r})\Big] \\ &- \int d^2z\frac{z^2}{2}\int\frac{d^2k'}{(2\pi)^2}\frac{e^{i(\mathbf{k}+\mathbf{k}')\cdot\mathbf{z}}}{(-i\omega_n-\xi_{k'})(i\omega_n-\xi_k)}\left[\vec{\Pi}^2+\sin 2\theta\left(\Pi_x^2-\Pi_y^2\right)\right] \\ &\quad \times\left[e_k\Delta_s^*(\mathbf{r})+d_k\Delta_d^*(\mathbf{r})\right]\Bigg\}, \end{aligned} \tag{3.109}$$

such that

$$c_k = 1+\cos k_1\cos k_2+\cos k_1+\cos k_2; \tag{3.110}$$

$$d_k = 1+\cos k_1\cos k_2-\cos k_1-\cos k_2; \tag{3.111}$$

$$e_k = \sin k_1\sin k_2. \tag{3.112}$$

With Eqs. (3.87), (3.108), and (3.109), one immediately obtains the coefficients of the GL free energy (2.15) for the AvH model:

$$\{\alpha_s\ ,\ \alpha_d\} = \frac{1}{V} - \frac{1}{4}\int\frac{d^2k}{(2\pi)^2}\frac{\{c_k\ ,\ d_k\}}{\xi_k}\tanh\left(\frac{\xi_k}{2T}\right), \tag{3.113}$$

$$\{\beta_1\ ,\ \beta_2\ ,\ \beta_3\ ,\ \beta_4\} = \frac{T}{16}\sum_{\omega_n}\int\frac{d^2k}{(2\pi)^2}\frac{\{c_k^2\ ,\ d_k^2\ ,\ 4c_kd_k\ ,\ c_kd_k\}}{(\omega_n^2+\xi_k^2)^2}, \tag{3.114}$$

$$\{\gamma_s\ ,\ \gamma_d\} = T\sum_{\omega_n}\int\frac{d^2k}{(2\pi)^2}\frac{\sin^2k_1\left(t_{11}+2t_{20}\cos k_2\right)^2+\sin^2k_2\left(t_{11}+2t_{20}\cos k_1\right)^2}{(\omega_n^2+\xi_k^2)^2}\{c_k\ ,\ d_k\}, \tag{3.115}$$

$$\gamma_\nu = -2T\sum_{\omega_n}\int\frac{d^2k}{(2\pi)^2}\frac{e_k^2\left(t_{11}+2t_{20}\cos k_1\right)\left(t_{11}+2t_{20}\cos k_2\right)}{\left(\omega_n^2+\xi_k^2\right)^2}. \tag{3.116}$$

Note that $\beta_3 = 4\beta_4$, as was found in the EH model, Eq. (3.107). The same result has been obtained within GL theory [135], and in previous continuum calculations [137, 138]. This generic feature of the free energy (2.15) is a direct consequence of the symmetry between the s-wave and d-wave order parameters and the underlying bond (or directionally-dependent) gap functions from which they are derived. The above expressions above are not analytically tractable because the AvH dispersion (3.42) has a complicated angular dependence. As shown in Section 3.3.2, at optimal hole doping $\langle n \rangle \sim 0.2$, the d-wave transition temperature found using Eq. (3.80) is ~ 100 K. The coefficients of the GL free energy have been determined numerically for $T \approx T_d$ at optimal doping:

$$\begin{aligned}
F_s &= F_n - 11.3\left(1 - \frac{T}{T_d}\right)|\Delta_d|^2 + 10.8|\Delta_s|^2 + 38.7|\Delta_s|^4 + 5720|\Delta_d|^4 \\
&+ 603\Big[|\Delta_s|^2|\Delta_d|^2 + \frac{1}{4}\left(\Delta_s^{*2}\Delta_d^2 + \Delta_d^{*2}\Delta_s^2\right)\Big] \\
&+ 2.69|\vec{\Pi}\Delta_s|^2 + 7.38|\vec{\Pi}\Delta_d|^2 \\
&+ 1.50\Big[(\Pi_y\Delta_s)^*(\Pi_y\Delta_d) - (\Pi_x\Delta_s)^*(\Pi_x\Delta_d) + H.c\Big] + \frac{h^2}{8\pi}. \qquad (3.117)
\end{aligned}$$

The coefficients β_2 and β_3 are large precisely because of the stability of d-wave superconductivity in this model (see the discussion in Section 3.3.2). This is most easily demonstrated by evaluating the Matsubara sums appearing in Eqs. (3.114), which may be re-written in terms of (3.68):

$$\begin{aligned}
T\sum_{\omega_n}\frac{1}{(\omega_n^2 + \xi_k^2)^2} &= -\frac{1}{2\xi_k}\frac{\partial}{\partial \xi_k}\left[T\sum_{\omega_n}\frac{1}{\omega_n^2 + \xi_k^2}\right] \\
&= \frac{1}{8\xi_k^2}\left[\frac{\tanh^2(\xi_k/2T)}{T} + 2\frac{\tanh(\xi_k/2T)}{\xi_k} - \frac{1}{T}\right]. \qquad (3.118)
\end{aligned}$$

The largest contribution from the integrands in (3.114) come from the terms of order d_k^n/ξ_k^3, since $\xi_k \to 0$ and $c_k \to 0$ near the van Hove singularity and optimal doping, while d_k stays finite. The AvH model strongly suppresses terms involving s-wave components.

The GL coefficients indicate that a low-temperature transition to a time-reversal breaking phase, induced by inhomogeneities, is not likely to occur. This may be understood qualitatively by the observation that s-wave components are not favoured in the AvH model. The equation (2.41) defining the second transition temperature T^* may be re-written as:

$$\beta_3\Delta_d^2(T^*) + 2\alpha_s(T^*) = 0, \qquad (3.119)$$

where the result $\beta_3 = 4\beta_4$ has been used. Since β_3 is extremely large, T^* must be small even if Δ_d is strongly suppressed near an inhomogeneity. The subdominant transition temperature is therefore not likely to be finite. In contrast, the EH model is more likely to give rise to a finite T^*, particularly for densities approaching the crossover to bulk s-wave superconductivity.

The maximum value of the s-wave component nucleated in the vortex core, calculated numerically using (3.91), (3.93), (3.102), (3.113), and (3.115), is shown as a function of hole density $\langle n_h \rangle \equiv 1 - \langle n \rangle$ in Fig. 3.6. It may be seen that the induced s-wave component in the AvH model can be at most 5% of the bulk d-wave value; this estimate is obtained for $\langle n_h \rangle \sim 25\%$ and $T \to 0$, where it is assumed that $\alpha_d(T) \propto (1 - T/T_d)$ for all T. This small subdominant component results in spite of a large temperature-independent gradient coefficient ratio ($\gamma_\nu/\gamma_d \sim 20\%$ near optimal doping) that is found to increase monotonically with doping, up to the largest densities studied. The small size of the s-wave component in the AvH model may be partly due to an effective on-site repulsion, which is built into the Hamiltonian by constraining holes to move within a single spin sublattice of an antiferromagnetic background.

The EH model can allow for a large subdominant s-wave component $s_{\mathrm{max}}/d_{\mathrm{bulk}} \sim 20 - 30\%$ with a suitable choice of parameters, such as low T, V_0 and large $\langle n_h \rangle, V_1$. Furthermore, the s-wave component induced by external currents is approximately four times larger than the maximum s-wave gap nucleated in a magnetic vortex; for sufficiently low temperatures and densities in the EH model, the s-wave and bulk d-wave components can become comparable. As the on-site repulsion is increased, however, the induced s-wave component is suppressed.

The GL d-wave coherence length $\xi(T)$ is calculated numerically with the aid of (2.27), and is shown as a function of hole concentration $\langle n_h \rangle$ for $T = 0.9T_d$ in Fig. 3.7. As expected, $\xi(T)$ becomes shorter with decreasing $\langle n_h \rangle$. For hole densities up to 30% filling, the AvH model leads to $\xi \sim a/\sqrt{1 - T/T_d}$ where a is a lattice spacing (≈ 3.8 Å). This short coherence length is roughly in agreement with experimental observations for the cuprates [59, 65, 66, 161]. The EH model yields similar d-wave coherence lengths for $V_1 = 2t, 3t$. These short ξ_d strictly violate the initial GL condition that the gap functions vary over a longer length scale than the Fermi wavelength $k_F^{-1} \sim 1a - 2a$ (see Section 3.2). The GL equations derived thus far must capture

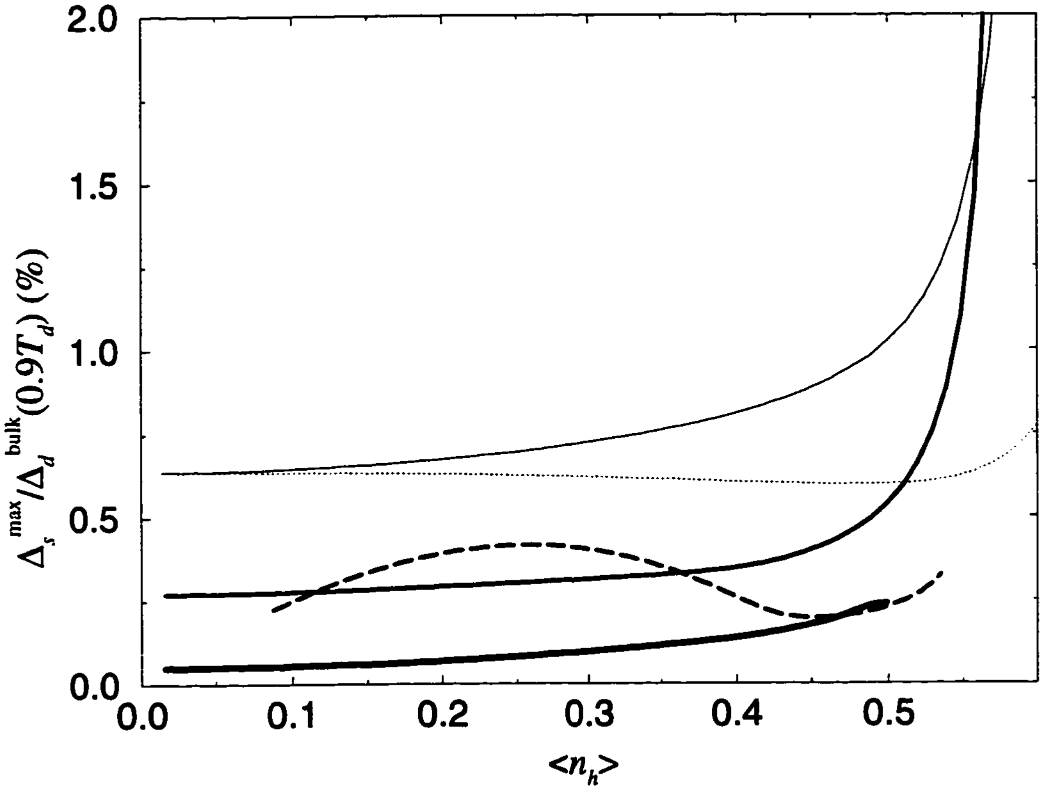

Figure 3.6: The relative magnitude of the maximum s-wave component induced in the vortex core $s_{\rm max}/d_{\rm bulk}$ is calculated numerically and is given as a function of hole density $\langle n_h \rangle$ for temperatures $T = 0.9T_d$. The dashed line, corresponding to results for the AvH model, indicates that the induced s-wave component is largest near optimal doping ($\langle n_h \rangle \sim 20\%$). Results for the EH model are given for comparison, where in the hole representation $\langle n_h \rangle = 0$ corresponds to $\mu = 0$. Solid lines (in order of decreasing thickness) correspond to $V_1 = t, 2t, 3t$ with $V_0 = 0$, while the dotted line is for $V_1 = 3t, V_0 = 4t$.

at least some of the essential physics, however, since the conclusions obtained by integrating the GL equations [134, 135, 137] closely match the results of numerical investigations of short-ξ_d superconductors [129]. The validity of the GL equations derived above is further confirmed by the microscopic analyses of inhomogeneous d-wave superconductors presented in Chapters 4 and 5.

3.5 Extension of the GL Equations

As discussed in Section 2.3, the current and magnetic field distribution around an isolated vortex of a d-wave superconductor is anisotropic in general. The fourfold symmetry results when an s-wave component is induced in the vicinity of the vortex core, and when higher-order d-wave gradient terms are included in the GL free energy. To assess the relative importance of these two contributions to anisotropy, the coefficients of the higher-order terms included in (2.15), and $\gamma_{d(s)-}$ in particular, must be determined microscopically. The derivation of the coefficients η_s and η_d that appear in (2.18) and (2.19) requires extending the second term on the right hand side of Eq. (3.37) to include gradients of the gap functions. Applying similar techniques to those described in previous sections, one obtains for the EH model:

$$\begin{aligned}\{\eta_s\ ,\ \eta_d\}^{\mathrm{EH}} &= -4T\sum_{\omega_n}\int\frac{d^2k}{(2\pi)^2}\frac{\xi_k^2\left(\nabla_{k_x}\xi_k\right)^2}{\left(\omega_n^2+\xi_k^2\right)^4}\{16{a'_k}^4\ ,\ b_k^4\} \\ &\approx -\frac{31\zeta(5)N'v_F^2}{32\pi^4T^4}\left\{\left(\frac{\mu}{D}+\frac{\epsilon}{4}\right)^4\ ,\ \frac{3}{8}\left(\frac{\mu+D}{D}\right)^4\right\},\end{aligned} \tag{3.120}$$

where the analytical solution is valid in the continuum limit, and $\zeta(5)\approx 1.037$. For the AvH model,

$$\{\eta_s\ ,\ \eta_d\}^{\mathrm{AvH}} = -2T\sum_{\omega_n}\int\frac{d^2k}{(2\pi)^2}\frac{\xi_k^2\left[\left(\nabla_{k_1}\xi_k\right)^2+\left(\nabla_{k_2}\xi_k\right)^2\right]}{\left(\omega_n^2+\xi_k^2\right)^4}\{c_k^2\ ,\ d_k^2\}. \tag{3.121}$$

The coefficients of the fourth-order gradient terms can be derived by evaluating in the thermodynamic limit terms in (3.43) and (3.47) that have been ignored until now. After some manipulation, one obtains

$$\{\gamma_{s\pm}\ ,\ \gamma_{d\pm}\}^{\mathrm{EH}} = -\frac{T}{48}\sum_{\omega_n}\int d^2z\int\frac{d^2k\,d^2k'}{(2\pi)^4}\frac{e^{i(\mathbf{k}+\mathbf{k}')\cdot\mathbf{z}}}{(-i\omega_n-\xi_{k'})(i\omega_n-\xi_k)}$$

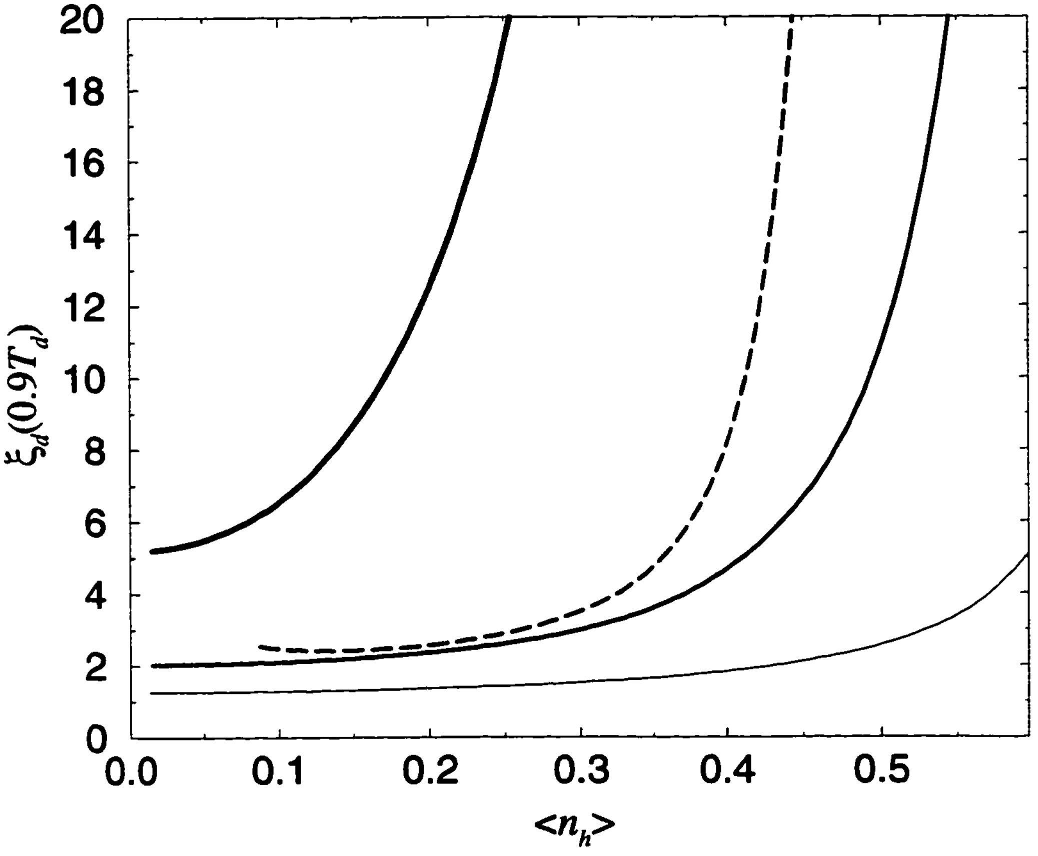

Figure 3.7: The numerical d-wave Ginzburg-Landau coherence length $\xi_d(T)$, measured in units of a lattice spacing, is shown for $T = 0.9T_d$ as a function of hole concentration $\langle n_h \rangle$. The dashed line corresponds to the AvH model while the solid lines (in order of decreasing thickness) correspond to the EH model for $V_1 = t, 2t, 3t$ and $V_0 = 0$.

$$\times\, x^2\left(x^2 \pm 3y^2\right)\left\{4{a'_k}^2\,,\; b_k^2\right\}, \tag{3.122}$$

$$\begin{aligned}\left\{\gamma_{s\pm}\,,\;\gamma_{d\pm}\right\}^{\mathrm{AvH}} &= -\frac{T}{48}\sum_{\omega_n}\int d^2z\int\frac{d^2k\,d^2k'}{(2\pi)^4}\cdots\\ &\quad\times\left(r_1+r_2\right)^2\left[\left(r_1+r_2\right)^2 \pm 3\left(r_1-r_2\right)^2\right]\left\{c_k\,,\; d_k\right\}, \end{aligned}\tag{3.123}$$

where the ellipsis represents the k-dependent part of the integrand. The fourth-order gradient terms can be evaluated analytically in the EH model for weak to intermediate coupling and low densities:

$$\left\{\gamma_{s+}\,,\;\gamma_{s-}\right\} = -\frac{31\zeta(5)N'}{512}\left(\frac{v_F}{\pi T}\right)^4\left\{3\left(\frac{\mu}{D}+\frac{\epsilon}{4}\right)^2,\; 0\right\}, \tag{3.124}$$

$$\left\{\gamma_{d+}\,,\;\gamma_{d-}\right\} = -\frac{31\zeta(5)N'}{2048}\left(\frac{v_F}{\pi T}\right)^4\left\{5\left(\frac{\mu+D}{D}\right)^2,\; 2\left(\frac{\mu+D}{D}\right)^2\right\}. \tag{3.125}$$

The analytical results obtained for the EH model indicate that all the higher-order terms in the free energy (2.18) and (2.19) have a negative sign compared with the second-order terms. The overall sign of these higher-order terms is not significant, however, as long as the order parameters are sufficiently small and slowly varying. While both of these conditions are satisfied near T_c, one also finds $\gamma_{s(d)+}/\gamma_{s(d)} \sim (v_F/\pi T)^2 \to 0$ as $\mu \to -D$. At low densities, the EH model predicts a vanishing γ_{s-} coefficient, consistent with the expectation that the free energy of a continuum s-wave superconductor should have spherical symmetry. Furthermore, $\gamma_{d+}/\gamma_{d-} = 5/2$, as was found by Ichioka *et al.* within a continuum model [136].

The analytical results for the EH model do not adequately address whether anisotropy in the free energy is primarily due to the existence of the subdominant order parameter or fourth-order gradients. For a bulk s-wave superconductor, the induced d-wave order parameter clearly breaks circular symmetry since $\gamma_\nu \neq 0$ for $\mu > -D$ while $\gamma_{s-} = 0$. Yet stronger coupling, lattice effects, or Fermi surface anisotropy could lead to a non-vanishing γ_{s-}, which could compete with the γ_ν^2/α_d coefficient in the free energy (2.37). For a bulk d-wave superconductor, assuming that $\alpha_s \approx 1/V_1$, one finds:

$$\frac{\gamma_\nu^2}{\alpha_s\gamma_{d-}} \approx -\frac{196\zeta(3)^2 V_1 N(0)}{31\zeta(5)}\left(\frac{\mu}{D}+\frac{\epsilon}{4}\right)^2, \tag{3.126}$$

which is of order $-V_1/t$. This result indicates that the 'subcritical' coefficient γ_v^2/α_s and the 'asymmetric' coefficient γ_{d-} enter the free energy (2.37) with the same sign, and give similar contributions to the anisotropy. Since d-wave superconductivity is favoured for densities closer to half-filling, however, Fermi surface anisotropy may significantly alter the analytical results.

The ratios $\gamma_v^2/\alpha_{d(s)}\gamma_{s(d)-}$ have been calculated numerically for $T = T_c$ and are shown in Fig. 3.8. Virtually indistinguishable results have been obtained for all temperatures $0.5T_c \leq T \leq T_c$ (not shown). The numerics make clear that the ratios are always larger than zero. Unlike the weak-coupling prediction, both γ_{s-} and γ_{d-} are finite and positive in their regimes of applicability $\mu \to -D$ and $\mu \to 0$, respectively. The positive sign for γ_{s-} is due to the factor of -3 in the integrands of (3.122) and (3.123); it is finite due to lattice and stronger-coupling effects neglected in the analytical calculations. The change in sign for γ_{d-}, compared with the analytical result, is mostly due to Fermi surface anisotropy. Thus, the contributions of the subcritical and asymmetric coefficients to anisotropy are in fact competing. For most densities and coupling strengths, the contribution of $\gamma_{s(d)-}$ dominates, and the asymmetric gradient term in the free energy (2.37) is positive. In the EH model, the subcritical coefficient may dominate, but only for densities very near the crossover from bulk s-wave to d-wave condensation (or vice versa); in this regime $\alpha \to 0$ and the asymmetric gradient term is negative.

It is not presently clear if the overall sign of the anisotropic fourth-order gradient term in the free energy (2.37) has any physical significance. Previous microscopic investigations of the EH model within the context of Bogoliubov-de Gennes (BdG) theory [129] demonstrated marked anisotropy in the structure of the d-wave component near the core of an isolated vortex. Parameters chosen correspond to a substantial s-wave component nucleated near the vortex core, i.e. $\gamma_v^2/\alpha_s \gg \gamma_{d-}$, and therefore a large negative coefficient for the asymmetric gradient term. The quasiclassical Eilenberger formalism also has been used to investigate microscopically the vortex structure in d-wave superconductors [136]. Even though induced s-wave components were neglected in this work, the same four-fold symmetry of the d-wave gap function was found. In this model, the Fermi surface is assumed to be isotropic so

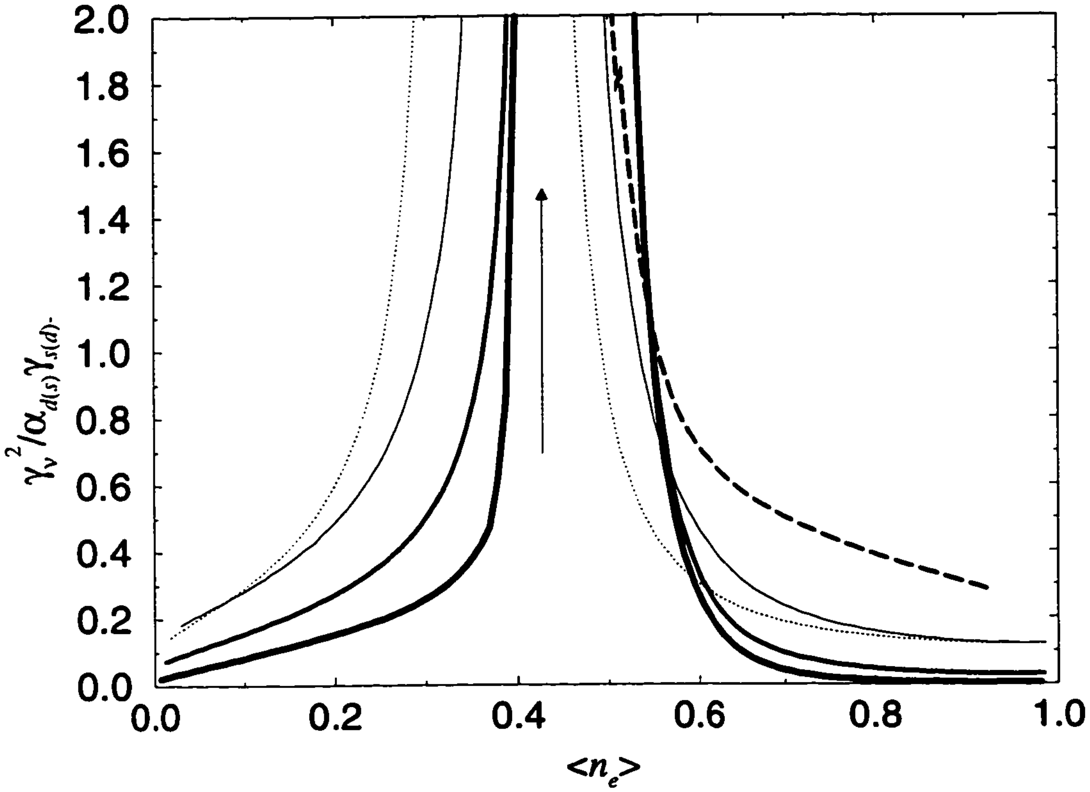

Figure 3.8: The ratio $\gamma_v^2/\alpha_{d(s)}\gamma_{s(d)-}$ is shown as a function of electron concentration $\langle n_e \rangle$ for $T = T_c$. Solid lines (in order of decreasing thickness) correspond to the EH model for $V_1 = 1.3t$, $2t$, $3t$ with $V_0 = 0$, while the dotted line is for the EH model with $V_1 = 3t$, $V_0 = 4t$. The dashed line gives the results for the AvH model in the electron notation such that $\langle n_e \rangle = 1 - \langle n_h \rangle$. To the left (right) of the arrow is shown $\gamma_v^2/\alpha_d\gamma_{s-}$ ($\gamma_v^2/\alpha_s\gamma_{d-}$) corresponding to bulk s-wave (d-wave) superconductivity.

the γ_{d-} coefficient is negative as well; the same result is obtained in the low-density approximation employed above. Very recent BdG calculations, however, which incorporate the effects of Fermi surface anisotropy, indicate that the sign of the asymmetric gradient term may partly determine the orientation of the vortex lattice with respect to the crystal lattice [162, 163].

For completeness, the coefficients $\eta_{s(d)}$ and $\gamma_{s(d)+}$ also have been determined numerically for both the EH and AvH models. Both coefficients are always negative and in general it is found that for the EH model $\eta_{s(d)} \sim 10\gamma_{s(d)+} \sim 100|\gamma_{s(d)-}|$, and $\gamma_{s(d)+}$ is of the same order as $\gamma_{s(d)}$ at T_c. For the AvH model at optimal doping and T_c, one obtains:

$$\begin{aligned} F_s^{\mathrm{AvH}} &= F_n - 11.3\left(1 - \frac{T}{T_d}\right)|\Delta_d(\mathbf{r})|^2 + 5720|\Delta_d(\mathbf{r})|^4 + 7.38|\vec{\Pi}\Delta_d(\mathbf{r})|^2 \\ &- 16300|\Delta_d(\mathbf{r})\vec{\Pi}\Delta_d(\mathbf{r})|^2 - 16.5|\vec{\Pi}^2\Delta_d(\mathbf{r})|^2 + 2.65|(\Pi_y^2 - \Pi_x^2)\Delta_d(\mathbf{r})|^2 + \frac{h^2}{8\pi}. \end{aligned} \tag{3.127}$$

The large value of η_d is due to the stability of d-wave superconductivity in the AvH model, as disussed in Sections 3.3.2 and 3.4.2; the leading contribution to the integrand of (3.121) is of order $1/\xi_k^5$. For both models, the relative sizes of $\eta_{s(d)}$ and $\gamma_{s(d)+}$ compared with the magnitude of $\gamma_{s(d)}$ clearly demonstrates that the GL theory derived in this chapter is only strictly valid quite near T_c.

3.6 Summary and Discussion

The Ginzburg-Landau equations for a d-wave superconductor have been derived within the context of two microscopic lattice models used to describe the high-T_c materials: the extended Hubbard model and the Antiferromagnetic-van Hove model. It has been possible to quantitatively investigate how the lattice and external inhomogeneities generate and govern the interplay between co-existing s-wave and d-wave order parameters. The relative magnitudes of the various GL coefficients, as well as their temperature and density dependence, also have been ascertained.

Microscopic models describing the cuprates predict a significant admixture of an

s-wave component in inhomogeneous d-wave superconductors. The results for both models are qualitatively similar, though the subdominant components tend to be larger in the EH model. In the presence of external magnetic fields and currents, the magnitude of the s-wave component is proportional to the gradient coefficient ratio γ_ν/γ_d. It has been found that within a broad and experimentally relevant parameter space both microscopic models yield $\gamma_\nu/\gamma_d \sim 0.1 - 0.4$. In the mixed-state, the s-wave component nucleated in the core of a magnetic vortex may be as large as 30% at low temperatures. Isolated vortices will become appreciably anisotropic, and the flux lattice will deviate from that of a triangle. The oblique flux lattice that results, with an angle between primitive vectors $\phi \approx 70° - 80°$ [134, 135], is consistent with recent experimental observations for YBCO [143, 144]. The subdominant components induced by external currents are generally larger, and the induced s-wave components may become comparable to the magnitude of the bulk d-wave gap.

In order to determine the sources of anisotropy in the GL free energy, the influence of Fermi surface anisotropy and lattice effects has been investigated numerically for both microscopic models. It has been shown that the asymmetric gradient term in the d-wave gap function contributes a four-fold symmetry comparable to that of the s-wave component over much of the phase diagram. Furthermore, since these contributions appear with opposite sign, their effects tend to compete.

Wherever possible, comparison has been made with previous derivations of the GL coefficients within continuum models. It should be emphasized, however, that lattice models provide considerably more information regarding the density and coupling-dependence of the GL coefficients, which in turn regulate the admixture of s-wave and d-wave components in unconventional superconductors. The results clearly indicate that s-wave components are always present in inhomogeneous d-wave materials for temperatures below T_d, even in the absence of a separate s-wave pairing channel.

The primary objective of the present work has been to demontrate that microscopic lattice models used to describe the cuprates yield GL coefficients in a physically interesting regime. In particular, the calculation reveals values for the coefficients which favour subdominant real s-wave components nucleated by external magnetic fields or currents, and imaginary s-wave components near intrinsic inhomogeneities.

The GL free energy derived in this chapter, therefore, may be a useful reference for the theoretical investigation of high-T_c materials in the presence of inhomogeneities.

Chapter 4

Twin Boundaries

4.1 Introduction

4.1.1 Properties

The high-T_c superconductor $YBa_2Cu_30_{6+x}$ (YBCO) is a tetragonal Mott insulator in its parent state ($x = 0$), due to the presence of two proximal *ab*-oriented antiferromagnetic CuO_2 planes in its unit cell. As the doping x increases, additional oxygen atoms occupy sites between the copper-oxide planes, and charge carriers in the form of holes appear in the antiferromagnetic layers. A superconducting instability, as well as a tetragonal to orthorhombic phase transition, occurs for oxygen doping at approximately $x = 0.4$ [164]. The highest superconducting transition temperature for this material ($T_c \approx 93$ K) is obtained at 'optimal doping' $x \approx 0.95$ [165]. At this doping, the inter-plane oxygens have formed almost continuous *a*- or *b*-oriented CuO chains, leading to a maximum orthorhombic distortion of the unit cell, corresponding to $a = 3.821$ Å and $b = 3.885$ Å for *b*-oriented chains, and vice versa [166]. The large anisotropy of the normal-state resistivities $\rho_c/\rho_a \approx 35$ and $\rho_c/\rho_b \approx 75$ observed experimentally [41] (with *b*-oriented chains) indicates a weak coupling of carriers in the *c*-direction (whose unit cell length is 11.65 Å), but enhanced normal-state transport along the chains. This conclusion is corroborated in the superconducting state by the anisotropy of the penetration depths [69, 70, 72]:

$\{\lambda_a, \lambda_b, \lambda_c\} \approx \{1500, 1000, 6500\}$ Å.

In general, optimally-doped YBCO minimizes its formation energy by the process of twinning, i.e. separating into a patchwork of regions, called twins, with different orthorhombic orientations [167]. The two possible twin domains have unit cell parameters *abc* and *bac*. The domain walls separating the twins are aptly named 'twin boundaries,' and are oriented in the [110] and $[1\bar{1}0]$ directions. In pure optimally-doped samples, or if a small number of the copper sites have been substituted by Zn or Ni impurities, the twin boundaries are approximately 10 Å wide and are separated by an average distance of order 200 Å. The twin boundary becomes wider (up to approximately 40 Å), and increasingly tetragonal, with decreasing x and with Al or Fe-doping [168]. Since Al and Fe preferentially substitute for copper atoms in the chains [169], while Zn and Ni are thought to replace planar Cu [170], the twin boundary properties appear to correlate with the degree of chain disorder. Most important, however, is that the twin boundary regions have a depleted oxygen content relative to the twin domains [171]. This observation makes intuitive sense: the chain orientation must rotate by 90° over the short length scale of the twin boundary width, which implies that the twin boundary region is at least oxygen-disordered if not fully stoichiometric.

Twin boundaries are thought to significantly influence both the superconducting and normal-state properties of YBCO. These intrinsic defects are known to effectively pin magnetic vortices against perpendicular flux flow [172, 173, 174, 175, 176], and are thought to enhance vortex channeling in the parallel direction [177, 178, 179, 180]. In addition, investigations of YBCO in external *c*-oriented magnetic fields near H_{c2} clearly indicate that vortices are preferentially located in the vicinity of twin boundaries [181], which locally distorts the Abrikosov flux lattice [182]. The pinning properties of twin boundaries may also help explain why the critical currents of YBCO thin films far exceed those of bulk materials [183, 184, 185, 186]. Perhaps the most convincing experimental evidence to date that twin boundaries play an important role in both the superconducting and normal-state properties of YBCO has been recently obtained by Villard *et al.* [187]. The normal-state resistivity and the self-field critical current, measured on unidirectionally-twinned samples in the absence of external magnetic fields, showed 6-fold and 25-fold anisotropy respectively between the directions perpendicular and parallel to the twin boundaries.

Twin boundaries most likely act as weak superconducting links at low temperatures. Since their width is comparable to the superconducting coherence length $\xi(0) \approx$ 16-30 Å [59, 161], twin boundaries probably behave as short Josephson junctions [188] between adjacent twin domains. The weak-link suppression of superconductivity in the twin boundaries would be a direct consequence of the local oxygen depletion discussed above, since both the local T_c and consequently the local magnitude of the superconducting order parameter are proportional to the doping. Strongly coupled superconducting microdomains of width $\sim$ 40 Å have been invoked in order to explain the behaviour of the low-temperature critical current in YBCO thin films [189]. The experimental evidence, therefore, is beginning to resolve the long-standing theoretical question of whether superconductivity is enhanced [190, 191] or suppressed [192] at the twin boundary.

4.1.2 π Junctions and Half-Integral Vortices

The large *ab*-plane critical currents (of order 10^5 A/cm^2) observed in twinned YBCO [187] indicate that adjacent twin domains must be strongly Josephson coupled. Further insight into the characteristics of the twin boundary Josephson junctions may be obtained by considering the predominantly *d*-wave character of the superconducting order parameter in YBCO (refer to Chapter 1 for details). The Josephson interface energy can be written [193]:

$$E_J(\varphi) = -\frac{I_c\phi_0}{2\pi c}\cos(\varphi - \alpha), \tag{4.1}$$

where α is the junction phase, I_c is the critical current through the junction, and φ is the phase difference between the two order parameters on either side of the interface. If the lobes facing the twin boundary of these predominantly *d*-wave order parameters have the same sign then $\varphi = 0$; if they have the opposite sign, $\varphi = \pi$. If $\varphi = 0$, the Josephson energy is minimized with $\alpha = 0$, while $\varphi = \pi$ would require $\alpha = \pi$; these two cases are labeled 0- and π-junctions, respectively. The tunneling current is by convention positive for a 0-junction, and negative for a π-junction.

Twin boundaries in d-wave superconductors are π-junctions. To make this clear, a series of YBCO domains separated by a number of parallel twin boundaries and a single perpendicular grain boundary are shown schematically in Fig. 4.1. Recall that the lobes of the order parameter are aligned with the underlying crystal lattice (oriented 45° to the twin boundary), and a and b are interchanged in adjacent twin domains. Either the d-wave gap changes sign across the twin boundary, or it doesn't; these two possibilities correspond to a 0-junction and a π-junction twin boundary, respectively. Most of the experimental evidence supporting a d-wave superconducting order parameter in YBCO, however, has been obtained using heavily-twinned YBCO samples. Assuming that equal volumes of the *abc* and *bac* twin domains comprise the sample, then 0-junction twin boundaries imply that the d-wave component should average to zero, leaving only the finite s-wave component that is always present in orthorhombic d-wave superconductors. Unless one particular twin domain dominates the sample [194, 195], one must conclude that twin boundaries are π-junctions [196]. The strong phase-locking of the d-wave component across the twin boundary allows for the large perpendicular critical current I_c.

Thus far, φ in Eq. 4.1 has been assumed to vary discontinuously across the Josephson junction. Removing this restriction, the relative phase obeys the Sine-Gordon equation [197, 198]

$$\lambda_J^2 \frac{d^2\varphi(x)}{dx^2} = \sin\left[\varphi(x) - \alpha(x)\right], \tag{4.2}$$

where x is the direction perpendicular to the interface. The Josephson penetration depth $\lambda_J = (\phi_0/2\pi\tilde{d}I_c)$ is the characteristic length scale for spatial variations of φ parallel to the junction, and is of order 10 μm in YBCO grain boundaries ($\tilde{d}$ is the interface width plus twice the sum of the London penetration depth, and $\phi_0 = hc/2e$ is the superconducting flux quantum). The spatial variations of the relative phase induces a local magnetic flux $\tilde{\Phi}$ at the junction, given by [199]:

$$\tilde{\Phi}(x) = \frac{\phi_0}{2\pi}\frac{d\varphi(x)}{dx}. \tag{4.3}$$

From Eq. 4.3, it is apparent that there will be a spontaneously-induced half-integer $(\phi_0/2)$ flux quantum in zero external field, at any intersection of an odd number

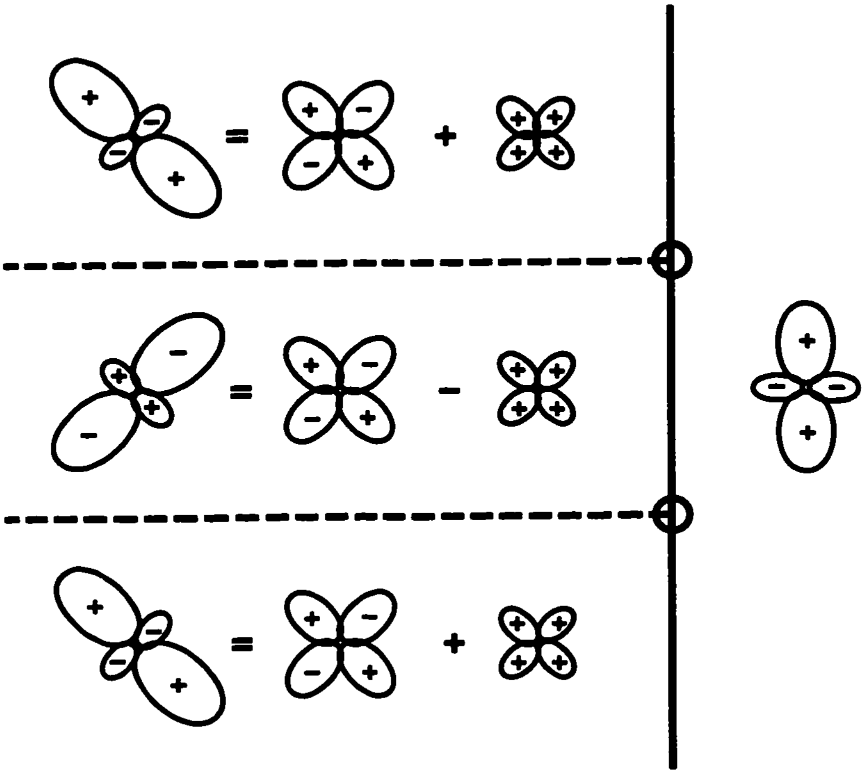

Figure 4.1: Domains of orthorhombic YBCO are shown separated by twin boundaries (dashed lines) and a grain boundary (solid line). The two grains are 45° misaligned. The orientations of the *d*-wave and *s*-wave components, required by the macroscopic *d*-wave symmetry of the sample on both sides of the grain boundary, are illustrated. Circles at the twin/grain boundary intersections are spontaneously-generated flux.

of π-junctions [200] (i.e. when the relative phase of the order parameter changes by π across one of the junctions). Note that such a flux quantum would not usually be found in a long isolated π-junction such as a twin boundary, since it would be impossible to nucleate a (finite) Josephson vortex over its entire length. Rather, a half-integer flux quantum should be found at each twin/grain boundary intersection shown in Fig. 4.1 [201, 202], or at two corners of the triangular grain boundary shown in Fig. 4.2.

Spontaneous half-integer flux quanta have been observed in superconducting quantum interference device (SQUID) experiments on corner-junction grain boundaries of YBCO [120]. Since π-junctions can only be found in superconductors with unconventional pairing symmetries, these results have strongly reinforced the hypothesis that the high-T_c materials are *d*-wave superconductors.

4.1.3 Fractional Vortices

In at least one series of SQUID experiments [203], the flux measured in grain boundaries and junctions in the absence of external magnetic fields were found to be different from 0 or $\phi_0/2$, which suggests that important physics has been neglected in the above discussion. The system under investigation, a triangular grain of YBCO included in a bulk YBCO thick film with a different *ab*-plane orientation, is illustrated in Fig. 4.2. For reasons discussed above, two half-integer flux quanta should be spontaneously generated at the intersection of the 0-junction and the two π-junctions. Note that the conventional superconducting flux quantization condition for the external YBCO grain would be satisfied in this case, since the total flux enclosed adds to an integer flux quantum. In actuality, however, much smaller flux quanta were measured, and were found at all three corners as well as along the edges, while the total flux enclosed remained ϕ_0.

Flux quanta smaller than integer multiples $\phi_0/2$, called fractional vortices, are inconsistent with time-reversal symmetry. This can be demonstrated by considering a flux Φ trapped at a grain-boundary corner. Reversing time changes the sign of the magnetic field; yet the single-valuededness of the superconducting wavefunction

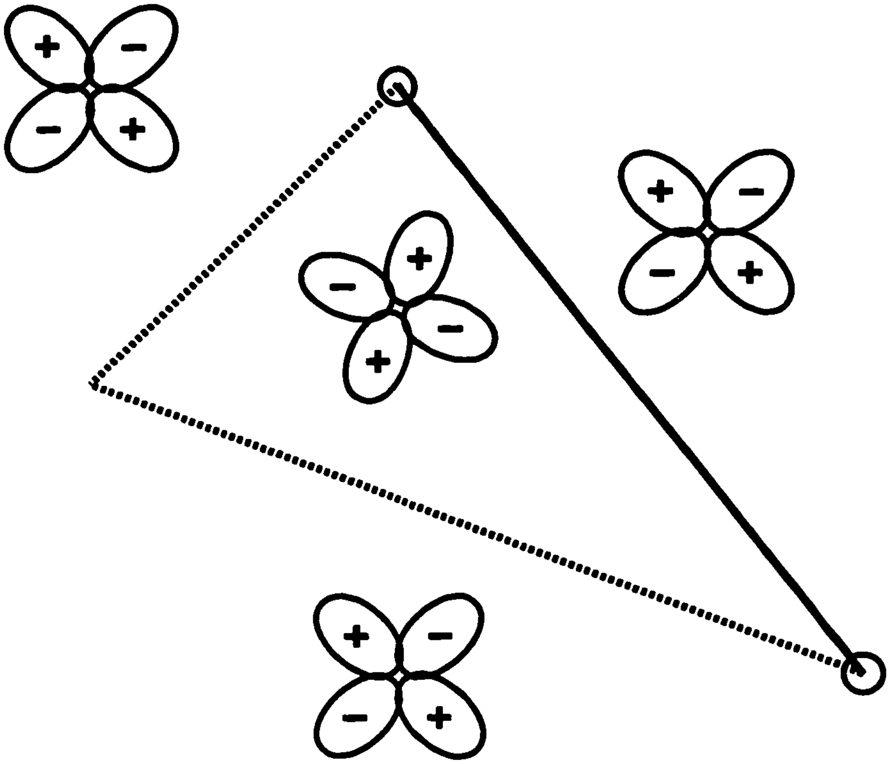

Figure 4.2: The triangular grain boundary defines the perimeter of a YBCO inclusion with a different *ab*-plane orientation from that of the external grain. Solid and dotted lines are 0- and π-junctions, respectively. Circles are spontaneous half-integer flux quanta. The order parameter is assumed to be pure *d*-wave for simplicity.

stipulates that this time-reversed flux $-\Phi$ can only differ from the original flux by $n\phi_0$, $\Phi = -\Phi + n\phi_0$. Thus, one immediately obtains $\Phi = n\phi_0/2$ in time-reversal preserving systems [199].

In the SQUID experiments, the size of the triangular inclusion is comparable to the Josephson penetration depth. One might expect, therefore, that the vortices located at the corners have sufficiently coalesced to ensure that the sum of their flux adds to an overall unit quantum. In fact, the vortices are all found to be highly localized on a length scale much shorter than λ_J. Furthermore, it is not clear how overall flux quantization could be guaranteed for time-reversal breaking triangular inclusions much larger than λ_J.

One resolution of this apparent contradiction is that the observed flux is an effective magnetic field due to the presence of spontaneous screening currents flowing parallel, but not across, the junctions [203]. Recall from Section 2.4 that this is precisely the low-temperature prediction of the Ginzburg-Landau theory; the phase-variation of a complex s-wave component gives rise to currents flowing parallel to the boundary. The magnitudes of these spontaneous supercurrents are proportional to the degree of $\mathcal{T}$-violation, which is governed by the angle the grain boundary makes with the orientation of the d-wave order parameter [204]. The Cooper pair-breaking effect, and therefore the currents, are largest when the grain boundaries are oriented at a 45° angle to the underlying lattice. The d-wave component is completely unperturbed by a perfectly smooth 90° grain boundary. Since faceting of the grain boundaries leads to small variations of this angle [205], the magnitude of the currents near the boundary could be highly variable, leading to the experimentally-observed localized fractional flux. Furthermore, the condition that the total enclosed flux equal ϕ_0 is naturally satisfied within this interpretation, since the currents can equivalently be interpreted as diamagnetically screening a physical (quantised) magnetic field penetrating the misaligned inclusion.

The existence of a time-reversal breaking imaginary s-wave component near interfaces may also explain the anomalous results of several other experiments on YBCO [206, 207, 208]. In particular, Dynes *et al.* [208] have measured large currents in c-axis tunnel junctions between the conventional s-wave superconductor Pb and both twinned and untwinned YBCO. A c-axis junction between an s-wave and a pure d-wave superconductor is simultaneously a 0- and π-junction, corresponding to the s-wave order parameter coupling to the positive and negative lobes of the d-wave order parameter, respectively. The resulting interference between the positive and negative tunneling currents should lead to their overall cancellation. The orthorhombicity of YBCO, however, distends either the positive or negative lobes, giving rise to an additional small real s-wave component in the bulk [85]. This could certainly couple to the isotropic s-wave order parameter of the lead, yielding the observed tunneling currents between Pb and untwinned YBCO. In twinned YBCO, however, the small real s-wave component should average to zero assuming an equal proportion of either twin domain in the sample, since the s-wave component changes sign across a π-junction twin boundary (Fig. 4.1).

Three explanations for the experimentally-observed tunneling currents between Pb and twinned YBCO are plausible. First, one twin domain may be more abundant than another; though counter-intuitive, this possibility may have been recently confirmed [209, 194, 195]. Second, YBCO may not be a d-wave superconductor. In spite of the mounting evidence to the contrary, the experiments by Dynes *et al.* are often cited as evidence for s-wave superconductivity in these materials [81, 94, 95]. A third explanation is that a time-reversal symmetry breaking imaginary s-wave component, induced in the vicinity of twin boundaries, is coupling to the lead [130]. If twin boundaries are indeed weak superconducting links, which appears to be the case (as discussed in Section 4.1.1), their 45° orientation with respect to the d-wave order parameter certainly makes them maximally pair-breaking [204].

To date, there is no direct confirmation of $\mathcal{T}$-violation near twin boundaries. Recent SQUID measurements of vortices trapped by twin boundaries in YBCO found no evidence of fractional flux [181]. Yet in the absence of additional inhomogeneities intersecting the twin boundaries, such as impurities or grain boundaries, it is not clear where localized fractional vortices would be nucleated. Rather, the time-reversal breaking would be manifested as constant spontaneous supercurrents flowing parallel to, and in opposite directions on either side of, the twin boundary. These supercurrents are equivalent to the diamagnetic currents screening a continuous physical

c-oriented magnetic field penetrating the length of the twin boundary. The field decays perpendicular to the twin boundary over a length scale of the London penetration depth $\lambda_L \approx 1500$ Å. Since the size of the SQUID pickup loop is approximately 8 μm^2 [181], however, the effective field may average to a value far smaller than can be resolved using this technique. Thus, the possibility of $\mathcal{T}$-violation near twin boundaries has not been ruled out by these experiments.[1]

4.1.4 Outline

Twin boundaries in YBCO are investigated numerically using the extended Hubbard model employed in the previous chapter. In Section 4.2, the Bogoliubov-de Gennes equations are derived for a d-wave superconductor in the presence of twin boundaries and an external electric potential. This formalism is equivalent to the Gor'kov description, but is more conducive to numerical analysis. The possibility of a low-temperature time-reversal breaking phase in the absence of an external field is explored in Section 4.3, with emphasis on the temperature and density-dependence of subdominant imaginary components. The results are compared with the GL predictions, outlined in Section 2.4. The free energy is considered in Section 4.4 in order to verify whether $\mathcal{T}$-violation is favoured for these systems. In Section 4.5, quasiparticle localization and spontaneous currents near twin boundaries are studied. The results are compared with the GL predictions and with recent tunneling experiments. The results are summarized in Section 4.6.

4.2 Derivation of the BdG Equations

The Hamiltonian for the extended Hubbard model is (see Chapter 3):

$$\mathcal{H} = -\sum_{\langle ij\rangle\sigma} t_{ij} c^{\dagger}_{i\sigma} c_{j\sigma} - \mu \sum_{i\sigma} n_{i\sigma} - \sum_{i\sigma} \mu^{I}_{i} n_{i\sigma} - V_0 \sum_{i} n_{i\uparrow} n_{i\downarrow} - \frac{V_1}{2} \sum_{\langle ij\rangle\sigma\sigma'} n_{i\sigma} n_{j\sigma'}, \tag{4.4}$$

where the sums are over spin and nearest-neighbours on the square lattice, t_{ij} is a direction-dependent hopping parameter used to model orthorhombicity, μ is the

---

[1] The observation of a Wohlleben effect [96] on clean but twinned samples would confirm the presence of spontaneous currents near twin boundaries.

chemical potential, μ^I is a site-dependent impurity potential representing the depletion of the carrier density at the twin boundary, and V_0 and V_1 are on-site and nearest-neighbour interactions, respectively ($V > 0$ denotes attraction). Choosing the unit cell as shown in Fig. 4.3, the Fermi destruction operator may be re-expressed as:

$$c_{i\sigma} \equiv c_\sigma(\mathbf{r})e^{i\mathbf{p}\cdot\mathbf{r}/2}, \tag{4.5}$$

where $\mathbf{r} \equiv r_\alpha \hat{r} + R_\alpha \hat{R}$ with $\hat{r} \equiv -\hat{x} + \hat{y}$ perpendicular and $\hat{R} \equiv \hat{x} + \hat{y}$ parallel to the twin direction (the lattice spacing has been set to unity for simplicity). The index α labels the two basis points in the unit cell, and r_α takes integer values from 1 to unit cell length N, while R_α takes values from 1 to the total number of unit cells W in the system. The momentum $\mathbf{p} \equiv p\hat{r} + q\hat{R}$ is included in order to allow for supercurrents resulting from an external potential, discussed in Section 5.3. Imposing periodic boundary conditions on the system

$$\begin{aligned} c_\sigma(\mathbf{r})e^{i\mathbf{p}\cdot\mathbf{r}/2} &= c_\sigma(\mathbf{r} + N\hat{r} + W\hat{R})e^{i\mathbf{p}\cdot\mathbf{r}/2}e^{i(pN+qW)/2} \\ &= c_\sigma(\mathbf{r})e^{i\mathbf{p}\cdot\mathbf{r}/2}e^{i(pN+qW)/2} \end{aligned} \tag{4.6}$$

constrains the components of the momenta: $p = 4\pi m/N$ and $q = 4\pi m'/W$, with m (m') integers between 0 and $N-1$ ($W-1$).

Except for the momentum q, the Hamiltonian is translationally invariant in the [110]-direction. It is convenient to exploit this symmetry by labeling states in the $\hat{R}$-direction by an index k:

$$c_\sigma(\mathbf{r})e^{i\mathbf{p}\cdot\mathbf{r}/2} = \sum_k e^{ikR}c_{k\sigma}(r)e^{i\mathbf{p}\cdot\mathbf{r}/2}, \tag{4.7}$$

where periodic boundary conditions require $k = 2\pi n/W$, where n is an integer between 0 and $W-1$. Inserting (4.5) into (4.4) yields the effective Hamiltonian, bilinear in Fermi operators:

$$\begin{aligned} \mathcal{H}_{\text{eff}} &= -\sum_{r_\alpha k\sigma\vec{\delta}} t_{\vec{\delta}} c^\dagger_{k\sigma}(r_\alpha + \vec{\delta})c_{k\sigma}(r_\alpha)e^{-i\mathbf{p}\cdot\vec{\delta}/2} - \sum_{r_\alpha k\sigma}\left(\mu + \mu^I(r_\alpha)\right)c^\dagger_{k\sigma}(r_\alpha)c_{k\sigma}(r_\alpha) \\ &+ \sum_{r_\alpha k}\left\{\Delta^*_\circ(r_\alpha)c_{k\downarrow}(r_\alpha)c_{-k-q\uparrow}(r_\alpha) + H.c.\right\} \end{aligned}$$

$$+ \quad \frac{1}{2}\sum_{r_\alpha k \vec{\delta}} \left\{\Delta^*_{\vec{\delta}}(r_\alpha)\left[c_{k\downarrow}(r_\alpha)c_{-k-q\uparrow}(r_\alpha+\vec{\delta}) - c_{k\uparrow}(r_\alpha)c_{-k-q\downarrow}(r_\alpha+\vec{\delta})\right] + H.c.\right\}, \tag{4.8}$$

where the (spin-singlet) gap functions are defined by

$$\begin{aligned} \Delta_0(\mathbf{r}) &\equiv V_0\langle c_\uparrow(\mathbf{r})c_\downarrow(\mathbf{r})\rangle \\ \Rightarrow \Delta_0(r_\alpha) &= V_0\sum_k\langle c_{k\uparrow}(r_\alpha)c_{-k-q\downarrow}(r_\alpha)\rangle \\ &= -V_0\sum_k\langle c_{k\downarrow}(r_\alpha)c_{-k-q\uparrow}(r_\alpha)\rangle; \end{aligned} \tag{4.9}$$

$$\begin{aligned} \Delta_\delta(\mathbf{r}) &\equiv V_1\langle c_\uparrow(\mathbf{r}+\vec{\delta})c_\downarrow(\mathbf{r})\rangle \\ \Rightarrow \Delta_\delta(r_\alpha) &= V_1\sum_k\langle c_{k\uparrow}(r_\alpha+\vec{\delta})c_{-k-q\downarrow}(r_\alpha)\rangle \\ &= -V_1\sum_k\langle c_{k\downarrow}(r_\alpha+\hat{\delta})c_{-k-q\uparrow}(r_\alpha)\rangle, \end{aligned} \tag{4.10}$$

where $\langle\ldots\rangle$ denotes a vacuum expectation value, and the nearest-neighbour links

$$\begin{aligned} \vec{\delta} &= \{\hat{x}\,;\ -\hat{x}\,;\ \hat{y}\,;\ -\hat{y}\} \\ &= \left\{\hat{0}\,;\ \hat{r}-\hat{R}\,;\ \hat{r}\,;\ -\hat{R}\right\} \end{aligned} \tag{4.11}$$

connect sites with different basis indices.

It is interesting to note that the momentum $\mathbf{p}$ appears explicitly only in the kinetic term of (4.8); consequently, the effect of external currents is to modify the normal-state dispersion from the usual tight-binding case (see Section 3.2):

$$\epsilon(\mathbf{k}) = -2t_x\cos(k_x + p_x/2) - 2t_y\cos(k_y + p_y/2). \tag{4.12}$$

In the continuum limit, one obtains to lowest-order in $\mathbf{k}$:

$$\epsilon(\mathbf{k}) = \epsilon^\circ(\mathbf{k}) + v(\mathbf{k})\cdot\mathbf{p}, \tag{4.13}$$

where $\epsilon^\circ(\mathbf{k}) = t_x(-2 + k_x^2) + t_y(-2 + k_y^2)$ is the (anisotropic) conventional normal-state dispersion. Eq. (4.13) is the usual starting-point for analytical investigations of superconductors in the presence of supercurrents [210].

The Hamiltonian given by (4.8) may be diagonalized by employing the canonical Bogoliubov-Valatin transformation [211, 212]

$$
\begin{aligned}
c_{k\uparrow}(r_\alpha,t) &\equiv \sum_n \left[\gamma_{n\uparrow} u_{n,k}(r_\alpha) e^{-i\varepsilon_n t} - \gamma^\dagger_{n\downarrow} v^*_{n,k}(r_\alpha) e^{i\varepsilon_n t}\right] && (4.14)\\
c_{k\downarrow}(r_\alpha,t) &\equiv \sum_n \left[\gamma_{n\downarrow} u_{n,k}(r_\alpha) e^{-i\varepsilon_n t} + \gamma^\dagger_{n\uparrow} v^*_{n,k}(r_\alpha) e^{i\varepsilon_n t}\right], && (4.15)
\end{aligned}
$$

of the electron operators, where $u_{n,k}$ and $v_{n,k}$ are the hole-like and particle-like quasiparticle amplitudes respectively, and the fermionic quasiparticle creation ($\gamma^\dagger_n$) and annihilation (γ_n) operators satisfy

$$
\begin{aligned}
\langle \gamma^\dagger_m \gamma_n \rangle &= f_n \delta_{mn}, && (4.16)\\
\langle \gamma_n \gamma^\dagger_m \rangle &= (1 - f_n)\delta_{mn}, && (4.17)
\end{aligned}
$$

such that

$$f_n = \frac{1}{\exp\{\beta\varepsilon_n\} + 1} \tag{4.18}$$

is the Fermi-Dirac distribution for the quasiparticle excitations, and $\beta = 1/k_B T$. The antisymmetry of the original electron operators

$$\left\{c_{k\sigma}\,,\; c^\dagger_{k'\sigma'}\right\} = \delta_{kk'}\delta_{\sigma\sigma'} \tag{4.19}$$

yields the normalization condition

$$\sum_n \left[|u_{n,k}|^2 + |v_{n,k}|^2\right] = 1 \tag{4.20}$$

for each k.

The quasiparticle amplitudes may be found by solving the equations of motion (compare Eq. (3.15)):

$$i\frac{\partial c_{k\sigma}(r_\alpha,t)}{\partial t} = \left[c_{k\sigma}(r_\alpha,t), \mathcal{H}_{\text{eff}}\right]\Big|_{t=0}. \tag{4.21}$$

After some straightforward algebra, one obtains the Bogoliubov-de Gennes (BdG) equations [211, 73]:

$$\begin{pmatrix} \hat{\xi} & \hat{\Delta} \\ \hat{\Delta}^* & -\hat{\xi}' \end{pmatrix} \begin{pmatrix} u_{n,k}(r_\alpha) \\ v_{n,-k-q}(r_\alpha) \end{pmatrix} = \varepsilon_n \begin{pmatrix} u_{n,k}(r_\alpha) \\ v_{n,-k-q}(r_\alpha) \end{pmatrix}, \tag{4.22}$$

such that

$$\begin{aligned}
\hat{\xi} u_{n,k}(r_\alpha) &= -\sum_{\vec{\delta}} t_\delta e^{-i\mathbf{p}\cdot\vec{\delta}/2} u_{n,k}(r_\alpha + \vec{\delta}) - \left[\mu + \mu^I(r_\alpha)\right] u_{n,k}(r_\alpha), \\
\hat{\xi}' v_{n,-k-q}(r_\alpha) &= -\sum_{\vec{\delta}} t_\delta e^{+i\mathbf{p}\cdot\vec{\delta}/2} v_{n,-k-q}(r_\alpha + \vec{\delta}) - \left[\mu + \mu^I(r_\alpha)\right] v_{n,-k-q}(r_\alpha), \\
\hat{\Delta} u_{n,k}(r_\alpha) &= \Delta_0(r_\alpha) u_{n,k}(r_\alpha) + \sum_{\vec{\delta}} \Delta_\delta(r_\alpha) u_{n,k}(r_\alpha + \vec{\delta}).
\end{aligned} \tag{4.23}$$

The equations (4.22) are subject to the self-consistency requirements

$$\Delta_0(r_\alpha) = V_0 \sum_{nk} u_{n,k}(r_\alpha) v^*_{n,-k-q}(r_\alpha) \tanh\left(\frac{\beta\varepsilon_n}{2}\right), \tag{4.24}$$

$$\Delta_\delta(r_\alpha) = \frac{V_1}{2} \sum_{nk\vec{\delta}} \left[u_{n,k}(r_\alpha + \vec{\delta}) v^*_{n,-k-q}(r_\alpha) + u_{n,k}(r_\alpha) v^*_{n,-k-q}(r_\alpha + \vec{\delta})\right] \tanh\left(\frac{\beta\varepsilon_n}{2}\right), \tag{4.25}$$

where the sum is over positive energy eigenvalues ε_n only. These equations may be obtained immediately by substituting Eqs. (4.14) and (4.15) into (4.9) and (4.10). It is instructive to note that the BdG equations are formally quite similar to the matrix version of the Gor'kov equations (3.20) derived in Section 3.2. Indeed, the GL equations could have been derived starting from (4.22) and (4.25), if they were modified to include an external magnetic field [73].

It is important to stress that the BdG equations are explicitly translationally invariant along $\hat{R}$, even in the presence of external currents. The quasiparticle amplitudes and gap functions transform as follows:

$$\begin{aligned}
u_{n,k}(r_\alpha \hat{r} + \hat{R}) &= e^{ik} u_{n,k}(r_\alpha \hat{r}), \\
v_{n,-k-q}(r_\alpha \hat{r} + \hat{R}) &= e^{i(k+q)} v_{n,-k-q}(r_\alpha \hat{r}), \\
\Delta(r_\alpha \hat{r} + \hat{R}) &= e^{-iq} \Delta(r_\alpha \hat{r}).
\end{aligned} \tag{4.26}$$

Hence, the two coupled BdG equations transform as:

$$\hat{\xi} u_{n,k}(r_\alpha \hat{r} + \hat{R}) + \hat{\Delta} v_{n,-k-q}(r_\alpha \hat{r} + \hat{R}) = \varepsilon_n u_{n,k}(r_\alpha \hat{r} + \hat{R})$$

$$\Rightarrow \hat{\xi} e^{ik} u_{n,k}(r_\alpha \hat{r}) + e^{-iq} \hat{\Delta} e^{i(k+q)} v_{n,-k-q}(r_\alpha \hat{r}) \;=\; \varepsilon_n e^{ik} u_{n,k}(r_\alpha \hat{r}), \qquad (4.27)$$

$$\begin{aligned} \hat{\Delta}^* u_{n,k}(r_\alpha \hat{r} + \hat{R}) - \hat{\xi}' v_{n,-k-q}(r_\alpha \hat{r} + \hat{R}) &= \varepsilon_n v_{n,-k-q}(r_\alpha \hat{r} + \hat{R}) \\ \Rightarrow e^{iq} \hat{\Delta}^* e^{ik} u_{n,k}(r_\alpha \hat{r}) - \hat{\xi}' e^{i(k+q)} v_{n,-k-q}(r_\alpha \hat{r}) &= \varepsilon_n e^{i(k+q)} v_{n,-k-q}(r_\alpha \hat{r}). \qquad (4.28) \end{aligned}$$

Since the exponentials cancel in both Eqs. (4.27) and (4.28), the BdG matrix is indeed translationally invariant along $\hat{R}$.

The total current in the superconductor is obtained using Eqs. (3.50) and (3.51). The kinetic energy contribution to the current is

$$\begin{aligned} \mathbf{j}(r_\alpha) &= i \sum_{k\sigma\vec{\delta}} t_{\vec{\delta}} e^{-i\mathbf{p}\cdot\vec{\delta}/2} \vec{\delta} \langle c^\dagger_{k\sigma}(r_\alpha + \vec{\delta}) c_{k\sigma}(r_\alpha) \rangle \\ &= 2i \sum_{nk\vec{\delta}} t_{\vec{\delta}} e^{-i\mathbf{p}\cdot\vec{\delta}/2} \vec{\delta} \Big[u^*_{n,k}(r_\alpha + \vec{\delta}) u_{n,k}(r_\alpha) f_n \\ &\qquad + v^*_{n,-k-q}(r_\alpha) v_{n,-k-q}(r_\alpha + \vec{\delta})(1 - f_n) \Big]. \qquad (4.29) \end{aligned}$$

Note that the total current is translationally invariant along $\hat{R}$, even in the presence of a momentum q.

The orthorhombicity of YBCO is modeled by an anisotropy in the hopping parameters, which reflects the increased electronic mobility associated with the chains [213]. Throughout the present work $t_y/t_x = 1.5$ is used, which approximates the observed a-b anisotropy in the magnetic penetration depth [72], and $V_0 = -V_1 = -3t_x$.[2] The chemical potential μ is chosen to ensure bulk d-wave superconductivity. Twin boundaries of up to $4|\hat{r}|$ width (corresponding to approximately 22 Å) are investigated, with $t_y = t_x$ and $\mu^I \leq 0$ within the twin. The translational invariance of physical observables in the $\hat{R}$ direction (parallel to the twin boundary) allows for much larger system sizes than are usually accessible within BdG theory. By exploiting this symmetry, the conventional $2NW \times 2NW$ BdG matrix becomes block diagonal, and one rather solves W different $2N \times 2N$ matrices, greatly reducing the *cpu*-time required. The largest system studied is $N = 100|\hat{r}|$ in length with $W = 400$ k-states,

---

[2] Alternatively, one might have chosen an isotropic hopping integral t but anisotropic nearest-neighbour coupling. I have verified that this choice reproduces qualitatively all of the results presented below, though the ab-anisotropy in many normal-state properties of untwinned YBCO certainly makes this a poorer choice.

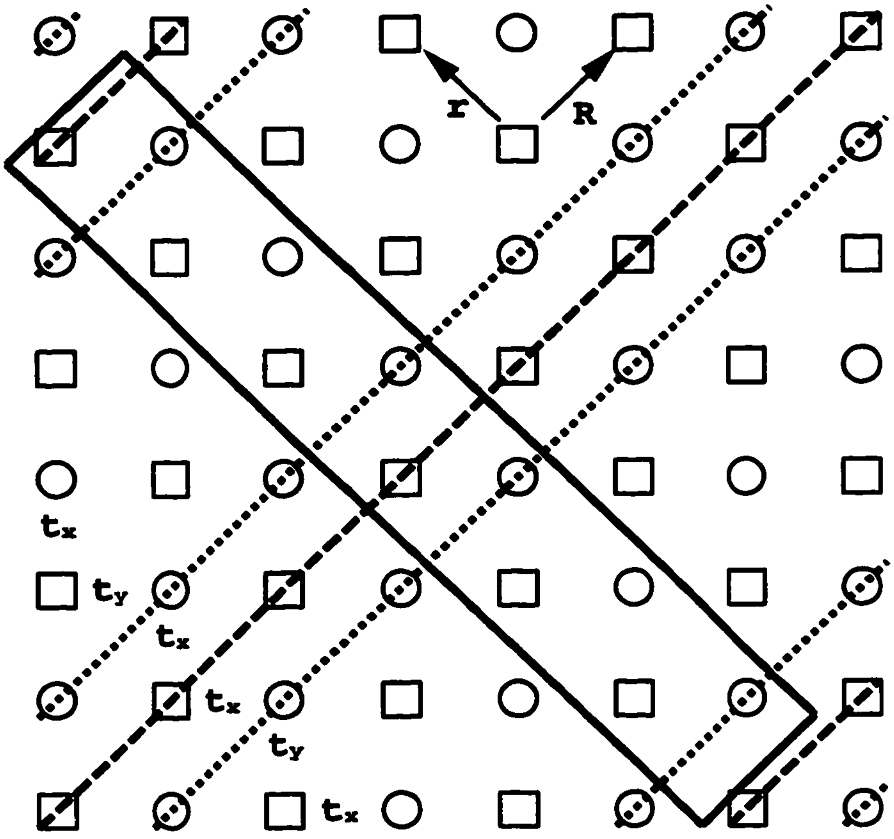

Figure 4.3: The unit cell of the finite-size system for the BdG calculations is shown as a solid line superimposed on a square lattice. Long and short dashed lines represent twin boundaries of width 0 and $|\hat{r}|$, respectively. Basis points are labeled by circles and squares.

or $100 \times 400 \times 2 = 80\,000$ sites (for the tunneling conductance Figs. 4.11 and 4.12), and the smallest system has $N = 50$ and $W = 30$. Periodic boundary conditions are assumed throughout.

4.3 Time-reversal Breaking

In the absence of external currents, physical observables are translationally invariant in the $\hat{R}$ direction parallel to the twin boundary. The system sizes then can be made sufficiently large to ensure that the gap functions approach their uniform (bulk) values at the center of a twin domain (i.e. midway between the twin edges which define the boundaries of the region). With the hopping anisotropy $t_y/t_x = 1.5$, the extended and on-site s-wave components have bulk values that are approximately 10% of Δ_d, consistent with experimental evidence for YBCO [131].

As shown in Fig. 4.4, at a twin boundary of zero width ($W_T = 0$) and $\mu^I = 0$, the dominant d-wave component of the order parameter is virtually unaffected. The extended and on-site s-wave components go from their near-bulk values to zero over a single lattice spacing r, and reverse their sign relative to Δ_d on either side of the boundary. As the impurity strength is increased at low temperatures, however, the d-wave and s-wave components become increasingly perturbed from their bulk values over the coherence length $\xi_{d+s}(T)$, where $\xi_{d+s}(0) \approx |\hat{r}|$ in the present work. When the magnitude of the d-wave component in the twin boundary is suppressed to approximately half its bulk value, an additional imaginary s-wave component may be nucleated near the twin edge, breaking time-reversal symmetry. Most important for the c-axis results of Dynes [208] is that, unlike the real s-wave components, these imaginary components have the same sign in adjacent twin domains, and could therefore remain finite even in a heavily-twinned sample. No evidence for a phase transition to a bulk $\mathcal{T}$-violating state in a uniform system has been found at any temperature in the present work.

For clarity, the real and imaginary parts of the various components of the order parameter are shown in Fig. 4.5 for a larger system with $N = 100$, $\mu^I = -10t_x$, $\mu = -t_x$, $T = 0$, and boundary width $W_T = 4|\hat{r}|$. While all the components go to zero

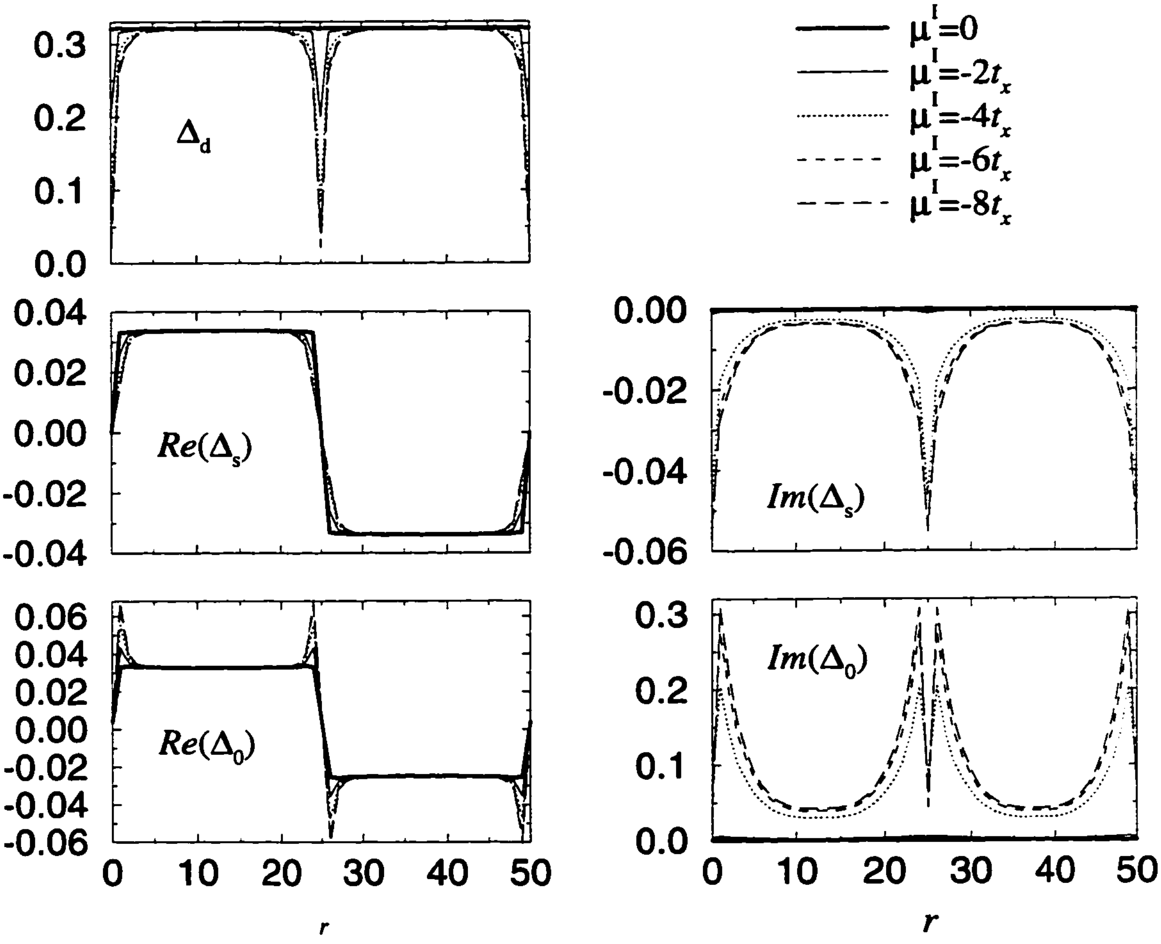

Figure 4.4: The real and imaginary components of the d-wave, extended and on-site s-wave gap functions are shown as a function of impurity potential μ^I and distance r perpendicular to the twin boundary. Results are obtained using $\mu = -t_x$, $T = 0$, and twin width $W_T = 0$. Twin boundaries are centered at positions $r = 0$ (which is equivalent to $r = 50$ by periodic boundary conditions) and $r = 25$ in units of $|\hat{r}|$.

rapidly within the twin boundary because of the carrier depletion, both the real and imaginary parts of the s-wave gap functions are enhanced near the twin edge. In the immediate vicinity of the twin boundary, the real s-wave components are perturbed from their bulk values over a short distance comparable to $\xi_{d+s}(0)$. This reflects the local nucleation of additional s-wave components through spatial variations of the dominant d-wave component, through the mixed-gradient terms in the GL free energy (2.17). The presence of finite complex gap functions in the bulk, however, implies that the imaginary components vary over a different characteristic distance $\xi_{is}(0) \gg \xi_{d+s}(0)$. This longer length scale is consistent with the GL predictions [130] discussed in Section 2.4.

It is also evident from Figs. 4.4 and 4.5 that when the d-wave component is sufficiently perturbed at the twin boundary, the size of $Im(\Delta_0)$ may become comparable to the bulk value of Δ_d. Indeed, the magnitude of this imaginary component is approximately equal to the value a real isotropic component would have been, had the on-site interaction been attractive rather than repulsive. In general, it would be energetically unfavourable for such a large subdominant pairing channel to be induced solely through spatial variations of the d-wave component. Indeed, previous BdG studies of inhomogeneous d-wave superconductors indicate an empirical upper bound of approximately 30% for the magnitude of a subdominant s-wave component relative to Δ_d [214, 129]. Similar results are obtained in Section 3.4. It is more likely that, if the dominant channel is sufficiently perturbed from its bulk value, the conditions may be conducive towards a second phase transition to a $\mathcal{T}$-violating state at a lower temperature.

In order to illustrate that a second phase transition may indeed occur in these systems, the real and imaginary components of the order parameter are shown in Fig. 4.6 as a function of temperature and $\hat{r}$ for a large fixed carrier depletion $\mu^I = -10t_x$. While the real parts of the order parameter exhibit a relatively weak temperature dependence, the imaginary s-wave components grow rapidly below $T^* \approx 0.5T_c$. It appears, therefore, that the imaginary components are decoupled from the other pairing channels because their magnitudes are governed solely by their couplings $|V_{0,1}|$ and the temperature relative to T^*. It should be underlined, however, that the d-wave channel

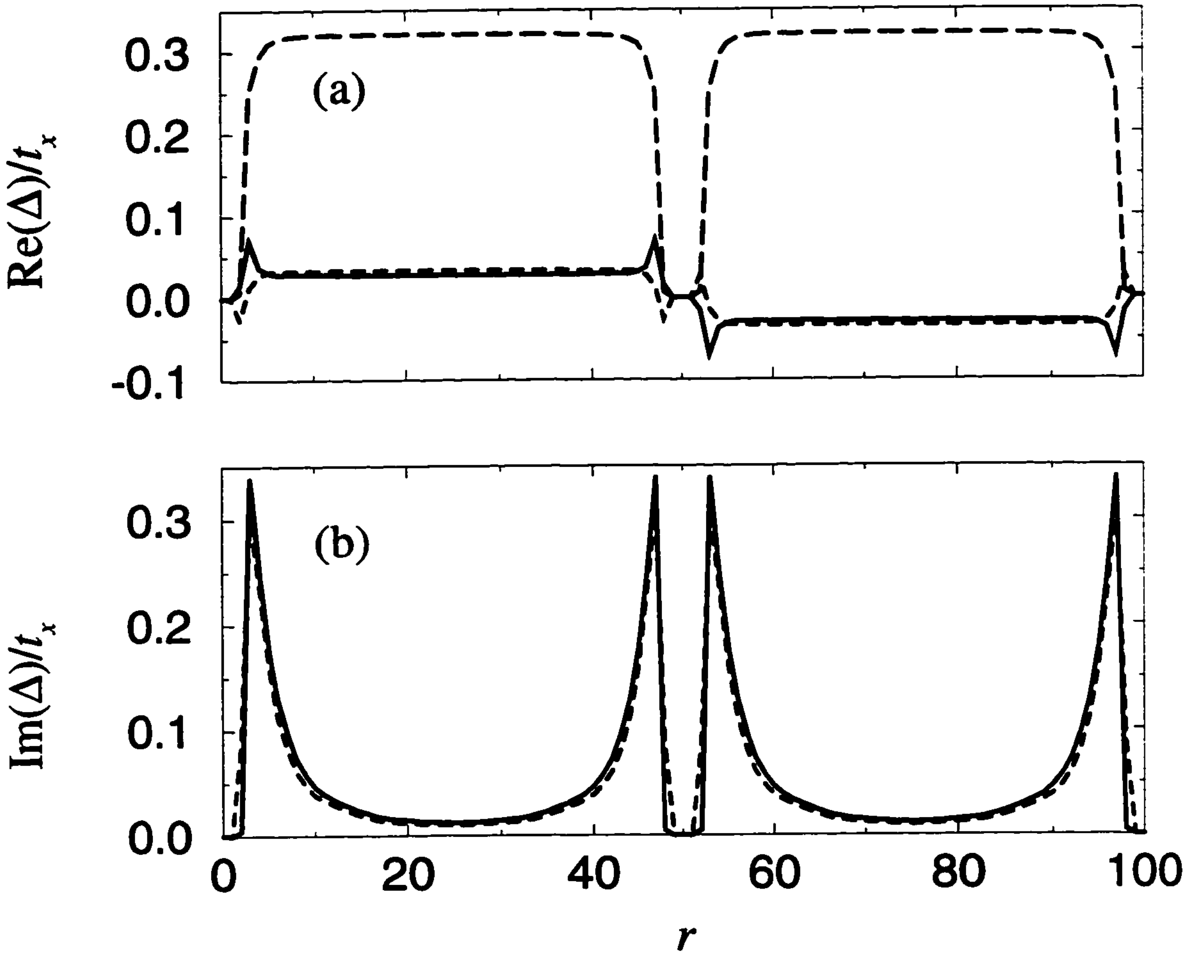

Figure 4.5: The (a) real and (b) imaginary components of the d-wave, on-site, and extended s-wave gap functions (corresponding to long-dashed, short-dashed, and solid lines respectively) are shown as a function of distance r perpendicular to the twin boundary. In (b), $\mathrm{Im}(\Delta_s)$ is multiplied by a factor of -10 to facilitate comparison with $\mathrm{Im}(\Delta_0)$. Results are obtained using $\mu = -t_x$, $\mu^I = -10t_x$, $T = 0$, and twin width $4|\hat{r}|$. Twin boundaries are centered at positions $r = 0$ (which is equivalent to $r = 100$ by periodic boundary conditions) and $r = 50$ in units of $|\hat{r}|$.

must be strongly suppressed locally in order to stabilize the imaginary components.

As shown in Fig. 4.7, the maximum size of the imaginary s-wave component that is nucleated near the twin boundary is extremely sensitive to the temperature, impurity strength, and the width of the twin boundary. At zero temperature, Fig. 4.7(a), a $\mathcal{T}$-violating state first appears for $\mu^I \approx -2.7t_x$ at all electron densities for an impurity line (when $W_T = 0$). As the impurity strength increases, the perturbation of the d-wave component, and the maximum values of the imaginary s-wave components, begin to saturate. For all twin boundary widths, the imaginary components are found to vary as $\sqrt{1 - \mu_c^I/\mu^I}$ near the critical impurity strength μ_c^I. For $W_T > 0$, however, a lower $|\mu_c^I|$ can give rise to $\mathcal{T}$-violation at zero temperature. Time-reversal breaking is favoured near wider twin boundaries since the d-wave component is already suppressed by approximately 20% in a locally tetragonal region (with $t_x = t_y$) even for $\mu^I = 0$.[3] Increasing W_T beyond approximately $3|\hat{r}|$ has no further effect. This result, valid for all electron densities, is also consistent with the GL prediction [130] that local tetragonal symmetry could favor a time-reversal breaking state at low temperature (see Section 2.4).

The growth of all the s-wave components with decreasing chemical potential reflects the impending instability of the system against bulk dominant s-wave superconductivity at slightly lower electron densities, as has been discussed in Section 3.3. As the temperature is increased at finite μ^I, the imaginary component decreases to zero with the mean-field behaviour $\sqrt{1 - T/T^*}$ associated with a second-order phase transition. The transition temperature T^* is strongly density-dependent, scaling roughly with Δ_d. The same T^* is obtained for wider twin boundaries at a given density, though the magnitudes of the imaginary s-wave components increases with increasing W_T.

---

[3] In fact, the opposite is the case very near $\mu = -t_x$, where there is a van Hove singularity in the orthorhombic density of states. As a result, the d-wave gap is smaller and the transition temperature T_c is larger than it would be for a locally tetragonal region at the same chemical potential (recall from Fig. 3.1 that the van Hove singularity for $t_x = t_y$ is at $\mu = 0$; with an orthorhombic distortion this is split). It should be pointed out, however, that the results depicted in Fig. 4.7a are for $\mu = -t_x$, and are qualitatively identical to those obtained at all other fillings.

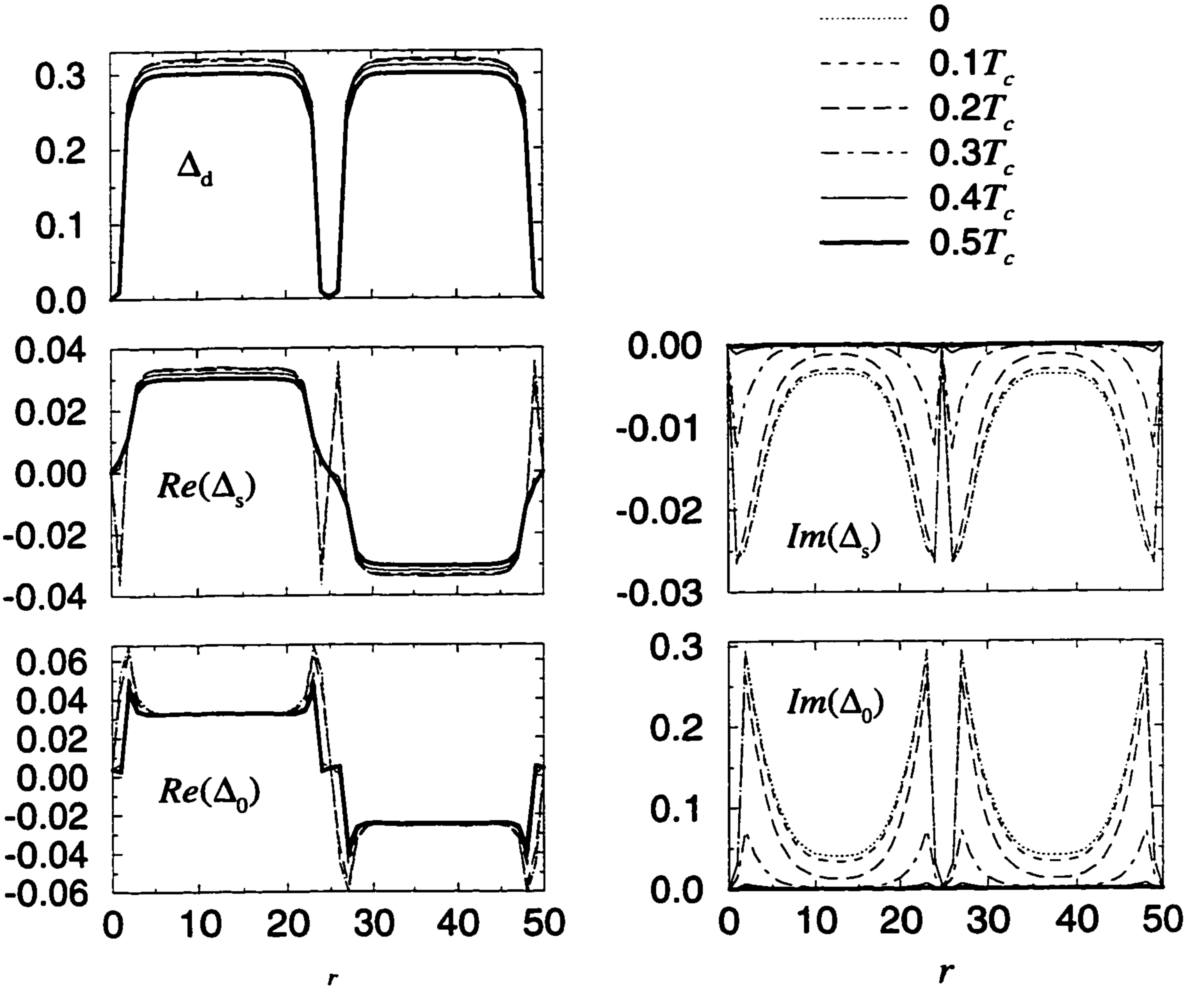

Figure 4.6: The real and imaginary components of the d-wave, extended and on-site s-wave gap functions are shown as a function of reduced temperature T/T_c and distance r perpendicular to the twin boundary. Results are obtained using $\mu = -t_x$, $\mu^I = -10t_x$, and twin width $4|\hat{r}|$. Twin boundaries are centered at positions $r = 0$ (which is equivalent to $r = 50$ by periodic boundary conditions) and $r = 25$ in units of $|\hat{r}|$.

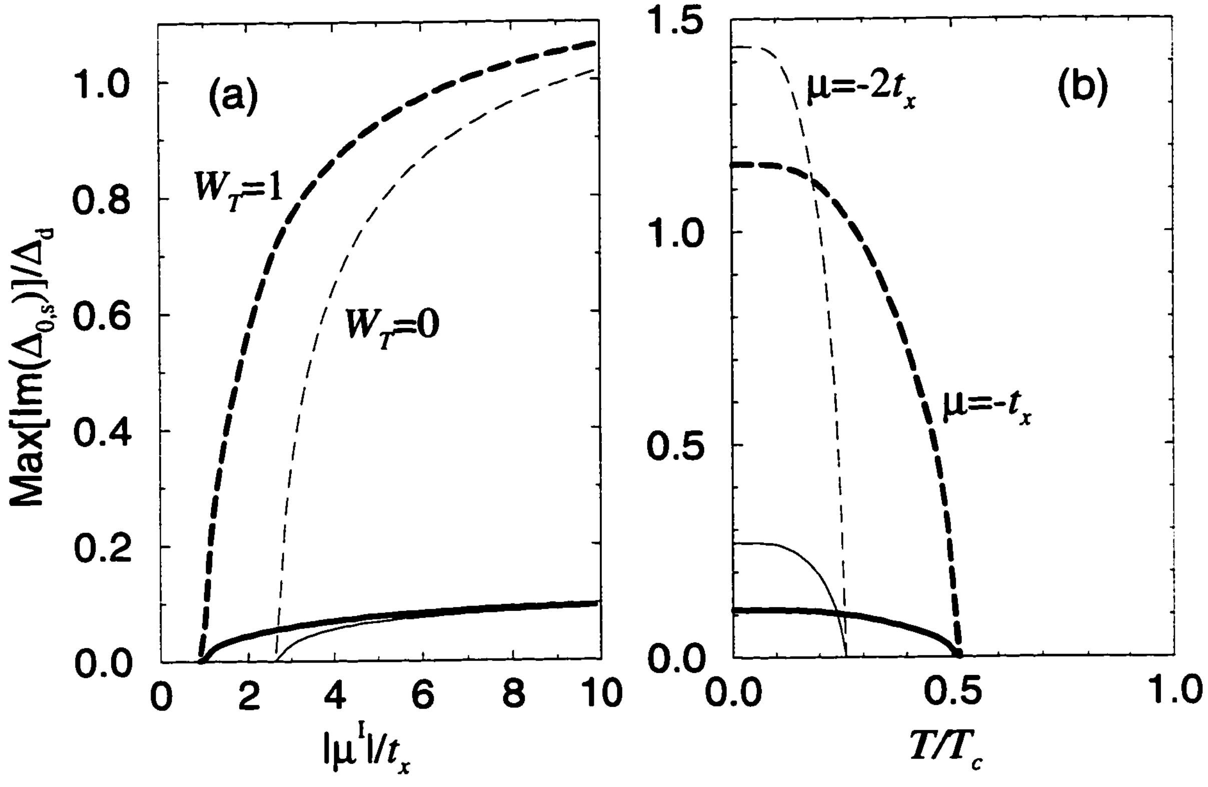

Figure 4.7: The maximum value of the imaginary on-site (dashed lines) and extended s-wave (solid lines) components relative to the bulk value of the d-wave order parameter are shown as a function of (a) $|\mu^I|$ (note $\mu^I \le 0$) and W_T at zero temperature and $\mu = -t_x$, and (b) T/T_c and μ. In (a) thin and thick lines correspond to twin boundary widths $W_T/|\hat{r}| = 0$ and 1, respectively. In (b), thin and thick lines denote results for $\mu = -2t_x$ and $\mu = -t_x$, and $\mu^I = -100t_x$, and $W_T = 0$ are chosen.

4.4 Free Energy

It is important to determine whether a time-reversal breaking phase is indeed favoured by the system below a finite temperature T^*. In particular, the $\mathcal{T}$-violating state should have a lower total free energy than that of the $\mathcal{T}$-preserving state, obtained by forcing the imaginary components to remain zero. The relevant (Gibbs) free energy is given by:

$$F(T) \equiv \langle \mathcal{H} \rangle - TS, \tag{4.30}$$

where the first term is the ground-state expectation value of the Hamiltonian (4.4), and S is the usual entropy associated with the fermionic excitations [215]:

$$S = -2 \sum_n \Big[f_n \ln f_n + (1 - f_n) \ln (1 - f_n) \Big]. \tag{4.31}$$

The experimental signature of a second phase transition at a lower temperature T^* would be a discontinuity in the specific heat [64]:

$$C_V(T) \equiv T \frac{\partial S}{\partial T} \equiv -T \frac{\partial^2 F(T)}{\partial T^2}. \tag{4.32}$$

The quartic terms of the Hamiltonian expectation value appearing in (4.30) may be simplified using a variant of Wick's theorem [155]:

$$\begin{aligned} \langle c^\dagger_\upsilon(\mathbf{r}+\vec{\delta}) c_\sigma(\mathbf{r}+\vec{\delta}) c^\dagger_{\sigma'}(\mathbf{r}) c_{\sigma'}(\mathbf{r}) \rangle &= \langle c^\dagger_\sigma(\mathbf{r}+\vec{\delta}) c_\sigma(\mathbf{r}+\vec{\delta}) \rangle \langle c^\dagger_{\sigma'}(\mathbf{r}) c_{\sigma'}(\mathbf{r}) \rangle \\ &- \langle c^\dagger_\sigma(\mathbf{r}+\vec{\delta}) c^\dagger_{\sigma'}(\mathbf{r}) \rangle \langle c_\sigma(\mathbf{r}+\vec{\delta}) c_{\sigma'}(\mathbf{r}) \rangle, \end{aligned} \tag{4.33}$$

This linearization and the Bogoliubov transformation (4.14) and (4.15) allow the various expectation values of $\langle \mathcal{H} \rangle$ to be evaluated. After some work, one obtains

$$\begin{aligned} \langle \mathcal{H} \rangle &= -2 \sum_{nk\vec{\delta}r_\alpha} t_{\vec{\delta}} e^{-i\mathbf{p}\cdot\vec{\delta}/2} \Big[u^*_{n,k}(r_\alpha + \vec{\delta}) u_{n,k}(r_\alpha) f_n \\ &\qquad + v^*_{n,-k-q}(r_\alpha) v_{n,-k-q}(r_\alpha + \vec{\delta})(1 - f_n) \Big] \\ &- 2 \sum_{r_\alpha} \left(\mu + \mu^I_{r_\alpha} \right) a(r_\alpha) - V_0 \sum_{r_\alpha} a^2(r_\alpha) - 2V_1 \sum_{r_\alpha \vec{\delta}} a(r_\alpha) b_\delta(r_\alpha) \\ &- \frac{1}{V_0} \sum_{r_\alpha} |\Delta_0(r_\alpha)|^2 - \frac{1}{V_1} \sum_{r_\alpha \vec{\delta}} |\Delta_\delta(r_\alpha)|^2, \end{aligned} \tag{4.34}$$

where

$$a(r_\alpha) \equiv \sum_{nk} \left[|u_{n,k}(r_\alpha)|^2 f_n + |v_{n,-k-q}(r_\alpha)|^2 (1 - f_n) \right]; \tag{4.35}$$

$$b_\delta(r_\alpha) \equiv \sum_{nk} \left[\left|u_{n,k}(r_\alpha + \vec{\delta})\right|^2 f_n + \left|v_{n,-k-q}(r_\alpha + \vec{\delta})\right|^2 (1 - f_n) \right]. \tag{4.36}$$

The factors of 2 appearing in the free energy expression (4.34) arise from the spin-degeneracy.

The temperature-dependence of the free energies for both the normal and superconducting states are shown in Fig. (4.8) for $\mu = -t_x$ and $\mu = -2t_x$. As expected, the superconducting free energy is always lower than the normal-state free energy below T_c, where the latter is obtained by forcing the gap functions to be zero everywhere. Furthermore, the $\mathcal{T}$-violating state is the true ground state of the system at low temperatures because its free energy is noticeably lower than that found for the $\mathcal{T}$-preserving state, obtained by forcing the gap functions to be real at each iteration of the BdG equations. The free energies are found to split at the same temperature T^* shown in Fig. 4.7b. It is interesting to note that the entropy contribution to the free energy of the $\mathcal{T}$-violating state is much lower than that found for the $\mathcal{T}$-preserving state, which is consistent with the existence of a finite gap in the excitation spectrum below T^*.

The energy difference between the superconducting and normal states can be thought of as the Bose-like condensation energy of the Cooper pairs comprising the superconductor (see also Section 2.1). The thermodynamic critical magnetic field H_c therefore may be estimated from the difference in the total free energies [64]:

$$\frac{H_c^2(T)}{8\pi} = F_n(T) - F_s(T). \tag{4.37}$$

Assuming that $t_x \approx 10^{-2}$ eV, obtained using $T_c = 0.51 t_x \approx 60$ K, the critical fields at zero temperature are estimated to be $H_c^c \approx 160$ T and 90 T for $\mu = -t_x$ and $\mu = -2t_x$, respectively. The smaller value of H_c obtained for $\mu = -2t_x$ is due to the diminished preference for bulk d-wave superconductivity at lower electron densities, associated with the proximity to a bulk s-wave instability. Since $H_{c2} = \kappa\sqrt{2}H_c$

with $\kappa \approx 100$, however, the upper critical fields are much larger than the experimental value of $H_{c2}^{c}(0) \approx 120$ T for optimally-doped YBCO [65, 66]. This discrepancy is due to the unphysically large coupling constant $V_1 = 3t_x$ chosen in the present calculations. The coherence lengths can estimated from these upper critical fields using $\xi^2(0) = \phi_0/2\pi H_{c2}(0)$; one obtains $\xi(0) \approx 1.2$ Å and 1.6 Å for $\mu = -t_x$ and $\mu = -2t_x$, respectively. While the values are far too small, the increase in the coherence length with decreasing chemical potential (or hole density) corroborates the Ginzburg-Landau results of Section 3.4.1. It should be noted that the extra condensation energy associated with the appearance of imaginary components would be manifested as a sudden increase in $H_{c2}(T)$ below T^*. This effect is presently experimentally inaccessible, however, due to the large upper critical fields at these low temperatures.

The specific heat for the normal and superconducting states are shown in Fig. 4.9 for both $\mu = -t_x$ and $\mu = -2t_x$. The heat capacities clearly show anomalies at both T_c and the subdominant transition temperature T^* found in Fig. 4.8 and Fig. 4.7b for the same parameters. The unusually large discontinuity in the specific heat at T_c (particularly for $\mu = -t_x$) is consistent with experimental observations [50]. The comparable size of the jump at T^*, and the thermodynamic nature of the specific heat, implies that a significant fraction of the total condensate is taking part in the new $\mathcal{T}$-violating superconducting channel. The apparent bulk character of the phase transition is an artifact because the system size chosen is relatively small. The length scale ξ_{is} for the decay of the imaginary components greatly exceeds the distance between the twin boundaries. In larger systems, where the imaginary component has decayed to essentially zero in the bulk, the specific heat jump would be smaller. Experimentally, the largest specific heat anomaly should be evident in heavily-twinned samples at optimal doping, where the chains are virtually fully-formed and the twinning is most pronounced. No such feature has been experimentally observed. Very recent microwave data obtained for clean but heavily-twinned samples of optimally-doped YBCO, however, suggests that there is a second phase transition at low temperatures [216].

The finite value of the specific heat at low temperatures $T \sim 0$ in the $\mathcal{T}$-preserving

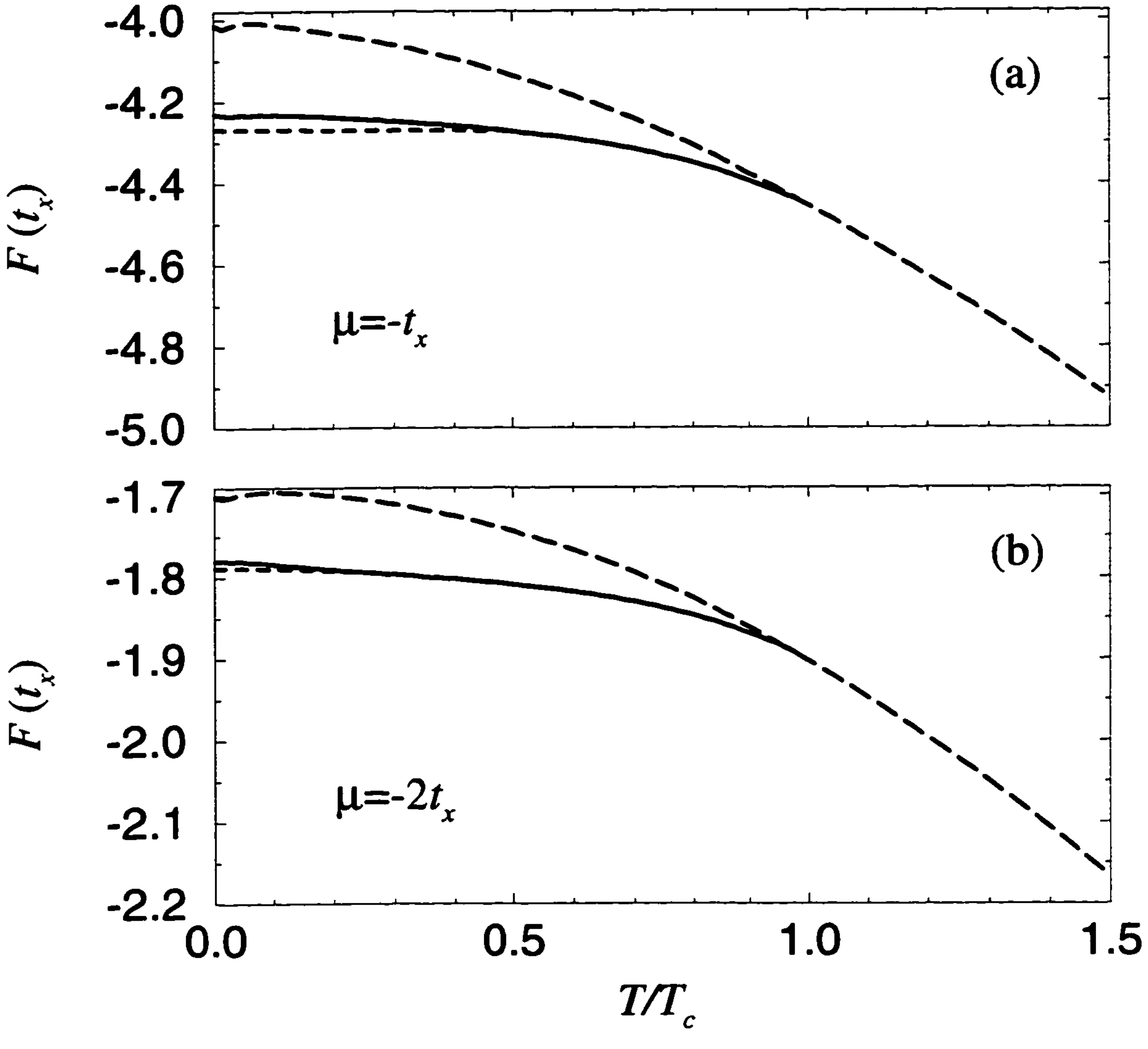

Figure 4.8: The free energies per site for the normal state (dashed line), $\mathcal{T}$-preserving superconductor (solid line), and $\mathcal{T}$-violating superconductor (dotted line) are shown as a function of reduced temperature T/T_c for $\mu = -t_x$ (a) and $\mu = -2t_x$ (b). The twin boundary has zero width $W_T = 0$. The unphysical impurity strength $\mu^I = -100t_x$ on the twin boundary is chosen to yield as large $\mathcal{T}$-violating s-wave components as possible. Results are obtained for a lattice with $30 \times 40 \times 2$ sites. Note that a time-reversal breaking state is favoured below $T^* < T_c$.

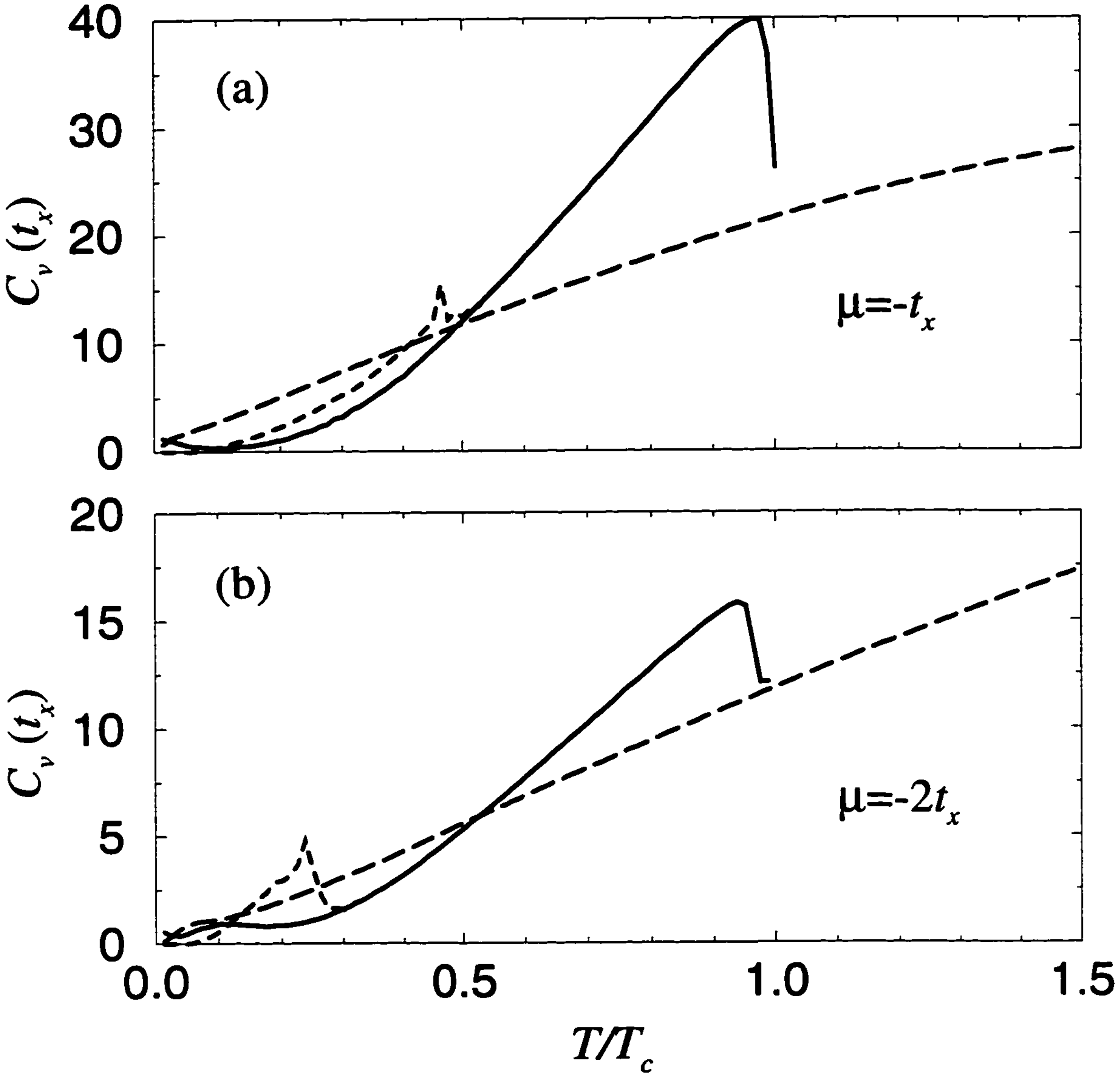

Figure 4.9: The specific heat in eV/K for the normal (dotted) and superconducting (solid) states are shown as a function of reduced temperature T/T_c for $\mu = -t_x$ (a) and $\mu = -2t_x$ (b). The temperature of the lower discontinuity is identical with T^*, as shown in Fig. 4.7.

superconducting state is most likely due to the presence of low-lying quasiparticle states localized in the vicinity of the twin boundary; these states disappear in the $\mathcal{T}$-violating phase where there is a finite (imaginary) gap. No such feature is found in uniform systems. A similar behaviour of the heat capacity has been observed experimentally for optimally-doped YBCO with Zn impurities which act as unitary scatterers [50]. Low-energy quasiparticles, localized near unitary scatterers, are thought to be a generic feature of superconductors such as the cuprates with short coherence lengths [214, 218, 219]. The issue of quasiparticle localization will be discussed further in the next section.

4.5 Localization and Spontaneous Currents

The local suppression of the superconducting order parameter, as occurs in a vortex core or in the vicinity of a pair-breaking inhomogeneity, naturally leads to the formation of bound states. As illustrated in Fig. 4.10(a), these localized states might be naïvely characterized as the quasiparticles occupying the low-energy eigenstates of an order-parameter 'potential well' [217]. While intuitive, this description is overly simplistic. The excitations, as well as the shape of the potential well, must be determined self-consistently through the solution of the full BdG equations (4.22)-(4.25). Furthermore, midgap states occur at (110) surfaces in d-wave superconductors even when spatial variations of the order parameter are neglected [113, 220]; the states are caused by interference between the positive and negative lobes of the gap function, as described below.

A standard approach to the analytical solution of the BdG equations near an extended inhomogeneity, such as a superconductor—normal (insulator)—superconductor microjunction, is to approximate the order-parameter potential in the neighbourhood of the defect, and then determine the resulting quasiparticle amplitudes u and v. Since the quasiparticles vary on a short length scale $k_F^{-1} \ll \xi(0)$ (as is certainly the case for conventional superconductors), one may employ the WKBJ approximation [113, 220, 221, 222]:

$$\psi(\mathbf{x}) \equiv \begin{pmatrix} \bar{u}(\mathbf{x}) \\ \bar{v}(\mathbf{x}) \end{pmatrix} = e^{-i\mathbf{k}_F\cdot\mathbf{x}} \begin{pmatrix} u(\mathbf{x}) \\ v(\mathbf{x}) \end{pmatrix}, \tag{4.38}$$

which neglects rapid variations. Assuming that the system is translationally invariant in the direction parallel to the junction, one obtains in the continuum limit the Andreev equations [221, 223]:

$$\begin{aligned} -im^{-1}k_F\frac{d\bar{u}(r)}{dr} + \hat{\Delta}(r)\bar{v}(r) &= \varepsilon\bar{u}(r), \\ im^{-1}k_F\frac{d\bar{v}(r)}{dr} + \hat{\Delta}(r)\bar{u}(r) &= \varepsilon\bar{v}(r). \end{aligned} \tag{4.39}$$

The wavefunctions satisfying these equations are shown schematically in Fig. 4.10(b) for a normal metal–narrow insulator–*d*-wave superconductor junction. An electron incident to the interface from the normal metal side experiences both conventional and Andreev reflection. In the absence of external currents or fields, the Andreev-reflected hole traverses the time-reversed path of the incident particle. The transmitted electron- and hole-like quasiparticles experience different order-parameter potentials, depending on the angle of the junction with respect to the underlying crystal lattice of the superconductor. Except for the [100] and [010] orientations, the lobes of the *d*-wave gap (which are parallel to the crystal axes) will not face the junction. The resulting destructive interference between the quasielectron and quasihole wavefunctions gives rise to so-called Andreev bound states near the interface [113, 220, 224, 225, 226], much like standing waves in a classical system. Clearly, this pair-breaking effect is maximum for [110] junctions. It should be kept in mind, however, that for quasi-one dimensional scatterers such as these, the quasiparticle states are extended in the direction parallel to the interface.

Bound states are a generic feature of conventional superconductors in the presence of pair-breakers, such as vortices [227, 228], magnetic impurities [229, 230, 231], or insulating barriers [232]. The bound states are manifested in the local density of states as a low-energy band inside the superconducting gap. Sufficiently large impurity concentrations can lead to gapless superconductivity [233]. Since the quasiparticles

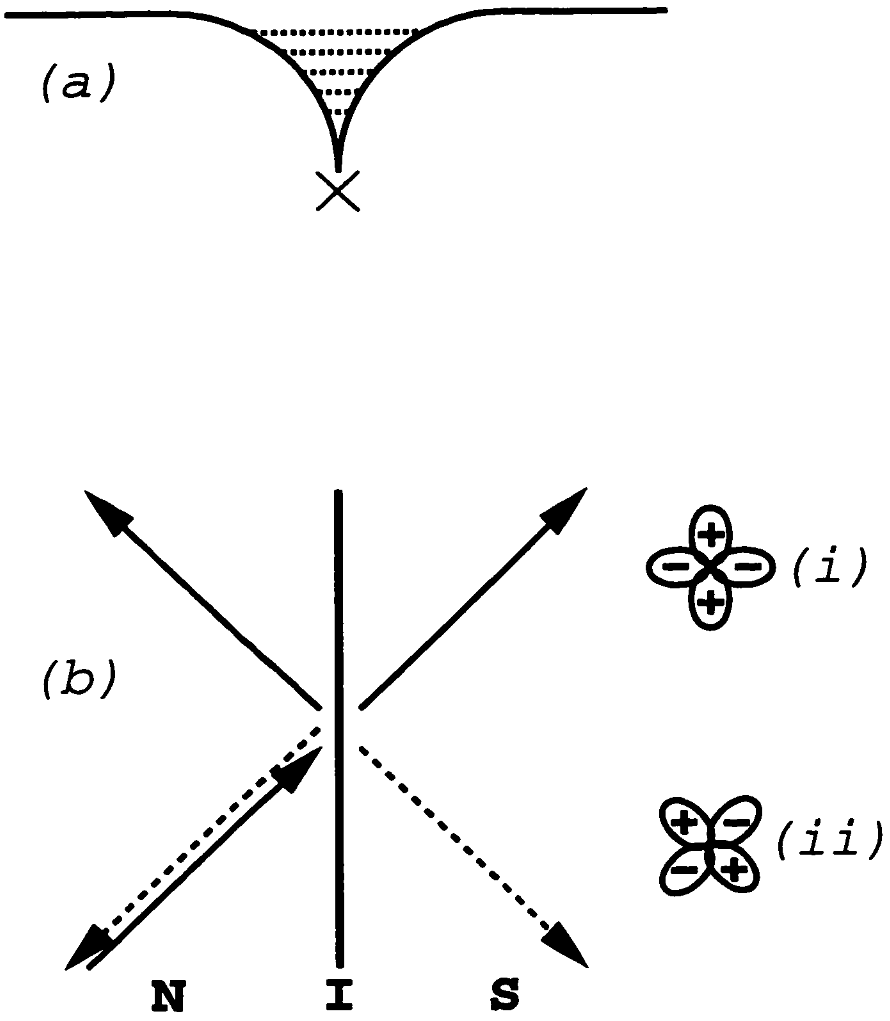

Figure 4.10: The schematic in (a) illustrates quasiparticle states residing in the potential well associated with a suppressed superconducting order parameter. The normal and Andreev scattering processes are depicted in (b). For orientation of the *d*-wave order parameter shown in (i) and (ii), the hole- and electron-like quasiparticles experience the same and different pair potentials, respectively.

occupying the band can carry current, the spectra obtained in scanning-tunneling microscopy (STM) and tunnel-junction experiments exhibit a 'zero-bias conductance peak' (ZBCP) in the differential conductance:

$$\frac{\partial I(r)}{\partial V} \propto -\sum_{nk} \left[|u_{n,k}(r)|^2 f'\left(V - \varepsilon_n\right) + |v_{n,k}(r)|^2 f'\left(V + \varepsilon_n\right) \right], \tag{4.40}$$

where f' is the voltage-derivative of a Fermi function, and V is an applied bias. Note that the tunneling conductance at zero temperature is identical to the local density of states, since $f'(x, T = 0) = -\delta(x)$, where $\delta(x)$ is a Dirac-delta function. In high-T_c materials, the ZBCP is a ubiquitous feature in the superconducting state since virtually any inhomogeneity is pair-breaking for an anisotropic gap [107, 108]. It is presently controversial, however, whether the Andreev states in dirty d-wave superconductors are localized [214, 218] or extended [234]. Recent numerical investigations of d-wave superconductors in the presence of random unitary non-magnetic scatterers indicate that the quasiparticle excitations are indeed highly localized, but only if the coherence length is sufficiently short (approaching k_F) [214]. Clearly, in this regime the quasiclassical approximation (4.38) breaks down.

From Fig. 4.4(a), one expects a ZBCP in the tunneling conductance with a size that increases with impurity strength, but that decreases with distance from the center of the twin boundary. The predicted STM results for this model are shown in Fig. 4.11. While the tunneling conductance exhibits low-temperature features that are no doubt finite-size effects, the ZBCP is a well-defined feature at zero voltage for $\mu^I = 0$ and $-2t_x$ at zero temperature. As $|\mu^I|$ increases, however, the ZBCP develops a dip in the center which deepens and widens. This is evidently a signature of the $\mathcal{T}$-violation illustrated in Figs. 4.4 and 4.7. Note that the overall magnitude of the tunneling conductance drops rapidly with increasing $|\mu^I|$ for $r = 0$, reflecting the progressive depletion of carrier density at the twin boundary center.

Fig. 4.12 shows the temperature-dependence of the differential conductance for system parameters chosen in Fig. 4.5. The zero-temperature maximum peak-to-peak splitting of the ZBCP is found to be approximately $0.2t_x \sim 2\,\text{meV}$, where $t_x \approx 10^{-2}\,\text{eV}$ (see Section 4.4). The ZBCP diminishes with increasing temperature and distance

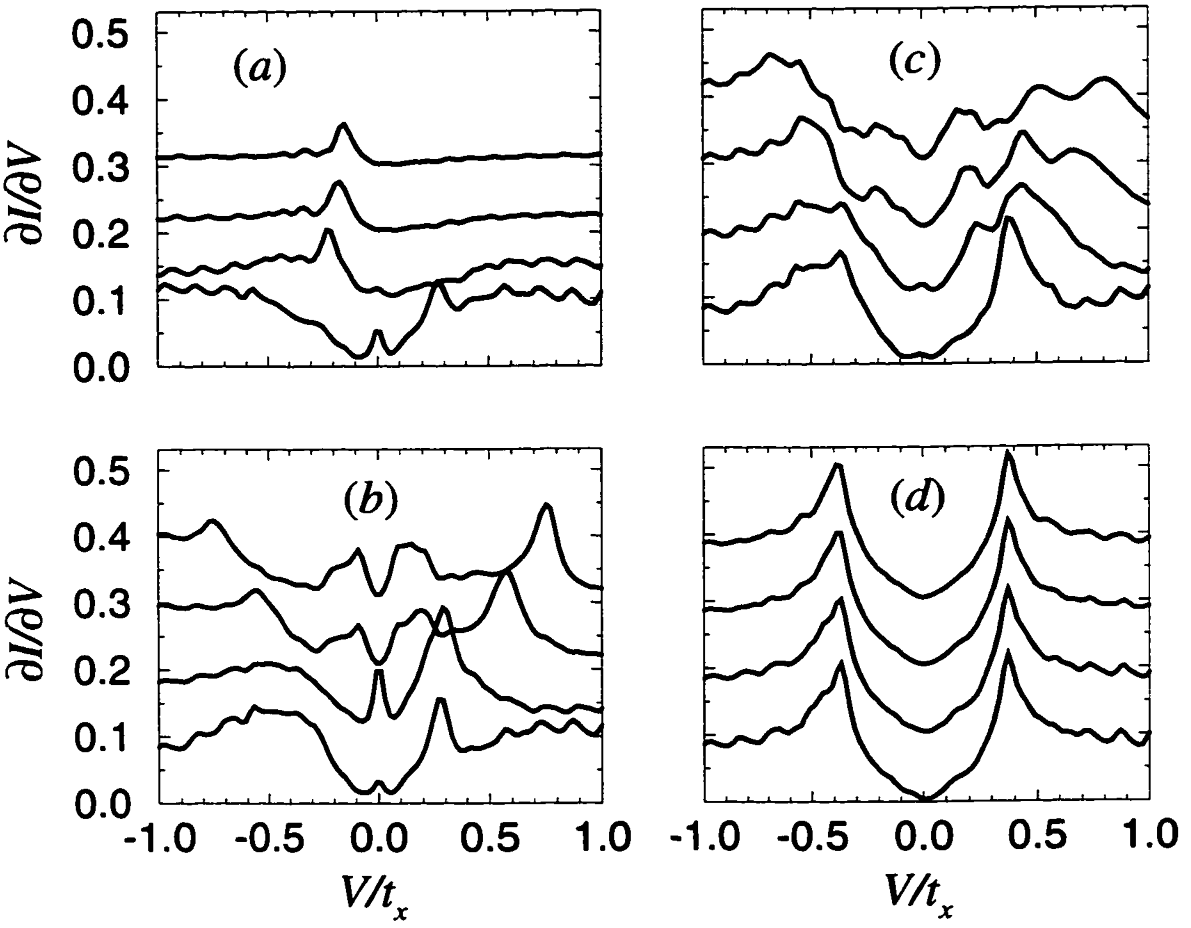

Figure 4.11: A low-energy portion of the tunneling conductance at and near a twin boundary is shown as a function of energy, distance r from the twin boundary center where (a) through (c) correspond to 0 through $2|\hat{r}|$ while (d) illustrates the bulk, and impurity strength $\mu^I = 0$ (lower), $\mu^I = -2t_x$ (offset 0.1), $\mu^I = -4t_x$ (offset 0.2), and $\mu^I = -6t_x$ (offset 0.3). Parameters are as in Fig. 4.4.

from the twin boundary. It is evident that the low energy band splits at a temperature $0.1T_c \approx 6\,\mathrm{K}$ which is considerably lower than the $T^* \sim 0.5T_c$ estimated from Fig. 4.7b. This discrepancy is most likely due to thermal smearing of the local density of states associated with the Fermi factors in (4.40). A comparable splitting of the zero-energy peak has been recently observed in tunneling spectra of YBCO surfaces [235], and has been interpreted as a clear signature of $\mathcal{T}$-violation [236].

The splitting of the ZBCP in the absence of external fields is consistent with the presence of spontaneous supercurrents associated with local $\mathcal{T}$-violation [204, 235, 236]. The spatial variation of the *s*-wave components' phase relative to Δ_d implied by Fig. 4.5 leads to currents flowing parallel to the twin surface and in opposite directions on either side of the twin boundary, as shown in Fig. 4.13. The strong impurity potential therefore mimics a line of temperature-dependent magnetic flux passing through the twin boundary and oriented parallel to the *c*-axis. The currents can be interpreted as the diamagnetic response of the superconductor attempting to screen this effective field. Assuming that the spontaneous currents flowing around the twin boundary exactly cancel the effective field, one obtains from $h^2/8\pi = \sum_r j_R$ and $t_x \approx 10^{-2}$ eV the effective field strength in Tesla: $h_{\rm eff} \approx 12$ T.

The splitting of the Andreev band occurs whenever supercurrents are present in the system. The energies of the quasiparticle excitations and the Andreev bound states are shifted by the currents, as shown explicitly by Eq. (4.13). Furthermore, STM studies of both conventional and high-T_c superconductors in the mixed state find a well-defined ZBCP when the tunneling tip is positioned at the center of a vortex; the ZBCP splits with increasing distance from the core, where supercurrents attempt to screen the magnetic field. [144, 227].

4.6 Summary and Discussion

The role of twin boundaries in orthorhombic *d*-wave superconductors has been investigated numerically within the Bogoliubov-de Gennes formalism. Twin boundaries are modeled as tetragonal and carrier-depleted regions of finite width. The results indicate that a time-reversal breaking phase may be favoured in the vicinity of the twin

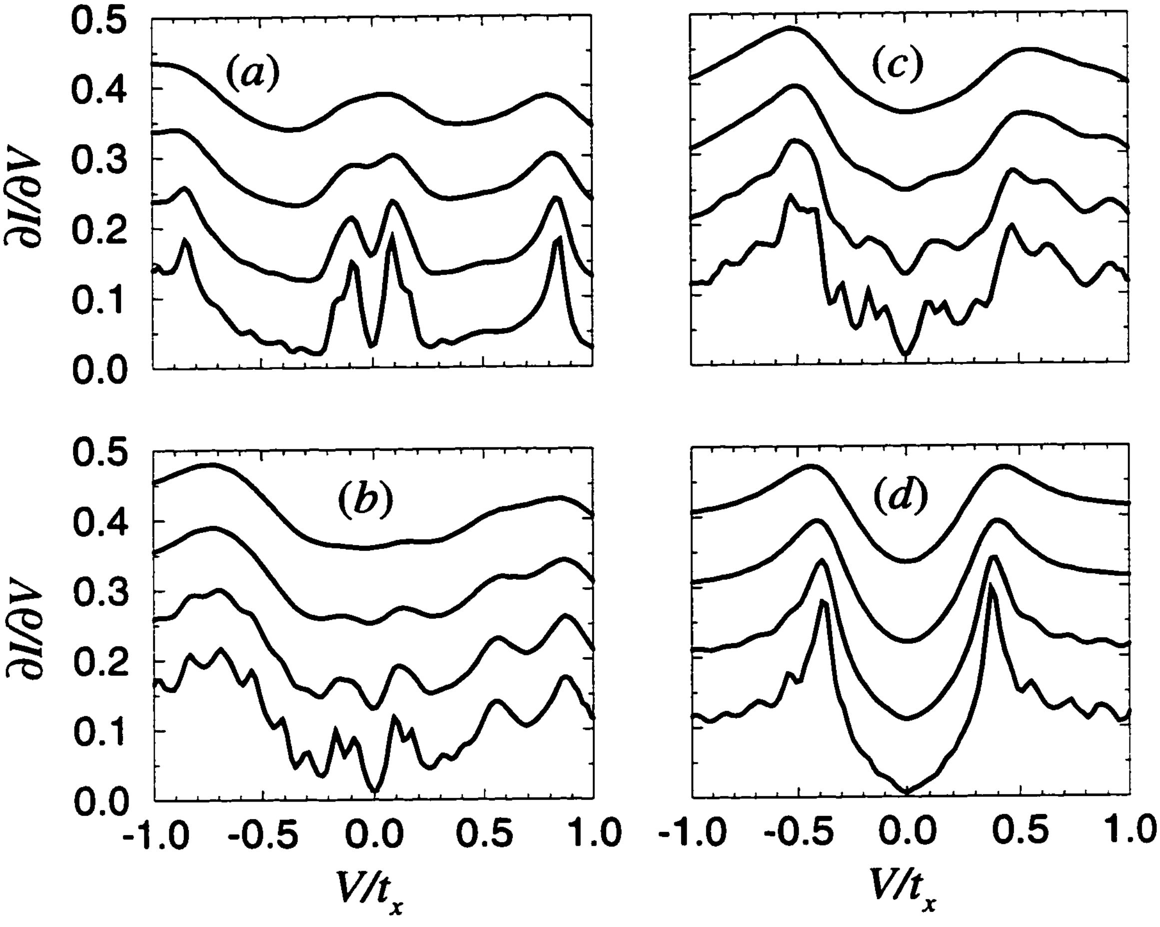

Figure 4.12: A low-energy portion of the tunneling conductance near a twin boundary is shown as a function of energy, distance r from the twin edge, and temperature. Panels (a) through (c) correspond to $|\hat{r}|$ through $3|\hat{r}|$ while (d) illustrates the bulk. Temperatures are $T = 0$ (lower), $T = 0.05T_c$ (offset 0.1), $T = 0.1T_c$ (offset 0.2) and $T = 0.15T_c$ (offset 0.3). Parameters are as in Fig. 4.5.

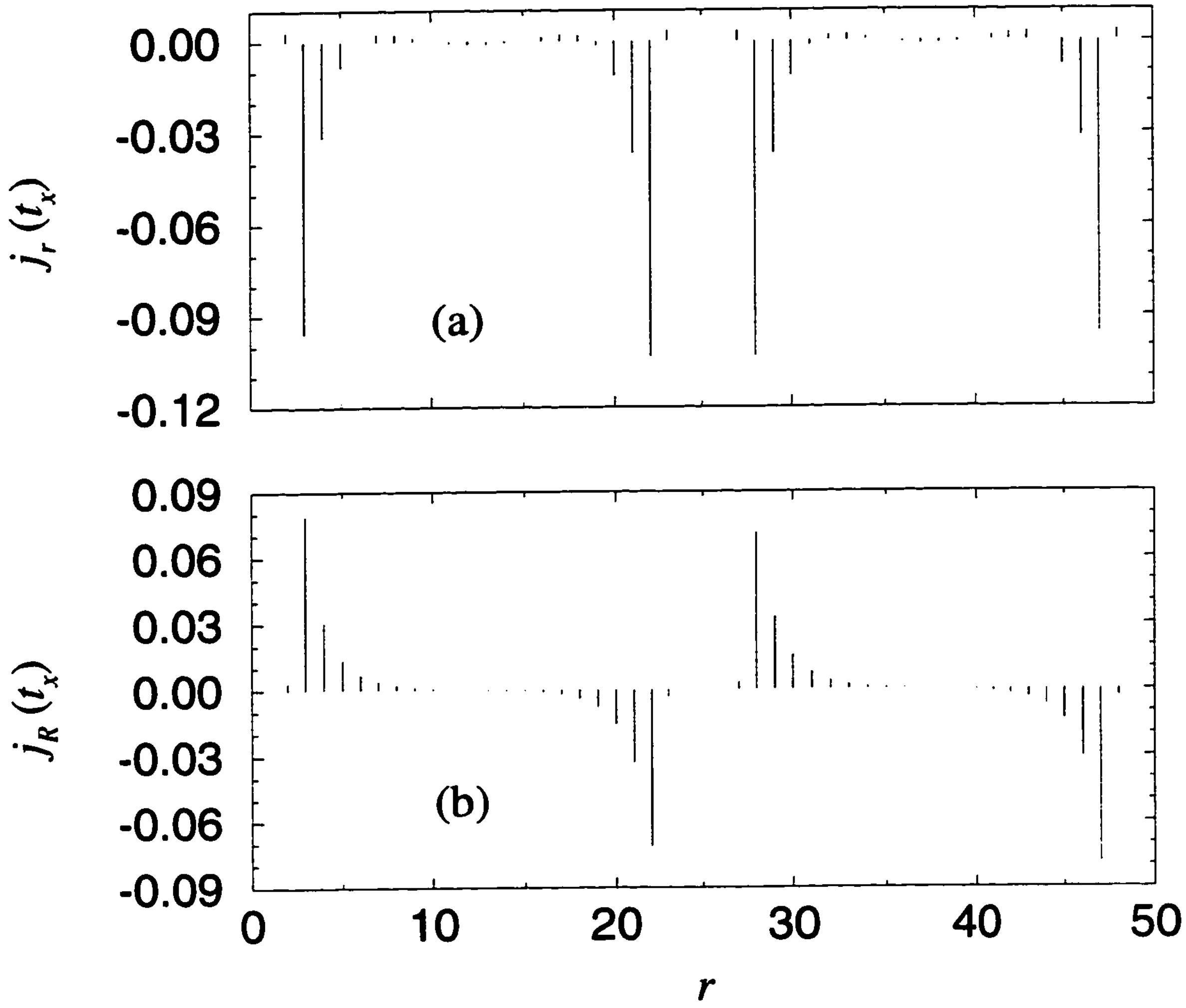

Figure 4.13: The magnitude of the spontaneous supercurrents in the (a) $\hat{r}$ perpendicular and (b) $\hat{R}$ parallel direction to the twin boundary are shown as a function of perpendicular distance $\hat{r}$. Parameters are as in Fig. 4.5.

edge at a subdominant transition temperature $T^* < T_c$, where T^*/T_c scales approximately with the size of the bulk d-wave gap. In general, imaginary s-wave components associated with the $\mathcal{T}$-violation arise only at low temperatures $T^* < 0.5T_c$, as long as the dominant d-wave component is suppressed by the weak link to less than half its bulk value. The magnitudes of the imaginary components and T^* are proportional to the chemical potential and carrier depletion in the twin boundary. These imaginary s-wave gap functions could be responsible for the finite Josephson currents observed in c-axis tunnel junctions to heavily-twinned YBCO [208].

In addition to possible imaginary subdominant components, quasiparticle states are found in the vicinity of the twin boundary, caused by Andreev processes at the interface. These states are localized in the direction perpendicular to the twin boundary, and are exhibited as a low-energy peak in the tunneling density of states, related to the zero-bias conductance peak (ZBCP) found in tunneling experiments. In the time-reversal breaking phase, the ZBCP splits due to the presence of spontaneous currents flowing near the twin edge. The results are comparable with recent tunneling data for YBCO surfaces [235].

Although the theoretical results predict time-reversal breaking near twin boundaries, there is presently no conclusive experimental evidence for a second phase transition in bulk YBCO materials. A second discontinuity in the specific heat at low temperatures has not been observed experimentally. SQUID measurements of vortices pinned by twin boundaries failed to detect the fractional flux that would indicate a time-reversal breaking state. Yet, $\mathcal{T}$-violation provides a likely explanation for the fractional flux observed at grain boundary junctions [203], and for the splitting of the ZBCP in surface tunneling experiments [235]. Furthermore, very recent microwave measurements on ultraclean but heavily-twinned YBCO samples provide evidence that another superconducting component may be stabilized at a low temperature $T^* \sim 0.5T_c$ [216]. Twin boundaries, unlike wide-angle grain boundaries, may be strongly-coupled Josephson junctions which only weakly perturb the d-wave order parameter. Thus, time-reversal breaking near twin boundaries may be a small effect, the detection of which could be quite challenging experimentally.

Chapter 5

Critical Currents

5.1 Introduction

A great deal of experimental effort has recently been focused on the behaviour of high-T_c materials in the presence of external currents. Of particular relevance for potential applications are the critical current characteristics of YBCO or BSCCO wires and tapes [237]. Supercurrent densities are predominantly limited by depairing at low temperatures, and dissipation due to flux flow at higher temperatures [238, 239]. Since the high-T_c materials have short coherence lengths and most likely a d-wave order parameter, depairing results not only globally due to the external currents (see Section 2.5), but also locally in the vicinity of small defects in the lattice. In particular, extended inhomogeneities such as grain boundaries and possibly twin boundaries in YBCO act as weak links at low temperatures, reducing current densities in granular and heavily-twinned thin films [171, 240, 241]. Large-angle grain boundaries were responsible for low critical currents in early granular high-T_c samples [240]. At higher temperatures the coherence length diverges, so these small defects have less influence on the local order parameter, but self-field effects become more important. In this regime twin and grain boundaries enhance critical currents by effectively pinning magnetic vortices against flux flow [172, 173, 174, 175, 176, 242, 243, 244].

The GL theory of critical currents outlined in Section 2.5 is applicable to superconductors in restricted geometries such as wires, tapes, and thin films. It is not clear, however, whether this formalism is appropriate in the low-temperature regime where self-field effects may be neglected. Furthermore, in d-wave superconductors, the GL equations are complicated by the presence of subdominant s-wave components, which may be induced by external currents, orthorhombicity, or intrinsic defects such as impurities, grain boundaries, and twin boundaries. In practice, analytical results can only be obtained in clean systems, and near T_c where the s-wave components are guaranteed to be small. In contrast, the BdG formalism discussed in the previous chapter is ideal for the investigation of critical currents in YBCO. The BdG approach is self-consistent, valid at all temperatures, and naturally incorporates many of the inhomogeneities relevant to physical systems.

In this chapter, the behaviour of d-wave superconductors in the presence of external currents is investigated numerically within the BdG formalism, and using the extended Hubbard model. Only depairing effects are considered. In Section 5.2, external currents in clean systems are studied. The anisotropy of the current response is characterized, the superfluid density is determined, and comparison is made with experimental measurements for the penetration depth. The induction of subdominant s-wave components by the external currents is considered, and contact is made with the GL analysis of Section 2.5. The temperature-dependence of the critical current is calculated and compared with experimental data for YBCO thin films. Systems with twin boundaries are studied in Section 5.3. The critical current through the weak-link is determined as a function of twin boundary width and carrier depletion at zero temperature. The induced currents in the vicinity of the twin boundary are characterized for both initially time-reversal breaking and $\mathcal{T}$-preserving states.

5.2 Clean Case

5.2.1 Theory

In the absence of any intrinsic defects causing spatial variations, the BdG equations (4.22) are translationally invariant in all directions. The resulting single-body problem is most conveniently studied using a conventional square $N \times N$ Bravais lattice with primitive vectors $\hat{x}$ and $\hat{y}$ (the lattice constant a is taken to be unity for convenience). A simple way to simulate an applied current in such uniform systems is to give the gap functions a center-of-mass momentum $\mathbf{p}$. This may be accomplished by defining

$$u(\mathbf{r}) \equiv U_k e^{i(\mathbf{k}+\mathbf{p}/2)\cdot\mathbf{r}} \quad ; \quad v(\mathbf{r}) \equiv V_k e^{i(\mathbf{k}-\mathbf{p}/2)\cdot\mathbf{r}}; \tag{5.1}$$

$$\Rightarrow \psi(\mathbf{r}) \sim u(\mathbf{r})v^*(\mathbf{r}) = |\psi|e^{i\phi(\mathbf{r})} = |\psi|e^{i\mathbf{p}\cdot\mathbf{r}}. \tag{5.2}$$

where $\mathbf{k} = k_x\hat{x} + k_y\hat{y}$ are wavevectors of the first Brillouin zone, and the momentum is $\mathbf{p} = p_x\hat{x} + p_y\hat{y}$ with $(p_x, p_y) = 4\pi(m,n)/N$ $(m, n = 0, 1, 2, \ldots, N-1)$. As discussed in detail in Section 5.3, this approach is no longer strictly applicable in non-uniform systems.

The BdG equations (4.22) are now written

$$\begin{aligned} (\xi_k^{(1)} - E_k)U_k + \Delta_k V_k &= 0; && (5.3) \\ \Delta_k^* U_k - (\xi_k^{(2)} + E_k)V_k &= 0, && (5.4) \end{aligned}$$

where the $k-$dependent gap function Δ_k is

$$\Delta_k = \Delta_0 + 2a_k\Delta_s + 2b_k\Delta_d, \tag{5.5}$$

with $a_k = \cos k_x + \cos k_y$, and $b_k = \cos k_x - \cos k_y$. The dispersions $\xi_k^{(1)}$ and $\xi_k^{(2)}$ are

$$\begin{aligned} \xi_k^{(1)} &= -2\left[t_x\cos(k_x + p_x/2) + t_y\cos(k_y + p_y/2)\right] - \mu; && (5.6) \\ \xi_k^{(2)} &= -2\left[t_x\cos(k_x - p_x/2) + t_y\cos(k_y - p_y/2)\right] - \mu. && (5.7) \end{aligned}$$

The two equations (5.3) and (5.4) may be combined to yield the quasiparticle excitation energies in the presence of external currents:

$$E_k = \frac{\xi_k^{(1)} - \xi_k^{(2)}}{2} + \sqrt{\left(\frac{\xi_k^{(1)} + \xi_k^{(2)}}{2}\right)^2 + |\Delta_k|^2}. \tag{5.8}$$

With the normalization $U_k^2 + V_k^2 = 1$, one also obtains the coherence factors

$$U_k^2 = \frac{E_k + \xi_k^{(2)}}{2E_k + \xi_k^{(2)} - \xi_k^{(1)}} \quad ; \quad V_k^2 = \frac{E_k - \xi_k^{(1)}}{2E_k + \xi_k^{(2)} - \xi_k^{(1)}}. \tag{5.9}$$

The solutions of the BdG equations (5.8) and (5.9) are subject to the self-consistency requirement

$$\{\Delta_0\ ;\ \Delta_s\ ;\ \Delta_d\} = \sum_{\mathbf{k}} \frac{\Delta_k \{V_0\ ;\ V_1 a_k/4\ ;\ V_1 b_k/4\}}{2E_k + \xi_k^{(2)} - \xi_k^{(1)}} \tanh\left(\frac{E_k}{2T}\right). \tag{5.10}$$

It is instructive to consider the continuum limit corresponding to the low-density approximation of the tight-binding model. In this limit,

$$\xi_k^{(1)} = -2(t_x + t_y) + [t\mathbf{k}]\cdot\mathbf{k} - \mu + [t\mathbf{k}]\cdot\mathbf{p}; \tag{5.11}$$

$$\xi_k^{(2)} = -2(t_x + t_y) + [t\mathbf{k}]\cdot\mathbf{k} - \mu - [t\mathbf{k}]\cdot\mathbf{p}, \tag{5.12}$$

where the convenient notation $[t\mathbf{q}] \equiv t_x q_x \hat{x} + t_y q_y \hat{y}$ has been introduced. Inserting these expressions into (5.8) and (5.9) yields

$$E_k = E_k^{\circ} + [t\mathbf{k}]\cdot\mathbf{p}\quad ;\quad U_k^2 = \frac{1}{2}\left(1 + \frac{\xi_k}{E_k^{\circ}}\right)\quad ;\quad V_k^2 = \frac{1}{2}\left(1 - \frac{\xi_k}{E_k^{\circ}}\right), \tag{5.13}$$

where

$$E_k^{\circ} = \sqrt{\xi_k^2 + |\Delta_k|^2} \tag{5.14}$$

are the unperturbed quasiparticle excitation energies and ξ_k is either (5.11) or (5.12) with $\mathbf{p} = 0$. Thus, in the continuum case the superfluid momentum shifts the energy spectrum, but not the coherence factors. In the absence of the momentum $\mathbf{p}$, the expressions (5.8) and (5.9) correctly reduce to their usual BCS limits, though with a k-dependent gap and a tight-binding dispersion which is either (5.6) or (5.7) with $\mathbf{p} = 0$.

Once convergence has been established, the resulting (single-particle) current from (4.29) is written

$$\begin{aligned}\mathbf{j} = 4\sum_{\mathbf{k}} \Big\{ & t_x \left[\sin(k_x + p_x/2)|U_k|^2 f_k - \sin(k_x - p_x/2)|V_k|^2(1 - f_k)\right]\hat{x} \\ & + t_y \left[\sin(k_y + p_y/2)|U_k|^2 f_k - \sin(k_y - p_y/2)|V_k|^2(1 - f_k)\right]\hat{y}\Big\},\end{aligned} \tag{5.15}$$

where the Fermi factor is $f_k = (e^{E_k/T} + 1)^{-1}$. The current may be related to the Cooper-pair momentum through

$$\begin{aligned} 2e\mathbf{j} &= e n_s \mathbf{v}_s \\ &= \frac{2en_s}{2m^*}\mathbf{p} \\ &= 2en_s[t\mathbf{p}], \end{aligned} \tag{5.16}$$

where the transfer integral is inversely proportional to the effective mass, $t_z \equiv (1/2m_z^*)$. Since the currents break Cooper pairs, the superfluid density $n_s = n_s(\mathbf{p})$ should decrease with increasing momentum $\mathbf{p}$. As discussed in Section 2.5, the order parameter, which is proportional to the superfluid density, is a non-monotonic function of the supercurrent. The relation between $\mathbf{j}$ and $\mathbf{p}$ with $n_s = n_s(0)$ is therefore only strictly valid for very small applied currents, where the superfluid density approaches its unperturbed value:

$$n_s = \lim_{\mathbf{p}\to 0} \frac{\mathbf{j}}{[t\mathbf{p}]}. \tag{5.17}$$

Since Eq. (5.17) is valid for all temperatures, one may use it to determine the (London) penetration depth, through the local relation $\lambda_L^{-2}(T) \propto n_s(T)$. This procedure for the determination of the superfluid density is analogous to a linear-response theory [155, 245], but in the present case the proportionality constant between λ_L and n_s cannot be obtained microscopically.

The explicit expression for the current (5.15) may be evaluated in the continuum limit (5.13). After some straightforward algebra, the current is written:

$$\begin{aligned} \mathbf{j} &\approx \int \frac{d^2k}{(2\pi)^2} \left[1 - \frac{\xi_k}{E_k^\circ} \tanh\left(\frac{E_k}{2T}\right)\right] \Big([t\mathbf{p}] - 2[t\mathbf{k}]\Big) \\ &\approx [t\mathbf{p}]\langle n\rangle, \end{aligned} \tag{5.18}$$

where $\langle n\rangle$ is the expectation value of the temperature-dependent density (the particle number) in the absence of a current. With (5.17), one immediately obtains $n_s = \langle n\rangle$ in the continuum. This result is strictly valid only at the bottom of the tight-binding band, where d-wave superconductivity is not favoured (see Section 3.3[1]). In fact, in this limit $\langle n\rangle \to 0$. Incorporating the Fermi surface anisotropy associated with densities closer to half-filling would require the inclusion of higher-order corrections. Furthermore, the approximation $E_k \approx E_k^\circ$ employed in the derivation of the continuum current (note the argument of the tanh) is inaccurate for d-wave superconductors since E_k° can vanish in the vicinity of the line nodes.

---

[1] An orthorhombic distortion does not significantly alter the $T_c - \mu$ phase diagram discussed in detail in Section 3.3.

As the Fermi surface becomes increasingly anisotropic, the ratio $n_s(0)/\langle n\rangle$ will decrease. Stated another way, the effective mass is no longer be simply inversely proportional to the transfer integral as in Eq. (5.16); rather, it is a k-dependent 'mass tensor', defined by the Fermi surface geometry [246]:

$$\left(\frac{1}{m^*}\right)_{ij} = \frac{1}{\hbar^2}\frac{\partial^2 E_k}{\partial k_i \partial k_j}. \tag{5.19}$$

Since near half-filling ($\mu \to 0$) the Fermi surface is very flat (see Fig. 1.1b), the effective mass m^* may become quite large. If one assumes that n_s and $\langle n\rangle$ are equal by definition, however, then any observed decrease in n_s with filling measures the increase in average effective mass.

Both Eqs. (5.16) and (5.18) indicate that the resulting current is not generally parallel to the superfluid velocity in orthorhombic superconductors. Given a Cooper-pair momentum with equal $\hat{x}$- and $\hat{y}$-components, the resulting current will be larger along $\hat{y}$ if the effective mass of the charge carriers is lower in this direction (i.e. $t_y > t_x$). By implication, an applied momentum $\mathbf{p} = p\hat{r}$ perpendicular to a twin boundary (see Section 4.2) will also yield a component along $\hat{R}$.

5.2.2 Results

The response of a d-wave superconductor to an applied current has been investigated numerically for clean tetragonal and orthorhombic systems. In order to facilitate comparison with the results of the previous chapters, the parameters chosen are $V_0 = -3t_x$, $V_1 = 3t_x$, and $t_y = 1.5t_x$ in the orthorhombic case. This choice gives rise to d-wave superconductivity at all temperatures, with subdominant s-wave components in orthorhombic systems. The finite-size system employed contains $N = 300$ k-points in both the $\hat{x}$- and $\hat{y}$-directions. The allowed Cooper-pair momenta, parametrizing the applied currents, are therefore $\mathbf{p} = (4\pi/300)(m\hat{x} + n\hat{y})$, $m, n = 0, 1, 2, \ldots, N-1$. In practice, the gap equations for a given applied momentum $\mathbf{p}$ (5.10) are iterated numerically until double precision accuracy is obtained, at which point the resulting current (5.15) is evaluated.

In Fig. 5.1, the current response at zero temperature is shown as a function of the reduced d-wave component $f^2 \equiv |\Delta_d|^2/\Delta_d^\circ|^2$, where Δ_d° is the unperturbed value. Results are obtained for 300×300-site tetragonal and orthorhombic lattices. As expected from the GL theory (Section 2.5), the d-wave component decreases steadily with increasing $\mathbf{p}$, while the supercurrent reaches a maximum at the critical current. The data points left of the current maximum are almost certainly due to finite-size effects and are therefore unphysical, so the current maximum is interpreted as the true critical current. The supercurrent peaks for $f_c^2 \sim 0.85$, which is much larger than the GL estimate of $f_c^2 = 2/3$. As the temperature increases (not shown), the critical current shifts to lower f^2, and the 'tail' left of the current maximum shortens. Just below T_c the behaviour closely matches the GL predictions.

The current response shown in Fig. 5.1 is a highly anisotropic function of the applied momentum orientation. In tetragonal systems, the supercurrent is maximum for $\mathbf{p}$ parallel to the x or y axes, and is a minimum for $\mathbf{p}$ in the diagonal direction. This result is consistent with the presence of line nodes along $k_x = k_y$ in d-wave superconductors. Less supercurrent can flow in a direction where the energy gap vanishes, due to the larger number of single-particle excitations. In contrast, for orthorhombic systems the maximum current is found for applied momenta along the y axis, while the minimum occurs along the x axis; for $\mathbf{p} \parallel \hat{x} + \hat{y}$ the response is intermediate between these two extremes. The anisotropy of the resulting currents reflects enhanced superconducting transport along the chains, oriented along $\hat{y}$ or b. In addition, the presence of finite subdominant s-wave components even in the uniform case shifts the nodes away from $k_x = \pm k_y$, and thus the Cooper pairs with momentum in this direction experience a well-defined gap to excitations. To date, no experimental evidence for such critical current anisotropy has been observed either in tetragonal or orthorhombic high-T_c materials.

Fig. 5.2 shows the variation of the zero temperature superfluid density, which is calculated from Eq. (5.16), with the applied current or superfluid velocity $[t\mathbf{p}] = \mathbf{v}_s/2$. The data are identical to those shown in Fig. 5.1. For a given direction of the Cooper-pair momentum, the superfluid density is found to decrease linearly with the velocity until the critical momentum $\mathbf{p}_c$, at which point it drops rapidly to zero. This linear behaviour is consistent with d-wave, but not conventional s-wave, superconductiv-

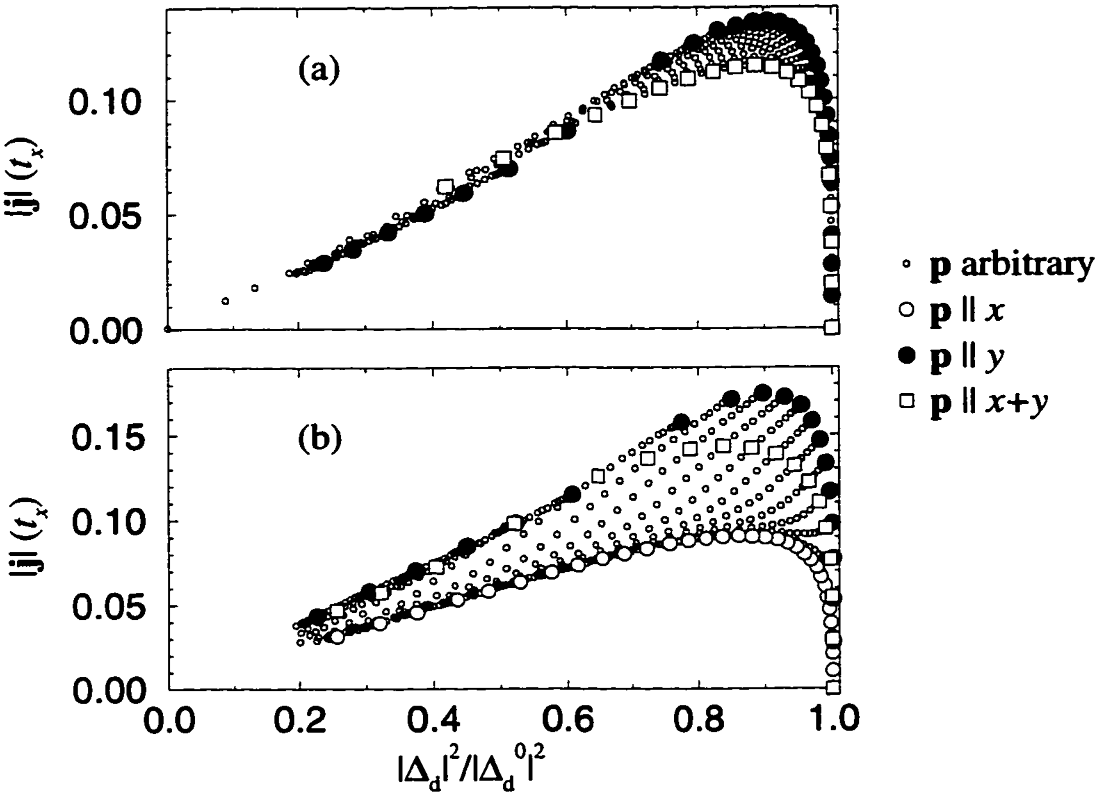

Figure 5.1: The magnitude of the current at zero temperature is shown as a function of reduced gap $f^2 = |\Delta_d|^2/|\Delta_d^\circ|^2$, where Δ_d° is the unperturbed d-wave component. Results are obtained for 300 × 300-site tetragonal (a) and orthorhombic (b) lattices, with parameters $V_0 = -3t_x$, $V_1 = 3t_x$, $\mu = -t_x$, and $t_y/t_x = 1.5$ for the orthorhombic case. Data are shown for superfluid velocity $\mathbf{v}_s$ oriented in all directions (circles) as well as along $\hat{x}$ (large open circles), $\hat{y}$ (large filled circles), and $\hat{x} + \hat{y}$ (squares).

ity [102]. For very small applied currents, the extrapolation of the superfluid density to $\mathbf{p} = 0$ yields values that are approximately half the zero temperature result for $\langle n \rangle$ calculated independently: for tetragonal and orthorhombic systems, $\langle n \rangle$ are respectively 0.69 and 0.76, where half-filling corresponds to $\langle n \rangle = 1$. The small superfluid densities illustrate the importance of Fermi surface anisotropy: the average effective mass that may be inferred is approximately twice the bare carrier mass. At half-filling or optimal doping, the calculations give $m^* \approx 3m$ which is consistent with experimental results [6, 74, 75, 76, 77].

The data shown in Fig. 5.2 show a dependence on the direction of the superfluid flow which is consistent with the results shown in Fig. 5.1. It is interesting to note that in tetragonal superconductors, the unperturbed superfluid density (obtained by extrapolating $\mathbf{p} \to 0$) is found to be essentially isotropic. This result corroborates previous analytical calculations for *d*-wave superconductors at zero temperature [102]:

$$\mathbf{j} = \rho \mathbf{v}_s \left(1 - \alpha \frac{|\mathbf{v}_s|}{2\Delta_{/} v_F} \right), \tag{5.20}$$

where ρ is the density, and $\alpha = 1$ or $1/\sqrt{2}$ for $\mathbf{v}_s$ parallel to $\hat{x} + \hat{y}$ or $\hat{x}$, respectively; clearly, the resulting supercurrent is independent of direction when $\mathbf{v}_s \to 0$. Anisotropy in the tetragonal case appears only for finite external currents: in general, $n_s(\hat{x}) > n_s(\hat{x} + \hat{y})$. This observation is consistent with the analytical result (5.20), where the magnitude of the nonlinear term is a factor of $\sqrt{2}$ larger for currents applied along the gap nodes. Unsurprisingly, in orthorhombic systems the superfluid density is largest in the direction parallel to the chains, whereas it is smallest in the perpendicular direction.

The anisotropy in the superconducting transport is reflected in the London penetration depth, which is proportional to the superfluid density n_s:

$$\lambda_L^{-2}(T) = \left(\frac{4\pi e^2}{m^* c^2} \right) n_s(T) = \left(\frac{2\pi}{\phi_0} \right)^2 8\pi t \, n_s(T) \tag{5.21}$$

(see Section 1.1.2). Fig. 5.3 depicts the temperature-dependence of the unperturbed superfluid density, calculated from Eq. (5.17). While the the data suffer from finite-size effects, since the smallest applied momentum on a 300 × 300-site lattice is

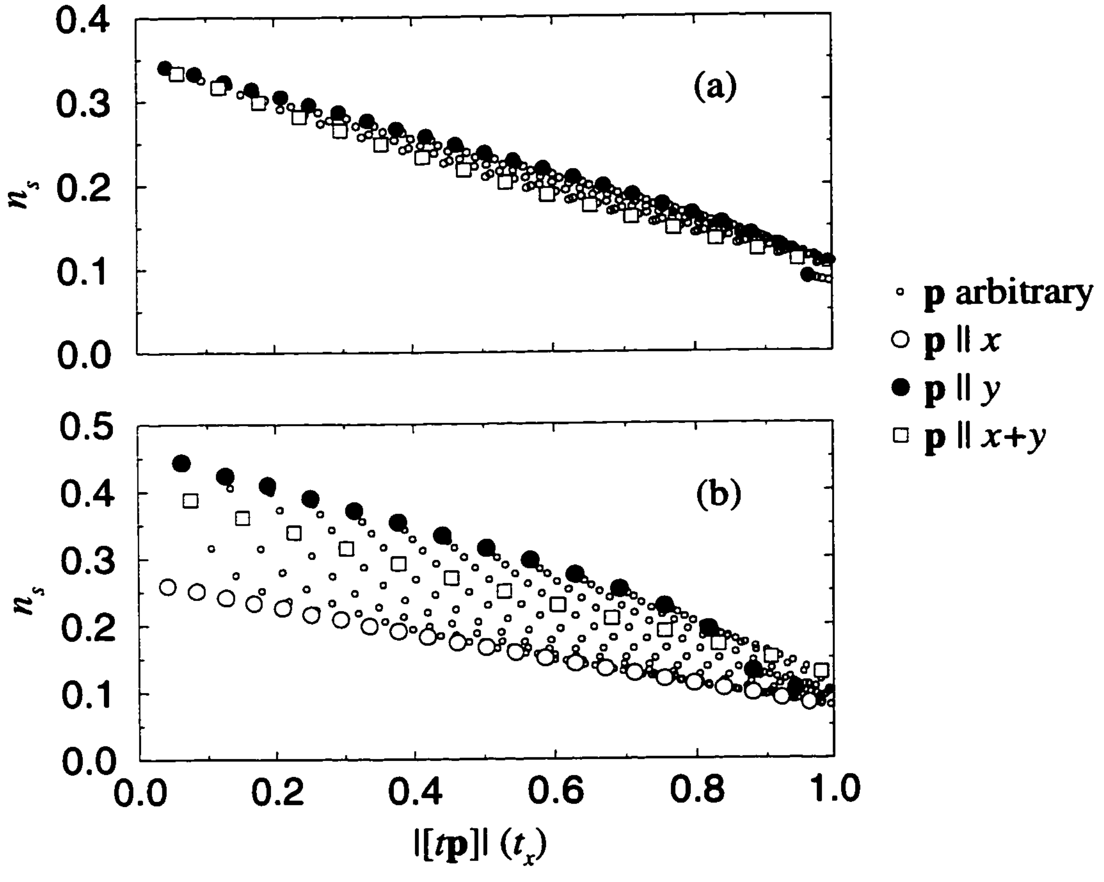

Figure 5.2: The zero-temperature superfluid density is shown as a function of the magnitude and orientation of the applied Cooper-pair momentum, for tetragonal (a) and orthorhombic (b) systems. Parameters and symbols are as in Fig. 5.1.

$|[t\mathbf{p}]| \approx 0.04$, the results agree remarkably well with experiments on the cuprates. Over a large temperature range, the superfluid density decreases linearly with T/T_c. This behaviour is consistent with theoretical predictions for the low-temperature penetration depth in a superconductor with gap nodes [99, 100, 101, 102] and measurements of the penetration depth for ultraclean samples of YBCO [98] (see also Section 1.3.1). In addition, the linear temperature-dependence of the superfluid density near T_c corroborates the mean-field scaling law predicted by the GL theory (Section 2.1). The resulting anisotropy of the penetration depths for the orthorhombic case $\lambda_a^2/\lambda_b^2 \approx 1.7$ closely matches experiment [69, 70, 71, 72], and demonstrates that the choice of the normal-state hopping ratio $t_y/t_x = 1.5$ adequately models transport in YBCO.

For a smaller electron density ($\mu = -2t_x$), the zero-temperature superfluid density is a larger fraction of $\langle n\rangle$, reflecting the lower anisotropy of the Fermi surface. In general, the ratio $n_s/\langle n\rangle \sim 1/m^*$ is found to decrease with carrier density, though the superfluid density itself increases. This result appears to be at odds with experiment [78]. It should be noted, however, that the present toy model employs electrons, rather than holes, as the charge carriers. Furthermore, while it yields a d-wave superconducting order parameter, the present theory only employs a variant of the usual BCS weak-coupling approach which does not necessarily fully describe the superconducting state of the cuprates.

As discussed in Section 2.5 within the framework of GL theory, the presence of external currents may induce subdominant s-wave components in clean d-wave superconductors. Fig. 5.4 shows the magnitudes of Δ_0 and Δ_s as a function of applied Cooper-pair momentum at zero temperature. In tetragonal systems, external currents are found to induce subdominant components unless $\mathbf{p}$ is oriented along the diagonal, in agreement with the GL theory. The induced real s-wave components grow with increasing superfluid velocity. A current directed along $\hat{x}$ induces isotropic and extended s-wave components with negative and positive sign relative to Δ_d, respectively; the same current along $\hat{y}$ switches the relative signs of Δ_0 and Δ_s. In short, the induced s-wave components reverse their sign through a 90° rotation of the applied current's orientation, which corroborates the $\cos 2\theta$ dependence of s/d

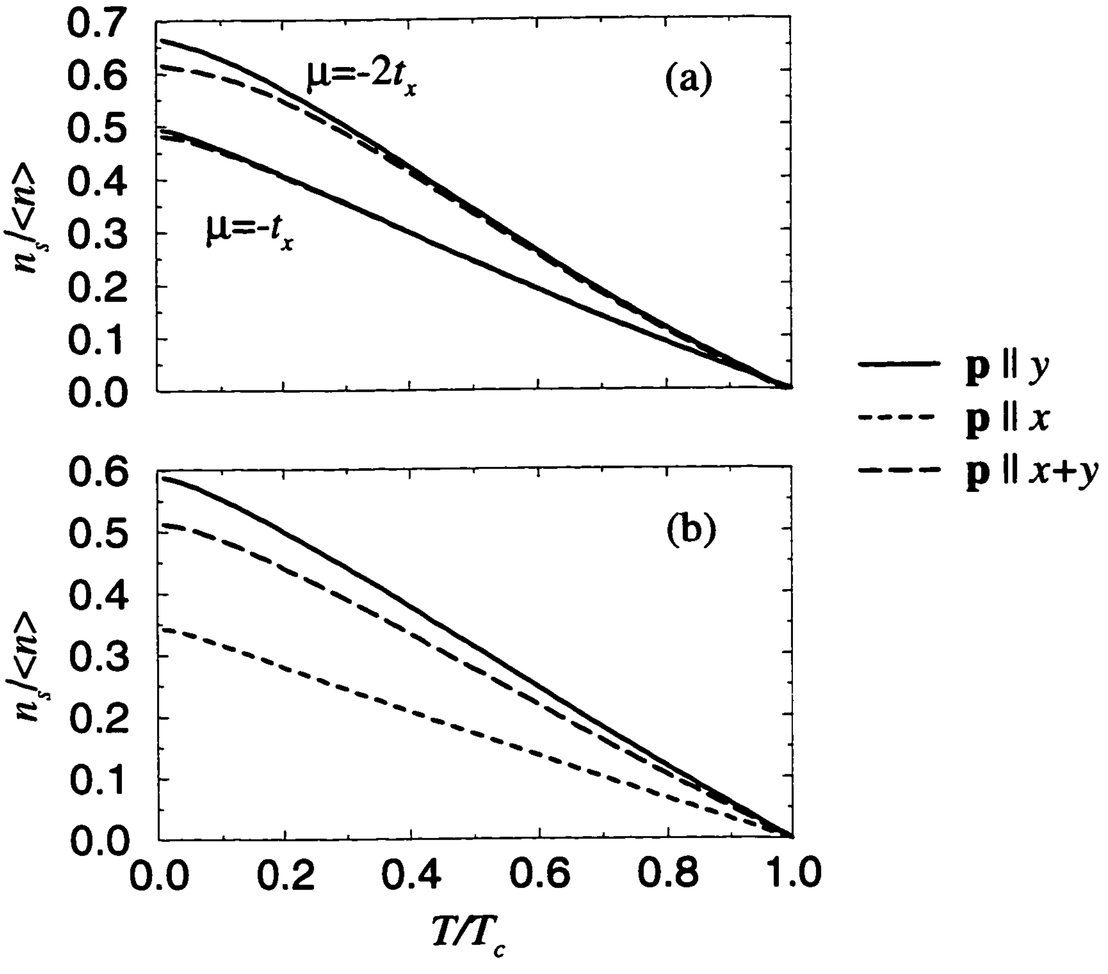

Figure 5.3: The superfluid density, normalized to the zero temperature particle number, is shown as a function of reduced temperature T/T_c for tetragonal (a) and orthorhombic (b) systems. The data are shown for a minimal applied current oriented along $\hat{y}$ (solid), $\hat{x}$ (short dashed), and $\hat{x}+\hat{y}$ (long dashed). Parameters are chosen to match those of Fig. 5.1, except in (a) the results for both $\mu=-t_x$ and $\mu=-2t_x$ are shown.

predicted by GL theory (see Section 2.5.2). At $\mathbf{p}_c$, the magnitudes of Δ_0 and Δ_s are approximately 10% of Δ_d, which in turn has been reduced by the currents.

In orthorhombic systems, the existing subdominant components are either enhanced or suppressed by the superfluid flow. Cooper-pair momenta oriented along the x-axis have the smallest effect, decreasing Δ_0 by approximately 10% at $\mathbf{p}_c$, and increasing the extended s-wave component to the same degree. Currents parallel to the chains, in contrast, have a profound influence. At $\mathbf{p}_c$, the isotropic component virtually doubles in size, while Δ_s almost completely disappears. In the absence of an on-site interaction, these results yield the curious conclusion that currents parallel to the y-axis induce orthorhombicity in tetragonal superconductors, and 'tetragonality' in orthorhombic systems. Momenta directed along the diagonal have a similar, though not as pronounced, effect as b-oriented currents, reflecting the lack of gap nodes in this direction. The subdominant components are found to be least perturbed when $p_x/p_y \approx 2$ for small applied momenta, which crosses over to $p_x/p_y \approx 3$ for large momenta. This clearly indicates that the orientation of the gap nodes varies with applied currents.

While the present formalism does not consider self-field effects that are known to be important at higher temperatures (see Section 2.5.1), it is nevertheless worthwhile to consider the temperature-dependence of the critical current. The critical current, defined as the maximum current response to an applied Cooper-pair momentum (see Fig. 5.1), is shown as a function of reduced temperature $t = T/T_c$ in Fig. 5.5. The results for both the orthorhombic and tetragonal systems are nearly indistinguishable. Near T_c, the critical current is found to vary as $j_c(T)/j_c(0) \sim (1-t)^{3/2}$, in agreement with the GL theory discussed in Section 2.5. At low temperatures, the critical current decreases with the composite power-law behaviour

$$j_c(T)/j_c(0) = 1 - \alpha t - \beta t^2, \tag{5.22}$$

where the best fit to the data yields $\alpha \approx 0.17$ and $\beta = 1.85$.

Surprisingly, the temperature-dependence of the critical current shows a remarkable superficial resemblance to experimental results for thin films of YBCO in the absence of external fields [239, 240]. In particular, the critical currents for clean

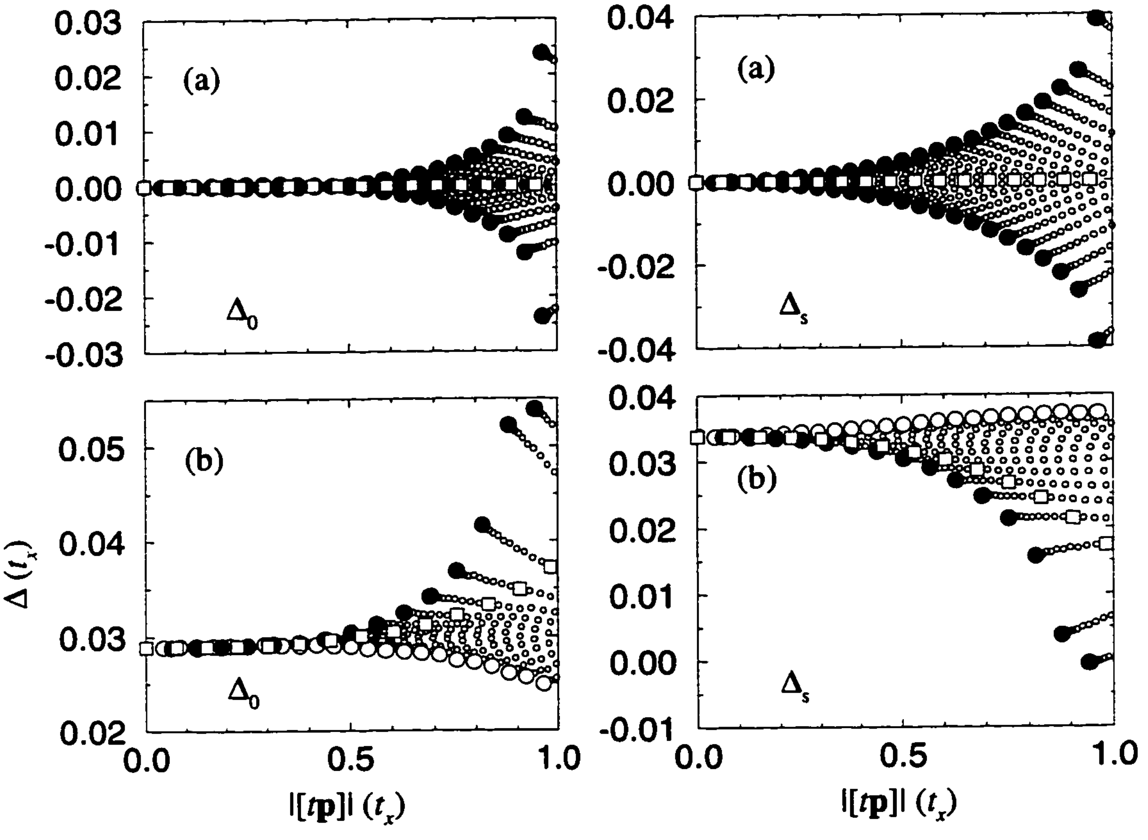

Figure 5.4: The s-wave components at zero temperature induced by the external currents are shown as a function of the direction and magnitude of the applied Cooper-pair momentum. The magnitude of the on-site (left) and extended (right) s-wave components are shown for tetragonal (a) and orthorhombic (b) systems. Parameters and symbols are as in Fig. 5.1.

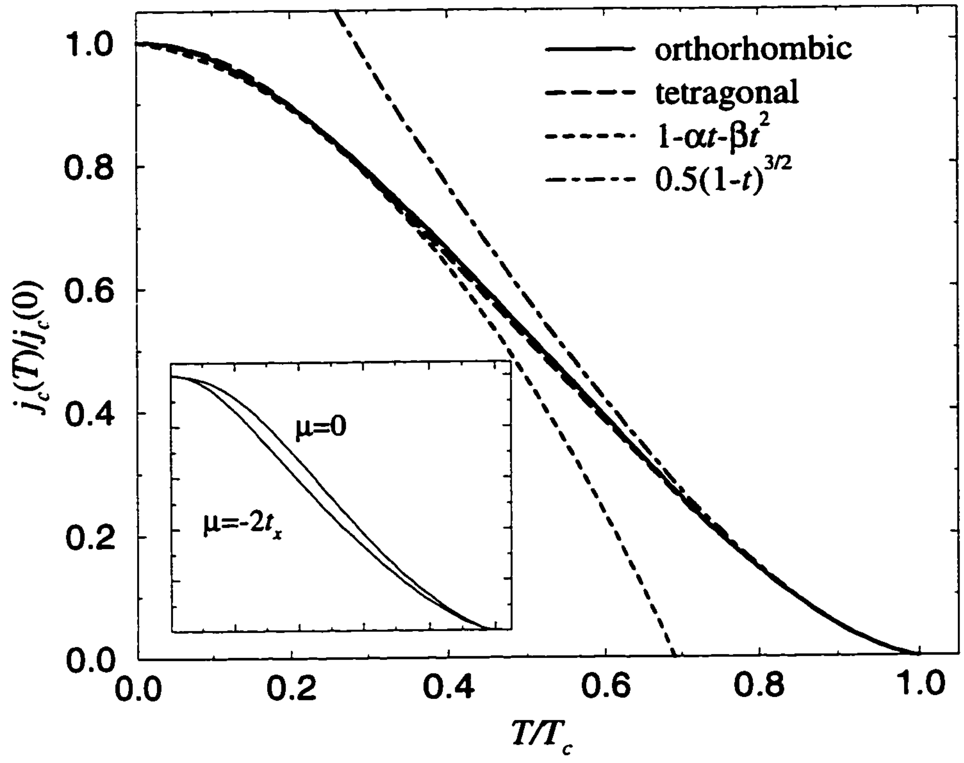

Figure 5.5: The normalized critical current $j_c(T)/j_c(T)$ is shown as a function of reduced temperature $t = T/T_c$ for both the orthorhombic (solid line) and tetragonal (dashed line) cases, and chemical potential $\mu = -t_x$. The low-temperature (dotted) and high-temperature (dot-dashed) behaviours are shown for comparison. The best fit at low temperatures is found for $\alpha = 0.17$ and $\beta = 1.85$. Parameters used are $-V_0 = V_1 = 3t_x$. The inset shows the variation of the temperature-dependent critical current with chemical potential.

materials are found to follow Eq. (5.22) at low to intermediate temperatures. Such behaviour is often explained in terms of the Anderson-Kim 'flux creep' model, where α and β are related to the vortex pinning energy [238, 250, 251, 252]. As the carrier density decreases from half-filling, the low-temperature plateau of the critical current shortens. This behaviour is either due to a decrease in the magnitude of the *d*-wave gap, or the Fermi surface anisotropy, at lower densities. Similar results are found experimentally; in underdoped materials the critical current follows the GL behaviour to lower temperatures. In the present system, however, neither the internal field associated with the currents nor the influence of intrinsic defects is considered, so the low-temperature behaviour of the critical current must have an origin different from flux creep. Indeed, the values of α and β obtained above are not close to those derived from experimental data, $\alpha = 0.72$, $\beta = 0.38$ [240]. It should be noted, however, that the mechanisms limiting critical currents in both clean and granular high-T_c materials are not presently well-understood, as discussed in [239].

5.3 Twin Boundaries

As discussed in Section 4.1.1, twin boundaries significantly influence the transport properties of YBCO, particularly at high temperatures where their flux-pinning properties are important. At low temperatures, the maximum supercurrents that may be supported by the high-T_c superconductors are largely limited by the intrinsic weak links, such as grain and twin boundaries. While critical current densities in YBCO have been greatly improved in recent years by minimizing large-angle grain boundaries in these materials [247], twin boundaries remain ubiquitous. While twin boundaries most likely act as weak superconducting links, their role in determining critical currents of YBCO at low temperatures remains unclear. It would be interesting to explore the consequences of external currents for many of the intriguing properties of *d*-wave superconductors near twin boundaries discussed in Chapter 4. In the present section, the behaviour of twinned YBCO in the presence of supercurrents is investigated numerically within the context of the BdG formalism described in the previous chapter, with particular emphasis on critical currents, time-reversal breaking, and bound states.

It should be emphasized at the outset that, in spatially non-uniform systems, the simulation of an applied current by the application of a Cooper-pair momentum cannot fully describe the behaviour of the resulting currents. A completely self-consistent calculation requires the determination of the vector potential. Since the inclusion of the vector potential would greatly complicate the present formalism, however, it is disregarded in the calculations. Thus, the results presented below are at best a first approximation of the correct current distributions in the sample.

In order to determine how the twin boundary structure affects its capacity to support supercurrents, the critical current densities in the twin boundary region have been calculated as a function of width W_T and impurity potential μ^I. Assuming YBCO at optimal doping, the chemical potential is set to zero (corresponding to electron density $\langle n \rangle = 1$). This choice not only yields the highest d-wave transition temperature in the bulk (see Section 3.3), but also simplifies the connection between the carrier depletion and the impurity potential. In this case, μ^I is identified as the chemical potential in the twin boundary region. For $\mu^I < -2.2t_x$, d-wave superconductivity is no longer locally favoured, while for $\mu^I = -5t_x$, the local carrier density vanishes completely (note that the bandwidth is $10t_x$ in the orthorhombic system). Using this approach, the theory best approximates the experimental observation that the strength of electromagnetic coupling across weak links is proportional to the local oxygen concentration [248, 249].

The critical currents at the center of a twin boundary are shown as a function of local chemical potential in Fig. 5.6 for widths $W_T = 2\hat{r}$ and $4\hat{r}$. It is found that the magnitudes of the critical current and the d-wave component in the twin boundary region scale closely with the local transition temperature as the impurity strength is varied. As the twin boundary width W_T is increased, carrier depletion more effectively suppresses both the d-wave gap function and the critical current. The critical chemical potential (at which no current flows through the link) is approximately $\mu_c^I \approx -1.75$ for $W_T = 4|\hat{r}|$, corresesonding to a low normal state density $\langle n \rangle = 0.43$. At this impurity strength, the twin boundary is equivalent to a d-wave — s-wave — d-wave junction, with the d-wave superconductor oriented at 45° to the interface. Due to the interference between the d-wave lobes, no supercurrent can flow across the twin boundary. Essentially the same result is obtained in uniform systems; the critical current is virtually zero near the cross-over to bulk s-wave superconductivity.

It is important to note that $|\mu_c^I|$ is significantly larger than that required to induce a zero-temperature time-reversal breaking state (see Fig. 4.7 in Section 4.3). The empirical criterion for $\mathcal{T}$-violation is that Δ_d in the link must be suppressed to approximately half its bulk value. Thus, $\mathcal{T}$-violating twin boundaries may support substantial critical currents.

The magnitude and direction of currents in the vicinity of a twin boundary are shown schematically in Fig. 5.7. Far from the twin edge, the current response is identical to that of a clean orthorhombic material. As shown in Section 5.2.1, the resulting current has components both parallel and perpendicular to the applied Cooper-pair momentum $\mathbf{p}$. This effect is due to the enhanced carrier mobility along the chains in the $(\hat{r} + \hat{R})$-direction since $t_y/t_x > 1$, and necessarily vanishes for applied momenta $\mathbf{p} = p_x$ or p_y. Like subdominant (bulk) s-wave gap functions in orthorhombic systems, the induced transverse component reverses its direction on either side of the twin boundary. If both twin domains occurred with equal probability, this component will average to zero; otherwise, there will generally be a net flow of charge perpendicular to an applied current. In the tetragonal twin boundary region, the applied and resulting currents are always collinear.

At this level of approximation, which neglects the vector potential, the twin edge behaves as an unphysical source and sink for current. Treated properly, the currents in the vicinity of the twin boundary would be enhanced in order to ensure that $\nabla \cdot \mathbf{j} = 0$ everywhere. Current conservation could be restored artificially in the present model by increasing the hopping parameter within the twin boundary. Nevertheless, the present calculation probably captures the correct qualitative behaviour of the currents near the twin boundary.

When the impurity strength is sufficient to give rise to a local $\mathcal{T}$-violating state, spontaneous currents flow in the vicinity of the twin boundary. These are shown in Fig. 4.13 and 5.7 for a twin boundary with essentially complete carrier depletion ($\mu^I = -10t_x$). For non-zero Cooper-pair momentum, the resulting current is found to

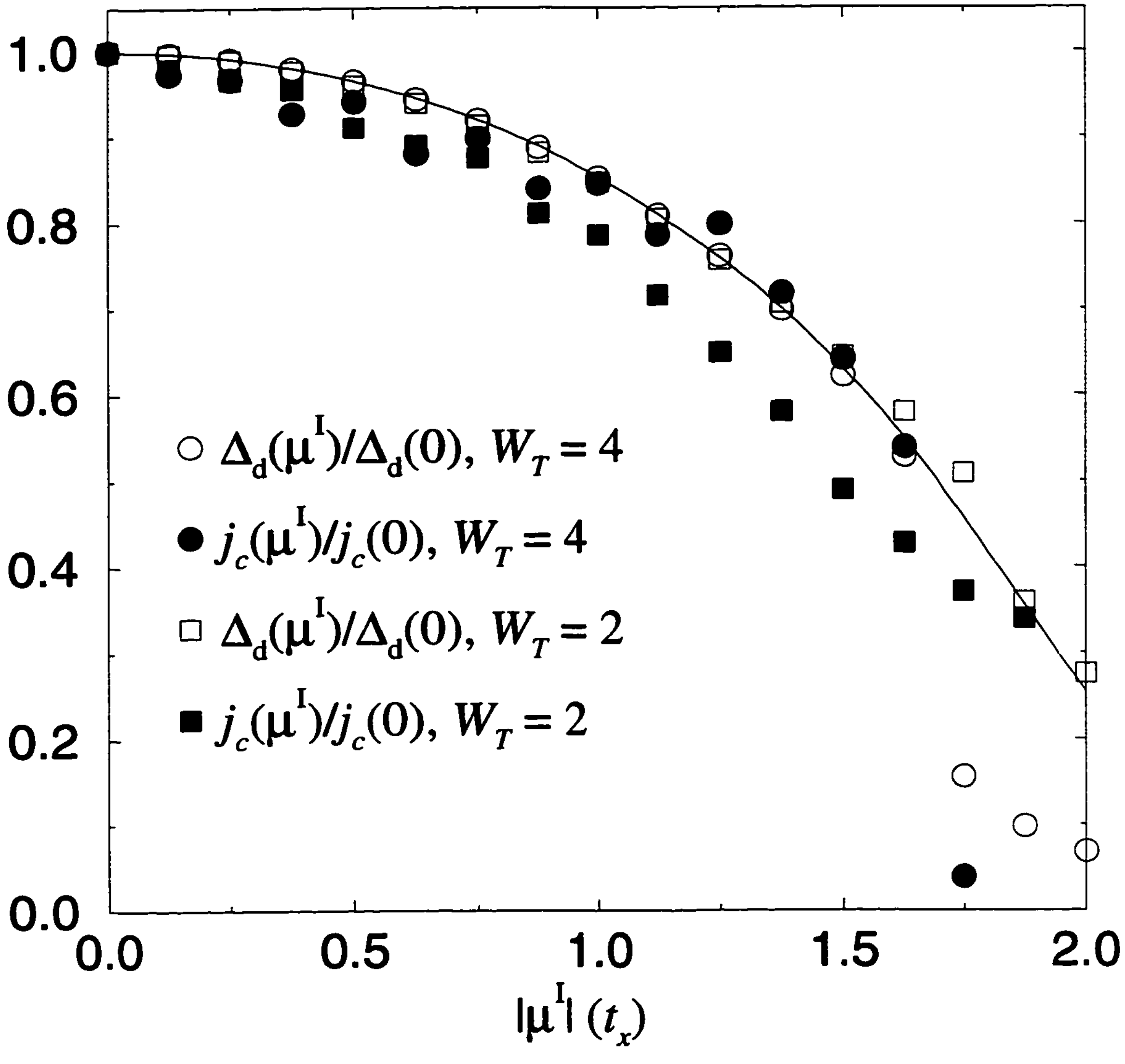

Figure 5.6: The zero-temperature critical current (filled symbols), and magnitude of the d-wave component (open symbols) in a twin boundary, are shown normalized to their values at $\mu^I = 0$. Results are obtained for two twin boundary widths $W_T = 2\hat{r}$ (squares) and $4\hat{r}$ (circles). The local reduced transition temperature $T_c(\mu^I)/T_c(\mu^I = 0)$ (solid line) is shown for comparison. Results are obtained on a 50 × 50 × 2-site lattice using $-V_0 = V_1 - 3t_x$.

be perturbed by the supercurrents only in the vicinity of the twin boundary. Beyond two or three lattice spacings, the behaviour is indistinguishable from that of the bulk. This result should be qualitatively correct for applied momentum parallel to the twin boundary; a fully self-consistent calculation would increase the resulting currents only in the vicinity of the twin edge (indeed, $\nabla \cdot \mathbf{j} \neq 0$ only at the particular points defining the twin edge). The results for perpendicular applied momentum $\mathbf{p} = p\hat{r}$ are not physical, however; the complete absence of current within the twin boundary region would likely force the perpendicular currents in the sample to vanish. The present approximation should improve as the carrier depletion decreases. In general, however, the effects of time-reversal breaking in the current-carrying state appear to be negligible.

As discussed in Sections 4.5 and 5.2.1, currents shift the low energy quasiparticle spectrum. In the time-reversal breaking phase, the spontaneous currents gave rise to a splitting of the zero-bias conductance peak, or ZBCP, in the tunneling conductance. The application of a center-of-mass momentum to the Cooper pair has the same effect, as illustrated in Fig. 5.8. The $\mathcal{T}$-preserving ground state at zero temperature displays a well-defined ZBCP at the twin edge in the absence of external currents. As the currents increase, significant changes in the tunneling density of states occurs. The ZBCP is shown to split while decreasing in size. The extent of the splitting is comparable to that caused by spontaneous currents, shown in Figs. 4.11 and 4.12. Indeed, the magnitudes of external currents for moderate Cooper-pair momenta are comparable to those of spontaneous currents in a strongly $\mathcal{T}$-violating state. Such a splitting of the ZBCP is often observed in tunneling spectra of high-T_c materials in the presence of external magnetic fields [232, 235, 253, 254]. The splitting is due to diamagnetic screening currents near the surface. The external currents are also strongly pair-breaking, as demonstrated by the pronounced suppression of the coherence peaks at $V = \Delta_d$ and the gradual 'filling in' of the superconducting gap. This effect is particularly noticeable in the bulk tunneling spectra, where there are no additional low-energy features. The large number of quasiparticle excitations caused by the depairing effectively washes out the ZBCP near the twin boundary.

The behaviour of a time-reversal breaking superconducting state in the presence

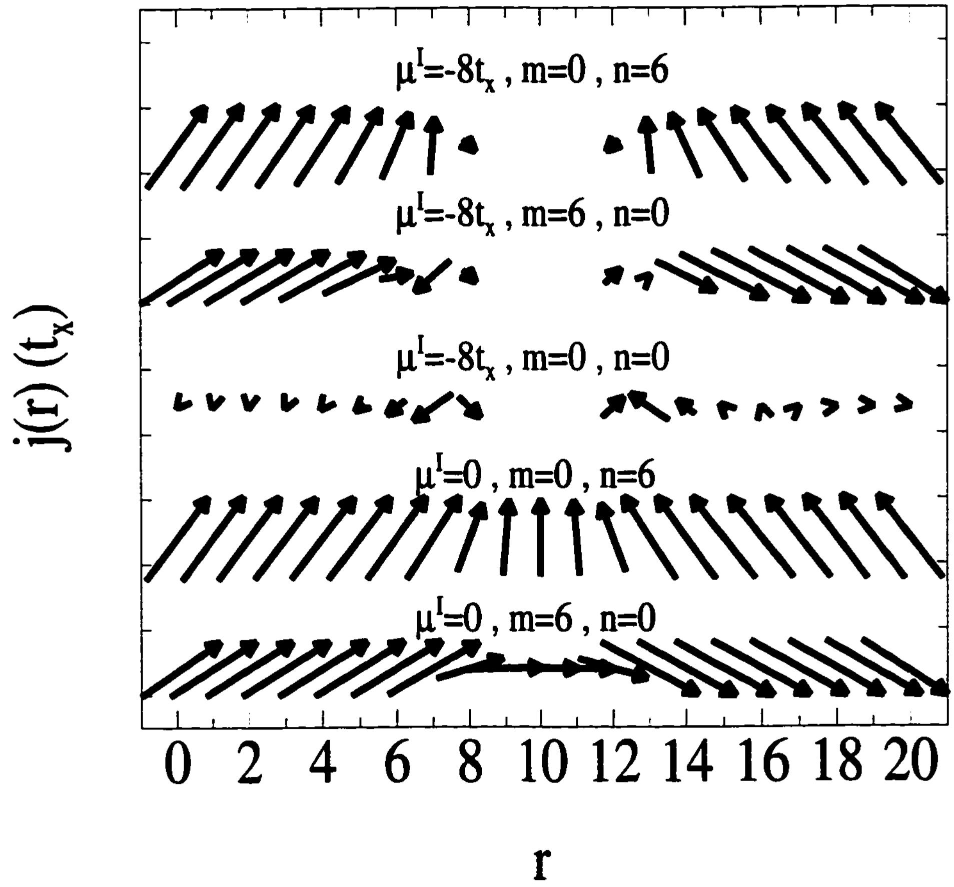

Figure 5.7: The magnitudes and directions of currents resulting from applied Cooper-pair momenta are shown as a function of distance perpendicular to a twin boundary. The length and direction of the arrows denote the current magnitude and orientation, respectively. Vertical and horizontal arrows correspond to directions parallel and perpendicular to the twin boundary. The system chosen contains 50×50×2 sites, but only those in the vicinity of the twin boundary are included for clarity; the twin boundary is $4\hat{r}$ wide and centered at $r = 10$. The applied momenta $\mathbf{p} = 2\pi/50\left(m\hat{r} + n\hat{R}\right)$ are just under the critical value $|\mathbf{p_c}|$ for a clean system. Parameters are $-V_0 = V_1 = 3t_x$, $\mu = -t_x$ and $t_y/t_x = 1.5$.

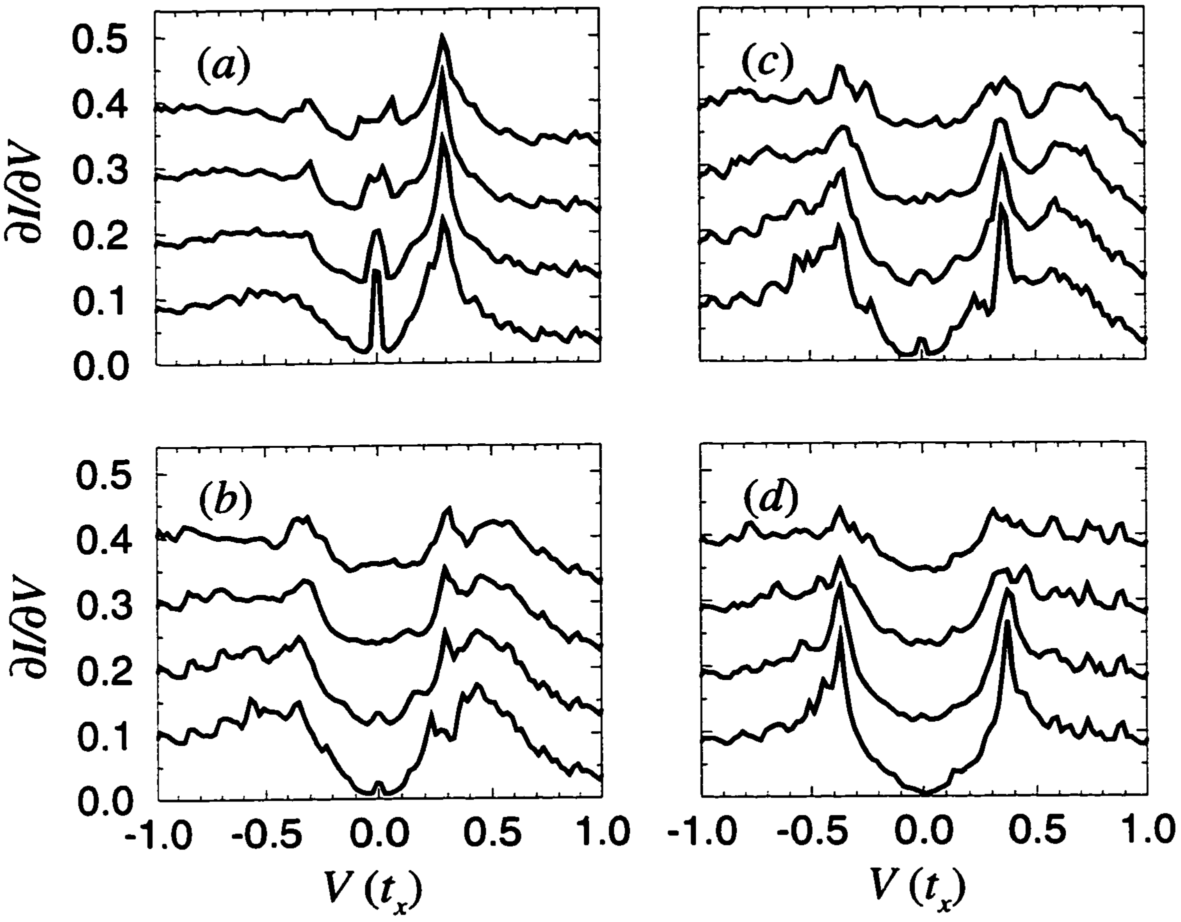

Figure 5.8: A low-energy portion of the zero-temperature tunneling conductance near a twin boundary is shown as a function of energy, distance r from the twin edge where (a) through (c) correspond to $|\hat{r}|$ through $3|\hat{r}|$ while (d) illustrates the bulk, and applied Cooper-pair momentum $\mathbf{p} = 0$ (lower), $\mathbf{p} = (4\pi/100)\hat{p}$ (offset 0.1), $\mathbf{p} = (8\pi/100)\hat{p}$ (offset 0.2), and $\mathbf{p} = (12\pi/100)\hat{p}$ (offset 0.3). Parameters chosen are $-V_0 = V_1 = 3t_x$, $\mu = -t_x$, $\mu^I = -2t_x$, and $W_T = 0$, which yield a time-reversal preserving d-wave ground state in the absence of external currents.

of external currents may help to clarify the experimental evidence for $\mathcal{T}$-violation in YBCO. As discussed in Section 4.1.3, the imaginary s-wave component associated with the $\mathcal{T}$-violation may be the reason for the finite c-axis tunneling currents observed to flow between twinned YBCO and Pb [208]. As described in Chapter 4, while the real s-wave components have opposite signs in adjacent twin domains, the imaginary components always have the same sign (see also Figs. 4.4 and 4.6). Only these imaginary components would remain in heavily-twinned samples, and would couple to the isotropic s-wave BCS order parameter of the lead, yielding the observed c-axis tunneling currents.

Fig. 5.9 illustrates the behaviour of the imaginary s-wave components for a $\mathcal{T}$-violating system in the presence of an applied Cooper-pair momentum, oriented either parallel or perpendicular to the twin boundary. The results are striking when compared with the current-free results (Section 4.3, Figs. 4.4-4.6). As soon as the external currents become finite, the imaginary s-wave component within a given twin domain gradually reverses its sign. This behaviour is independent of the relative positions of the twin boundary, as well as the magnitude and orientation of the external current. Thus, a nominal voltage applied in the ab-direction should rapidly suppress the c-axis tunneling currents measured by Dynes *et al.*, if the imaginary s-wave components in YBCO are indeed coupling to the order parameter of the lead. In contrast, small currents have virtually no effect on the real components, except for a negligible suppression of Δ_d and enhancement of Δ_0 and Δ_s found for clean systems.

It is not clear how the behaviour of the imaginary components will be altered by a fully self-consistent calculation of the resulting currents. The data presented above indicate that there should be only minor corrections for applied momenta parallel to the twin boundary, or for perpendicular applied momenta with weak carrier depletion in the twin boundary. In the absence of a more sophisticated calculation, more experimental data is required in order to determine whether imaginary components are indeed present near twin boundaries in YBCO.

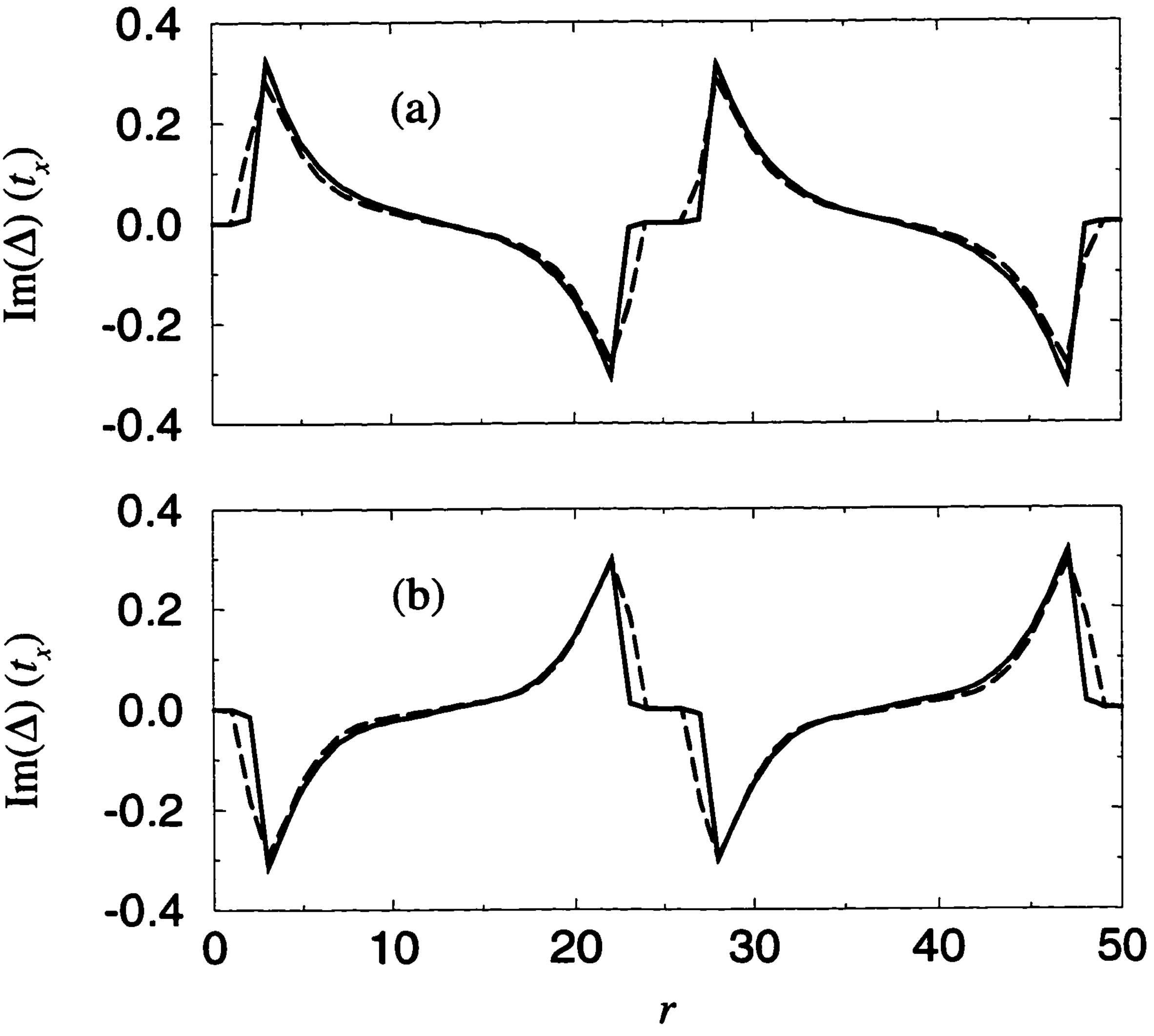

Figure 5.9: The imaginary components of Δ_0 (solid line) and Δ_s (dashed line) at zero temperature are shown as a function of distance r perpendicular to the twin boundary for finite external currents (a) $\mathbf{p} = (4\pi/50)\hat{r}$ and (b) $\mathbf{p} = (4\pi/50)\hat{R}$. The extended s-wave component is multiplied by a factor of -10 in order to facilitate comparison with the on-site component. Results are obtained on a $50 \times 50 \times 2$-site lattice using $\mu = -t_x$, $-V_0 = V_1 = 3t_x$, $\mu^I = -8t_x$, and $W_T = 4|\hat{r}|$.

5.4 Summary and Discussion

In this chapter, the response of *d*-wave superconductors to external currents has been addressed within the context of Bogoliubov-de Gennes theory. Only depairing effects have been considered. The results for both clean and twinned systems have provided a more detailed understanding of the superfluid characteristics of inhomogeneous high-T_c materials at low temperatures. Furthermore, several predictions are made for the behaviour of YBCO in the presence of external currents.

In clean materials, the induced currents have been calculated as a function of Cooper-pair momentum and temperature. The superfluid densities and critical currents are found to be highly anisotropic both in tetragonal and orthorhombic systems. In tetragonal materials, the current response is maximized for momenta applied along either a or b, and minimized for external currents directed along the diagonals. In orthorhombic materials, the orientations of the applied and resulting currents are different, due to the inherent anisotropy in charge transport. The center-of-mass momentum elicits a response when oriented parallel to the chains that is almost double the response when oriented along a. The resulting anisotropy, as well as the linear temperature-dependence, of the ab-plane penetration depth closely matches experimental data for YBCO [69, 70, 71, 72, 98]. The temperature-dependence of the critical current also resembles the experimental results [239, 240], even though self-field effects are ignored in the theoretical analysis. The behaviour is found to agree with the predictions of GL theory at high temperatures, while at low temperatures the critical current has a power-law temperature-dependence that is sensitive to carrier concentration.

The induction and perturbation of subdominant s-wave components by external currents has been studied in detail for clean tetragonal and orthorhombic d-wave superconductors. In tetragonal materials, Cooper-pair momenta along a or b generate, and determine the magnitude of, both isotropic and extended s-wave components. The sign of the s-wave components relative to Δ_d reverses as the applied current rotates by 90°, as predicted by GL theory. The magnitude of the subdominant components is found to be at most 10% of the d-wave gap at the critical current.

In orthorhombic materials, the existing s-wave components are either enhanced or suppressed by the external currents. At the critical current, the extended s-wave component is almost completely suppressed by Cooper-pair momenta parallel to the chains.

The consequences of a Cooper-pair momentum have been investigated for a twinned YBCO thin film. The current response in the vicinity of the twin boundary has been studied for both the time-reversal-preserving and $\mathcal{T}$-violating phases. In the former case, the applied momenta split the zero-bias conductance peak, demonstrating that the currents indeed shift the quasiparticle energies. In the latter case, even very small applied currents drastically alter the spatial-dependence of existing imaginary components: in each twin, the imaginary components average to zero. Thus, the c-axis tunneling currents between YBCO and Pb observed experimentally [208] may rapidly vanish in the presence of an applied ab-oriented current.

The critical current through the twin boundary has been calculated with the width and carrier depletion of the twin boundary as the adjustable parameters. The transition temperature for a uniform tetragonal d-wave superconductor provides a good estimate for the critical current in the carrier-reduced twin boundary region. A parameter regime is found such that twin boundaries may both support significant critical currents as well as favour local $\mathcal{T}$-violation.

Chapter 6

Conclusions

The behaviour of $d_{x^2-y^2}$-wave (d-wave) superconductors in the presence of inhomogeneities has been investigated both analytically and numerically. Two microscopic lattice models used to describe the high-T_c superconductors have been employed in the calculations: the extended Hubbard (EH) model, and the Antiferromagnetic van Hove (AvH) model. The inhomogeneities considered have been external magnetic fields, twin boundaries, and external currents.

Whenever inhomogeneities give rise to variations of the d-wave order parameter, subdominant components arise. In lattice models, these components tend to have s-wave symmetry, since both d-wave and s-wave gap functions are generated by the same nearest-neighbour coupling. The mechanism through which the subdominant components are generated is different for each of the inhomogeneities studied in this thesis, however. External magnetic fields nucleate s-wave components through spatial variations of the d-wave component in the vortex core. Twin boundaries suppress the d-wave gap function, locally favouring an additional superconducting phase transition with an imaginary s-wave gap function as secondary order parameter. External currents induce subdominant s-wave components through phase variations of the d-wave component. The characteristics of the s-wave components, such as their magnitude relative to the d-wave gap function, and length scale for variations, are also found to depend strongly on the nature of the inhomogeneity.

The magnitude of the s-wave components nucleated in the core of a magnetic vortex has been determined within Ginzburg-Landau (GL) theory. The GL equations have been derived microscopically within the context of the EH and AvH models. While the results depend strongly on carrier density, coupling strength, and temperature, the models suggest that the maximum subdominant components induced in the vortex could be as large as $20 - 30\%$ of the bulk d-wave gap function. Such appreciable s-wave components should give rise to a significant four-fold anisotropy of the vortex core, and distort the Abrikosov flux lattice from triangular. Similar, but competing, effects are also found to result from Fermi surface anisotropy. The results compare favourably with recent tunneling and small angle neutron experiments on the cuprates.

The behaviour of the superconducting order parameter near twin boundaries has been investigated numerically using the Bogoliubov-de Gennes (BdG) formalism, within the context of an orthorhombic EH model. The twin boundaries are represented by tetragonal regions of variable width, with a locally reduced carrier density. At low temperatures, subdominant components are found to be induced through two distinct mechanisms. The spatial variations of the d-wave gap function near a carrier-depleted twin boundary induces real s-wave components, approximately doubling the existing small s-wave gap functions. As in the vortex core, the additional components disappear over a length scale of the d-wave coherence length. If the d-wave component is strongly suppressed, to approximately half its bulk value or more, a local phase transition to a time-reversal breaking state may occur at a low temperature T^*. The order parameter characterizing the secondary superconducting phase is an imaginary s-wave component which may be large compared with the d-wave gap, and which varies over an independent length scale. The magnitudes of the imaginary components, and the value of T^*, are found to depend strongly on the electron density and the twin boundary attributes. The results provide an explanation for recent tunneling data.

The behaviour of d-wave superconductors in the presence of external currents has been investigated numerically within the BdG formalism and the EH model. Both clean systems and those containing twin boundaries have been considered. Real s-wave components are found to be either induced or suppressed by phase variations of the *d*-wave component. The characteristics of the subdominant gap functions depend on the orientation and magnitude of the external currents. In the time-reversal breaking phase, the existing imaginary *s*-wave components are strongly perturbed by the currents, with novel and observable consequences for tunneling experiments. The temperature- and direction-dependences of the superfluid density and depairing critical currents have also been calculated, and compare favourably with experimental measurements on YBCO where data is available.

Appendix A

Lattice Taylor Expansions

In this appendix the lattice Taylor expansion for a slowly-varying periodic function in the presence of an external magnetic field is derived. The scale of spatial variations must be longer than the lattice spacing, but shorter than the system size (otherwise one could simply employ the usual Taylor expansion) and penetration depth. The derived Taylor series is then used to compute the low-order gradient terms of the self-consistent gap equations.

In the presence of a gauge field, the lattice derivative operating on an aribtrary function $f(\mathbf{r})$ is

$$i(\hat{z}\Pi_z)f(\mathbf{r}) = e^{i\frac{4\pi}{\phi_0}A_z(\mathbf{r})}f(\mathbf{r}+\hat{z}) - f(\mathbf{r}), \tag{A.1}$$

where $\hat{z} = \hat{x}, \hat{y}$. For reasons that will become clear shortly, this equation may be re-written:

$$e^{i\frac{4\pi}{\phi_0}A_z(\mathbf{r})}f(\mathbf{r}+\hat{z}) = i(\hat{z}\Pi_z)f(\mathbf{r}) + f(\mathbf{r}). \tag{A.2}$$

The second derivative is the left-hand side of (A.1) operating twice:

$$-(\hat{z}\Pi_z)^2 f(\mathbf{r}) = e^{i\frac{4\pi}{\phi_0}2A_z(\mathbf{r})}f(\mathbf{r}+2\hat{z}) - 2e^{i\frac{4\pi}{\phi_0}A_z(\mathbf{r})}f(\mathbf{r}+\hat{z}) + f(\mathbf{r}). \tag{A.3}$$

With (A.2), this in turn may be re-written:

$$e^{i\frac{4\pi}{\phi_0}2A_z(\mathbf{r})}f(\mathbf{r}+2\hat{z}) = -(\hat{z}\Pi_z)^2 f(\mathbf{r}) + 2i(\hat{z}\Pi_z)f(\mathbf{r}) + f(\mathbf{r}). \tag{A.4}$$

Similarly, one obtains

$$e^{i\frac{4\pi}{\phi_0}3A_z(\mathbf{r})}f(\mathbf{r}+3\hat{z}) = -i(\hat{z}\Pi_z)f(\mathbf{r}) - 3(\hat{z}\Pi_z)^2 f(\mathbf{r}) + 3i(\hat{z}\Pi_z)f(\mathbf{r}) + f(\mathbf{r}). \tag{A.5}$$

It becomes successively more obvious that the coefficients of the lattice derivatives follow a geometric progression. One then obtains the lattice Taylor series:

$$\begin{aligned} e^{i\frac{4\pi}{\phi_0}nA_z(\mathbf{r})}f(\mathbf{r}+n\hat{z}) &= f(\mathbf{r})+n\,i(\hat{z}\Pi_z)f(\mathbf{r})-\frac{n(n-1)}{2}(\hat{z}\Pi_z)^2f(\mathbf{r}) \\ &- \frac{n(n-1)(n-2)}{6}i(\hat{z}\Pi_z)^3f(\mathbf{r}) \\ &+ \frac{n(n-1)(n-2)(n-3)}{24}(\hat{z}\Pi_z)^4f(\mathbf{r})+\ldots. \end{aligned} \tag{A.6}$$

Note that in the continuum limit $\hat{z}\to 0$, $n\to\infty$, $n\hat{z}\equiv z<1$ one recovers the usual Taylor series:

$$f(\mathbf{r}+z) = f(\mathbf{r})+z\hat{\Pi}_zf(\mathbf{r})+\frac{z^2}{2!}\hat{\Pi}_z^2f(\mathbf{r})+\frac{z^3}{3!}\hat{\Pi}_z^3f(\mathbf{r})+\frac{z^4}{4!}\hat{\Pi}_z^4f(\mathbf{r})+\ldots, \tag{A.7}$$

where

$$\hat{\Pi}_z \equiv \frac{\partial}{\partial z}+i\frac{4\pi}{\phi_0}A_z(\mathbf{r}) \tag{A.8}$$

is the continuum version of the lattice difference $i(\hat{x}\Pi_x)$.

The lattice Taylor series will now be applied to the first term in Eq. (3.37):

$$\frac{1}{V_\alpha}\Delta_\alpha^*(\mathbf{r}) = -T\sum_{\mathbf{r}'',\omega_n}\tilde{\mathcal{G}}^\circ(\mathbf{r}'',\mathbf{r},-\omega_n)\Delta^*(\mathbf{r}'')\tilde{\mathcal{G}}^\circ(\mathbf{r}'',\mathbf{r}+\vec{\alpha},\omega_n). \tag{A.9}$$

Making use of Eqs. (3.38) and (3.39), this may be re-expressed as

$$\begin{aligned} \frac{1}{V_\alpha}e^{i\frac{2\pi}{\phi_0}\mathbf{A}(\mathbf{r})\cdot\vec{\alpha}}\Delta_\alpha^*(\mathbf{r}) &\approx -T\sum_{\mathbf{r}'',\omega_n,\vec{\alpha}'}\mathcal{G}^\circ(\mathbf{r}''-\mathbf{r},-\omega_n)(-1)^{|\vec{\alpha}'|}e^{i\frac{2\pi}{\phi_0}\mathbf{A}(\mathbf{r})\cdot\vec{\alpha}'}\Delta_{\alpha'}^*(\mathbf{r}'') \\ &\quad\times\mathcal{G}^\circ(\mathbf{r}''-\mathbf{r}-\vec{\alpha}+\vec{\alpha}',\omega_n)e^{i\frac{4\pi}{\phi_0}\mathbf{A}(\mathbf{r})\cdot(\mathbf{r}''-\mathbf{r})} \\ &= -T\sum_{\mathbf{z},\omega_n,\vec{\alpha}'}(-1)^{|\vec{\alpha}'|}e^{i\frac{2\pi}{\phi_0}\mathbf{A}(\mathbf{r})\cdot\vec{\alpha}'}\mathcal{G}^\circ(\mathbf{z},-\omega_n)\mathcal{G}^\circ(\mathbf{z}-\vec{\alpha}+\vec{\alpha}',\omega_n) \\ &\quad\times e^{i\frac{4\pi}{\phi_0}\mathbf{A}(\mathbf{r})\cdot\mathbf{z}}\Delta_{\alpha'}^*(\mathbf{r}+\mathbf{z}) \end{aligned} \tag{A.10}$$

where $\mathbf{z}\equiv\mathbf{r}''-\mathbf{r}$. The gap functions Δ^* vary slowly compared to the Green functions $\mathcal{G}^\circ(\mathbf{z})$, which give an appreciable contribution only over a few small $\mathbf{z}\equiv m\hat{x}+n\hat{y}$.

For the EH model, the last line of Eq. (A.10) may be expanded in a lattice Taylor series about $\mathbf{z}$:

$$\begin{aligned}
&\frac{1}{V_\alpha} e^{i\frac{2\pi}{\phi_0}\mathbf{A}(\mathbf{r})\cdot\vec{\alpha}}\Delta^*_\alpha(\mathbf{r}) \\
&\quad = -T\sum_{m,n,\omega_n,\vec{\alpha}'} (-1)^{|\vec{\alpha}'|} e^{i\frac{2\pi}{\phi_0}\mathbf{A}(\mathbf{r})\cdot\vec{\alpha}'} \mathcal{G}^\circ(m\hat{x}+n\hat{y},-\omega_n)\mathcal{G}^\circ(m\hat{x}+n\hat{y}-\vec{\alpha}+\vec{\alpha}',\omega_n) \\
&\quad \times\Big\{\Delta^*_{\alpha'}(\mathbf{r}) + m\, i(\hat{x}\Pi_x)\Delta^*_{\alpha'}(\mathbf{r}) - \frac{m(m-1)}{2}(\hat{x}\Pi_x)^2\Delta^*_{\alpha'}(\mathbf{r}) + \ldots \\
&\quad\quad + n\, i(\hat{y}\Pi_y)\Delta^*_{\alpha'}(\mathbf{r}) - \frac{n(n-1)}{2}(\hat{y}\Pi_y)^2\Delta^*_{\alpha'}(\mathbf{r}) + \ldots \\
&\quad\quad - mn(\hat{x}\Pi_x)(\hat{y}\Pi_y)\Delta^*_{\alpha'}(\mathbf{r}) + \frac{m(m-1)n(n-1)}{4}(\hat{x}\Pi_x)^2(\hat{y}\Pi_y)^2\Delta^*_{\alpha'}(\mathbf{r}) + \ldots\Big\}.
\end{aligned} \tag{A.11}$$

Since the system contains a center of symmetry, all terms with an odd number of lattice derivatives will vanish. For tetragonal, but not orthorhombic systems, $\mathcal{G}^\circ(\pm m\hat{x}+n\hat{y}) = \mathcal{G}^\circ(\mp m\hat{x}-n\hat{y})$, so all terms with an odd number of $(\hat{x}\Pi_x)$ or $(\hat{y}\Pi_y)$ will also vanish. To fourth order in gradients, therefore, the first term of Eq. (3.37) for tetragonal systems becomes:

$$\begin{aligned}
&\frac{1}{V_\alpha} e^{i\frac{2\pi}{\phi_0}\mathbf{A}(\mathbf{r})\cdot\vec{\alpha}}\Delta^*_\alpha(\mathbf{r}) \\
&\quad = -T\sum_{m,n,\omega_n,\vec{\alpha}'} (-1)^{|\vec{\alpha}'|} e^{i\frac{2\pi}{\phi_0}\mathbf{A}(\mathbf{r})\cdot\vec{\alpha}'} \mathcal{G}^\circ(m\hat{x}+n\hat{y},-\omega_n)\mathcal{G}^\circ(m\hat{x}+n\hat{y}-\vec{\alpha}+\vec{\alpha}',\omega_n) \\
&\quad \times\Big\{\Delta^*_{\alpha'}(\mathbf{r}) - \epsilon^{\mathrm{EH}}_{x,1}(\hat{x}\Pi_x)^2\Delta^*_{\alpha'}(\mathbf{r}) - \epsilon^{\mathrm{EH}}_{y,1}(\hat{y}\Pi_y)^2\Delta^*_{\alpha'}(\mathbf{r}) \\
&\quad\quad - \epsilon^{\mathrm{EH}}_{x,2}(\hat{x}\Pi_x)^4\Delta^*_{\alpha'}(\mathbf{r}) - \epsilon^{\mathrm{EH}}_{y,2}(\hat{y}\Pi_y)^4\Delta^*_{\alpha'}(\mathbf{r}) - \epsilon^{\mathrm{EH}}_{xy,2}(\hat{x}\Pi_x)^2(\hat{y}\Pi_y)^2\Delta^*_{\alpha'}(\mathbf{r})\Big\}.
\end{aligned} \tag{A.12}$$

The coefficients of the gradient terms appearing in this equation and (3.43) are:

$$\epsilon^{\mathrm{EH}}_{x,1} = \frac{1}{2}|m|(|m|-1); \tag{A.13}$$

$$\epsilon^{\mathrm{EH}}_{y,1} = \frac{1}{2}|n|(|n|-1); \tag{A.14}$$

$$\epsilon^{\mathrm{EH}}_{x,2} = -\frac{1}{24}|m|(|m|-1)(|m|-2)(|m|-3); \tag{A.15}$$

$$\begin{aligned}\epsilon^{\mathrm{EH}}_{y,2} &= -\frac{1}{24}|n|(|n|-1)(|n|-2)(|n|-3); &\text{(A.16)}\\ \epsilon^{\mathrm{EH}}_{xy,2} &= -\frac{1}{4}|m|(|m|-1)|n|(|n|-1). &\text{(A.17)}\end{aligned}$$

The derivation of the gradient terms for the AvH model proceeds in a similar fashion, starting from (A.10). Since $\mathbf{z} = m\hat{r}_1 + n\hat{r}_2$, where $\hat{r}_1 = \hat{x} + \hat{y}$ and $\hat{r}_1 = \hat{x} - \hat{y}$, one obtains

$$\begin{aligned}&\frac{1}{V_\alpha} e^{i\frac{2\pi}{\phi_0}\mathbf{A}(\mathbf{r})\cdot\vec{\alpha}} \Delta^*_\alpha(\mathbf{r})\\ &\quad = -T \sum_{m,n,\omega_n,\vec{\alpha}'} (-1)^{|\vec{\alpha}'|} e^{i\frac{2\pi}{\phi_0}\mathbf{A}(\mathbf{r})\cdot\vec{\alpha}'} \mathcal{G}^\circ(m\hat{r}_1 + n\hat{r}_2, -\omega_n) \mathcal{G}^\circ(m\hat{r}_1 + n\hat{r}_2 - \vec{\alpha} + \vec{\alpha}', \omega_n)\\ &\quad \times\Big\{ \Delta^*_{\alpha'}(\mathbf{r}) + m\; i(\hat{r}_1\Pi_{r_1})\Delta^*_{\alpha'}(\mathbf{r}) - \frac{m(m-1)}{2}(\hat{r}_1\Pi_{r_1})^2\Delta^*_{\alpha'}(\mathbf{r}) + \ldots\\ &\quad\; + n\; i(\hat{r}_2\Pi_{r_2})\Delta^*_{\alpha'}(\mathbf{r}) - \frac{n(n-1)}{2}(\hat{r}_2\Pi_{r_2})^2\Delta^*_{\alpha'}(\mathbf{r}) + \ldots\\ &\quad\; - mn(\hat{r}_1\Pi_{r_1})(\hat{r}_2\Pi_{r_2})\Delta^*_{\alpha'}(\mathbf{r}) + \frac{m(m-1)n(n-1)}{4}(\hat{r}_1\Pi_{r_1})^2(\hat{r}_2\Pi_{r_2})^2\Delta^*_{\alpha'}(\mathbf{r}) \Big\}.\end{aligned} \tag{A.18}$$

The conversion to x- and y-gradients is accomplished by means of the transformations

$$\begin{aligned}(\hat{r}_1\Pi_{r_1}) &\equiv i\,(\hat{x}\Pi_x)\,(\hat{y}\Pi_y) + (\hat{x}\Pi_x) + (\hat{y}\Pi_y)\,; &\text{(A.19)}\\ (\hat{r}_2\Pi_{r_2}) &\equiv -i\,(\hat{x}\Pi_x)\,(\hat{y}\Pi_y) + (\hat{x}\Pi_x) - (\hat{y}\Pi_y)\,, &\text{(A.20)}\end{aligned}$$

which may be easily proved by the application of (A.2):

$$\begin{aligned}e^{i\frac{4\pi}{\phi_0}A_{r_1}(\mathbf{r})} f(\mathbf{r} + \hat{r}_1) &= e^{i\frac{4\pi}{\phi_0}(A_x(\mathbf{r})+A_y(\mathbf{r}))} f(\mathbf{r} + \hat{x} + \hat{y}) = i(\hat{r}_1\Pi_{r_1})f(\mathbf{r}) + f(\mathbf{r})\\ &= i(\hat{x}\Pi_x)f(\mathbf{r}+\hat{y}) + f(\mathbf{r}+\hat{y})\\ &= i^2(\hat{y}\Pi_y)(\hat{x}\Pi_x)f(\mathbf{r}) + i(\hat{x}\Pi_x)f(\mathbf{r}) + i(\hat{y}\Pi_y)f(\mathbf{r}) + f(\mathbf{r}).\end{aligned} \tag{A.21}$$

Equating the last term in the first line with the last line immediately yields (A.19), while (A.20) follows from the antisymmetry of the y-gradient term for $\hat{y} \to -\hat{y}$. Inserting (A.19) and (A.20) into (A.18), and discarding terms that vanish either due to centrosymmetry or orthorhombicity, one obtains:

$$
\begin{aligned}
&\frac{1}{V_\alpha} e^{i\frac{2\pi}{\phi_0}\mathbf{A}(\mathbf{r})\cdot\vec{\alpha}} \Delta^*_\alpha(\mathbf{r}) \\
&= -T \sum_{m,n,\omega_n,\vec{\alpha}'} (-1)^{|\vec{\alpha}'|} e^{i\frac{2\pi}{\phi_0}\mathbf{A}(\mathbf{r})\cdot\vec{\alpha}'} \mathcal{G}^\circ(m\hat{r}_1 + n\hat{r}_2, -\omega_n)\mathcal{G}^\circ(m\hat{r}_1 + n\hat{r}_2 - \vec{\alpha} + \vec{\alpha}', \omega_n) \\
&\times\Big\{\Delta^*_{\alpha'}(\mathbf{r}) - \epsilon^{\mathrm{AvH}}_{x,1}(\hat{x}\Pi_x)^2\Delta^*_{\alpha'}(\mathbf{r}) - \epsilon^{\mathrm{AvH}}_{y,1}(\hat{y}\Pi_y)^2\Delta^*_{\alpha'}(\mathbf{r}) \\
&\quad -\epsilon^{\mathrm{AvH}}_{x,2}(\hat{x}\Pi_x)^4\Delta^*_{\alpha'}(\mathbf{r}) - \epsilon^{\mathrm{AvH}}_{y,2}(\hat{y}\Pi_y)^4\Delta^*_{\alpha'}(\mathbf{r}) - \epsilon^{\mathrm{AvH}}_{xy,2}(\hat{x}\Pi_x)^2(\hat{y}\Pi_y)^2\Delta^*_{\alpha'}(\mathbf{r})\Big\}. \quad \text{(A.22)}
\end{aligned}
$$

The coefficients of the gradients terms here and in (3.47) are

$$\epsilon^{\mathrm{AvH}}_{x,1} = \frac{1}{2}\Big[|m|(|m|-1) + |n|(|n|-1) + 2mn\Big]; \tag{A.23}$$

$$\epsilon^{\mathrm{AvH}}_{y,1} = \frac{1}{2}\Big[|m|(|m|-1) + |n|(|n|-1) - 2mn\Big]; \tag{A.24}$$

$$
\begin{aligned}
\epsilon^{\mathrm{AvH}}_{x,2} = {} & -\frac{1}{24}\Big[|m|(|m|-1)(|m|-2)(|m|-3) + |n|(|n|-1)(|n|-2)(|n|-3)\Big] \\
& -\frac{1}{12}|m||n|\Big\{3(|m|-1)(|n|-1) \\
& \quad +2\Big[(|m|-1)(|m|-2) + (|n|-1)(|n|-2)\Big]\Big\};
\end{aligned} \tag{A.25}
$$

$$
\begin{aligned}
\epsilon^{\mathrm{AvH}}_{y,2} = {} & -\frac{1}{24}\Big[|m|(|m|-1)(|m|-2)(|m|-3) + |n|(|n|-1)(|n|-2)(|n|-3)\Big] \\
& -\frac{1}{12}|m||n|\Big\{3(|m|-1)(|n|-1) \\
& \quad -2\Big[(|m|-1)(|m|-2) + (|n|-1)(|n|-2)\Big]\Big\};
\end{aligned} \tag{A.26}
$$

$$\epsilon^{\mathrm{AvH}}_{xy,2} = -\frac{1}{4}\Big[\Big(|m|(|m|-1) + |n|(|n|-1)\Big)^2 - 4m^2n^2\Big]. \tag{A.27}$$

These coefficients are greatly simplified in the continuum limit, in which case one obtains:

$$\left\{\epsilon^{\mathrm{AvH}}_{x,1}\ ;\ \epsilon^{\mathrm{AvH}}_{y,1}\right\} = \left\{\frac{(r_1+r_2)^2}{2!}\ ;\ \frac{(r_1-r_2)^2}{2!}\right\};$$

$$\left\{\epsilon_{x,2}^{\mathrm{AvH}}\ ;\ \epsilon_{y,2}^{\mathrm{AvH}}\ ;\ \epsilon_{xy,2}^{\mathrm{AvH}}\right\} = \left\{\frac{(r_1+r_2)^4}{4!}\ ;\ \frac{(r_1-r_2)^4}{4!}\ ;\ \frac{(r_1^2-r_2^2)^2}{4}\right\}. \qquad \text{(A.28)}$$

Appendix B

Inversion of the Gap Functions

In this appendix the gap functions (3.60) and (3.61) are shown to be invertible. Specifically, the nearest-neighbour bond gap functions Δ_x and Δ_y may be expressed in terms of Δ_s and Δ_d. Though symmetry dictates that there must be at most two degrees of freedom per site (such as Δ_s and Δ_d, or Δ_x and Δ_y), the proof that these combinations indeed close the Hilbert space is in fact quite subtle.

The gauge-invariant definitions of the extended s-wave (3.60) and d-wave (3.61) gap functions are:

$$\begin{aligned}\Delta_d^s(\mathbf{r}) \;\equiv\; & \frac{1}{4}\Big[e^{-i\frac{2\pi}{\phi_0}A_x(\mathbf{r})}\Delta_x(\mathbf{r}) + e^{i\frac{2\pi}{\phi_0}A_x(\mathbf{r})}\Delta_{-x}(\mathbf{r}) \\ & \pm e^{-i\frac{2\pi}{\phi_0}A_y(\mathbf{r})}\Delta_y(\mathbf{r}) \pm e^{i\frac{2\pi}{\phi_0}A_y(\mathbf{r})}\Delta_{-y}(\mathbf{r})\Big], \qquad \text{(B.1)}\end{aligned}$$

where the upper (lower) sign corresponds to s-wave (d-wave). Furthermore, the lattice derivative (or finite difference) in the presence of the gauge field is

$$\begin{aligned}-i(\hat{z}\Pi_z)\Delta_{-z}(\mathbf{r}) &= e^{-i\frac{4\pi}{\phi_0}A_z(\mathbf{r})}\Delta_{-z}(\mathbf{r}+\hat{z}) - \Delta_{-z}(\mathbf{r}) \\ &= e^{-i\frac{4\pi}{\phi_0}A_z(\mathbf{r})}\Delta_z(\mathbf{r}) - \Delta_{-z}(\mathbf{r}). \qquad \text{(B.2)}\end{aligned}$$

Note the complex conjugation compared to Eq. (3.44). In the second line use has been made of the identity

$$\Delta_{-z}(\mathbf{r}+\hat{z}) \equiv \Delta_z(\mathbf{r}). \qquad \text{(B.3)}$$

Combining Eqs. (B.1) and (B.2), one obtains

$$\begin{aligned}\Delta_d^s(\mathbf{r}) &= \frac{1}{2}\left[e^{-i\frac{2\pi}{\phi_0}A_x(\mathbf{r})}\Delta_x(\mathbf{r}) \pm e^{-i\frac{2\pi}{\phi_0}A_y(\mathbf{r})}\Delta_y(\mathbf{r})\right] \\ &\quad +\frac{i}{4}\left[e^{i\frac{2\pi}{\phi_0}A_x(\mathbf{r})}(\hat{x}\Pi_x)\Delta_{-x}(\mathbf{r}) \pm e^{i\frac{2\pi}{\phi_0}A_y(\mathbf{r})}(\hat{y}\Pi_y)\Delta_{-y}(\mathbf{r})\right], \qquad \text{(B.4)}\end{aligned}$$

which may be immediately inverted to yield

$$\begin{aligned}\Delta_x(\mathbf{r}) &= e^{i\frac{2\pi}{\phi_0}A_x(\mathbf{r})}\left[\Delta_s(\mathbf{r}) + \Delta_d(\mathbf{r})\right] - \frac{i}{2}e^{i\frac{4\pi}{\phi_0}A_x(\mathbf{r})}(\hat{x}\Pi_x)\Delta_{-x}(\mathbf{r}); \\ \Delta_y(\mathbf{r}) &= e^{i\frac{2\pi}{\phi_0}A_y(\mathbf{r})}\left[\Delta_s(\mathbf{r}) - \Delta_d(\mathbf{r})\right] - \frac{i}{2}e^{i\frac{4\pi}{\phi_0}A_y(\mathbf{r})}(\hat{y}\Pi_y)\Delta_{-y}(\mathbf{r}). \qquad \text{(B.5)}\end{aligned}$$

The resulting equations for Δ_x and Δ_y appear to depend not only on Δ_s and Δ_d, but also on lattice derivatives. Since from (B.2) the finite difference is odd around $\mathbf{r}$, it might appear that the inversion involves p-wave gap functions that, as spin-triplets, should be prohibited. The physical origin of the derivative terms is that the system is not self-consistent. The degrees of freedom for a given site are constrained by the behaviour at adjacent sites, while the degrees of freedom at an adjacent site are determined by the behaviour of its near neighbours, etc. As shown below, all p-wave terms vanish when the self-consistency is imposed, due to the odd symmetry of the difference operator.

To make this point more explicit, consider the x-bond gap at a given site $\mathbf{r}$:

$$\Delta_x(\mathbf{r}) = e^{i\frac{2\pi}{\phi_0}A_x(\mathbf{r})}\left[\Delta_s(\mathbf{r}) + \Delta_d(\mathbf{r})\right] + \frac{1}{2}\left[\Delta_x(\mathbf{r}) - e^{i\frac{4\pi}{\phi_0}A_x(\mathbf{r})}\Delta_{-x}(\mathbf{r})\right], \qquad \text{(B.6)}$$

where (B.2) has been used. A (gauge-invariant) x-bond gap may also be written for the sites $\mathbf{r} + \hat{x}$ and $\mathbf{r} + 2\hat{x}$:

$$\begin{aligned}e^{-i\frac{4\pi}{\phi_0}A_x(\mathbf{r})}\Delta_x(\mathbf{r}+\hat{x}) &= e^{-i\frac{2\pi}{\phi_0}A_x(\mathbf{r})}\left[\Delta_s(\mathbf{r}+\hat{x}) + \Delta_d(\mathbf{r}+\hat{x})\right] \\ &\quad +\frac{1}{2}\left[e^{-i\frac{4\pi}{\phi_0}A_x(\mathbf{r})}\Delta_x(\mathbf{r}+\hat{x}) - \Delta_{-x}(\mathbf{r}+\hat{x})\right] \\ e^{-i\frac{4\pi}{\phi_0}2A_x(\mathbf{r})}\Delta_x(\mathbf{r}+2\hat{x}) &= e^{-i\frac{6\pi}{\phi_0}A_x(\mathbf{r})}\left[\Delta_s(\mathbf{r}+2\hat{x}) + \Delta_d(\mathbf{r}+2\hat{x})\right] \\ &\quad +\frac{1}{2}\left[e^{-i\frac{4\pi}{\phi_0}2A_x(\mathbf{r})}\Delta_x(\mathbf{r}+2\hat{x}) - \Delta_{-x}(\mathbf{r}+2\hat{x})\right]. \qquad \text{(B.7)}\end{aligned}$$

Making use of the identity (B.3), these three gap functions become

$$\begin{aligned}
\Delta_x(\mathbf{r}) &= e^{i\frac{2\pi}{\phi_0}A_x(\mathbf{r})}\Big[\Delta_s(\mathbf{r}) + \Delta_d(\mathbf{r})\Big] \\
&+ \frac{1}{2}\left[\Delta_x(\mathbf{r}) - e^{i\frac{4\pi}{\phi_0}A_x(\mathbf{r})}\Delta_{-x}(\mathbf{r})\right]; \qquad \text{(B.8)}
\end{aligned}$$

$$\begin{aligned}
e^{-i\frac{4\pi}{\phi_0}A_x(\mathbf{r})}\Delta_x(\mathbf{r}+\hat{x}) &= e^{-i\frac{2\pi}{\phi_0}A_x(\mathbf{r})}\Big[\Delta_s(\mathbf{r}+\hat{x}) + \Delta_d(\mathbf{r}+\hat{x})\Big] \\
&+ \frac{1}{2}\left[e^{-i\frac{4\pi}{\phi_0}A_x(\mathbf{r})}\Delta_x(\mathbf{r}+\hat{x}) - \Delta_x(\mathbf{r})\right] \qquad \text{(B.9)}
\end{aligned}$$

$$\begin{aligned}
e^{-i\frac{4\pi}{\phi_0}2A_x(\mathbf{r})}\Delta_x(\mathbf{r}+2\hat{x}) &= e^{-i\frac{6\pi}{\phi_0}A_x(\mathbf{r})}\Big[\Delta_s(\mathbf{r}+2\hat{x}) + \Delta_d(\mathbf{r}+2\hat{x})\Big] \\
&+ \frac{1}{2}\left[e^{-i\frac{4\pi}{\phi_0}2A_x(\mathbf{r})}\Delta_x(\mathbf{r}+2\hat{x}) - e^{-i\frac{4\pi}{\phi_0}A_x(\mathbf{r})}\Delta_x(\mathbf{r}+\hat{x})\right]. \\
&\qquad \text{(B.10)}
\end{aligned}$$

In the sum over all sites, the last term in (B.9) cancels the second-to-last term in (B.8), and the last term in (B.10) cancels the second-to-last term in (B.9). Identical results are found for Δ_y.

Clearly, at each iteration, the p-wave terms are pushed successively closer toward the system boundary. For periodic boundary conditions they disappear identically. The remaining terms, such as the last term in (B.8) and the second-to-last term in (B.10), would be equal by definition if the system contained only three sites in the $\hat{x}$-direction. This is not the case for general boundary conditions. Using open boundary conditions, for example, the p-wave terms have a finite contribution, but only on the lattice site just next to the boundary. The physical reason is that the number of degrees of freedom is slightly higher for these sites since there are fewer constraining neighbours. Periodic boundary conditions are assumed throughout the derivation of the GL equations.

References

[1] J.G. Bednorz and K.A. Müller, Z. Physik **64**, 189 (1986).

[2] M. Lagues *et al.*, Science **262**, 1850 (1993).

[3] J.-L. Tholence *et al.*, Phys. Lett. A **184**, 215 (1994).

[4] J.R. Waldram, *Superconductivity of Metals and Cuprates* (Institute of Physics Publishing, London, 1996).

[5] L.F. Mattheis, Phys. Rev. Lett. **58**, 1028 (1987).

[6] W.E. Pickett, Rev. Mod. Phys. **61**, 433 (1989).

[7] F.C. Zhang and T.M. Rice, Phys. Rev. B **37**, 3759 (1988).

[8] S.B. Bacci, R. Gagliano, R.M. Martin, and J.F. Annett, Phys. Rev. B **44**, 11 068 (1990).

[9] J.F. Annett and R.M. Martin, Phys. Rev. B **42**, 3929 (1990).

[10] O.K. Anderson *et al.*, Phys. Rev. B **49**, 4195 (1994).

[11] J. Hubbard, Proc. Roy. Soc. London A **243**, 336 (1957); ibid **276**, 238 (1963); ibid **281**, 1386 (1964).

[12] N.F. Mott, *Metal-Insulator Transitions* (Taylor and Francis, London, 1974).

[13] J. Rossat-Mignod *et al.*, Physica C **152**, 19 (1988); ibid **169**, 58 (1991); ibid **185-189**, 86 (1991).

[14] T.Thio *et al.*, Phys. Rev. B **38**, 905 (1988); ibid **41**, 231 (1990).

[15] R.J. Birgeneau and G. Shrane, in *Physical Properties of High-Temperature Superconductors*, D.M. Ginsberg, ed. (World Scientific, Singapore, 1989).

[16] J.M. Tranquada *et al.*, Phys. Rev. Lett. **60**, 156 (1988); J.M. Tranquada *et al.*, Phys. Rev. B **46**, 5561 (1992); B.J. Sternlieb *et al.*, Phys. Rev. B **47**, 5320 (1993).

[17] N. Pyka, L. Pintschovius, and A. Yu. Rumiantsev, Z. Phys. B **82**, 177 (1991).

[18] T. Imai, C.P. Slichter, A.P. Paulikas, and B. Veal, Phys. Rev. B **47**, 9158 (1993); R.L. Corey *et al.*, Phys. Rev. B **53**, 5907 (1996); C.P. Slichter *et al.*, Phil. Mag. B **74**, 545 (1996).

[19] S.M. Hayden *et al.*, Phys. Rev. Lett. **76**, 1344 (1996).

[20] G. Blumberg *et al.*, Phys. Rev. B **49**, 13 296 (1994).

[21] P.W. Anderson, Science **235**, 1196 (1987).

[22] A. Aharony *et al.*, Phys. Rev. Lett. **60**, 1330 (1988).

[23] F. Marsiglio, A. Ruckenstein, S. Schmitt-Rink, and C. Varma, Phys. Rev. B **43**, 10 882 (1991).

[24] G. Martinez and P. Horsch, Phys. Rev. B **44**, 317 (1991).

[25] Z. Liu and E. Manousakis, Phys. Rev. B **45**, 2425 (1992).

[26] J.R. Schrieffer *et al.*, Phys. Rev. B **39**, 11 663 (1989).

[27] B.I. Shraiman and E.D. Siggia, Phys. Rev. Lett. **61**, 467 (1988).

[28] N. Bulut, D.J. Scalapino and S.R. White, Phys. Rev. B **50**, 7215 (1994).

[29] A.P. Kampf, Phys. Rep. **249**, 219 (1994).

[30] K.J.E. Vos, R.J. Gooding, P.W. Leung, and L. Chen, Phys. Rev. B **51**, 12 034 (1995); P.W. Leung and R.J. Gooding, Phys. Rev. B **52**, R15 711 (1995); K.J.E. Vos and R.J. Gooding, Z. Phys. **101**, 79 (1996).

[31] E. Dagotto, A. Nazarenko, and M. Boninsegni, Phys. Rev. Lett. **73**, 728 (1994); E. Dagotto, A. Nazarenko and A. Moreo, Phys. Rev. Lett. **74**, 310 (1995); A. Nazarenko *et al.*, Phys. Rev. B **51**, 8676 (1995); A. Nazarenko and E. Dagotto, Phys. Rev. B **54**, 13 158 (1996).

[32] A.F. Barabanov, R.O. Kuzian, and L.A. Maksimov, J. Phys. C **3**, 9129 (1991).

[33] A.V. Chubukov, D.K. Morr, and K.A. Shakhnovich, Phil. Mag. B **74**, 563 (1996); A.V. Chubukov and D.K. Morr, unpublished.

[34] D.S. Marshall *et al.*, Phys. Rev. Lett. **76**, 4841 (1996); D.S. Marshall, Science **273**, 325 (1996).

[35] C. Kendziora, R.J. Kelley, and M. Onellion, Phys. Rev. Lett. **77**, 727 (1996).

[36] D.S. Dessau *et al.*, Phys. Rev. Lett. **71**, 2781 (1993).

[37] K. Gofron *et al.*, J. Phys. Chem. Solids bf 54, 1193 (1993); K. Gofron *et al.*, Phys. Rev. Lett. **73**, 3302 (1994).

[38] Z.-X. Shen and D.S. Dessau, Phys. Rep. **253**, 1 (1995).

[39] J.M. Harris *et al.*, Phys. Rev. B **54**, R15 665 (1996); P.J. White *et al.*, Phys. Rev. B **54**, R15 669 (1996).

[40] S. Martin *et al.*, Phys. Rev. Lett. **60**, 2194 (1988).

[41] T.A. Friedmann *et al.*, Phys. Rev. B **42**, 6217 (1990).

[42] T. Ito, Y. Nakamura, H. Takagi, and S. Uchida, Physica C **185-189**, 1267 (1991).

[43] T. Manako, Y. Shimakawa, Y. Kubo, and H. Igarashi, Physica C **185-189**, 1327 (1991).

[44] Z. Schlesinger *et al.*, Phys. Rev. Lett. **65**, 801 (1990); L.D. Rotter *et al.*, Phys. Rev. Lett. **67**, 2741 (1991).

[45] R.C. Yu *et al.*, Phys. Rev. Lett. **69**, 1431 (1992).

[46] K. Krishana *et al.*, Phys. Rev. Lett. **75**, 3529 (1995).

[47] N. Hamada *et al.*, Phys. Rev. B **42**, 6238 (1990).

[48] N.P. Ong *et al.*, Physica C **185-189**, 34 (1991).

[49] A.B. Kaiser and G. Mountjoy, Phys. Rev. B **43**, 6266 (1991).

[50] J.W. Loram *et al.*, Phil. Mag. B **65**, 1405; J.W. Loram, K.A. Mirza, J.R. Cooper, and W.Y. Liang, Phys. Rev. Lett. **71**, 1740 (1993); J.W. Loram *et al.*, Physica C **235-240**, 134 (1994).

[51] G. Mozurkewich *et al.*, Phys. Rev. B **46**, 11 914 (1992).

[52] P. Gammel *et al.*, Phys. Rev. Lett. **59**, 2592 (1987).

[53] C.E. Gough *et al.*, Nature **326**, 855 (1987).

[54] M. Takigawa, P.C. Hammel, R.H. Heffner, and Z. Fisk, Phys. Rev. B **39**, 7371 (1989).

[55] S.E. Barrett *et al.*, Phys. Rev. B. **41**, 6283 (1990); ibid, Phys. Rev. Lett **66**, 108 (1991).

[56] C.P. Slichter, J. Phys. Chem. Solids, **54**, 1439 (1993).

[57] H. Takagi *et al.*, Phys. Rev. B **40**, 2254 (1989); H. Takagi *et al.*, Phys. Rev. Lett. **69**, 2975 (1992).

[58] J.E. Evetts and P.H. Kes, in *Concise Emcyclopædia of Magnetic and Superconducting Materials*, J. Evetts, ed. (Pergamon Press, Oxford, 1992).

[59] A. Umezawa *et al*, Phys. Rev. B **38**, 2843 (1988); A. Umezawa *et al*, Phys. Rev. B **42**, 8744 (1990).

[60] V.V. Moshchalkov *et al.*, Physica C **175**, 407 (1991).

[61] D.L. Zheng *et al.*, Phys. Rev. B. **49**, 1417 (1994).

[62] H. Takagi *et al.*, Phys. Rev. B **40**, 2254 (1989).

[63] Y. Tokura, in *Physics of High-Temperature Superconductors*, S. Maekawa and M. Sato, eds. (Springer, Berlin, 1992).

[64] D. Saint-James, E.J. Thomas, and G. Sarma, *Type-II Superconductivity* (Pergamon Press, Oxford, 1969).

[65] E.Z. Meylikhov and V.G. Shapiro, Phys. Chem. Techn. **4**, 1437 (1991).

[66] U. Welp *et al.*, Phys. Rev. Lett. **62**, 1908 (1989); U. Welp *et al.*, Physica C **161**, 1 (1989).

[67] A.S. Alexandrov, Phys. Rev. B **38**, 925 (1988); ibid, Sov. Phys. J.E.T.P. **68**, 167 (1989); ibid, Physica C **158**, 337 (1989).

[68] J. Ranninger, Z. Phys. B **84**, 167 (1991).

[69] L. Krusin-Elbaum *et al.*, Phys. Rev. Lett. **62**, 217 (1989).

[70] A. Schilling, F. Hulliger, and H.R. Ott, Physica C **168**, 272 (1990).

[71] K. Zhang, Phys. Rev. Lett. **73**, 2484 (1994).

[72] D.N. Basov *et al.* Phys. Rev. Lett. **74**, 598 (1995).

[73] P.G. de Gennes, *Superconductivity of Metals and Alloys* (W.A. Benjamin, New York, 1966).

[74] G. Mante *et al.*, Z. Phys. B **80**, 181 (1990).

[75] C.G. Olson *et al.*, Phys. Rev. B **42**, 381 (1990).

[76] C.M. Fowler *et al.*, Phys. Rev. Lett. **68**, 534 (1991).

[77] J. Orenstein *et al.*, Phys. Rev. B **42**, 6342 (1990).

[78] Y.J. Uemura *et al.*, Physica C **162-164**, 857 (1989); Y.J. Uemura *et al.*, Phys. Rev. Lett. **66**, 2665 (1991).

[79] J. Bardeen, L.N. Cooper, and J.R. Schrieffer, Phys. Rev. **108**, 1175 (1957).

[80] Ch. Niedermayer *et al.*, Phys. Rev. Lett. **71**, 1764 (1993).

[81] D.J. Scalapino, Phys. Rep. **250**, 329 (1995).

[82] D.M. Paul *et al.*, Phys. Rev. Lett. **58**, 1976 (1987).

[83] A. Reller, J.G. Bednorz, and K.A. Müller, Z. Phys. B **67**, 285 (1987).

[84] J.J. Capponi *et al.*, Europhys. Lett. **3**, 1301 (1987).

[85] M. Sigrist and T.M. Rice, Z. Phys. B **68**, 9 (1987).

[86] M.K. Crawford *et al.*, Science **250**, 1390 (1990).

[87] M. Ronay, M.A. Frisch, and T.R. McGuire, Phys. Rev. B **45**, 344 (1992).

[88] J.P. Franck *et al.*, Phys. Rev. B **44**, 5318 (1991); J.P. Franck, S. Havker, and J.H. Brewer, Phys. Rev. Lett. **71**, 283 (1993).

[89] T.E. Faber and A.B. Pippard, Proc. Roy. Soc. London A **231**, 336 (1955).

[90] W. Brenig, Phys. Rep. **251**, 153 (1995).

[91] P. Monthoux, A. Balatsky, and D. Pines, Phys. Rev. Lett. **67**, 3448 (1991); ibid, Phys. Rev. B **46**, 14 803 (1992).

[92] N. Bulut and D.J. Scalapino, J. Phys. Chem. Solids **54**, 1109 (1993).

[93] D. Pines, Physica C **235-240**, 113 (1994);

[94] E. Dagotto, Rev. Mod. Phys. **66**, 763 (1994).

[95] D.J. Van Harlingen, Rev. Mod. Phys. **67**, 515 (1995).

[96] M. Sigrist and T.M. Rice, Rev. Mod. Phys. **67**, 503 (1995).

[97] A. Maeda *et al.*, Phys. Rev. Lett. **74**, 1202 (1995).

[98] W.N. Hardy *et al.*, Phys. Rev. Lett. **70**, 3999 (1993).

[99] F. Gross *et al.*, Z. Phys. B **64**, 175 (1986).

[100] C.H. Choi and P. Muzikar, Phys. Rev. B **37**, 5947 (1988).

[101] J. Annett, N. Goldenfeld, and S.R. Renn, Phys. Rev. B **43**, 2778 (1991).

[102] S.K. Yip and J.A. Sauls, Phys. Rev. Lett. **69**, 2264 (1992).

[103] A. Porch *et al.*, Physica C **214**, 350 (1993).

[104] M. Zhenxiang *et al.*, Phys. Rev. Lett. **71**, 781 (1993).

[105] J.E. Sonier *et al.*, Phys. Rev. Lett. **72**, 744 (1994).

[106] P.W. Anderson, Phys. Rev. Lett. **3**, 325 (1959).

[107] P.J. Hirschfeld and N. Goldenfeld, Phys. Rev. B **48**, 4219 (1993); P.J. Hirschfeld, O. Putikka, and D.J. Scalapino, Phys. Rev. B **50**, 10 250 (1994).

[108] A.V. Balatsky, A. Rosengren, and B.L. Altshuler, Phys. Rev. Lett. **73**, 720 (1994).

[109] K.A. Moler, *et al.*, Phys. Rev. Lett. **73**, 2744 (1994); K.A. Moler *et al.*, Phys. Rev. B **55**, 3954 (1997).

[110] M. Gurvitch *et al.*, Phys. Rev. Lett. **63**, 1008 (1989).

[111] D. Mandrus *et al.*, Nature **351**, 460 (1991).

[112] M. Beasley *et al.*, Physica C **185-189**, 227 (1991).

[113] C.-R. Hu, Phys. Rev. Lett. **72**, 1526 (1994).

[114] Z.-X. Shen *et al.*, Phys. Rev. Lett. **70**, 1553 (1990); Z.-X. Shen *et al.*, J. Chem. Solids **54**, 1169 (1993).

[115] L.C. Hebel and C.P. Slichter, Phys. Rev. **113**, 1504 (1959).

[116] J.A. Martindale *et al.*, Phys. Rev. Lett. **68**, 702 (1992); J.A. Martindale *et al.*, Phys. Rev. B **47**, 9155 (1993).

[117] D.A. Wollman, *et al.*, Phys. Rev. Lett. **71**, 2134 (1993); ibid **73**, 1872 (1994); D.A. Wollman, *et al.*, Phys. Rev. Lett. **74**, 797 (1995).

[118] D.A. Brawner and H.R. Ott, Phys. Rev. B **50**, 6530 (1994).

[119] A. Mathai *et al.*, Phys. Rev. Lett. **74**, 4523 (1995).

[120] C.C. Tsuei, *et al.*, Phys. Rev. Lett. **73**, 593 (1994); J.R. Kirtley *et al.*, Nature **373**, 225 (1995); C.C. Tsuei, *et al.* Science **271**, 329 (1996); C.C. Tsuei, *et al.* Nature **387**, 481 (1997).

[121] W. Braunisch *et al.*, Phys. Rev. Lett. **68**, 1908 (1992); W. Braunisch *et al.*, Phys. Rev. B **48**, 4030 (1993).

[122] V. Kataev *et al.*, Sov. Phys. J.E.T.P. Lett. **58**, 636 (1993).

[123] V.L. Ginzburg and L.D. Landau, Zh. Eksperim. i Teor. Fiz. **20**, 1064 (1950).

[124] J.D. Jackson, *Classical Electrodynamics* (John Wiley and Sons, New York, 1975), p. 216.

[125] A.A. Abrikosov, Sov. Phys. J.E.T.P. **5**, 1174 (1957).

[126] W.H. Kleiner, L.M. Roth, and S.H. Autler, Phys. Rev. **133**, A1266 (1964).

[127] R. Joynt, Phys. Rev. B **41**, 4271 (1990).

[128] M.B. Walker, Phys. Rev. B **53**, 5835 (1996).

[129] P.I. Soininen, C. Kallin, and A.J. Berlinsky, Phys. Rev. B **50**, 13 883 (1994).

[130] M. Sigrist, K. Kuboki, P.A. Lee, A.J. Millis, and T.M. Rice, Phys. Rev. B **53**, 2835 (1996); A.B. Kuklov and M. Sigrist, Int. J. Mod. Phys. B **11**, 1113 (1997); A. Huck, A. van Otterlo, M. Sigrist, unpublished (cond-mat/9705025).

[131] H. Aubin *et al.*, Phys. Rev. Lett. **78**, 2624 (1997).

[132] G.E. Volovik, Sov. Phys. J.E.T.P. Lett. **58**, 469 (1993).

[133] M. Ichioka, N. Enomoto, N. Hayashi and K. Machida, Phys. Rev. B **53**, 2233 (1996).

[134] A.J. Berlinsky *et al.*, Phys. Rev. Lett. **75**, 2200 (1995).

[135] M. Franz, *et al.*, Phys. Rev. B **53**, 5795 (1996).

[136] M. Ichioka, N. Hayashi, N. Enomoto, and K. Machida, Phys. Rev. B **53**, 15 316 (1996); N. Enomoto, M. Ichioka, and K. Machida, J. Phys. Soc. Jpn. **66**, 204 (1997).

[137] Y. Ren, J.-H. Xu and C.S. Ting, Phys. Rev. Lett. **74**, 3680 (1995); J.-H. Xu, Y. Ren and C.S. Ting, Phys. Rev. B **52**, 7663 (1995).

[138] J.-H. Xu, Y. Ren, and C.-S. Ting, Phys. Rev. B **53**, R2991 (1996).

[139] M. Ichioka, N. Enomoto, K. Machida, unpublished (cond-mat/9704147).

[140] K. Takanaka and K. Kuboya, Phys. Rev. Lett. **75**, 324 (1995).

[141] L.P. Gor'kov, Soviet Phys. JETP **9**, 1364 (1959); L.P. Gor'kov, Soviet Phys. JETP **10**, 998 (1960).

[142] I. Affleck, M. Franz, and M.H.S. Amin, Phys. Rev. B **55**, 704 (1997).

[143] B. Keimer *et al.*, J. Appl. Phys. **76**, 1 (1994).

[144] I. Maggio-Aprile *et al.*, Phys. Rev. Lett. **75**, 2754 (1995).

[145] M.B. Walker and T. Timusk, Phys. Rev. B **52**, 97 (1995).

[146] K.B. Lyons *et al.*, Phys. Rev. **B47**, 8195 (1993).

[147] M. Zapotocky, D.L. Maslov, and P.M. Goldbart, Phys. Rev. B **55**, 6599 (1997).

[148] J.J. Betouras and R. Joynt, Physica C **250**, 256 (1995); J.J. Betouras *et al.*, Appl. Phys. Lett. **69**, 2432 (1996).

[149] R. Micnas, J. Ranninger, S. Robaszkiewicz and S. Tabor, Phys. Rev. B **37**, 9410 (1988); R. Micnas, J. Ranninger and S. Robaszkiewicz, Rev. Mod. Phys. **62**, 113 (1990).

[150] Y. Wang and A.H. MacDonald, Phys. Rev. B **52**, R3876 (1995).

[151] A. Nazarenko, A. Moreo, J. Riera and E. Dagotto, Phys. Rev. B **54**, R768 (1996).

[152] A.A. Abrikosov, J.C. Campuzano and K. Gofron, Physica (Amsterdam) **214C**, 73 (1993).

[153] R. Fehrenbacher and M.R. Norman, Phys. Rev. Lett. **74**, 3884 (1995).

[154] A.A. Abrikosov, L.P. Gor'kov, and I.E. Dzyaloshinski, *Methods of Quantum Field Theory in Statistical Physics* (Prentice-Hall, New Jersey, 1963).

[155] A.L. Fetter and J.D. Walecka, *Quantum Theory of Many-Particle Systems* (McGraw-Hill, San Francisco, 1971).

[156] T. Matsubara, Prog. Theor. Phys. **14**, 351 (1955).

[157] Y. Nambu, Phys. Rev. **117**, 648 (1960).

[158] A.A. Abrikosov, L.P. Gor'kov, and I.E. Dzyaloshinski, Sov. Phys. J.E.T.P. **9**, 636 (1959).

[159] E.S. Fradkin, Sov. Phys. J.E.T.P. **9**, 912 (1959).

[160] G.D. Mahan, *Many-Particle Physics* (Plenum Press, New York, 1981).

[161] B. Oh *et al.*, Phys. Rev. B **37**, 7861 (1988).

[162] M. Franz, I. Affleck, and M.H.S. Amin, Phys. Rev. Lett. **79**, 1555 (1997).

[163] M. Franz, private communication.

[164] R.J. Cava *et al.*, Physica C **165**, 419 (1990).

[165] M.K. Wu, Phys. Rev. Lett. **58**, 908 (1987).

[166] J. Chrosch and E.K.H. Salje, Physica C **225**, 111 (1994).

[167] S. Fleshler *et al.*, Phys. Rev. B **47**, 14448 (1993).

[168] Y. Zhu *et al.*, Appl. Phys. Lett. **54**, 374 (1989); Y. Zhu, M. Suenaga, Y. Xu, and M. Kawasaki, Mater. Res. Soc. Symp. Proc. **159**, 413 (1990).

[169] Z. Cai and S.D. Mahanti, Phys. Rev. B **40**, 6558 (1989).

[170] Y. Xu *et al.*, Physica C **169**, 205 (1990).

[171] Y. Zhu and M. Suenaga, in "Interfaces in High-T_c Superconducting Systems," S.L. Shindé and D.A. Rudman, eds. Springer-Verlag, New York (1994).

[172] E.M. Gyorgy *et al.*, Appl. Phys. Lett. **55**, 283 (1989); E.M. Gyorgy *et al.*, Appl. Phys. Lett. **56**, 2465 (1990).

[173] W.K. Kwok *et al.*, Phys. Rev. Lett. **64**, 966 (1990).

[174] U. Welp *et al.*, Physica **235-240C**, 241 (1994).

[175] V.K. Vlasko-Vlasov *et al.*, Phys. Rev. Lett. **72**, 3246 (1994).

[176] H. Safar *et al.*, Phys. Rev. B **52**, R9875 (1995); H. Safar, S.R. Foltyn, Q.X. Jia, and M.P. Maley, Phil. Mag. B **74**, 647 (1996); H. Safar *et al.*, Appl. Phys. Lett. **68**, 1853 (1996).

[177] M. Oussena *et al.*, Phys. Rev. B **51**, 1389 (1995).

[178] C.A. Duran *et al.*, Nature **357**, 474 (1992); C.A. Duran *et al.*, Phys. Rev. Lett. **74**, 3712 (1995).

[179] U. Welp *et al.*, Phys. Rev. Lett. **74**, 3713 (1995).

[180] R.J. Wijngaarden *et al.*, Phys. Rev. B **55**, 3268 (1997).

[181] K.A. Moler, J.R. Kirtley, R. Liang, D. Bonn, and W.N. Hardy, Phys. Rev. B **55**, 12 753 (1997).

[182] L.Y. Vinnikov, L.A. Gurevich, G.A. Yemelchenko, and Y.A. Ossipyan, Solid State Commun. **67**, 421 (1988).

[183] M. Tachiki and S. Takachashi, Solid State Commun. **70**, 291 (1989); ibid **72**, 1083 (1989).

[184] T.L. Hylton and M.R. Beasley, Phys. Rev. B **41**, 11 669 (1990).

[185] K. Watanabe *et al.*, Appl. Phys. Lett. **65**, 1490 (1990).

[186] H. Jiang *et al.*, Phys. Rev. Lett. **63**, 1785 (1991).

[187] C. Villard *et al.*, Phys. Rev. Lett. **77**, 3913 (1996).

[188] B.D. Josephson, Phys. Lett. **1**, 251 (1962).

[189] J.R. Clem *et al.*, Phys. Rev. B **35**, 6637 (1987).

[190] A.A. Abrikosov, A.I. Buzdin, M.L. Kulic, and D.A. Kaptsov, Sov. Phys. J.E.T.P. **68**, 210 (1989).

[191] E.A. Shapoval, Sov. Phys. J.E.T.P. Lett. **61**, 132 (1995).

[192] G. Deutscher and K.A. Müller, Phys. Rev. Lett. **59**, 1745 (1987); G. Deutscher, IBM J. Res. Dev. **33**, 293 (1989).

[193] M. Sigrist and T.M. Rice, J. Phys. Soc. Jpn. **61**, 4283 (1992).

[194] A. Rosová, C. Boulesteix, and I. Vávra, Physica C **214**, 247 (1993).

[195] C. O'Donovan, M.D. Lumsden, B.D. Gaulin, and J.P. Carbotte, Phys. Rev. B **55**, 9088 (1997); M.D. Lumsden and B.D. Gaulin, unpublished.

[196] M.B. Walker and J. Luettmer-Strathmann, Phys. Rev. B **54**, 588 (1996); ibid, J. Low Temp. Phys. **105**, 483 (1996).

[197] R. Ferrell and R. Prange, Phys. Rev. Lett. **10**, 479 (1963).

[198] B.D. Josephson, Adv. Phys. **14**, 419 (1965).

[199] D.B. Bailey, M. Sigrist, and R.B. Laughlin, Phys. Rev. B **55**, 15 239 (1997).

[200] V.B. Geshkenbein and A.I. Larkin, Phys. Rev. B **36**, 235 (1987).

[201] J. Mannhart *et al.*, Phys. Rev. Lett. **77**, 2782 (1996).

[202] M.B. Walker, Phys. Rev. B **54**, 13 269 (1996).

[203] J.R. Kirtley, *et al.* Phys. Rev. B **51**, 12 057 (1995).

[204] M. Matsumoto and H. Shiba, J. Phys. Soc. Jpn. **64**, 3384 (1995); ibid **64**, 4867 (1995); ibid **65**, 2194 (1996).

[205] K.A. Moler *et al.*, Conference Proceedings of 10th Anniversary HTS Workshop on Physics, Materials, and Applications, Houston, Texas, March 12-16 (1996).

[206] P. Chaudhari and S.Y. Lin, Phys. Rev. Lett. **72**, 1048 (1994).

[207] A.J. Millis, Phys. Rev. B **49**, 15 408 (1994).

[208] A.G. Sun, D.A. Gajewski, M.B. Maple and R.C. Dynes, Phys. Rev. Lett. **72**, 2267 (1994); A.S. Katz, A.G. Sun, R.C. Dynes, and K. Char, Appl. Phys. Lett. **66**, 105 (1995); R. Kleiner *et al.*, Phys. Rev. Lett. **76**, 2161 (1996).

[209] B. Horovitz, G.R. Barsch, and J.A. Krumhansl, Phys. Rev. B **43**, 1021 (1991).

[210] K. Maki and T. Tsuneto, Prog. Theor. Phys. **27**, 228 (1962).

[211] N.N. Bogoliubov, Sov. Phys. J.E.T.P. **7**, 41 (1958).

[212] J.G. Valatin, Nuovo Cimento **7**, 843 (1958).

[213] W.A. Atkinson and J.P. Carbotte, Phys. Rev. B **52**, 10 601 (1995).

[214] M. Franz, C. Kallin, and A.J. Berlinsky, Phys. Rev. B **54**, R6897 (1996).

[215] A.H. Wilson, *Theory of Metals* (Cambridge University Press, Cambridge, 1958).

[216] H. Srikanth *et al.* Phys. Rev. B **55**, R14 733 (1997).

[217] H. Takayama, Y.R. Lin-Liu, and K. Maki, Phys. Rev. B **21**, 2388 (1980).

[218] P.A. Lee, Phys. Rev. Lett. **71**, 1887 (1993); Y. Hatsugai and P.A. Lee, Phys. Rev. B **48**, 4204 (1993).

[219] T. Xiang and J.M. Wheatley, Phys. Rev. B **51**, 11 721 (1995); T. Xiang, Phys. Rev. B **52**, 6204 (1995).

[220] J.H. Xu, J.H. Miller, and C.S. Ting, Phys. Rev. B **53**, 3604 (1996).

[221] A.F. Andreev, Sov. Phys. J.E.T.P. **19**, 1228 (1964); *ibid*, **22**, 455 (1966).

[222] J. Bardeen *et al.* Phys. Rev. **187**, 556 (1969).

[223] C. Bruder, Phys. Rev. B **41**, 4017 (1990).

[224] L.J. Buchholtz and G. Zwicknagl, Phys. Rev. B **23**, 5788 (1981); L.J. Buchholtz, M. Palumbo, D. Rainer, and J.A. Sauls, J. Low Temp. Phys. **101**, 1079 (1995); L.J. Buchholtz, M. Palumbo, and D. Rainer, *ibid*, 1099 (1995).

[225] Y. Tanaka and S. Kashiwaya, Phys. Rev. Lett. **74**, 3451 (1995).

[226] Yu.S. Barash, A.A. Svidzinsky, and I.E. Tamm, Phys. Rev. B **53**, 15 254 (1996); Yu.S. Barash, H. Burkhardt, D. Rainer, and P.N. Lebedev, Phys. Rev. Lett. **77**, 4070 (1996); Yu.S. Barash, A.A. Svidzinsky, H. Burkhardt, and P.N. Lebedev, Phys. Rev. B **55**, 15 282 (1997).

[227] H.F. Hess *et al.*, Phys. Rev. Lett. **62**, 214 (1989); H.F. Hess, R.B. Robinson, and J.V. Waszczak, Physica B **169**, 422 (1991).

[228] J.D. Shore, M. Huang, A. Dorsey, and J.P. Sethna, Phys. Rev. Lett. **62**, 3089 (1989).

[229] L. Yu, Acta Physica Sinica **21**, 75 (1965).

[230] H. Shiba, Prog. Theor. Phys. **40**, 435 (1968).

[231] A.I. Rusinov, Sov. Phys. J.E.T.P. Lett. **9**, 85 (1969).

[232] T. Walsh, Int. J. Mod. Phys. **6**, 125 (1992).

[233] A.A. Abrikosov and L.P. Gor'kov, Sov. Phys. J.E.T.P. **12**, 1243 (1961).

[234] A.V. Balatsky, M.I. Salkola, and A. Rosengren, Phys. Rev. B **51**, 15 547 (1995); M.I. Salkola, A.V. Balatsky, and D.J. Scalapino, Phys. Rev. Lett. **77**, 1841 (1996); A.V. Balatsky and M.I. Salkola, Phys. Rev. Lett. **76**, 2386 (1996).

[235] M. Covington *et al.* Phys. Rev. Lett. **79**, 277 (1997).

[236] M. Fögelstrom, D. Rainer, and J.A. Sauls, Phys. Rev. Lett. **79**, 281 (1997).

[237] B.A. Glowacki, in *Critical Current Limitations in High Temperature Superconductors*, M. Baran, W. Gorzkowski, and H. Szymczak, eds. (World Scientific, Singapore, 1992), p. 216.

[238] M. Tinkham, *Introduction to Superconductivity* (Krieger, Melbourne, 1975).

[239] H. Darhmaoui and J. Jung, Phys. Rev. B **53**, 14 621 (1996).

[240] P. Chaudhari *et al.*, Phys. Rev. Lett, **60**, 1635 (1988); D. Dimos, P. Chaudhari, J. Mannhart, and F.K. le Goues, Phys. Rev. Lett. **61**, 219 (1988); J. Mannhart *et al.*, Phys. Rev. Lett. **61**, 2476 (1988).

[241] S.P. Benz *et al.*, Phys. Rev. B **42**, 6165 (1990).

[242] S.L. Shindé *et al.*, Phys. Rev. B **41**, 8838 (1990).

[243] D.R. Nelson and V.M. Vinokur, Phys. Rev. B **48**, 13 060 (1993).

[244] G. Kaestner *et al.*, Physica C **243**, 281 (1995).

[245] D.J. Scalapino, S.R. White, and S.C. Zhang, Phys. Rev. B **68**, 2830 (1992).

[246] C. Kittel, *Introduction to Solid State Physics* (John Wiley and Sons, New York, 1961).

[247] X.D. Wu *et al.*, Appl. Phys. Lett. **65**, 1961 (1994); X.D. Wu *et al.*, Appl. Phys. Lett. **67**, 2397 (1995).

[248] Y. Zhu, Z.L. Wang, and M. Suenaga, Phil. Mag. A **67**, 11 (1993).

[249] N.D. Browning, J. Yuan, and L.M. Brown, Physica C **202**, 12 (1992); N.D. Browning *et al.*, Physica C **212**, 185 (1993).

[250] P.W. Anderson, Phys. Rev. Lett. **9**, 309 (1962).

[251] Y.B. Kim, Rev. Mod. Phys. **36**, 39 (1964).

[252] M. Tinkham, Helv. Phys. Acta **61**, 443 (1988).

[253] J. Lesueur, L.H. Greene, W.L. Friedmann, and A. Inam, Physica C **191**, 325 (1992).

[254] S. Kashiwaya, M. Koyanagi, M. Matsuda, and K. Kajimura, Physica B **194-196**, 2119 (1994).

IMAGE EVALUATION
TEST TARGET (QA-3)

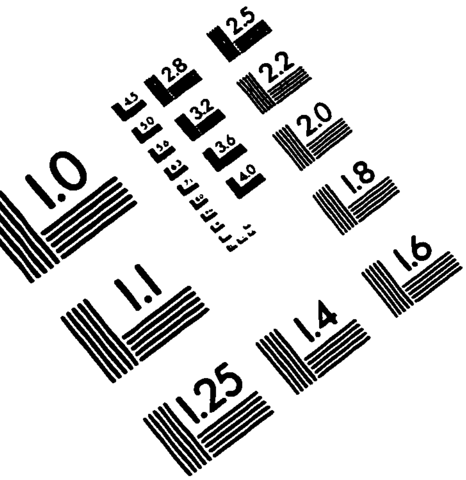

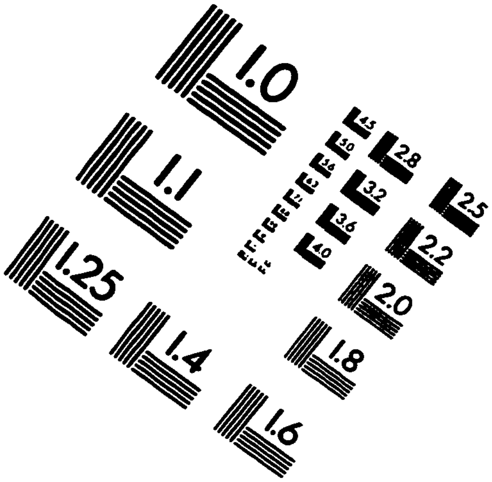

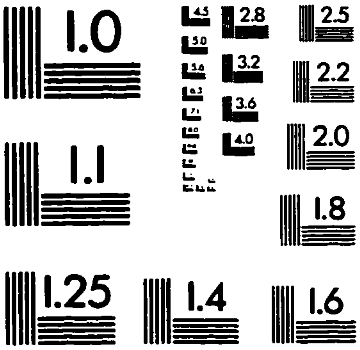

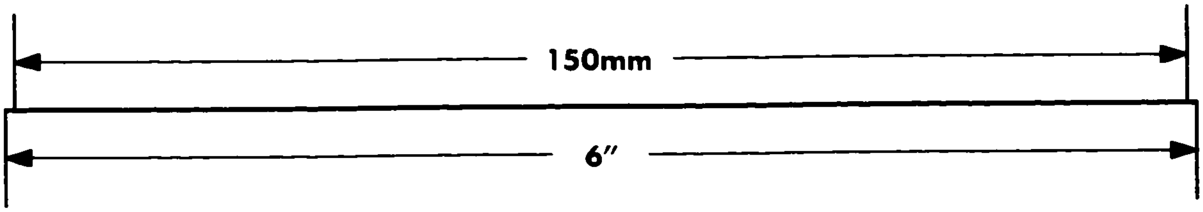

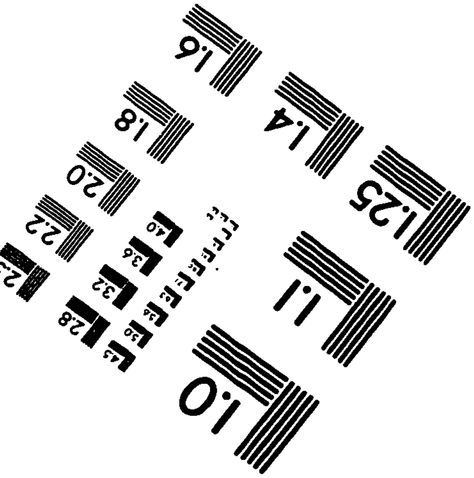

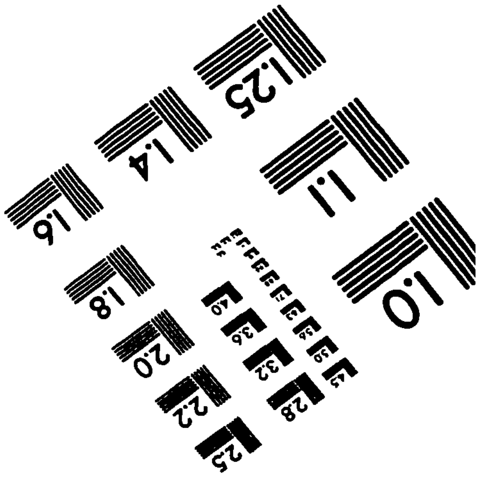

APPLIED IMAGE . Inc
1653 East Main Street
Rochester, NY 14609 USA
Phone: 716/482-0300
Fax: 716/288-5989

© 1993, Applied Image, Inc., All Rights Reserved